The benefit of muscle-actuated systems: internal mechanics, optimization and learning

Von der Fakultät Bau- und Umweltingenieurwissenschaften der Universität Stuttgart und
dem Stuttgarter Zentrum für Simulationswissenschaft
zur Erlangung der Würde einer Doktor-Ingenieurin (Dr.-Ing.)
genehmigte Abhandlung

Vorgelegt von

Isabell Wochner

aus Balingen

Hauptberichter:	Prof. Dr. Syn Schmitt
Mitberichter:	Prof. Dr. Seungmoon Song
Tag der mündlichen Prüfung:	06. September 2023

Universität Stuttgart
Institut für Modellierung und Simulation biomechanischer Systeme
Computational Biophysics and Biorobotics
CBB-003-2023

2023

Acknowledgments

Here, I want to thank all the people who have supported and accompanied me during my PhD journey. First of all, I am very thankful for the great support and mentorship of my advisor Syn Schmitt. He always had an open ear for my questions and ideas and gave me the freedom to develop my own research ideas while inspiring me to do research in the fascinating field of biomechanics. Furthermore, I would like to thank my examination committee members Seungmoon Song and Felix Fritzen for the excellent discussions and the valuable feedback and comments.

A big thank you also goes to my fantastic colleagues both from the CBB group as well as everyone else I worked with directly or indirectly. I am very grateful for the great collaboration and the many fruitful discussions (both scientific and personal). I would like to thank in particular Daniel Häufle, Gigi Schreiber, Johannes Walter, Julia Riede, Katrin Stollenmaier, Michael Günther, Nadine Badie, Oleksandr Martynenko, Pablo Chacon, Patrick Lerge, Pierre Schumacher, Simon Wolfen, and Tobias Nadler. Special thanks also go to Elsa Bunz, Maria Hammer, and Lennart Nölle who proofread parts of this thesis or provided me with valuable feedback for my defense talk. All of you contributed to this thesis to some extent and I thank you all for making my everyday work life fun.

Further, I would like to thank all my friends and family for their support and encouragement. In particular, I would like to thank my parents Corinna and Martin for their support and for always believing in me. Last but not least, I am deeply grateful to Sebi for your patience, your support in all matters, and for always being there for me.

Thank you all!

Declaration / Erklärung

Hiermit erkläre ich, dass ich die vorliegende Dissertation selbstständig und nur unter Verwendung der ausdrücklich bezeichneten Quellen und Literatur verfasst habe.

I hereby declare that I have written this dissertation independently, using only the specified resources and literature.

Isabell Wochner
Stuttgart, den 17.05.2023

Contents

List of Figures

List of Tables

Notation

This list contains only the most important symbols and abbreviations that are used several times throughout this thesis.

List of Symbols

General mathematical notation

f	function
$\frac{df}{dx}$	total derivative of f with respect to x
$\frac{\partial f}{\partial x}$	partial derivative of f with respect to x
$\dot{x}$	first time derivative of x
$\ddot{x}$	second time derivative of x
x_i	i-th element of vector x, typically, $i = 1, \ldots, n^{\text{musc}}$
x_t	current state x at a given time t
$x_{t-\delta}$	time-delayed state x at time $t - \delta$
x_{t+1}	state x at next time increment $t + 1$
$\overline{x}$	mean value of x
$\mathbb{E}(x)$	expected value of x
$\mathbb{R}$	set of real numbers

Rigid body mechanics

n^{DoF}	number of degrees of freedom
$\mathbf{q} \in \mathbb{R}^{n^{\text{DoF}}}$	vector of generalized coordinates, see Eq. (2.9)
$\boldsymbol{\mathcal{F}} \in \mathbb{R}^{n^{\text{DoF}}}$	generalized forces, see Eq. (2.9)
$\mathcal{L}(\mathbf{q}(t), \dot{\mathbf{q}}(t))$	Lagrangian, see Eq. (2.10)
T	kinetic energy of the system, see Eq. (2.10)
U	potential energy of the system, see Eq. (2.10)
$\mathbf{M} \in \mathbb{R}^{n^{\text{DoF}} \times n^{\text{DoF}}}$	symmetric, positive definite mass matrix, see Eq. (2.13)
$\mathbf{C} \in \mathbb{R}^{n^{\text{DoF}}}$	vector of the gravitational, centrifugal, and Coriolis forces, see Eq. (2.13)

Muscle-tendon notation

$u \in [u_{\text{min}}, 1]$	muscle stimulation [ ], see Eq. (2.1-2.2)
$a \in [a_{\text{min}}, 1]$	muscle activity [ ], see Eq. (2.1-2.2)
$\gamma \in [\gamma_{\text{min}}, 1]$	normalized calcium ion (Ca^{2+}) concentration [ ], see Eq. (2.1-2.2)

$l^{\mathrm{CE}}, l^{\mathrm{MTU}} \in \mathbb{R}$	length of a CE, and MTU [m], see Eq. (2.3)
$F^{\mathrm{MTU}} \in \mathbb{R}$	force of MTU [N], see Eq. (2.5)
$n^{\mathrm{musc}} \in \mathbb{R}$	number of muscles
$\tau^{MTU} \in \mathbb{R}$	torque produced by MTU [N m], see Eq. (2.6)
$r \in \mathbb{R}$	moment arm [m], see Eq. (2.8)
$l^{\mathrm{CE,opt}} \in \mathbb{R}$	optimal muscle fiber length (CE) [m], see Eq. (2.17)
$F^{\mathrm{max}} \in \mathbb{R}$	maximum isometric force [N], see Eq. (2.19)
$l^{\mathrm{SEE,0}} \in \mathbb{R}$	tendon slack length (SEE) [m], see Eq. (2.20)
$l^{\mathrm{S}} \in \mathbb{R}$	sarcomere length [m], see Eq. (2.17)
$l^{\mathrm{S,opt}} \in \mathbb{R}$	optimal sarcomere length [m], see Eq. (2.17)
$\mathrm{PCSA} \in \mathbb{R}^2$	physiological cross-sectional area [m^2], see Eq. (2.18)
$V^{\mathrm{mus}} \in \mathbb{R}^3$	muscle volume [m^3], see Eq. (2.18)

Control notation

x	state
u	control signal
u^{ff}	feedforward control signal, see Eq. (2.21)
u^{fb}	feedback control signal, see Eq. (2.21)
K	feedback gain, see Eq. (2.22)
x^{des}	desired state, see Eq. (2.22)
ℓ	loss function, see Eq. (2.29)
$\mathfrak{r}$	reward function, see Eq. (2.32)
o_t	observation at time t, see Eq. (2.32)

List of Abbreviations

AAS agonistic-antagonistic setup

ATD anthropometric test device

BE biarticular extensor

BEESR biarticular elbow extensor shoulder retroversion

BEFSA biarticular elbow flexor shoulder anteversion

BF biarticular flexor

CE contractile element

CPG central pattern generator

CSE cervical spine extension

CSF cervical spine flexion

CSSBL cervical spine side bend left

CSSBR cervical spine side bend right

DHM Digital Human Model

DoF Degree of Freedom

EBD elementary biological drive

EE elbow extension

EF elbow flexion

EI Embodied Intelligence

EMG electromyography

FE foot extension

FEM Finite Element Method

FF foot flexion

HAbd hip abduction

HAdd hip adduction

HE hip extension

HF hip flexion

IMU inertial measurement unit

KE knee extension

KF knee flexion

LSE lumbar spine extension

LSF lumbar spine flexion

LSSBL lumbar spine side bend left

LSSBR lumbar spine side bend right

MB Multibody

MEE monarticular elbow extensor

MEF monarticular elbow flexor

MPC model predictive control

MRI magnetic resonance imaging

MSA monoarticular shoulder anteversion

MSR monoarticular shoulder retroversion

MTU muscle-tendon unit

OC optimal control

ODE ordinary differential equation

PCSA physiological cross-sectional area

PDE partial differential equation

PEE parallel elastic element

PMHS post mortem human subject

RL reinforcement learning

RoM Range of Motion

SAbd shoulder abduction

SAdd shoulder adduction

SDE serial damping element

SE shoulder extension

SEE serial elastic element

SF shoulder flexion

SOT sensory organization test

Abstract

We are facing the challenge of an over-aging and overweight society. This leads to an increasing number of movement disorders and causes the loss of mobility and independence. To address this pressing issue, we need to develop new rehabilitation techniques and design innovative assistive devices. Achieving this goal requires a deeper understanding of the underlying mechanics that control muscle-actuated motion. However, despite extensive studies, the neural control of muscle-actuated motion remains poorly understood. While experiments are valuable and necessary tools to further our understanding, they are often limited by ethical and practical constraints. Therefore, simulating muscle-actuated motion has become increasingly important for testing hypotheses and bridge this knowledge gap. *In silico*, we can establish cause-effect relationships that are experimentally difficult or even impossible to measure. By changing morphological aspects of the underlying musculoskeletal structure or the neural control strategy itself, simulations are crucial in the quest for a deeper understanding of muscle-actuated motion. The insights gained from these simulations paves the way to develop new rehabilitation techniques, enhance pre-surgical planning, design better assistive devices and improve the performance of current robots.

The primary objective of this dissertation is to study the intricate interplay between musculoskeletal dynamics, neural controller and the environment. To achieve this goal, a simulation framework has been developed as part of this thesis, enabling the modeling and control of muscle-actuated motion using both model-based and learning-based methods. By utilizing this framework, musculoskeletal models of the arm, head-neck complex and a simplified whole-body model are investigated in conjunction with various concepts of motor control. The main research questions of this thesis are therefore:

1. How does the neural control strategy select muscle activation patterns to generate the desired movement, and can we use this knowledge to design better assistive devices?
2. How does the musculoskeletal dynamics facilitate the neural control strategy in accomplishing this task of generating desired movements?

To address these research questions, this thesis comprises a total of five journal and conference articles.

More specifically, contributions I-III of this thesis focus on addressing the first research question which aims to understand how voluntary and reflexive movements can be predicted. First, we investigate various optimality principles using a musculoskeletal arm model to predict point-to-manifold reaching tasks. By using predictive simulations, we demonstrate how the arm would move towards a goal if, for example, our neural control strategy would minimize energy consumption. The main finding of this contribution shows that it is essential to include muscle dynamics and consider tasks with more openly defined targets to draw accurate conclusions about motor control. Through our analysis, we show that a combination

of mechanical work, jerk and neuronal stimulation effort best predicts point-reaching when compared to human experiments.

Second, we propose a novel method to optimize the design of exoskeleton power units taking into account the load cycle of predicted human movements. To achieve this goal, we employ a forward dynamic simulation of a generic musculoskeletal arm model, which is first scaled to represent different individuals. Next, we predict individual human motions and employ the predicted human torques to scale the electrical power units employing a novel scalability model. By considering the individual user needs and task demands, our approach achieves a lighter and more efficient design. In conclusion, our framework demonstrates the potential to improve the design of individual assistive devices.

The third contribution focuses on predicting reflexive movements in response to sudden perturbations of the head-neck complex. To achieve this, we conducted experiments in which volunteers were placed on a table while supporting their heads with a trapdoor. This trapdoor was then suddenly released leading to a downward movement of the head until the reflexive reaction of the muscles stops the head from falling. We analyzed the results of these experiments, presenting characteristic parameters and highlighting differences between separate age and gender groups. Using this data, we also set up benchmark validations for a musculoskeletal head-neck model, including reflex control strategies. Our main findings are that there are large individual differences in reflexive responses between participants and that the perturbation direction significantly affects the reflexive response. Furthermore, we show that this data can be used as a benchmark test to validate musculoskeletal models and different muscle control strategies.

While the first three contributions focus on the research question (1), contributions IV-V focus on (2) whether and how the musculoskeletal dynamics facilitate the learning and control task of various movements. We utilize a recently introduced information-theoretic approach called control effort to quantify the minimally required information to perform specific movements. By applying this concept, we can for example quantify how much biological muscles reduce the neuronal information load compared to technical DC-motors. We present a novel optimization algorithm to find this control effort and apply it to point-reaching and walking tasks. The main finding of this contribution is that the musculoskeletal dynamics reduce the control effort required for these movements compared to torque-driven systems.

Finally, we hypothesize that the highly nonlinear muscle dynamics not only facilitate the control task but also provide inherent stability that is beneficial for learning from scratch. To test this, we employed various learning strategies for multiple anthropomorphic tasks, including point-reaching, ball-hitting, hopping, and squatting. The results of this investigation demonstrate that using muscle-like actuators improves the data-efficiency of the learning tasks. Additionally, including the muscle dynamics improves the robustness towards hyperparameters and allows for a better generalization towards unknown and unlearned perturbations.

In summary, this thesis enhances existing methods to control and learn muscle-actuated motion, quantifies the control effort needed to perform certain movements and demonstrates that the inherent stability of the muscle dynamics facilitates the learning task. The models, control strategies, and experimental data presented in this work aid researchers in science and industry to improve their predictions in various fields such as neuroscience, ergonomics, rehabilitation, passive safety systems, and robotics. This allows us to reverse-engineer how we as humans control movement, uncovering the complex relationship between musculoskeletal dynamics and neural controller.

Zusammenfassung

Wir stehen vor der Herausforderung einer überalternden und übergewichtigen Gesellschaft. Dies führt zu einer zunehmenden Anzahl an Bewegungsstörungen und hat den Verlust von Mobilität und Unabhängigkeit zur Folge. Um diese dringliche Problematik anzugehen, müssen neue Rehabilitationstechniken entwickelt und innovative Assistenzsysteme entworfen werden. Um dieses Ziel zu erreichen, ist ein tieferes Verständnis der zugrunde liegenden Mechanik, die die muskelaktuierte Bewegungen kontrolliert, erforderlich. Trotz umfangreicher Studien ist die neuronale Kontrolle muskelaktuierter Bewegungen jedoch nach wie vor kaum verstanden. Experimente sind zwar ein wertvolles und notwendiges Instrument, um unser Verständnis zu vertiefen, allerdings sind diese häufig durch ethische und praktische Einschränkungen limitiert. Daher wird die Simulation muskelgetriebener Bewegungen immer wichtiger, um Hypothesen zu testen und diese Wissenslücke zu schließen. *In silico* können wir Ursache-Wirkungs-Beziehungen herstellen, welche experimentell schwierig oder sogar unmöglich zu messen sind. Durch die Veränderung morphologischer Aspekte der zugrunde liegenden muskuloskelettalen Struktur oder der neuronalen Kontrollstrategie selbst, sind Simulationen von entscheidender Bedeutung bei der Suche nach einem tieferen Verständnis muskelgetriebener Bewegungen. Die aus diesen Simulationen gewonnenen Erkenntnisse ebnen den Weg für die Entwicklung neuer Rehabilitationstechniken, eine Erweiterung der präoperativen Planung, die Konstruktion besserer Assistenzsysteme und die Verbesserung aktueller Roboter.

Das Hauptziel dieser Dissertation ist die Untersuchung des komplexen Zusammenspiels zwischen muskuloskelettaler Dynamik und neuronaler Kontrolle. Um dieses Ziel zu erreichen, wurde im Rahmen dieser Arbeit ein Simulationsframework entwickelt, welches die Modellierung und Steuerung muskelgetriebener Bewegungen sowohl mit modellbasierten als auch mit lernbasierten Methoden ermöglicht. Unter Verwendung dieses Frameworks werden muskuloskelettale Modelle des Arms, des Kopf-Nacken-Komplexes und ein vereinfachtes Ganzkörpermodell in Verbindung mit verschiedenen Konzepten der motorischen Steuerung untersucht. Die Hauptforschungsfragen dieser Arbeit sind, (1) wie die neuronale Kontrollstrategie Muskelaktivierungsmuster auswählt, um die gewünschte Bewegung zu erzeugen und (2) wie die muskuloskelettale Dynamik die neuronale Kontrollstrategie bei der Bewältigung dieser Aufgabe unterstützt. Um diese Forschungsfragen zu beantworten, umfasst diese Arbeit insgesamt fünf Zeitschriften- und Konferenzartikel.

Genauer gesagt konzentrieren sich die Beiträge I-III dieser Arbeit auf die Beantwortung der ersten Forschungsfrage, die darauf abzielt zu verstehen, wie freiwillige und reflexive Bewegungen vorhergesagt werden können. Zunächst untersuchen wir verschiedene Optimalitätsprinzipien unter Verwendung eines muskuloskelettalen Armmodells zur Vorhersage von Punkt-zu-Mannigfaltigkeit-Armbewegungen. Mit Hilfe prädiktiver Simulationen zeigen wir, wie sich der Arm auf ein Ziel zubewegen würde, wenn beispielsweise unsere neuronale Kontrollstrategie den Energieverbrauch minimieren würde. Die Haupterkenntnis dieses Beitrags

zeigt, dass es unerlässlich ist, die Muskeldynamik einzubeziehen und Aufgaben mit offener definierten Zielen zu betrachten, um korrekte Schlussfolgerungen über die motorische Kontrolle zu ziehen. Durch unsere Analyse zeigen wir, dass eine Kombination aus mechanischer Arbeit, Ruck und neuronalem Stimulationsaufwand im Vergleich zu menschlichen Experimenten Armbewegungen am besten vorhersagt.

Zweitens schlagen wir eine neuartige Methode zur Optimierung des Designs von Exoskelett-Antriebseinheiten unter Berücksichtigung des Belastungszyklus der vorhergesagten menschlichen Bewegungen vor. Um dieses Ziel zu erreichen, verwenden wir eine dynamische Vorwärtssimulation eines generischen muskuloskelettalen Armmodells, welches zunächst skaliert wird, um verschiedene Personen darzustellen. Anschließend werden die vorhergesagten menschlichen Drehmomente zur Skalierung der elektrischen Leistungseinheiten unter Verwendung eines neuartigen Skalierbarkeitsmodells verwendet. Durch die Berücksichtigung der individuellen Bedürfnisse des Benutzers und der Aufgabenanforderungen ermöglicht unser Ansatz ein leichteres und effizienteres Design. Zusammenfassend lässt sich sagen, dass unser Framework das Potenzial hat, das Design von individuellen Assistenzsystemen zu verbessern.

Der dritte Beitrag konzentriert sich auf die Vorhersage reflexiver Bewegungen als Reaktion auf plötzliche Störungen des Kopf-Nacken-Komplexes. Zu diesem Zweck haben wir Experimente durchgeführt, bei denen Probanden auf einem Tisch platziert wurden, während ihr Kopf durch eine Falltür gestützt wurde. Diese Falltür wurde dann plötzlich ausgelöst, was zu einer Abwärtsbewegung des Kopfes führte, bis die reflexive Reaktion der Muskeln den Kopf am Fallen hinderte. Wir haben die Ergebnisse dieser Experimente analysiert, charakteristische Parameter dargestellt und die Unterschiede zwischen den einzelnen Alters- und Geschlechtsgruppen herausgestellt. Anhand dieser Daten haben wir auch Benchmark-Validierungen für ein muskuloskelettales Kopf-Nacken-Modell durchgeführt, welches auch Reflexkontrollstrategien umfasst. Unsere wichtigsten Ergebnisse zeigen, dass es große individuelle Unterschiede in den reflexiven Reaktionen zwischen den Teilnehmern gibt und dass die Störungsrichtung diese Reaktion signifikant beeinflusst. Darüber hinaus zeigen wir, dass diese Daten als Benchmark-Test für die Validierung von Muskel-Skelett-Modellen und verschiedenen Muskelkontrollstrategien verwendet werden können.

Während sich die ersten drei Beiträge auf die Forschungsfrage (1) konzentrieren, geht es in den Beiträgen IV-V um die Frage (2), ob und wie die muskuloskelettale Dynamik das Lernen und die Kontrolle verschiedener Bewegungen erleichtert. Wir verwenden einen kürzlich eingeführten informationstheoretischen Ansatz, den sogenannten “control effort”, um die minimal erforderlichen Informationen für die Ausführung bestimmter Bewegungen zu quantifizieren. Durch die Anwendung dieses Konzepts können wir zum Beispiel abschätzen, wie sehr biologische Muskeln die neuronale Informationslast im Vergleich zu technischen Gleichstrommotoren reduzieren. Wir stellen einen neuartigen Optimierungsalgorithmus vor, um diesen Kontrollaufwand zu ermitteln und wenden ihn auf Arm- und Gehbewegungen an. Das Hauptergebnis dieses Beitrags ist, dass wir zeigen, dass die Muskeldynamik den Kontrollaufwand für diese Bewegungen im Vergleich zu drehmomentgesteuerten Systemen reduziert.

Schließlich stellen wir die Hypothese auf, dass die hochgradig nichtlineare Muskeldynamik nicht nur die Steuerungsaufgabe erleichtert, sondern auch eine inhärente Stabilität bietet, die für das Lernen von Vorteil ist. Um dies zu testen, haben wir verschiedene Lernstrategien für mehrere anthropomorphe Aufgaben eingesetzt, darunter Armgreifbewegungen, das

Schlagen eines Balls, Hüpf und Kniebeuge-Bewegungen. Die Ergebnisse dieser Untersuchung zeigen, dass die Verwendung muskelähnlicher Aktuatoren die Dateneffizienz der Lernaufgaben verbessert. Darüber hinaus verbessert die Einbeziehung der Muskeldynamik die Robustheit gegenüber Hyperparametern und ermöglicht eine bessere Verallgemeinerung gegenüber unbekannten und nicht gelernten Perturbationen.

Zusammenfassend lässt sich sagen, dass diese Arbeit die bestehenden Methoden zur Kontrolle und zum Erlernen muskelgetriebener Bewegungen verbessert, den für die Ausführung bestimmter Bewegungen erforderlichen Kontrollaufwand quantifiziert und zeigt, dass die inhärente Stabilität der Muskeldynamik die Lernaufgabe erleichtert. Die in dieser Arbeit vorgestellten Modelle, Kontrollstrategien und experimentellen Daten ermöglichen Forschern sowohl in Wissenschaft als auch Industrie, ihre Vorhersagen in verschiedenen Bereichen wie Neurowissenschaften, Ergonomie, Rehabilitation, passive Sicherheitssysteme und Robotik zu verbessern. Auf diese Weise können wir nachvollziehen, wie wir als Menschen Bewegungen steuern, und die komplexe Beziehung zwischen der Dynamik des Bewegungsapparats und der neuronalen Steuerung aufdecken.

1. Introduction

1.1. The importance and challenge of understanding muscle-actuated motion

Every day, humans perform complex movements such as walking over uneven terrain, lifting and carrying objects, or playing sports. Remarkably, we have the innate ability to achieve these movements in a seemingly effortless way. For example, we can lift objects, such as a bottle of water, without needing to know the exact weight before we grasp it. These capabilities are the result of the complex interplay between the neural control system, the underlying biophysical structures and the environment. Understanding these interactions and the principles of human motion has fascinated scientists for centuries and is still an open challenge in biomechanics and motor control. Doing so, advances our knowledge of motor disorders on the one hand, and on the other hand, gives us the potential to predict motions in potentially harmful situations such as in automotive safety or ergonomics in general. Furthermore, an improved knowledge of the biological motor system can be beneficial in the design and construction of robots and assistive devices.

A multitude of experimental studies have been performed to elucidate and understand the cause-effect relations of biological motion. They range from studies investigating the mechanical properties of individual muscles over the investigation of intrinsic muscle properties in combination with control principles to the investigation of the interaction of human motion with the environment including assessing injury risks. One of the most well-known experiments in biomechanics is the work of Hill (1938) which is the foundation for modern models of muscle mechanics. With his experiments, he showed that the force production of a muscle is dependent on the contraction velocity of the muscle fiber. In addition to studying isolated muscle properties, modern experiments investigate how these intrinsic muscle properties interact with the neural control to maintain stable locomotion. For example, based on experiments with running guinea fowl that experience sudden drops, Daley et al. (2009) showed that intrinsic muscle properties increase the robustness towards unexpected perturbations. Furthermore, techniques such as electromyography have been extensively used in studies aiming to gain insights into the neural control of human walking, enabling us to infer the muscle coordination pattern (Winter and Yack, 1987; Murray et al., 1984).

While these experimental studies are necessary, they face various limitations due to the invasiveness of the techniques. For example, experimentally testing isolated changes in the musculoskeletal, sensory or neural system is difficult or ethically unacceptable. To tackle these challenges, musculoskeletal physics-based simulations have become helpful tools in recent decades. They allow us to understand the human system better, test hypotheses about neural control and movement, and to estimate values that are difficult to measure *in vivo*.

Typically, in the field of biomechanics, two different ways of using physics-based simulations have emerged: The *inverse* approach (also called tracking simulations) and the *forward* approach (also called predictive simulations). Until today, the most widely used method is still the inverse approach, for which experimental data of a motion is used as input for a human body model. Such data typically requires the analysis of multimodal sensors, such as motion capture data, e.g, using experimental markers, as well as neuronal state information recorded with electromyography, and ground reaction forces measured with force plates. Using such an inverse approach then allows the calculation of torques acting on the joints within the human body (Kuo, 1998; Zajac et al., 2002). Especially combined with state-of-the-art optimization, this approach is able to analyze the contribution of individual muscles (Crowninshield and Brand, 1981; Anderson and Pandy, 2001b; Erdemir et al., 2007). However, the use case of this method is limited to the study of motions that have been previously recorded experimentally. Hence, predictive simulations are required to analyze and predict new, unseen movements, as well as to test hypotheses about the neural control of human motion and pathological diseases.

In the realm of predictive simulations, models of the neural control system or bioinspired control strategies are used to drive the motion into future states and, thus, predict the time development of the musculoskeletal system. Using predictive simulations, we can ask “what if” questions, such as “what if the muscle activation pattern changes” or “what if the actuator dynamics are different”. They have been successfully applied to investigate maximum height jumps (Anderson and Pandy, 1999), three-dimensional walking (Song and Geyer, 2015), load sharing in the human spine (Meszaros-Beller et al., 2023), as a tool in forensics in a real crime case (Graevemeyer, 2023), and many more. In this thesis, mainly predictive simulations are used to investigate the interplay between the neural control system, the biophysical structures and the environment as shown in Figure 1.1. As visualized, this means taking into account the nonlinear muscle-tendon dynamics while developing bioinspired control strategies that drive the motion. Although these predictive simulations have been successfully applied to investigate human motion, there still remain challenges when it comes to muscle-actuated motion. In the following, I will discuss some of these challenges, which serve as the basis for this dissertation, as the contributions of this thesis aim to tackle these issues.

1.2. Challenges in predicting muscle-actuated motion

Human body models including muscle-tendon dynamics Biological motion is driven by muscles, a complex actuation principle of nature. For many years, it was regarded as overly complex and computationally expensive to model muscle-tendon dynamics in biomechanical simulations (Hume et al., 2019; De Groote and Falisse, 2021). Therefore, as an alternative to muscle-driven actuation, torque-actuated (or joint-actuated) motion is often used to model and simulate biomechanical systems in computer science, robotics, neuroscience, automotive safety and biomechanics. In muscle-actuated motion, the dynamics of muscles including activation and contraction dynamics, tendon dynamics and nonlinear muscle routing is explicitly modeled to produce joint torques, which in turn produce joint motion. However, in torque-actuated motion, the joint torques are directly controlled without modeling the muscles explicitly. While both approaches have advantages and disadvantages, the choice of

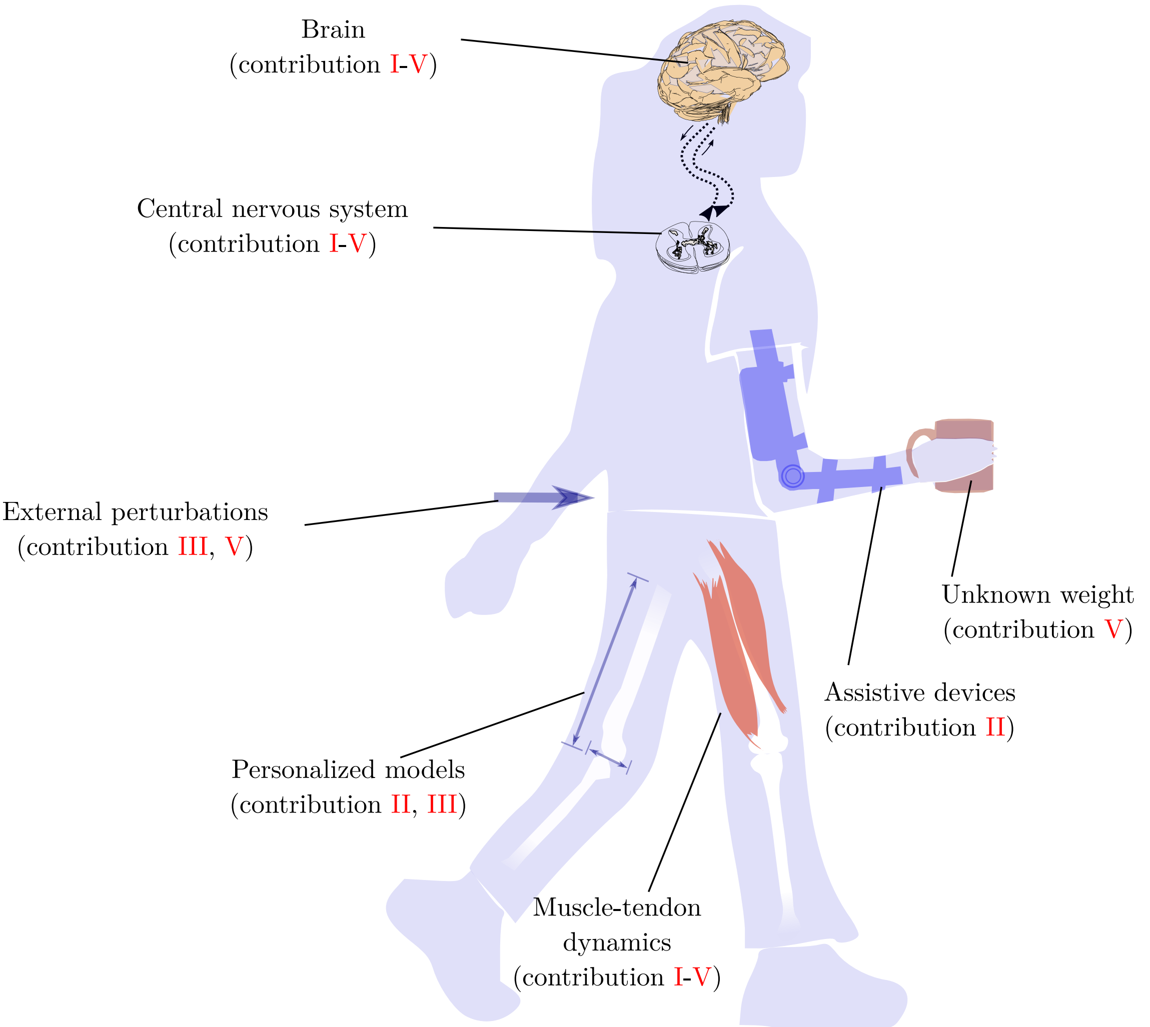

Figure 1.1.: Predictive simulations allow us to study the complex interplay between neural control, the human body and the environment. This thesis shows how muscle-actuated motion can be controlled for various locomotion and reaching tasks. To do so, the *brain* and *central nervous system* take into account and exploit the nonlinear *muscle-tendon dynamics*. The control concepts are also tested and extended for *personalized models* which are used to design and scale *assistive devices*. Additionally, I expose the learned motions to unknown and unlearned perturbations such as *lifting weights* or reacting to *external pushes*.

whether muscle dynamics is included depends on the specific research goals, the application and the available resources. For example, in the related field of computer animation, virtual humans are often modelled using torque-actuation, e.g. Wu and Popović (2010), or linearized versions of the muscle dynamics, e.g. Lee and Terzopoulos (2006), which simplifies the simulation. While it has been noted, that using torque-actuation is not biologically realistic and the predicted torque patterns are often unnatural or infeasible for humans to achieve (Komura et al., 2000; Jiang et al., 2019), it is still widely used in computer graphics and animation due to several challenges. One of the main challenges preventing the use of muscle dynamics is the high computational cost of muscle-actuated motion. Additionally, modeling realistic human models including muscles, requires complex modeling efforts and is considered too labor-intensive (Geijtenbeek et al., 2010; Jiang et al., 2019; McErlain-Naylor et al., 2021). Further, the high redundancy of the musculoskeletal system makes it challenging to develop control strategies (Komura et al., 2000) which is addressed in the next section.

Similarly, in the field of automotive safety, it is still common to use passive human body models, anthropomorphic test devices (ATDs, also known as crash-test dummies) or post-mortem human subjects (PMHS) to predict injury risks during vehicle collisions. While these models and surrogates are necessary and have been historically used successfully, they do not capture the full, complex dynamics of human motion. One reason for this is that crash-test dummies were developed for specific loading directions and severe impacts which makes it difficult to predict the injury risk for less severe impacts (Beeman et al., 2012). Furthermore, it is not possible to analyze the stress and deformation distribution in detail (Xu et al., 2018). To overcome this challenge, the use of active human body models has been proposed. Here, several studies have shown that a human body model can predict the human response better compared to standard crash test dummies such as the Hybrid III model (Östh et al., 2015). Other studies show that the head kinematics are altered by the reaction of the muscles (van der Horst et al., 1997; Siegmund et al., 2002; Putra et al., 2019). Nevertheless, modeling efforts and computational costs still limit the use of muscle-actuated models in automotive safety for similar reasons as the challenges previously mentioned.

This thesis aims to tackle these challenges and develop new methods to model human motion including muscle-tendon dynamics. Therefore, as part of this thesis, two simple models of a human arm and a human all-body model have been improved, developed and made available open-source (Appendix A, Appendix B). They include the activation dynamics, the muscle-tendon dynamics, and nonlinear muscle routing. Additionally, a recently developed Hill-type muscle material with a more realistic eccentric force-velocity relation and serial damping (Günther et al., 2007; Haeufle et al., 2014a; Kleinbach et al., 2017) has been incorporated in the detailed head-neck model of the commercially available THUMS v5 model (Iwamoto and Nakahira, 2015) as part of this thesis (contribution III, Wochner et al. (2022a)). This muscle model shows better model accuracy and accelerates the simulation time compared to the standard muscle model used in the simulation software LS-DYNA (Kleinbach et al., 2017).

Controlling muscle-actuated motion Closely linked to the challenges in modeling realistic human motion is the challenge of controlling muscle-actuated motion. While previous studies have shown impressive results in controlling muscle-driven motion, there still remain unsolved challenges. It has been stated that controlling muscle-driven motion is especially challenging due to the high dimensionality of the control space and the high nonlinearity of the muscle dynamics (Full and Koditschek, 1999; Wolpert et al., 2001). This difficulty in controlling highly nonlinear actuators is not only a challenge in biomechanics but also in robotics. Therefore, traditionally, actuators have been made as stiff as possible in robotic applications to allow for precise position control (Van Ham et al., 2009). However, nowadays, variable impedance actuators or other muscle-like actuators are on the rise due to their advantages in safety, energy-efficiency and the possibility to achieve highly dynamic motions (Vanderborght et al., 2013). This requires the control of highly nonlinear actuators or muscle-like actuators in both robotics, biomechanics and overlapping fields such as rehabilitation and human-robot interaction. Additionally, in these research fields, there is a need to develop controllers for more complex tasks that are able to adapt to dynamic environments (Song et al., 2021). One possibility to solve these challenges is to use learning approaches for movement control. However, these approaches typically require carefully designed reward functions and strategies to resolve the redundancy of the musculoskeletal system.

Therefore, this thesis contributes towards these challenges in various steps: I propose a method to solve the redundancy problem by investigating which optimality principles best explain human reaching motions. This is done using the example of point-to-manifold reaching tasks while accounting for muscle dynamics (contribution I, Wochner et al. (2020)). Extending this approach, this thesis demonstrates the control of muscle-actuated motion for a wide range of tasks, including variants of reaching and locomotion tasks using various learning concepts (contributions IV-V, Haeufle et al. (2020b); Wochner et al. (2022b)). While the challenge of how to control muscle-actuated motion is one of the core technical challenges of this work, it also gives insights into different research questions: It is investigated how robust the control of muscle-actuated motion is, for example, towards unknown perturbations of external pushes. Additionally, it is tested how the control of muscle-actuated motion can be adapted to lifting unknown weights. Furthermore, this work explores how the control task can be simplified by exploiting the morphology, e.g. using different actuator dynamics such as muscle or torque actuators. Finally, this thesis asks whether and how the learning task can benefit from the highly nonlinear muscle dynamics that provide inherent stability. To summarize, this work demonstrates and quantifies that the muscle dynamics counter-intuitively simplify the control (contribution IV, Haeufle et al. (2020b)). Furthermore, I show that including muscle dynamics is beneficial for more data-efficient and robust learning of anthropomorphic tasks (contribution V, Wochner et al. (2022b)).

Individualization and subject-specific modeling In the field of biomechanics, it is common to use generic models of the human body that represent an average person. However, while this lack of personalization may be sufficient for studying control phenomena that are decoupled from an individual, certain applications require individualized models (Saxby et al., 2020). For instance, when designing exoskeletons or assistive devices for rehabilitation or manual labor, individual models are essential to maximize the benefits of exoskeleton assistance (Slade et al., 2022). Similarly, individual differences in the human body, such as age, BMI, gender, and anthropometry, have been shown to affect injury risks which is critical for the design of safety systems for vehicles (Newgard and McConnell, 2008; Kent et al., 2009;

Carter et al., 2014). Specifically, individual reflexive responses to head-neck perturbations can influence the injury risks in traffic accidents, but also in recreational-related collisions (see Le Flao et al. (2018) for an overview). To understand these individual differences, it is necessary to develop individual models and adjusted control strategies. However, it is currently still infeasible to estimate all parameters for an individual model from medical imaging data. Additionally, collecting specific data from experiments is often a time-consuming and expensive process.

This thesis presents a scaling approach that allows to estimate individual parameters from generic models based on the height and weight of individual persons. This is similar to the idea of buying clothes with different sizes, e.g. S, M, and L. These scaled models are then used to dynamically predict the driving torques of various arm movements representing both manual labor and daily activities. In turn, these torques are used to design and scale a power unit as part of an exoskeleton (contribution II, Waldhof et al. (2022)). In addition to this personalization of the musculoskeletal system, this thesis also poses the question of how individual control adaptations, such as the sensitivity of the neuronal state in a reflex controller influence the biomechanical reflex response (contribution III, Wochner et al. (2022a)).

Validation and benchmark tests Another challenge that bars the widespread use of muscle-actuated models is the lack of verification and validation (Anderson et al., 2007; Fregly, 2021). Evaluating the validity of muscle-actuated models impacts clinical practice, medical device design or the testing of safety systems. Furthermore, this ensures the reliability of the models and the trust of our society in the results of the models. It has been identified that this requires the availability of open-source datasets including comprehensive experimental data and the development of standardized benchmark tests (Hicks et al., 2015).

As part of this thesis, novel experimental data are presented in a standardized 'falling heads' setup that allows the investigation of reflexive responses to head-neck perturbations. This data is used in combination with forward dynamic simulations to validate the used human body model and various control strategies. The setup of these experiments and their numerical equivalent is simple, making them ideally suited as benchmark tests for future validations in virtual test procedures (contribution III, Wochner et al. (2022a)). Indeed, the presented data has also been used in a follow-up study to compare three existing human body models with varying software codes and muscle materials (Martynenko et al., 2021).

1.3. Objectives and structure of this thesis

Concluding, the aim of this thesis is two-fold: First, I present control and modeling methods along with scaling approaches for individual persons aimed at addressing the challenges associated with muscle-actuated motion. Second, I demonstrate the benefits of muscle-actuated motion regarding control and learning by investigating a diverse range of human movements including reaching and locomotion tasks. By addressing these objectives, this thesis provides valuable insights into the complex interplay between the neural control system, biophysical structures, and the environment, as illustrated in Figure 1.1. Chapter 2 provides a comprehensive overview of the current state of the art in modeling and control of neuromusculoskeletal models. It also introduces the concept of embodied intelligence or morphological computation, highlighting how the morphology of the human body can be exploited to improve the control and learning capabilities. The objectives and contributions of this thesis are summarized in Chapter 3, and a detailed overview of the publications contributing to this thesis is given in Chapter 4. The corresponding publications answering the overarching research question of this thesis are presented in contributions I-V. Here, each contribution focuses on different sub-aspects, as indicated in the in Figure 1.1. Finally, a summary of the main findings and an outlook on future work is given in Chapter 5.

2. Methods and literature background

2.1. Musculoskeletal models

Computational musculoskeletal models describe the interaction between various biophysical structures including signals of the nervous systems, the chemical processes needed to activate the muscle, the force production in the muscles and their effect on the environment. Depending on the level of detail of the underlying model, they can be crucial in understanding healthy as well as pathological motions. The main reason behind this is that models of the musculoskeletal system can be used to test hypotheses of motor control and biomechanical dynamics by modifying parts of the model or their surrounding environment which would either not be possible or too dangerous *in vivo*. A schematic overview of the components required to model biophysical movements is shown in Figure 2.1.

Typically, we control, optimize or learn the muscle stimulation signal u which is the input to the nonlinear activation dynamics modeling the free-calcium ion concentration. The resulting

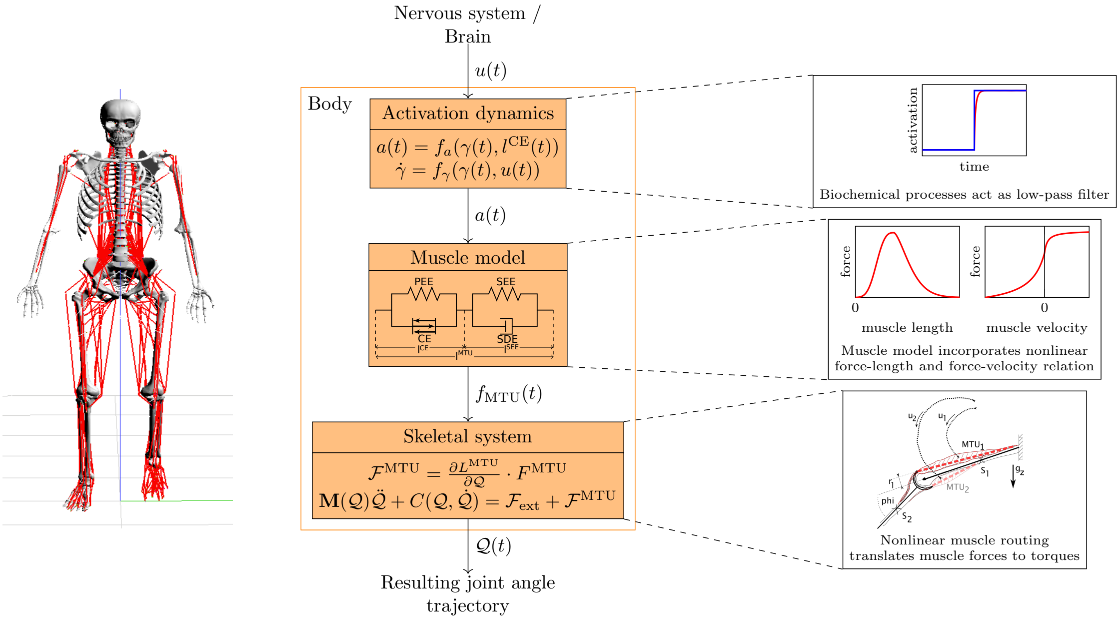

Figure 2.1.: Musculoskeletal modeling in a predictive simulation requires various components: the activation dynamics modeling the free-calcium concentration, the contraction dynamics modelled in the Hill-type muscle model, the anatomical muscle routing, which translates the muscle forces to torques acting on the joints, and finally the skeletal dynamics predicting the resulting joint angle trajectory.

activation signal a is then used to calculate the force F^{MTU} of the muscle-tendon unit (MTU) by taking into account the nonlinear force-length and nonlinear force-velocity relation as well as the nonlinear tendon elasticity. Finally, these forces are applied to the skeletal system by transforming the forces into torques using the anatomical muscle routing resulting in nonlinear lever arms. In the following, each of these components is described in more detail with a focus on how they are modelled in this thesis.

Activation dynamics The muscles are activated with the control signal u, which can be seen as a representation of signals coming from the central nervous system or the brain, and our case is typically modeled as the total neural excitation of all neuromuscular junctions of a muscle. This signal u is nonlinearly transformed into an activation signal. This activity a is modeled as a first-order differential equation depending on the normalized calcium ion concentration γ as introduced by Hatze (1977) and simplified by Rockenfeller et al. (Rockenfeller et al., 2015; Rockenfeller and Günther, 2018):

$$\dot{\gamma}_{\mathrm{t}} = M^{\mathrm{H}}(u_{\mathrm{t}} - \gamma_{\mathrm{t}}). \tag{2.1}$$

Next, this calcium ion concentration γ is nonlinearly mapped onto the muscles' activity

$$a_{\mathrm{t}} = \frac{a^{\mathrm{nll}} + \varpi}{1 + \varpi}, \tag{2.2}$$

with $\varpi(\gamma_{\mathrm{t}}, l_t^{\mathrm{CE}}) = (\gamma_{\mathrm{t}} \cdot \rho(l_t^{\mathrm{CE}}))^{\nu}$ and $\rho(l_t^{\mathrm{CE}}) = \gamma^{\mathrm{c}} \cdot \rho^{\mathrm{nll}} \cdot \frac{l_t^{\mathrm{CE}}}{l^{\mathrm{CE,opt}}}$. Note, that the subscript t denotes the time-dependency of the variables. The parameters l_t^{CE} and $l^{\mathrm{CE,opt}}$ denote the current and the optimal fiber length, respectively. All other variables $(M^{\mathrm{H}}, a^{\mathrm{nll}}, \gamma^{\mathrm{c}}, \rho^{\mathrm{nll}}, \nu)$ are constant parameters that are chosen muscle non-specifically (a detailed overview for the used models is given in the supplementary material, see Table B.5). From a control perspective, the characteristics of this activation dynamics a can be understood as a low-pass filter of the control signal u.

Nonlinear force-length relation In a biological muscle, the force production is dependent on the current length of the muscle fiber. The active force production is modeled by a nonlinear force-length relation characterized by a positive slope (ascending limb) at short muscle lengths and a negative slope (descending limb) at long muscle lengths. The maximum of this curve is reached at the optimal fiber length $l^{\mathrm{CE,opt}}$ (plateau region), where the maximum isometric force $F^{\max}$ is produced. This nonlinearity can be explained with the sliding filament theory (Gordon et al., 1966): Inside the sarcomere, the basic contractile unit of a muscle fiber, two myofilaments, the actin (thin) and myosin (thick) are sliding over one another. The myosin heads are attached to the actin filaments and can slide along the actin filaments. The sliding of the myosin heads along the actin filaments is driven by the energy released by the hydrolysis of ATP. The myosin heads are attached to the actin filaments by cross-bridges. Based on the geometrical overlap of these two sliding filaments, the number of formed cross-bridges changes. This is assumed to be proportional to the contractile force that is produced by the muscle fiber. Experimentally, this force-length relation can be measured using various techniques. The most common one is to attach a force transducer to the muscle, which is a device that

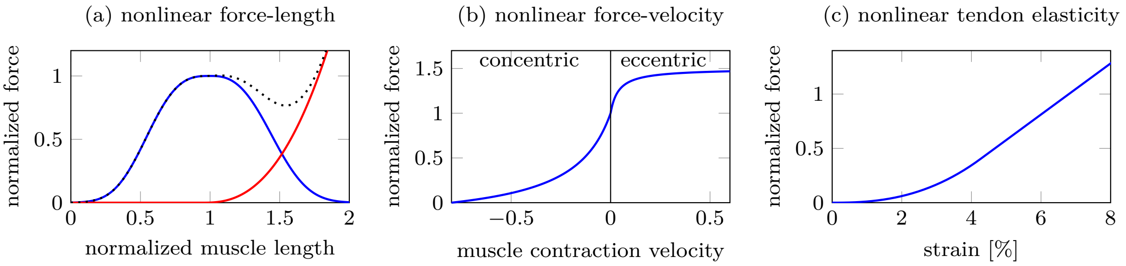

Figure 2.2.: Nonlinearities modeled in a Hill-type muscle model. (a) and (b) show a typical nonlinear force-length and force-velocity curve of the muscle, (c) shows the nonlinear tendon elasticity. All forces are normalized with respect to the maximum isometric force $F^{\max}$. The muscle length is normalized with respect to the optimal fiber length $l^{\mathrm{CE,opt}}$, and the tendon strain is normalized with respect to the tendon slack length $l^{\mathrm{SEE},0}$. Note, that while the force-length and force-velocity relation are plotted two-dimensionally, in reality, they form a surface. The shown curves are cross-sections of this force-length-velocity surface, where either the muscle length or the muscle velocity is kept constant.

measures the generated force. During the experiment, the muscle is fixed at different lengths while stimulating it. This leads to the generation of different forces depending on the current length. The resulting force-length relation is then fitted to a mathematical function as shown in the curve in Figure 2.2 (a). Additionally, this figure shows the passive force-length relation in red, which is the force generated by the muscle when inactive and stretched beyond its optimal fiber length. These passive forces are generated by the connective tissue surrounding the muscle fibers and can be characterized similarly to a nonlinear spring. The total force generated dependent on the current muscle length is the sum of the active and passive force, as shown in the black dashed curve in Figure 2.2 (a). Note, that this dependency is plotted for a fixed velocity (for a detailed discussion regarding this issue, I refer to Yeo et al. (2023)).

Nonlinear force-velocity relation Similar to the nonlinear generation of force depending on the current muscle fiber length, the force production of a muscle fiber also depends on the current velocity of the muscle fiber. This relation is also nonlinear and can be characterized by a decreasing force for faster shortening velocities (concentric contraction) and an increasing force when the muscle is externally stretched against its contraction direction (eccentric contraction). At the isometric point (velocity = 0) the maximum isometric force $F^{\max}$ is produced, and at the intersection of the curve with the x-axis (force = 0), the maximum contraction velocity is reached. The basis for this hyperbolic relationship was first described by Hill (1938) and an exemplary curve is visualized in Figure 2.2 (b). In Hill's original quick-release experiment, this relationship was measured by first fixing the muscle at a fixed length, then activating the muscle and finally releasing it to measure the initial shortening velocity while forcing it to resist against various loads.

Nonlinear tendon elasticity In addition to the biological muscle, the tendon needs to be modelled. Tendons attach the muscle to the bone and therefore, are responsible for the transmission of forces from the muscle to the bone. The tendon is a viscoelastic structure which is able to store and dissipate energy. It acts as a nonlinear spring where typically a nonlinear toe-region in the stress-strain curve is followed by a linear continuation until the tendon experiences mechanical failure at the risk of injury. This nonlinear force-strain behavior is visualized in Figure 2.2 (c). Note, that in the nonlinear toe-region, the fibers of tendons typically are slack until they are stretched beyond a certain threshold, which we call the tendon slack length $l^{\mathrm{SEE},0}$. Even though the tendon only passively contributes to the force generation, its compliance affects the force generation of the muscle. This can be intuitively understood by the following example: If the tendon is short and very stiff, the muscle length will change less compared to the case of a long and compliant tendon. This also directly impacts the current force-generation capacities of the muscle as the force is nonlinearly dependent on the current muscle length.

Hill-type muscle tendon model The Hill-type muscle model is a widely used model to describe the force production of biological muscles. It is based on the idea that muscle behavior can be modeled as an active viscoelastic element. To do so, the MTU is modeled as a spring-damper system including several components to represent different mechanical properties. Using this macroscopic muscle model, forces can be predicted based on the activity a as, e.g., given by Eq. 2.2. In this thesis, the used Hill-type muscle model (Hill, 1938; Günther et al., 2007; Haeufle et al., 2014a) includes four spring-damper components (see Fig. 2.3): The contractile element (CE) models the cross-bridge-cycle of the myosin heads attaching to the acting filaments and therefore, predicts the active force production of biological muscle fibers. This element incorporates the nonlinear *force-length* and nonlinear *force-velocity* relation of biological muscles. The parallel elastic element (PEE) models the passive connective tissue in the muscle belly and is arranged in parallel to the CE. Tendons and other compliant materials including their viscoelastic properties are modeled in series to the CE element using a serial elastic element (SEE) and a serial damping element (SDE). All in all, the governing model dependencies for all muscles $i = 1, ..., n$ are:

$$\dot{l}_i^{\mathrm{CE}} = f^{\mathrm{CE}}(l_i^{\mathrm{CE}}, l_i^{\mathrm{MTU}}, \dot{l}_i^{\mathrm{MTU}}, a_i) \tag{2.3}$$

$$\dot{a}_i = f^{a}(a_i, u_i, l_i^{\mathrm{CE}}) \tag{2.4}$$

$$F_i^{\mathrm{MTU}} = f^{\mathrm{MTU}}(l_i^{\mathrm{MTU}}, \dot{l}_i^{\mathrm{MTU}}, l_i^{\mathrm{CE}}, a_i)\,, \tag{2.5}$$

where the first differential equation (Eq. 2.3) denotes the *contraction dynamics* which models the velocity $\dot{l}^{\mathrm{CE}}$ of the contractile element. This contraction velocity is dependent on the current CE length l^{CE}, the length and contraction velocity of the muscle-tendon unit l^{MTU} and $\dot{l}^{\mathrm{MTU}}$ respectively, and the activity a. The latter is modeled by the *activation dynamics* (see Eq. 2.1,2.2,2.4). Finally, based on these differential equations, the force F_i^{MTU} for each muscle can be predicted.

Nonlinear moment arms The muscle-tendon units are attached at fixed insertion and origin points where the force acts along the routing path from one attachment point to the other. Based on this anatomical routing, nonlinear moment arms can be identified that translate

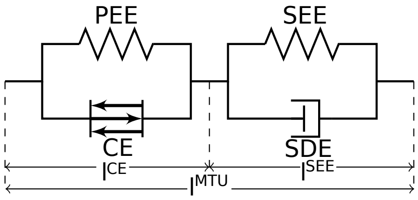

Figure 2.3.: The muscle-tendon model is modeled as lumped Hill-type muscle model (figure adapted from Haeufle et al. (2014a)).

the force of the muscle-tendon units into joint torques acting on the joint's center of rotation:

$$\tau^{MTU} = r \times F^{\mathrm{MTU}} \tag{2.6}$$

Furthermore, the fixed attachment of the muscle path also implies that the moment arm r and the length of the muscle-tendon unit l^{MTU} change if the joint angle changes. In order to get a mathematical description for the moment arm r, we can also make use of the principle of virtual work. This states that the total virtual work of forces acting on the system is zero for any virtual displacement. Therefore, the virtual work done by a muscle is equal to the virtual work of all external moments. The latter can be defined as the product of the moment τ^{MTU} with a virtual joint angle displacement $\delta\phi$, whereas the work of the muscle is the product of force generated by the muscle F^{MTU} with an infinitesimal displacement of the length of the muscle-tendon unit δl^{MTU} (Sherman et al., 2013):

$$\tau^{MTU} \cdot \delta\phi = F^{\mathrm{MTU}} \cdot \delta l^{\mathrm{MTU}} \tag{2.7}$$

Combining this equation with Eq. 2.6 we get an expression for the moment arms which is dependent on the muscle length l^{MTU} and the joint angle ϕ:

$$r = \frac{\delta l^{\mathrm{MTU}}}{\delta\phi} \tag{2.8}$$

This equation is helpful to measure moment arms experimentally. Moment arms can be measured visually with MRI scans for a fixed position by measuring the vertical distance between the muscle fiber and the joint center (*in vivo*). Alternatively, the so-called tendon-excursion method (An et al., 1984) based on Eq. (2.8) can be used, where position transducers measure the displacement of the muscle length l^{MTU} while the joint angle is rotated around the range of motion using, e.g., cadaver recordings. Based on this data, the muscle path around the joint can be modeled. There exist multiple numerical approaches to model this routing of the muscle path (Hoy et al., 1990; Delp et al., 1990; Garner and Pandy, 2000). The simplest one is to assume constant or polynomial functions that model the lever arms as a function of the joint angles. A more complex approach for modeling the muscle path around the joints is to model the routing via deflection ellipses (Hammer et al., 2019). If the length of the half-axes of all ellipses is set to zero, this approach can be simplified to the more commonly used fixed via-point approach for muscle routing. Based on the resulting moment arms of the muscles, the force F^{MTU} is translated to generalized torques acting on the degrees of freedom of the system.

Modeling the mechanical system There exist two computational methods to model the mechanical system of a musculoskeletal model: Multibody (MB) methods and the Finite Element Method (FEM). Typically, MB methods, also known as rigid body dynamics are used to model the motion of the system as interconnected rigid bodies. These methods are based on the principle of Newtonian mechanics describing the movement of solid bodies as a result of the action of forces. In contrast, the Finite Element Method is a numerical method to solve partial differential equations (PDEs) modeling the deformation and stress of flexible bodies. The FEM is based on the principle of solid continuum mechanics where the deformation of the body as a result of the acting forces is described by modeling a set of nodes and elements for which the equations are solved individually. In biomechanics, typically, MB methods are used to estimate internal body forces and understand muscle functions, whereas FEM can be used to investigate the loads on tissues, e.g., bone and cartilage. Both methods have different strengths and weaknesses; FE methods are typically computationally more demanding compared to MB methods but can be used to extract the deformation, strains and stresses of flexible bodies. Therefore, typically the underlying research questions determine which method is used to model the mechanical system.

Equations of motion describe the motion of physical systems as a function of time. They are used to model mechanical, chemical, quantum mechanical and robotic systems. To describe the dynamics of these systems, one can derive the Lagrange equation of motion (second kind) in generalized coordinates as a mathematical result from the calculus of variations:

$$\frac{d}{dt}\frac{\partial \mathcal{L}}{\partial \dot{q}_j} - \frac{\partial \mathcal{L}}{\partial q_j} = \mathcal{F}_j \tag{2.9}$$

In the given equation, $\mathbf{q}$ represent the generalized coordinates, while $\boldsymbol{\mathcal{F}}$ refer to generalized forces, i.e. internal and external forces acting on the system. It should be noted that in the case of muscle-actuation, the torques generated by the muscle-tendon units on each joint are included in the vector $\boldsymbol{\mathcal{F}}$. The term $\mathcal{L}(\mathbf{q}(t), \dot{\mathbf{q}}(t))$ is known as the Lagrangian and is conventionally defined as follows:

$$\mathcal{L} = T - U \tag{2.10}$$

where T denotes the total kinetic energy and U is the potential energy of the system. Using Eq. 2.9, we can then compute the partial derivatives analytically. Using the chain rule, we have:

$$\frac{d}{dt}\frac{\partial \mathcal{L}}{\partial \dot{q}_j} = \frac{\partial}{\partial q_j}\frac{\partial \mathcal{L}}{\partial \dot{q}_j} \cdot \dot{q}_j + \frac{\partial}{\partial \dot{q}_j}\frac{\partial \mathcal{L}}{\partial \dot{q}_j} \cdot \ddot{q}_j. \tag{2.11}$$

This results in

$$\underbrace{\frac{\partial}{\partial \dot{q}_j}\frac{\partial \mathcal{L}}{\partial \dot{q}_j} \cdot \ddot{q}_j}_{\mathbf{M}(\mathbf{q})\ddot{\mathbf{q}}} + \underbrace{\frac{\partial}{\partial q_j}\frac{\partial \mathcal{L}}{\partial \dot{q}_j} \cdot \dot{q}_j - \frac{\partial \mathcal{L}}{\partial q_j}}_{\mathbf{C}(\mathbf{q},\dot{\mathbf{q}})} = \mathcal{F}_j, \tag{2.12}$$

which can be rewritten to get the differential form of the equations of motion:

$$\mathbf{M}(\mathbf{q})\ddot{\mathbf{q}} + \mathbf{C}(\mathbf{q}, \dot{\mathbf{q}}) = \boldsymbol{\mathcal{F}}. \tag{2.13}$$

Here, $\mathbf{M} \in \mathbb{R}^{n^{\mathrm{DoF}} \times n^{\mathrm{DoF}}}$ denotes the symmetric, positive definite mass matrix and $\mathbf{C} \in \mathbb{R}^{n^{\mathrm{DoF}}}$ denotes the vector of the generalized gravitational, centrifugal, and Coriolis forces. Note, that this equation is written in an *inverse dynamics* form. This can be used to infer the forces that take the system from the current state to a future outcome. However, in this thesis, most problems are solved using *forward dynamic* predictions. Here, the goal is to predict future states (e.g. the angle trajectory $\mathbf{q}$) based on the forces that are applied externally or using muscles. To evaluate the angle trajectory, we can write the forward dynamics form:

$$\ddot{\mathbf{q}} = \mathbf{M}(\mathbf{q})^{-1}(\boldsymbol{\mathcal{F}} - \mathbf{C}(\mathbf{q}, \dot{\mathbf{q}})) \tag{2.14}$$

State of the system In the fields of cybernetics and control theory, typically a state vector x is used to uniquely describe the state of a system. Through the use of differential equations, this state vector tracks the evolution of the system over time, as determined by the underlying system dynamics. In most cases, the state vector includes kinematic variables that capture key features such as the current location and velocity of structures. When working with rigid-body assumptions, these kinematic variables can be represented in terms of the generalized joint angles $\mathbf{q}$ and their respective velocities $\dot{\mathbf{q}}$. Additionally, using a musculoskeletal model with a Hill-type muscle model (as outlined in Sec. 2.1) requires the solution of two additional differential equations for each muscle incorporated. As a result, the number of state variables increases, necessitating a formulation of the complete state vector x that encompasses all included muscles $i = 1, \ldots, n^{\text{musc}}$ and generalized coordinates $j = 1, \ldots, n^{\text{DoF}}$. This can be expressed as follows:

$$x \in \mathbb{R}^{2n^{\text{musc}}+2n^{\text{DoF}}} = \{q_j, \dot{q}_j, l_i^{\text{CE}}, \gamma_i\} \tag{2.15}$$

where n^{musc} and n^{DoF} denote the number of muscles and the number of generalized coordinates, respectively.

Generic and individual representations of musculoskeletal models To predict human musculoskeletal motion using the equations discussed previously, it is necessary to determine various parameters related to both the mechanical properties and muscle-related parameters influencing the muscles' force output. There are two general approaches for estimating these parameters: Using individual measurements to represent a specific human, or generic models that can be scaled and used to model representative humans. While the first approach is preferable because it allows for better prediction of the movements of individual patients, it is also more expensive and, for some parameters, ethically and experimentally infeasible. Hence, a generic baseline model is often used to represent averaged human motion, which is then scaled based on different individual measurements. This approach relies on statistical regression based on anthropometric data sets (Associates et al., 1978; Winter, 2009; DIN 33402-2:2005-12). Assuming linear correlation, a model parameter y can be calculated based on a known or measured anthropometric property x, using the following regression equation:

$$y = \frac{\sigma_y}{\sigma_x} c_{xy}(x - \overline{x}) + \overline{y}. \tag{2.16}$$

Here, the standard deviations and mean values of each distribution are denoted as σ_x, σ_y, and $\overline{x}$ and $\overline{y}$, respectively, and $c_{xy} \in (-1, 1)$ describes the correlation coefficient. This statistical approach can be used to estimate, e.g., a segment length based on measured body height. However, for certain research questions, modeling specific individuals may not be helpful. For instance, car occupant models (Pankoke and Siefert, 2007), pedestrian safety models (Decker et al., 2019; Pak, 2019) or ergonomic studies (Siefert et al., 2008) among others, often use representative quantities instead. Typically, three human sizes are chosen: F05, M50 and M95, which represent the 5th percentile female, the 50th percentile male and the 95th percentile male person, respectively. These representatives are commonly used in biomechanical studies because they cover the range between these model sizes (in body height and weight) representing roughly 90% of the entire human population. Based on existing data sets, it seems reasonable to assume a normal distribution of the anthropometric data. Therefore, instead of using the mean and standard variation in Eq. (2.16), it is equivalent to determining the values of the three different percentiles. Based on this approach, all mechanical parameters can be used to scale models to individual properties. More specifically, this includes the following mechanical parameters for a musculoskeletal model: lengths and inertia properties of all segments, location of the joint center and joint axis of rotation.

Furthermore, various musculoskeletal parameters need to be estimated and scaled including the nonlinear muscle routing, the optimal fiber length $l^{\mathrm{CE,opt}}$, the tendon slack length $l^{\mathrm{SEE,0}}$ and the maximal isometric force F^{max}. These parameters can be estimated using different methods, either based on (1) anthropometric dimensions or (2) experimental measurements such as joint angle-torque relationships (Garner and Pandy, 2003; De Groote et al., 2010), EMG-based muscle excitation (Lloyd and Besier, 2003; Falisse et al., 2016) or MRI-based muscle-tendon length measurements (Herzog et al., 1991; Blemker et al., 2007), which take into account the subject's specific moment-generating characteristics. In the following, I will briefly introduce the scaling of parameters based on anthropometric dimensions, as these methods are commonly used due to their ease of use and computational efficiency. One of the challenges related to estimating muscle-tendon parameters is measuring the optimal fiber length and tendon slack length, even with expensive imaging technologies such as ultrasound or MRI (Herzog et al., 1991; Blemker et al., 2007). Therefore, muscle-tendon parameters are often determined in cadaver studies as mean values and then scaled to the respective segment lengths. To determine the generic *optimal fiber length*, the mean fiber length $\bar{l}^{\mathrm{CE}}$ and mean sarcomere length $\bar{l}^{\mathrm{S}}$ are typically measured experimentally. The optimal fiber length is then calculated by dividing these two lengths and multiplying it by the optimal sarcomere length $l^{\mathrm{S,opt}}$:

$$l^{\mathrm{CE,opt}} = \frac{\bar{l}^{\mathrm{CE}}}{\bar{l}^{\mathrm{S}}} \cdot l^{\mathrm{S,opt}}. \tag{2.17}$$

Here, the optimal sarcomere length is defined as the sarcomere length at which maximum isometric tension is generated and has been estimated for humans to be $l^{\mathrm{S,opt}} = 2.7\mu\mathrm{m}$ (Walker and Schrodt, 1974). To scale this optimal fiber length, a simple approach is to rely on linear scaling based on the scaled segment lengths (Seth et al., 2018; Winby et al., 2008). To calculate the *maximal isometric force* F^{max} and scale it accordingly, the physiological cross-sectional area PCSA of the muscle needs to be determined, as it correlates with the maximum force. The muscle volume V^{mus} can be measured from cadavers or MRI scans (Wickiewicz et al., 1983; Handsfield et al., 2014). Assuming a cylindrical muscle belly shape, the PCSA can be calculated based on the optimal fiber length and the measured muscle volume V^{mus} as:

$$\mathrm{PCSA} = \frac{V^{\mathrm{mus}}}{l^{\mathrm{CE,opt}}}. \tag{2.18}$$

The subject-specific maximal isometric force in the Hill-type muscle model is then calculated by multiplying the specific maximum isometric stress σ of the muscle with the PCSA:

$$F^{\max} = \mathrm{PCSA} \cdot \sigma. \tag{2.19}$$

The specific maximum isometric stress of muscles is typically assumed to be in the range of $\sigma = 20 \cdots 35\mathrm{N}/\mathrm{cm}^2$ (see also Mörl et al. (2020) for a more detailed discussion regarding maximum isometric stresses). It is worth noting that the muscle volume has been found to scale with body mass, suggesting that the maximal isometric force can be scaled based on this quantity as well (Handsfield et al., 2014; van der Krogt et al., 2016). Finally, as mentioned earlier, measuring the *tendon slack length* $l^{\mathrm{SEE},0}$ experimentally is challenging due to the nonlinear origin-insertion paths of the muscle-tendon unit. Therefore, it is often scaled subject-specifically. In the case of the spine and thorax muscles, one assumption used also in this thesis (contribution III) is that these muscles are at their optimal length when standing upright. Consequently, the following assumption can be made for these muscles (Rupp et al., 2015; Wochner et al., 2022a; Meszaros-Beller et al., 2023):

$$l^{\mathrm{SEE},0} = l^{\mathrm{MTU}} - l^{\mathrm{CE,opt}}. \tag{2.20}$$

For limb muscles, it is typically preferred to either optimize the tendon slack length based on measured relationships of fiber length and joint angle or match experimentally measured peak isometric torques at certain joint angles. The former approach is also employed in this thesis to scale the optimal fiber length and tendon slack length at representative poses for the muscles of the arm model (contribution II).

In conclusion, the scaling of musculoskeletal models using Hill-type models involves often estimating generic muscle-tendon parameters from cadavers or MRI methods and then using subject-specific scaling methods. Various methods can be used, ranging from simple linear scaling methods based on individual anthropometrics (Seth et al., 2018; Winby et al., 2008) to more complex nonlinear scaling methods that match experimentally measured joint angle-moment curves (Garner and Pandy, 2003; De Groote et al., 2010), or EMG-based muscle excitation (Lloyd and Besier, 2003; Falisse et al., 2016) among other approaches. For a more detailed discussion on the scaling of musculoskeletal models using Hill-type models, refer to Winby et al. (2008); Heinen et al. (2016) and Modenese et al. (2016).

Computational simulation frameworks of biomechanical models There exists a wide range of different simulation frameworks to predict human musculoskeletal motion. These frameworks can be divided into two main categories depending on whether they use the multibody approach or the finite element method to model the musculoskeletal system. Regarding the latter, one of the most widely used frameworks is the FE simulation software LS-Dyna. LS-Dyna is a commercial software package that is used to simulate the dynamic behavior of mechanical systems. It is based on the finite element method and can be used to simulate a wide range of different mechanical systems. There exist several advanced FE human body models that integrate active muscles into the body, for an overview, I refer to the supplementary material of Wochner et al. (2022a). While these detailed FE simulations are able to describe the behavior of tissues with greater detail e.g. to evaluate the injury risks in traffic accidents, they are computationally more expensive and therefore not suitable for research questions focusing on complex movements with many degrees of freedom. Therefore, another alternative is to use multibody simulation platforms such as OpenSim (Delp et al., 2007; Seth et al., 2018), Anybody (Rasmussen et al., 2003; Damsgaard et al., 2006), MuJoCo (Todorov et al., 2012), biorbd (Michaud and Begon, 2021) or demoa (Schmitt, 2022). Additionally, platforms that build upon existing simulation frameworks were recently released that accelerate the underlying simulators and combine them with control libraries, e.g. SCONE (Geijtenbeek, 2019) based on optimal control and MyoSuite (Caggiano et al., 2022) using learning methods. While all these frameworks are able to model the muscle and tendon mechanics, skeletal dynamics and neural inputs, they differ in the details of the implementation and the underlying mathematical models. While some of these details are openly discussed in the literature, e.g. the trade-off between modeling tendon accurate in OpenSim and the computational speed in MuJoCo (Ikkala and Hämäläinen, 2022; Wang et al., 2022), others are more difficult to compare due to the proprietary nature of the software (e.g. Anybody or simulation engine HyFyDy of SCONE). Additionally, one of the few comparison studies that were carried out recently (Kim et al., 2018; Trinler et al., 2019) compared the accuracy and results of OpenSim and Anybody. While they argued that the shown differences in the outputs are mainly due to model choices, a complete benchmark across different frameworks comparing existing tools to simulate human musculoskeletal motion is still missing. Therefore, it is at the moment still up to the user and the underlying research question to carefully decide which framework to use based on different modeling assumptions.

2.2. Theories and concepts of biological movement control

The following section introduces several concepts of biological movement with a focus on control. These concepts lay the foundation for the following chapters and are therefore briefly discussed here.

Motor equivalence problem One fundamental challenge when trying to control biological movement is that every movement can be produced by a possibly infinite number of motor actions. The reason behind this is the highly redundant musculoskeletal system including 244 kinematic degrees of freedom (DoF) (Morecki et al., 1984) and roughly 630 skeletal muscles of the human body (Prilutsky and Zatsiorsky, 2002). This redundancy problem was first stated by Bernstein (1966) and is called the motor equivalence problem. It can be separated into two sub-problems: A controller needs to solve both the kinematic redundancy and the kinetic redundancy. This means that the controller has to decide and plan how to move the joints to achieve a certain posture to resolve the kinematic redundancy. Additionally, the controller has to decide how to activate the muscles to achieve these joint movements to resolve the kinetic redundancy. While from a technical viewpoint, this might seem overly complicated, this redundancy also gives rise to motor variability. This means that our movements can be more robust, and we can select alternative patterns when one or multiple muscles lose their function temporarily or permanently (e.g. due to fatigue or diseases) (Rasmussen et al., 2001; Sohn et al., 2019).

Optimality To overcome this challenge of controlling a highly redundant system, researchers often assume that through evolution, the brain and central nervous system have adapted to perform movements in an optimal manner. To be more specific, controlling a movement optimally means that a set of motor actions is selected to fulfill a certain task while optimizing a specific cost function. Commonly used examples of such cost functions include maximizing smoothness (Flash and Hogan, 1985; Todorov and Jordan, 1998), reducing energy consumption (Srinivasan and Ruina, 2006) or minimizing effort (Ackermann and Van den Bogert, 2010). This optimality assumption is based on the observations of several experiments: Starting from the early 50s, several researchers performed various arm movements with human participants. In these experiments, participants were asked to point from plate-to-plate (Fitts, 1954), from point-to-point (Abend et al., 1982) or even move their hand between multiple points (Harris and Wolpert, 1998). Surprisingly, they noted that the resulting trajectories were highly stereotypical even though there exist infinitely many possibilities to perform these motions. Typically, however, humans tend to move the hand roughly in a straight line with a bell-shaped velocity profile.

Similar to experimental evidence for optimality in arm-reaching, several studies also investigated walking in animals and humans. Again, it was shown that gait patterns tend to be highly stereotypical. For example, it has been demonstrated that metabolic energy expenditure is minimal for the preferred walking pattern. This metabolic cost can be measured experimentally by monitoring oxygen consumption while walking on a treadmill. It was shown that walking requires less energy consumption than running for speeds below 2 m/s, whereas above 2 m/s running is more energy-efficient than walking. This speed limit correlates directly with the threshold humans typically choose for switching gaits which confirmed the hypothesis that gaits are adopted to minimize energy costs (McNeill Alexander, 2002). More specifically, this concept is called cost of transport and means that biological locomotion maximizes the distance traveled given a certain energy budget (Alexander, 2003). Indeed, several experiments showed that at preferred walking speed, the cost of transport is minimal (Ralston, 1976; Cavagna and Kaneko, 1977; Holt et al., 1991). In addition to these and other experiments, assuming optimality in forward dynamic simulations has been used to explain and predict human movement in various tasks. More details about optimal control will be given in Sec. 2.3.

Feedforward and feedback control To find muscle stimulations that generate and control a desired movement, various control approaches exist. They can be distinguished into two general strategies, namely feedforward and feedback control. While feedforward control predicts the future motor command in an anticipatory way, feedback control uses sensory feedback to adjust the motor command based on the error between the current and the desired state. Although these concepts originate from the field of technical control, it is widely accepted that both strategies are also used in human and animal locomotion (Desmurget and Grafton, 2000). Mathematically, we can formulate this as follows:

$$u_{\mathrm{t}} = u_t^{\mathrm{ff}} + u_t^{\mathrm{fb}}, \tag{2.21}$$

$$u_{\mathrm{t}} = u_t^{\mathrm{ff}} + K_t \cdot f^{\mathrm{fb}}(x_{\mathrm{t}} - x_t^{\mathrm{des}}). \tag{2.22}$$

Here, u is the motor command, u^{ff} and u^{fb} represent the feedforward and feedback component, respectively, and K is the feedback gain. f^{fb} represents the feedback function dependent on the current state x and the desired state x^{des}. In biological motor control, this feedback function relies on a multitude of sensory information from the body, including proprioceptive feedback from the muscles, the skin, as well as visual, auditory and vestibular information. One commonly known example of such a feedback loop are stretch reflexes, or more specifically the patellar tendon reflex, where a physician taps the patellar tendon of a patient to elicit a knee-jerk response. A simple explanation for this reflex is that the muscle spindle detects the stretch of the muscle and sends this signal to the spinal cord. This, in turn, triggers a signal to the motor neurons that causes the muscle to contract, thereby reducing the stretch of the muscle (see Reschechtko and Pruszynski (2020) for a more detailed discussion about stretch reflexes). While such short-latency reflexes are used to regulate the muscle's activity, force, and stiffness, also more complex longer-latency responses are embedded in our control system to maintain balance and coordinate movement. Nevertheless, using only feedback control is not sufficient for stable and robust movement control. For example, Moritz and Farley (2004) showed that for human hopping on surfaces with randomized but expected ground stiffness, a modulation of the feedforward pattern increases the mechanical stability. Additionally, Gordon et al. (2020) showed that running guinea fowls are able to tune their feedforward control strategies in reaction to perturbations in an uneven terrain after the loss of proprioceptive feedback. This inclusion of feedforward actuation in biological systems is not only beneficial but also crucial due to the need to counteract large delays in sensory feedback pathways, especially compared to technical systems. Therefore, one theory in motor control states that this anticipatory component is achieved by learning an *internal model* estimating how the motor command will be transformed into an actual movement. It has been hypothesized, that the cerebellum is responsible for this internal model learning. This internal model is then used to predict the future state of the system and to adjust the motor command accordingly in a feedforward fashion (Kawato, 1999; Wolpert et al., 1998). In this thesis, both feedforward and feedback approaches are investigated in combination with exploiting the intrinsic muscle properties.

2.3. Computational approaches to human motor control

Humans and animals have the remarkable ability to control a wide variety of movements in uncertain environments while adapting to new situations. While many previous studies have investigated the control of these movements in simulations and robotics, we still do not fully understand the underlying strategies of the brain and the central nervous system. However, there exists a multitude of proposed control strategies ranging from more technical to bioinspired approaches which enable controlling musculoskeletal models in biomechanical simulations or bioinspired robots. Please note, that the focus of this chapter is on the computational control of the musculoskeletal system without relying on experimental data. There exist a multitude of approaches that use for example electromyography-informed musculoskeletal models to estimate tissue loadings (Lloyd et al., 2005; Manal and Buchanan, 2013; Sartori et al., 2015; Pizzolato et al., 2015). Other approaches rely on experimental trajectory data for motion mimicking (Lee et al., 2010; Hong et al., 2019; Lee et al., 2019).

While both, the EMG-informed approach and motion-capture-driven control are powerful tools, they do not allow us to make predictive statements in 'what if' scenarios. Therefore, I present some of the main approaches of computational control of neuromusculoskeletal models in the literature. Note, that while these approaches are grouped for the ease of the reader, some of these approaches can also be combined in multiple ways. They are ordered ranging from more bioinspired to more computational approaches. However, this distinction is not always clear based on the exact implementation, exploitation or learning strategy.

Muscle Length Feedback Controller One of the simplest controllers used in biological motor control combines a feedforward command u_t^{open} with a feedback command u_t^{closed} incorporating proprioceptive muscle length feedback. The combined hybrid controller for each muscle stimulation $u_{i,t}$ can be formulated as:

$$u_{i,t} = u_{i,t}^{\text{open}} + u_{i,t}^{\text{closed}}. \tag{2.23}$$

The open-loop part represents the activation of the α-motoneurons and therefore, changes the rest lengths and stiffness of the muscles without any sensory feedback. Using this open-loop stimulation, learned movements can be performed. The closed-loop part in Eq. (2.23) is also called the λ-model and represents the activation of γ-motoneurons whenever the muscle spindle detects changes in muscle length l_{CE} and the speed of change in muscle length v_{CE}. Therefore, a more detailed form of Eq. (2.23) for a single muscle is given as:

$$u_{\text{t}} = u_t^{\text{open}} + \left[\frac{k^p}{l^{\text{CE,opt}}} \left(l_{t-\delta}^{\text{CE}} - \lambda_t \right) + \frac{k^d}{l^{\text{CE,opt}}} \left(v_{t-\delta}^{\text{CE}} - \dot{\lambda}_t \right) \right] \tag{2.24}$$

In this equation, k^p and k^d represent the proportional and the derivative gain, and $l^{\text{CE,opt}}$ stands for the optimal fiber length of the contractile element. λ and $\dot{\lambda}$ represent the desired fiber length and velocity, respectively and their difference is calculated to the time-delayed muscle fiber length $l_{t-\delta}^{\text{CE}}$ and velocity $v_{t-\delta}^{\text{CE}}$.

Using this controller, several studies have shown that it is possible to predict fast goal-directed single-joint movements (Kistemaker et al., 2006; Bayer et al., 2017), or to predict the response to two-degree-of-freedom point-to-point arm movements supported by assistive force (Stollenmaier et al., 2020) and even walking in 2D (Günther and Ruder, 2003). In this thesis, this controller was the basis to predict reflexive responses to head-neck-perturbations (contribution III, Wochner et al. (2022a)) and to predict the torque trajectories of different scaled human arm models to optimally design and scale exoskeleton power units (contribution II, Waldhof et al. (2022)).

Neuromechanical Feedback Control Based on the previously discussed muscle length feedback controller, several methods have been presented that use and extend this approach by relying on multiple biologically motivated reflexes or incorporating them in a hierarchical way. These simple feedback laws rely on proprioceptive sensory data such as muscle length, speed and force feedback emulating the feedback signals from muscle spindles and Golgi tendon organs. One of the most commonly used approaches is based on the controller proposed by Geyer and Herr (2010). This controller is able to predict gait patterns of a two-dimensional musculoskeletal model which closely matches natural human gait. In a later work by Song and Geyer (2015), this was further extended for three-dimensional walking and running and tested against perturbations, including walking across various terrains such as slopes, stairs and obstacles. Another controller using and extending the framework of the muscle length feedback controller, is the hierarchical approach introduced by Walter et al. (2021). While the lowest layer in this controller is similar to Eq. (2.24), additional layers are added. These layers account for a transformation of an abstract postural plan in terms of joint angles or torques to muscle lengths. To do so, Jacobi matrices are used that take into account muscle geometry and stiffness to resolve the redundancy problem. This approach has been used, e.g., to model standing and squatting movements (Walter et al., 2021).

Central Pattern Generators and Decomposition in Movement Patterns Central Pattern Generators are distributed networks or neural circuits which produce rhythmic movement patterns without requiring sensory feedback. While the role of feedfoward control in humans remains a topic of ongoing debate, this type of control could play a crucial role in generating rhythmical movements such as walking, running, breathing or chewing. However, simple and low-dimensional sensory feedback can be used as input signals to modulate the rhythmic pattern and shape the high-dimensional pattern. In nature, evidence for the possibility of generating such signals was found by isolating the spinal cord of lampreys (Cohen and Wallén, 1980), salamanders (Delvolvé et al., 1999) or frog embryos (Soffe and Roberts, 1982). Surprisingly, if these deafferented animals are then stimulated with simple electrical or chemical signals, the resulting activity pattern still resembles the original pattern during intact locomotion. Mathematically, these pattern generators can be described by a set of coupled amplitude-controlled phase oscillators. Each oscillator i is described by the following differential equation (Sproewitz et al., 2008):

$$\dot{\phi}_i = \omega_i + \sum_j \omega_{ij} r_j \sin(\phi_j - \phi_i - \varphi_{ij}) \tag{2.25}$$

$$\theta_i = x_i + r_i \cos(\phi_i). \tag{2.26}$$

Here, x_i, r_i, and ϕ_i are the offset, amplitude and phase of oscillator i, respectively. ω_i determines the intrinsic frequency of oscillator i, whereas ω_{ij} and φ_{ij} represent the coupling weight and phase shift between oscillator i and j, respectively, determining how much the oscillators influence each other. The generated CPG trajectories θ_i are then used to control the movement of the model, e.g. by using them as angle reference trajectories. Alternatively, the output can be directly used as muscle activation patterns, where a simple sinusoidal pattern can be used to alternate between the stimulations of flexing and extending muscles. This concept has been successfully applied to control the bipedal walking of a neuromechanical model (Taga et al., 1991; Dzeladini et al., 2014), to create oscillatory hand movements (Haeufle et al., 2020a) and to control various swimming and walking robots (Ijspeert and Crespi, 2007; Ijspeert et al., 2007; Spröwitz et al., 2013) to name but a few. They have been highly successfully applied to these various rhythmic tasks due to their distributed control, their ability to deal with redundancies provided by fast reflex loops and the ability to modulate locomotion patterns.

Muscle synergy control Several researchers have proposed that the central nervous system (CNS) uses a modular control strategy to control the redundant musculoskeletal system. Following with this hypothesis, a set of muscles denoted as ”muscle synergies”, are activated together to perform a certain task. This phenomenon can be exploited as a control strategy, involving the simultaneous activation of multiple muscles in response to a single input, thereby contributing to specific movements (Lacquaniti et al., 2012; Bizzi and Cheung, 2013). Therefore, this approach effectively mitigates the challenge posed by the redundancy problem. Fundamentally, the main idea of this concept is that muscle activity profiles can be decomposed into a series of muscle synergies based on simple, usually linear combinations of a few muscle activation patterns. Mathematically, this can be expressed as follows:

$$u_{i,t} = \sum_{j=1}^{n_{\text{synergy}}} p_{j,t} \cdot \omega_{ij}, \tag{2.27}$$

where $p_{j,t}$ represents the time-dependent pattern associated with the j-th synergy, and ω_{ij} represents the weight corresponding to the j-th synergy and i-th muscle.
One common approach for extracting these synergies involves statistical methodologies such as non-negative matrix factorization or principal component analysis to decompose recorded EMG signals originating from numerous muscles into a set of synergies. Subsequently, these synergies can be used to control the movement of musculoskeletal models or assistive devices. However, there are also counterarguments challenging the existence of muscle synergies. For example, it has been argued that while the results of previously investigated tasks reveal a low dimensionality of these experiments, this might not be surprising considering the imposed task constrained. Moreover, evidence that humans can train individual muscles contradicts the hypothesis that the control synergies of the CNS are solely based on muscle grouping, for a detailed discussion see (Tresch and Jarc, 2009). Despite the ongoing debate, muscle synergies have been successfully applied to simulate human walking (Neptune et al., 2009; Mehrabi et al., 2019), pedaling (Raasch and Zajac, 1999), reaching movements (Nori and Frezza, 2005), and have been employed in controlling anthropomorphic robots (Averta et al., 2020), among numerous other studies.

Impedance Control Impedance control is a control strategy which is based on the idea of controlling the impedance or more specifically the stiffness of the system to resist deviations or externally induced motions (Hogan, 1984a,b). In the biological system, this modulation can be achieved by changing the muscular co-contraction leading to a modified biomechanical response of the controlled limb. Experiments have shown that humans exploit this strategy to control and stabilize arm movements in unstable dynamic environments (Burdet et al., 2001; Franklin et al., 2007). Interestingly, impedance is also modulated during the learning process: During initial exploration, errors are large, and therefore, a large stiffness is required to stabilize the movement. As the movement becomes more accurate, the stiffness decreases (Franklin et al., 2008). When trying to implement this concept to control neuromechanical models, typically inverse dynamics is used to estimate the required forces and torques to stabilize the movement. In its most general form, the required torques τ are calculated by the following equation:

$$\tau = Z \cdot (x - x_{\text{des}}), \tag{2.28}$$

where Z represents the impedance matrix, x represent the actual trajectory and x_{des} the desired goal position or trajectory. While in robotics, these trajectories are typically defined as end-effector or joint angle positions, this equation can also be reformulated for the antagonistic muscle torques based on individual muscle stimulations u (Mitrovic et al., 2010). While this control strategy has the disadvantage of requiring high control and sensing frequencies, as well as an accurate inverse model, it nevertheless has proven to be a powerful tool to control arm movements (Hogan, 1984a), biped robot locomotion (Park, 2001), and various rehabilitation orthosis (Mat Dzahir and Yamamoto, 2014).

Optimal Control As introduced earlier, there is evidence that humans and animals are able to perform movements in an optimal manner, which makes optimal control a promising approach to control musculoskeletal models. In optimal control, typically a loss function ℓ is minimized which depends on the current state $x_{\mathrm{t}} \in R^{n_x}$ and the applied input $u_{\mathrm{t}} \in R^{n_u}$ at a given time t:

$$\min_{\pi_t} J = \min_{\pi_t} \sum_{t=0}^{T} \ell(x_{\mathrm{t}}, u_{\mathrm{t}}, t), \tag{2.29}$$

$$\text{subject to } x_{\mathrm{t+1}} = f(x_{\mathrm{t}}, u_{\mathrm{t}}, t), \tag{2.30}$$

$$u_{\mathrm{t}} = \pi_t(x_0, ..., x_{\mathrm{t}}). \tag{2.31}$$

This loss function ℓ is subject to the system dynamics f (for more details see Sec. 2.1) and is used to find an optimal policy π_t which applies the input u, in our case muscle stimulations, to the system. There exist two commonly used direct transcription methods to solve this trajectory-optimization problem: Direct shooting and direct collocation (Kelly, 2017). In the first case, the idea is to start from a given start point x_0 and based on selected control inputs u, the system dynamics is calculated and simulated in forward-dynamics fashion to generate a prediction (shoot in the future). Based on the calculated prediction, the loss function ℓ and the constraints are evaluated and used to generate a new guess u as input to the system. This approach is often compared to the idea of aiming with a cannon where the goal is e.g. to find the initial velocity of a cannonball. In this example, one first selects a velocity, uses it to simulate the forward dynamics of the system, and then compares the endpoint of the cannonball trajectory to the desired endpoint. Based on this distance, the initial velocity can be re-adjusted iteratively. In contrast to this, when using collocation methods the entire state and control trajectory is represented using polynomial splines. To ensure the physical validity of this approach, intermediate collocation points are used. At these points, the derivatives of the polynomial need to match the dynamics (the derivative of the state).

Currently, both approaches are widely used in biomechanics to solve the optimal control problem for locomotion tasks due to their different advantages and disadvantages. The major difference is that shooting is more akin to natural learning and is able to handle neural delays, motor noise and perturbations whereas collocation solves the problem extremely fast and is less sensitive to the controls and initial state.

Using optimal control, researchers were able to predict walking for healthy and pathological gaits (Anderson and Pandy, 2001a; Falisse et al., 2019), investigate different optimality principles for optimal gaits (Ackermann and Van den Bogert, 2010; Miller et al., 2012b), and predict the effects of using assistive devices (Handford and Srinivasan, 2018). To tackle these problems, recently different new software tools were introduced including OpenSim Moco (Dembia et al., 2020), e.g. to predict and assist with squat-to-stand motions, Bioptim (Michaud et al., 2022), e.g. to predict a twisting somersault and Scone (Geijtenbeek, 2019), e.g. used for walking predictions with muscle weaknesses.

In this thesis, optimal control was used to investigate optimality principles for point-reaching (contribution I, (Wochner et al., 2020)) and to test whether muscle-actuated motion is beneficial for learning (contribution V, (Wochner et al., 2022b)).

Model Predictive Control Model predictive control (MPC) is an optimal control-based method which tries to solve the general optimal control problem (Eq. 2.29) in a receding-horizon fashion for a shorter time horizon ($N \leq T$). In contrast to the approaches discussed in the previous section, the control problem is solved recursively, where only the first element of the predicted control strategy u_0 is applied to the system. Afterwards, the control horizon is shifted to the new initial state $x_{\mathrm{t}+1}$ and a new optimization loop starts where the knowledge of the previously applied u_t can be leveraged as an initial guess for the optimizer. In contrast, to purely open-loop optimal control, MPC has the advantage to deal with uncertainties and counter-act perturbations. Furthermore, it can be argued that it seems highly unlikely that we as humans employ infinitely long trajectory predictions rather than using smaller, finite prediction horizons (Mehrabi et al., 2017). However, these advantages come with the disadvantage of an increased computational burden due to the fact that the optimization problem needs to be solved repeatedly. Nevertheless, this concept has been successfully applied to predict muscle stimulations in human reaching tasks (Mehrabi et al., 2017) and to predict walking patterns for humanoids (Zhang et al., 2019). In this thesis, both optimal control and model predictive control are used to compare whether muscle-actuated motion is beneficial for learning in terms of data-efficiency and robustness (contribution V, (Wochner et al., 2022b)).

Reinforcement Learning In contrast to optimal control, where typically a loss function ℓ is minimized, in reinforcement learning the reward $\mathfrak{r}_{\mathrm{t}}$ is maximized. Reinforcement learning is a machine learning framework where an agent interacts with the environment and gets different rewards based on the selected action and experience (closed-loop strategy). Here, conventionally the goal is to maximize the expected cumulative reward. To reach this goal, a policy $\pi(u_{\mathrm{t}}|o_{\mathrm{t}})$ is learned that defines the behavior by choosing actions u_{t} that the agent should take based on the current observation o_{t}. Here, the latter is a function of the state x_{t}, which typically is only partially available to the agent. Based on the chosen action u_{t}, the system dynamics f defines the transition to a new state $x_{\mathrm{t}+1}$. Due to interactions with the environment, the policy π is optimized over time to maximize the expected reward:

$$\max_{\pi_t} J = \max_{\pi_t} \mathbb{E} \sum_{t=0}^{T-1} \beta^{t-1} \mathfrak{r}_{\mathrm{t}} \tag{2.32}$$

where $\beta \in [0, 1]$ is a discount factor weighting long-term rewards less strongly. Note, that this policy can be either stochastic or deterministic and one of the biggest challenges in

RL is to design good policies. Even though reinforcement learning can be understood as a biologically-inspired strategy, there exist several challenges while applying RL strategies to control muscles: Muscle actuators are set up in a highly redundant, antagonistic setup with a high dimensional state (e.g. up to 600 muscles in the human body). Furthermore, due to the low-pass filter characteristics of the nonlinear activation dynamics, short muscle twitches often do not generate large torques on the joint level which makes the exploration difficult. Therefore, many recently published RL control schemes for musculoskeletal motions use various simplifications: Either only a few muscles are actuated, simplified muscle models are used or muscle synergies are extracted before RL methods are deployed, as well as relying on reward shaping or motion mimicking for specific tasks. Using these restrictions, RL control schemes have been used to accomplish arm-reaching (Joos et al., 2020; Fischer et al., 2021; Caggiano et al., 2022) or even more complex locomotion tasks (La Barbera et al., 2021; Kidziński et al., 2018; Lee et al., 2019; Kidziński et al., 2020; Song et al., 2021; Schumacher et al., 2022; Qin et al., 2022).

2.4. Intelligence by design: Benefits of biomechanical properties

Through evolution, humans and animals have developed structures and patterns which increase their fitness and embodied intelligence. Fitness in a biological context is seen as the probability of having reproductive success in the sense of passing genes along to the next generation. Mathematically, this probability can be optimized by maximizing a function depending on the velocity, acceleration, endurance, energetic economy, and maneuverability among other characteristics which results in an improvement of the underlying organism in terms of structure, material and morphology. These emergent properties often result in an increased physical intelligence and have led to the development of the concept of morphological computation or embodied intelligence (Paul, 2006; Iida and Pfeifer, 2006; Pfeifer and Bongard, 2006; Blickhan et al., 2007; McEvoy and Correll, 2015; Ghazi-Zahedi et al., 2021). This embodied intelligence (EI) is directly encoded in the body and interacts with neural intelligence, such as the brain or nervous system. For humans and animals, embodied intelligence simplifies controlling and perceiving their bodies autonomously in unstructured and uncertain domains through their physical design. Here, the focus is on the benefits of the physical design of *biomechanical* systems and more specifically their morphology. The term morphology is used to describe the shape and structure of an organism or the physical design of a system. More specifically throughout this thesis, morphology is understood by taking into account the following structures and properties of the human body: The number of segments, the segment lengths, how they are connected (e.g. joints), the mass distribution of the organism, its actuator and sensor characteristics, material properties and the placement of actuators and sensors. The goal of the research field of embodied intelligence is to understand why evolution favored certain morphologies and how these morphologies can be used to design technical machines. This is crucial for the development of wearable devices assisting humans as well as robots that can operate in unstructured and uncertain environments. In the following, some beneficial properties of biological structures or movement patterns that enable EI in muscle-actuated systems are discussed.

Benefits of biological shape morphology: Number of links, link sizes and type of connection The concept of exploiting shape morphology to achieve walking movements can be traced back to one of the earliest examples known as the *passive dynamic walker*: The main idea behind this concept is that it is possible to achieve walking movements by simply exploiting the dynamics and gravity without requiring any external actuation. In his seminal work, McGeer et al. (1990) demonstrated that this concept can be used to build technical walking machines by connecting simple mechanical segments via joints in a human-like shape without the use of motors or controllers, which are able to mimic the natural gait of human walking patterns. To accomplish this, the walking machine relies on the design of its components and their mass distribution. In addition, including knees into these systems (McGeer, 1990), further enhances foot clearance and stability. This concept of using the general shape design of a biomechanical system to reduce computational effort was later also extended to three-dimensional systems (Collins et al., 2001) and used to design various hybrid bipedal robots (van der Linde, 1999; Paul et al., 2003; Wisse and Van Frankenhuyzen, 2006).

Benefits of biological passive structures Including elasticity, several authors showed that the material properties of passive structures can be beneficial for locomotion: One example is the inclusion of tendons that can be used to store energy and reduce the energy consumption of the system. It has been shown that biological tendons act as nonlinear serial springs and can be used to store and release mechanical energy during ground contact e.g. Alexander et al. (1982); Alexander (1991); Biewener and Roberts (2000). This spring-like bouncing mechanism (Ishikawa et al., 2005) also improves the shock tolerance which potentially reduces stretch-induced muscle injuries (Roberts and Azizi, 2010; Konow and Roberts, 2015). This has been used as inspiration to create robotic tendons, parallel and serial elastic actuators (SEA's) (Pratt and Williamson, 1995) to use the elastic properties to reduce peak power and energy demands on the motor. They have been included in assistive devices to support walking (Hollander et al., 2006; Au et al., 2007) as well as in legged robots (Robinson et al., 1999; Spröwitz et al., 2013; Hutter et al., 2016; Hubicki et al., 2016). These robotic systems give further evidence that the material properties can increase the efficiency of locomotion by storing and releasing energy as well as improving stability and balance while walking on uneven terrain.

In addition to exhibiting spring-like behavior, certain damping properties in series to the contractile element, such as tendons, aponeuroses and titin, have been identified as beneficial for locomotion. This is particularly relevant in cases where high-frequency oscillations occur, such as when legs impact the ground, as these oscillations can result in damage or even rupture of the tendons. To test this hypothesis, Günther et al. (2007) conducted a study in which they compared a Hill-type model with and without serial damping to experimental data obtained from a piglet muscle-tendon complex. Their findings indicate that serial damping is sufficient to explain the damping of high-frequency vibrations of low amplitudes, thus confirming the protective role of damping in locomotion. In this thesis, such a serial damping element is included as part of the Hill-type muscle model (Hill, 1938; Günther et al., 2007; Haeufle et al., 2014a) that is used in the numerical simulations (see also SDE in Figure 2.3).

Another example of beneficial passive structures in biology are the ligaments in the human spine, which have been shown to reduce the workload of the back muscles and spinal discs.

During forward bending, both the back muscles and the passive structures in the spine are stretched and therefore, store energy. When returning to an upright posture, the passive structures release this energy, assisting the back muscles in extending the spine (White, 1990; Adams and Dolan, 2005; Adams et al., 2012). This reduces the workload of the back muscles and the compressive forces in the spine. In particular, structures such as the supraspinous ligament and the strong posterior band of the lumbodorsal fascia have longer lever arms than the back muscles due to their anatomical placement. Consequently, any extensor moment generated by these passive structures exerts a smaller compressive force on the spine (Dolan and Adams, 1993; Adams et al., 2012). This mechanism has been utilized in the design of passive exoskeletons or exosuits that reduce the metabolic cost, back strain, and spinal disc compression (Koopman et al., 2020; Chang et al., 2020; Ali et al., 2021).

Benefits of biological sensors Morphological computation not only simplifies the control task but is also closely linked to a facilitated perception of the body and its environment, potentially leading to a simpler computation of the motor control. One example from the field of vision is how the retina acts as a pre-processor and distills significant incoming sensory data before sending it to the brain (Gollisch and Meister, 2010). Hence, the retina is able to discard redundant information, while the processing in the brain is accelerated, for example regarding pattern recognition and interpretation. Such beneficial features have inspired both the design of so-called neuromorphic vision sensors (Liao et al., 2021), as well as novel machine learning techniques such as convolutional neural networks (Hubel and Wiesel, 1968; Fukushima, 1980; LeCun et al., 1989).

Further, it has been discussed that sensor fusion is crucial to improve robustness and provide contextual information for motor control. For example, human standing balance requires various sensor signals, including vestibular, visual, auditory and somatosensory information. If such an integration of sensory cues is not functional, this might lead to balance impairments. In patients, this effective, adaptive and intelligent combination of sensory signals can be probed using the sensory organization test (SOT) (Nashner et al., 1982; Nashner and Peters, 1990). This SOT test is used to assess the ability of the central nervous system to integrate sensory information from different modalities. It consists of a series of balance tasks where the patient's senses are perturbed by moving the supporting standing platform and removing or distorting vision. Therefore, the motor response is tested based on the ability to integrate vestibular, visual and proprioceptive sensory inputs and in healthy subjects this ability allows maintaining postural stability in stance. This test demonstrates the power of our biological sensor fusion to combine different sensory modalities to improve the balance and control task.

Benefits of biological actuator placement Another notable example of biological embodied intelligence is the strategic placement of actuators in biological systems. In these systems, actuators are arranged in an antagonistic setup, where at least two muscles, positioned on opposite sides of a joint, generate torques that induce the rotation of this specific joint. This setup is crucial because muscles can only actively contract, necessitating the ability to flex and extend joints by producing torques in opposing directions. This placement of muscles in an antagonistic setup also means that always at least twice as many actuators are needed, compared to a classical robotic system e.g. employing DC motors. While at first glance this might seem unnecessarily complex from a technical viewpoint, this agonistic placement offers the biological system the distinct advantage of *co-contraction* allowing for a modulated joint stiffness without altering the net joint torque. This mechanical impedance provides a stabilization mechanism unaffected by neural time delays and therefore, also acts as a zero-delay preflexive response to perturbations (Hogan, 1984a; Loeb, 1995).

Furthermore, also biarticular muscles, spanning across two or more joints, are present in biological systems. Therefore, these muscles also generate torques at multiple joints simultaneously. Including biarticular muscles has been argued to enhance locomotion efficiency by facilitating energy transfer towards distal joints (Junius et al., 2017; van Ingen Schenau et al., 1987). For instance, during jumping, it was shown that power is transferred from the knee extensor to plantar flexion due to the biarticular muscle gastrocnemius, resulting in a higher jumping height. Furthermore, biarticular muscles help to prevent the leg from over-extension by securing the zigzag configuration of the leg and consequently, providing stability (Seyfarth et al., 2006). This, in turn, reduces the computational demand of the controller, which can rely on the inherent stability of the system.

To summarize, in this section evidence was presented that the morphology of biological systems simplifies challenges for control and perception for uncertain, complex and novel environments. This is due to the fact that the morphology of the biological system is designed in a way that it can be controlled and perceived without the need for complex controllers or sensors. This is in contrast to technical systems where the morphology is often designed to be as simple as possible to reduce the cost of the system. The examples given above demonstrate how the design of the morphology of a system can be beneficial for the control and perception of the system. In the next section, I will focus very specifically on one morphological aspect, namely the actuator or more specifically, the inherent muscle properties.

2.5. Benefits of intrinsic muscle properties

Muscles have highly nonlinear dynamics which from a classical control perspective makes it difficult to use them for movement control. Nevertheless, several studies have shown that including intrinsic muscle properties in biophysical models can be beneficial due to three major reasons: 1. It was hypothesized and shown that muscle-like properties improve the stability and robustness of the system. 2. Additionally, it was shown that muscle-like properties can simplify the control problem by reducing the required amount of information processing (morphological computation). This thesis gives further evidence that the neural information load is reduced using muscle-like properties for pointing and walking movements (contribution IV, Haeufle et al. (2020b)). 3. Finally, this thesis contributes to understanding the benefits of muscle-like properties for the problem of learning anthropomorphic movements. It was shown that muscle-like properties can improve the data-efficiency, are less sensitive towards hyperparameters and more robust towards force perturbations not present during learning (contribution V, Wochner et al. (2022b)). In the following, a brief overview of the existing studies that investigated the benefits of muscle-like properties is given.

Muscles provide stability and robustness Several researchers (Wagner and Blickhan, 1999; Eriten and Dankowicz, 2009) investigated the stability properties of a two-link model representing the human lower limb with muscle-like properties. To do so, analytical investigations based on Lyapunov stability and Floquet multipliers were applied to a simple motion such as knee bending. It was shown that the nonlinear force-velocity and force-length relationship improve the stability of the system. Going one step further, it was shown that these muscle-like properties such as the nonlinear force-velocity and the nonlinear force-length relation also improves resistance to perturbations: van Soest and Bobbert (1993) compared high-jumping movements in a purely torque-driven model to a model driven by muscles. While the original movement was comparable, small perturbations of the initial position or angular velocities revealed that the muscle-driven model was more robust to perturbations. More specifically, this zero-time delay feedback mechanism requires no adaptation of the muscle stimulation pattern as a response towards the perturbations. Similar to this, Gerritsen et al. (1998) compared a purely torque-driven model to three different models modeling separate properties of muscles, including a model with the nonlinear force-velocity relation, a model with the nonlinear force-length relation and a model which combined both properties. They investigated these models for planar walking movements and applied both static and dynamic perturbations. Their results showed that only the model including the combination of both muscle-like properties was able to resist all perturbations. Furthermore, their results suggested that mainly the force-length relation is responsible for resisting static perturbations whereas the force-velocity relation is responsible for resisting dynamic perturbations. Later, this work was extended to walking motions in 3D (John et al., 2013). They showed that both the force-length-velocity properties of the muscle fibers as well as the tendon elasticity have a stabilizing effect towards perturbations applied in a variety of directions.

Quantification of how much muscles simplify control In addition to these studies, researchers suggested that muscle-like properties might counterintuitively *simplify* the control problem by reducing the required amount of information processing by the controller (Full and Koditschek, 1999; Holmes et al., 2006; Blickhan et al., 2007). For example, Geyer et al. (2003) showed that steady-state hopping is possible with only a constant stimulation pattern and simple length or force feedback instead of a more complex, optimized stimulation pattern. They concluded, that the control is largely simplified by exploiting the musculoskeletal dynamics in combination with the reflex dynamics. While this study and the studies mentioned earlier on stability provided qualitative evidence that control is simplified, the actual control effort was not quantified. Currently, two major information-theoretic approaches exist to quantify the contribution of the morphology of the system to the control problem: The metric of morphological computation (Zahedi et al., 2010; Zahedi and Ay, 2013) and the metric of control effort (Haeufle et al., 2014b). In the first approach, the Kullback-Leibler divergence $\mathrm{MC_W}$ is used to quantify how much the distribution of the current observation depends on both the previous state and the actuator signal, compared to depending only on the actuator signal. If this metric $\mathrm{MC_W}$ is small, the morphology of the system contributes less to the control problem and the physical properties are not exploited. This concept has been applied, for example, to compare the morphological computation of a hopping task with DC-motor driven actuators, linearized muscle and nonlinear muscle actuators (Ghazi-Zahedi et al., 2016). The results confirmed that indeed the nonlinear muscle-like properties contribute to the morphological computation. This type of ”morphological computation“ was also quantified through the metric of control effort (Haeufle et al., 2014b). In this second approach, the control effort is defined as the minimal amount of information required to perform a certain movement and can be directly used to measure and compare the information load of different morphologies, e.g., for hopping tasks. This thesis contributes to investigating this concept also for point-reaching and walking tasks (contribution IV, Haeufle et al. (2020b)) in order to quantify the benefits of muscle-actuators in terms of neural information load. The results show that indeed the control effort is reduced if muscle-like properties are used.

3. Objectives and contributions

The overarching goal of this thesis is to improve the control and modeling of biomechanical systems for simulations and robotics, particularly by investigating the complex interplay between the neural controller and underlying biophysical structures. To achieve this objective, I employ neuro-musculoskeletal models of the human body capable of predicting human motion during voluntary movements and reflexive movements using forward dynamics. The central research question that is tackled in this thesis, is the following:

Overarching research question

How does the complex interplay between the neural controller and underlying structures enable us humans to generate movements?

To address this question, I examine the intricate relationship between the neural controller, which represents the brain and central nervous system, and the underlying structures, including the musculoskeletal system and the proprioceptive feedback it provides. The neural controller is modelled using bioinspired control strategies to drive muscle-actuated models, while the underlying structures include the nonlinear actuator dynamics of the muscle-tendon unit, accounting for all nonlinearities that arise through the activation and the contraction dynamics, as well as the elasticity of the tendon. In addition, the anatomical routing with its nonlinear lever arms and the antagonistic setup of biological muscles are taken into account. Further, muscles in combination with the muscle spindle provide the possibility of proprioception and thus, the ability to sense the position and movement of limbs and trunk. Therefore, I also consider the inherent proprioceptive feedback. To address this research question, I tackle five objectives, each with its sub-questions, that correspond to a separate publication (see also an overview of publications in Sec. 4). The first three publication focus on how we can control and predict movements while accounting for muscle dynamics, whereas the last two publications focus on unveiling how the muscle morphology contributes to the neural control by simplifying the learning and control task. Specifically, the following sub-questions are addressed in this thesis:

1. How can we predict voluntary movements at the example of point-reaching movements?
2. How can we predict voluntary movements to design individual assistive devices?
3. How can we predict individual human motion in reflexive situations?
4. How can we quantify the contribution of the underlying structures to the neural control?
5. Is the learning task facilitated by the biological motor system?

These research questions are consecutively addressed by the following contributions.

Contribution 1: How can we predict voluntary movements at the example of point-reaching movements?

In the study of human motor control, it is widely assumed that through learning, adaptation, and evolution, the brain and the central nervous system have developed a strategy to solve the problem of redundancy by selecting a specific optimality principle. This principle narrows down the range of possible actions to perform voluntary movements. However, determining which optimality principle the brain potentially employs is still a topic of investigation for researchers. One of the main challenges in studying human arm movements is the limited ability of commonly used tasks, such as point-to-point reaching movements, to distinguish between different optimality principles. To overcome this limitation, point-to-manifold or point-to-bar experiments have recently been proposed that are employed in this study. Furthermore, prior studies that predicted human arm movements based on optimality principles have often neglected the underlying biophysical structures, specifically the muscle dynamics. This simplification was previously necessary due to computational complexity, but recent advancements in musculoskeletal modeling and optimization techniques have made it possible to include muscle dynamics in the study of human motor control and biomechanics. Including muscle-actuated dynamics is crucial because the actuator morphology can significantly influence movement outcomes. For example, Pinter et al. (2012) showed that different conclusions about motor control can be drawn depending on the actuator morphology. In the first contribution of this thesis (chapter I, Wochner et al. (2020)), we investigate the effect of the underlying biophysical structures on the selection of the optimal control by testing whether accounting for muscle dynamics is essential to accurately predict human reaching movements. Our findings suggest that including muscle dynamics is crucial to predicting human reaching movements accurately. To this end, we explore a combination of previously proposed cost functions to predict how the brain selects the optimal muscle stimulations for point-to-manifold reaching movements. We show that a combined cost function taking into account mechanical work, jerk, and neuronal stimulation effort best predicts human reaching while accounting for muscle dynamics. This finding underscores the importance of including muscle dynamics in the study of human motor control while also considering more open-ended movement tasks, such as point-to-manifold reaching.

Contribution 2: How can we predict voluntary movements to design individual assistive devices?

Building on the findings of the previous contribution, the next contribution (chapter II, Waldhof et al. (2022)) aims to improve the design of individual assistive devices, such as exoskeletons, by taking into account the load cycle of predicted human movements and muscle dynamics in the prediction of voluntary arm movements. In order to achieve this goal, we evaluate whether employing a coupled forward-dynamic approach of subject-specific arm models in combination with a novel scalability model for the electrical power unit can improve its performance. Currently, the design of exoskeletons is often based on generic models that do not take into account individual differences between persons. This leads to a mismatch between the exoskeleton and the individual, therefore, reducing the exoskeleton's performance.

To address this issue, we use subject-specific arm models in combination with our scaling approach to optimize the design of exoskeletons. In our study, we evaluate the performance of the exoskeletons by supporting three different representative models performing typical tasks while considering muscle dynamics. By considering individual user needs and task demands, our proposed scaling approach results in a lighter and more efficient design. Our framework demonstrates the potential to improve the design of individual assistive devices, such as exoskeletons, and provides valuable insights for designing personalized assistive devices for individuals with motor impairments or in manually demanding tasks.

Contribution 3: How can we predict individual human motion in reflexive situations?

While the first two contributions focus on voluntary movements, the third contribution (chapter III, Wochner et al. (2022a)) aims to investigate muscle-actuated motion while resisting perturbations. The response of individuals to sudden perturbations can significantly affect their injury risks in various scenarios, including traffic accidents, physical assaults, and sports or recreation-related collisions. Some of the most common injuries in these situations are head and neck injuries, such as traumatic brain injuries, concussions or whiplash-associated disorders. In this contribution, we conducted perturbation experiments where volunteers were placed on a table with an additional trapdoor that was suddenly released. This sudden drop led to a free-falling movement of the head until the volunteers' reflexes reacted to the perturbation stopping the downward movement. In addition to the physical experiments, we also conducted simulations, where two different simple reflex controllers based on the muscle length were implemented demonstrating that this reflexive behavior can be predicted. Based on these controllers, we showed that a higher sensitivity of the neuronal state (in terms of sensitivity to the stretching of the muscle) can help to reduce acceleration peaks. Additionally, we showed that the reflexive behavior is different for the supine case (extension of head-neck muscles) compared to the prone case (flexion of head-neck muscles) in terms of vertical displacement and peak accelerations. This difference can be explained by the ability of the extensor muscles to create a larger moment compared to the flexor muscles due to their muscle mass difference, as well as the postural role of the extensor muscles. These two findings based on the muscle-actuation dynamics have implications for designing safer vehicles or sports equipment: Developing mechanisms to alert humans to upcoming perturbations, such as using sound signals, might change their sensitivity, and thus their reflexive behavior. Furthermore, the direction of applied force matters, such as sitting frontal versus backward in a vehicle, which might have direct implications for injury risks of concussions or whiplash-associated disorders.

Contribution 4: How can we quantify the contribution of the underlying structures to the neural control?

While the first three contributions focused on the control of voluntary and reflexive muscle-actuated movements, and used these predictions to design individual assistive devices, the fourth contribution (chapter IV,Haeufle et al. (2020b)) investigates whether muscle-actuated motion also simplifies the control task. To do so, we quantify the minimally required information that is needed to control a certain movement. This concept is called control effort, and the key idea is to compare different morphologies, such as actuator dynamics, and determine which morphology requires less information to generate a desired movement. More specifically, in this contribution, we compared models driven by idealized torque actuators to muscle-driven motion and optimized for the minimally required information. This can be done by varying the resolution of the control and sensor signals both in time and amplitude. Our results show that neuromuscular models require less information to generate point-reaching and walking movements compared to their torque-driven counterparts. Therefore, these results support the hypothesis that muscle-actuation motion simplifies control by off-loading computation to the morphological structure.

Contribution 5: Is the learning task facilitated by the biological motor system?

While previous literature showed that muscle-actuated motion simplifies the control by improving stability and robustness, it has not yet been shown that muscle-actuated motion also benefits the learning task. When looking at current robotic systems, we see that they struggle with real-world scenarios and are still outperformed by humans in terms of robustness, versatility and learning of new tasks. The major hypothesis of this work (chapter V,Wochner et al. (2022b)) is that the underlying muscle actuator dynamics provide inherent stability, favorable to learning from scratch. We test this hypothesis by applying different learning strategies to various anthropomorphic tasks such as reaching, hitting a ball, hopping, squatting and high-jumping. Based on this, we show three main findings: First, we showed that the learning of anthropomorphic tasks is more data-efficient when using muscle-actuated motion compared to torque-driven motion. Second, we showed that muscle-like actuators are less sensitive toward hyperparameter variations. Third, the learned policies using muscle-like actuators are more robust towards unknown and unlearned force perturbations and generalize better across perturbations in transfer tasks.

4. List of publications and personal contributions

As mentioned in the previous chapters, this thesis is based on five publications. These publications all answer the overarching research question of this thesis of how muscle-actuated motion can be beneficial for the control and modeling of biomechanical systems. These publications were written and realized with the help of different people. All publications have been accepted and published in peer-reviewed venues. In the following, I would like to summarize their main finding and highlight my personal contributions to each of the publications to which all the co-authors agreed.

Manuscript 1 (Wochner et al., 2020)

Title: Optimality Principles in human point-to-manifold reaching accounting for muscle dynamics

Authors: Isabell Wochner, Danny Driess, Heiko Zimmermann, Daniel F. B. Haeufle, Marc Toussaint, Syn Schmitt

Journal: Frontiers in Computational Neuroscience

Year: 2020

Link: https://doi.org/10.3389/fncom.2020.00038 (see also for electronic supplementary material)

Summary: Multiple studies have shown that human arm movements are highly stereotypical. Therefore, a common assumption in human motor control is that the redundancy in musculoskeletal motions can be solved using optimality principles that have evolved through evolution, learning and adaptation. However, optimality principles were typically only tested for point-to-point reaching tasks, which do not allow for a good discrimination between different principles. Furthermore, previous studies neglected the nonlinear muscle dynamics in the prediction of movement trajectories. To overcome these limitations, we compared different optimality principles using musculoskeletal simulations to synthesize point-to-manifold reaching experiments. The main novelty compared to previously published work is that we included the muscle dynamics to predict these optimal movements based on both isolated and combined cost functions using forward dynamic simulations.

Main finding: Our study shows that a combination of optimality principles including mechanical work, jerk and neuronal stimulation effort best predicts point-to-manifold reaching if muscle dynamics are included.

Contribution: Together with Syn Schmitt and Marc Toussaint, I contributed to the project concept. I set up and performed all the numerical experiments and analyzed the resulting data under the supervision of Syn Schmitt. I created all the figures of the manuscript, wrote the first draft and contributed significantly to all parts of the text during the draft and revision process.

Manuscript 2 (Waldhof et al., 2022)

Title:	Design and Scaling of Exoskeleton Power Units Considering Load Cycles of Humans
Authors:	Marcel Waldhof, Isabell Wochner, Katrin Stollenmaier, Nejila Parspour, Syn Schmitt
Journal:	Robotics
Year:	2022
Link:	https://doi.org/10.3390/robotics11050107
Summary:	Exoskeletons can be used to support humans in manually exhausting or dangerous environments as well as provide assistance for patients with pathological conditions. One major drawback of current exoskeletons is the lack of personalization and individualization. To tackle this challenge, we present a method to scale an arm model in combination with a power unit to represent external assistance for different humans. Based on our scaled musculoskeletal arm model, different torque profiles resulting in various motions are predicted.
Main finding:	Based on these scaled torque profiles, we optimized and scaled a power unit as part of an exoskeleton for different users, which led to better performance and a lighter design.
Contribution:	Together with Marcel Waldhof, Katrin Stollenmaier and Syn Schmitt, I contributed to the project concept. Together with Katrin Stollenmaier, I scaled the arm model and conducted different reaching tasks. I wrote the first draft of the arm model chapter and large parts of the manuscript. Furthermore, I contributed significantly to all parts of the text. During the review process, I was responsible for addressing all questions regarding the biomechanical modeling and results.

Manuscript 3 (Wochner et al., 2022a)

Title:	Falling Heads: investigating reflexive responses to head-neck perturbations
Authors:	Isabell Wochner, Lennart V. Nölle, Oleksandr V. Martynenko, Syn Schmitt
Journal:	Biomedical Engineering OnLine
Year:	2022
Link:	https://doi.org/10.1186/s12938-022-00994-9 (see also for electronic supplementary material)
Summary:	Head-neck injuries can occur in various scenarios ranging from sports-related impacts to car accidents. These injuries are affected by the reflexive responses to head-neck perturbations, which we investigated in this study. Compared to previously published work, the main novelty is two-fold: We used a perturbation setup (called 'falling heads') with two different force directions, namely flexion and extension. Furthermore, we compared this setup to numerical experiments with a muscle reflex controller.
Main finding:	The main results of this study show that the head-neck responses and potential injury risks are affected by the force direction as well as by human diversity, such as biological sex and age.
Contribution:	Together with Syn Schmitt, I designed the project concept and research questions. I analyzed the experimental data, set up the numerical methods and created all figures. I wrote the first draft of the manuscript and was responsible for the revision process (including comments to reviewers, new analysis and re-writing).

Manuscript 4 (Haeufle et al., 2020b)

Title:	Muscles reduce neuronal information load: quantification of control effort in biological vs. robotic pointing and walking
Authors:	Daniel FB Haeufle, Isabell Wochner, David Holzmüller, Danny Driess, Michael Günther, Syn Schmitt
Journal:	Frontiers in Robotics and AI
Year:	2020
Link:	https://doi.org/10.3389/frobt.2020.00077 (see also for electronic supplementary material)
Summary:	To generate movements in complex and uncertain environments, humans rely on their typical biomechanical structure, including the highly nonlinear muscle dynamics, to provide stability. The research question of this study was whether the biological morphology also simplifies the control in the sense of reducing the computational burden. Recently, a new concept called control effort that measures the minimally required information to generate movements was introduced to quantify this morphological computation. In this work, we implemented an optimization algorithm to find this control effort more efficiently.
Main finding:	We showed that muscle-driven models require less information to generate movements such as point-reaching and walking compared to their torque-driven counterparts.
Contribution:	I implemented, analyzed and processed the control effort for the point-reaching movements. Together with Daniel FB Haeufle, I drafted the first version of the paper and contributed significantly to all parts of the text with the focus on the point-reaching tasks, optimization approaches and effects of delays.

Manuscript 5 (Wochner et al., 2022b)

Title:	Learning with Muscles: Benefits for Data-Efficiency and Robustness in Anthropomorphic Tasks
Authors:	Isabell Wochner, Pierre Schumacher, Georg Martius, Dieter Büchler, Syn Schmitt, Daniel FB Haeufle
Journal:	CoRL (Conference on Robotics and Learning)
Year:	2022
Link:	https://openreview.net/forum?id=Xo3eOibXCQ8
Summary:	Humans have the remarkable ability to learn new and challenging tasks and control their movements in complex and uncertain environments. We hypothesize that to achieve this, humans rely on their biomechanical structure, including the highly nonlinear muscle dynamics, to provide stability. The research question of this study was whether the learning of muscle-actuated systems also benefits from this morphology. Previous research showed that applying state-of-art learning techniques to muscle-actuated systems is possible. However, it still needs to be determined whether the learning of such systems also benefits from the highly nonlinear muscle dynamics. To investigate this, we applied different learning strategies to a wide variety of anthropomorphic movements in this study.
Main finding:	We showed that highly nonlinear muscle dynamics are beneficial for learning in terms of data-efficiency, hyperparameter sensitivity and robustness.
Contribution:	Together with Pierre Schumacher, Daniel FB Haeufle and Syn Schmitt, I designed the project concept and formulated the research hypothesis. I implemented, analyzed and created all the results for the OC and MPC cases. I created the first draft of the manuscript and contributed significantly to all parts of the text during the draft and review phases.

5. Discussion and future work

Summary and impact of this thesis The aim of this thesis is to improve the understanding of the control of human movement, with a focus on the underlying muscle dynamics. This is achieved using both model-based and learning-based strategies to control musculoskeletal models. These control strategies and models are validated using existing experimental data and novel data presented within this thesis. The overall findings demonstrate that predictive simulations for musculoskeletal models serve as a powerful tool for studying human movement. Moreover, this knowledge can be translated to biorobotic applications such as developing better robots or exoskeletons.

More specifically, contribution I explores the prediction of human point-to-manifold reaching by investigating different optimality principles within a forward dynamic simulation that incorporates muscle dynamics. The results showed that a combination of mechanical work, jerk and neuronal stimulation effort best predicts these reaching tasks. Furthermore, it is revealed that a single set of muscle stimulations in an open-loop control strategy is in principle capable of predicting these movements due to the inherent nonlinearities involved. Moreover, this contribution emphasizes the importance of using more openly defined movement tasks such as point-to-manifold reaching to distinguish between different optimality principles. Building upon this, the used arm model was scaled to represent different individual persons in contribution II. This enables the investigation of how the scaling of the model and different tasks impact the resulting torque profiles and load cycles. Consequently, this information can be applied to scale an exoskeleton power unit on an individual basis, leading to a better performance and a lighter design. Note, that the *same* bioinspired control signal effectively predicts the movement of different, individual persons. This is a significant advantage of robustness and generalization that helps to understand the guiding principles of voluntary human movement. In contribution III, a similar control scheme is employed, using a refined head-neck model to investigate reflexive movements. Additionally, novel experimental data is presented which can be used as a benchmark test for comparing different muscle control strategies and validating existing Human Body Models directly. This represents a crucial step towards improving predictive simulations using musculoskeletal models, which are used in many applications such as in the rapidly growing field of human-centered engineering and virtual testing in automotive and occupant safety.

While the first three contributions (contributions I-III) focus on improving the control and modeling of various human movements using muscle dynamics, the last two contributions (contributions IV-V) quantify the contribution of muscle dynamics to the control and the learning of human movement. In contribution IV, I together with the co-authors showed that muscle dynamics can reduce the neural information load for point-reaching and walking movements compared to idealized torque actuators. To do so, control effort was used as a measure to quantify the information load. This contribution characterized the minimum needed information to successfully generate a movement by optimizing for the minimal signal resolution and amplitude in both control and sensing. Going one step further, in contribution V, I showed that muscle dynamics can also improve the learning of human movement. This is achieved by reducing the amount of data needed to learn a movement and by improving the robustness of the learned movement. For a more detailed discussion of each of the contributions, I refer to the discussion section in the respective contributions (contributions I-V).

In chapter 3, I raised the overarching research question of this thesis of how the complex interplay between the neural controller and underlying structures enables us humans to generate movements. In conclusion, the first three contributions of my thesis demonstrated that (i) a combination of optimality principles is able to explain point-reaching movements, but it is crucial to consider more openly defined tasks such as point-to-manifold reaching and to account for muscle dynamics, (ii) predictive arm simulations can be used to scale exoskeletons correctly to support individual people, and (iii) reflexive movements of the head-neck complex can be predicted using a simple reflex controller that relies on internal muscle length sensing as low-level feedback. Finally, the last two contributions of my thesis showed that it is crucial to include muscle dynamics to (iv) simplify the control e.g. for pointing and walking movements, and (v) learn robust motions more data-efficiently.
In the following, I will discuss additional findings and thoughts and how they can be embedded in future work.

Fairness of comparing different morphologies To make statements about embodied intelligence, one possibility is to compare different morphologies. This requires careful consideration of the control setup and evaluation criteria to allow for a fair comparison. While these points might seem trivial at first glance, overlooking or neglecting them can lead to misleading results. Therefore, one should consider the following points:

First, the **control scheme** should be independent of the underlying morphology. Early work in this direction typically used minimalistic control schemes, such as simple oscillatory drives for swimming (Ziegler et al., 2006), walking (Iida and Pfeifer, 2006), and flying (Wood, 2007). While they powerfully demonstrated the potential of morphological computation, the associated control schemes were specifically designed and engineered for a specific morphology or required individual fine-tuning for each morphology. Due to this coupling of morphology and motion, it is difficult to compare different morphologies with such specifically crafted control strategies as this might implicitly bias the comparison. This is why optimal control or learning methods are a good choice to eliminate the dependency between the controller and the morphology, as mentioned also by (Rückert and Neumann, 2013; Yesilevskiy et al., 2018). By leveraging such learning methods, a control signal is found that is optimal for the considered task based on some cost function or reward. Therefore, the same control scheme can be used for all models. Note, that if the control scheme is specifically designed for the underlying morphology, an alternative approach to estimate embodied intelligence should be used: For instance, the concept of morphological computation (Zahedi et al., 2010; Zahedi and Ay, 2013), introduced earlier and detailed in Section 2.4 provides a framework that allows the investigation of one specific morphology even with a specifically designed control scheme, as demonstrated e.g. in (Haeufle et al., 2020a). However, this is outside the scope of my thesis, where I mostly focused on comparing different morphologies to make statements about embodied intelligence.

Second, if optimal control or learning methods are used, the **cost function** or reward function needs to be carefully designed to be independent of inherent differences of the underlying morphologies. This is especially important if the final loss of this cost function or reward function is used as the main performance metric to compare different *actuator* morphologies, e.g. as in this thesis where typically idealized torque actuators are compared to muscle-like actuators. Usually, including a cost term that penalizes the control variable squared (u^2) is a good choice in optimal control because it acts as a regularization term and simplifies the computation. However, in the case of comparing actuators minimizing u^2 would represent either minimizing muscle stimulations or minimizing the torque input signals which is not a linear transformation. Hence, evaluating the final loss of such a cost function would lack coherence. Instead, in the case of comparing different actuator morphologies, the comparison metric should always be action-space-agnostic to allow for a fair comparison. This allows to use the same reward function for all models, e.g. as shown in Wochner et al. (2022b). Of course, another possibility is to use morphology-dependent cost terms but choose another metric for the comparison (e.g. control effort as shown in Contribution IV).

Third, when comparing different actuator morphologies, meticulous consideration of the **maximum capacities** of these actuators becomes crucial to ensure meaningful and valid comparisons. For example, in this thesis, I compared idealized torque actuators with muscle-like actuators. To ensure comparability, it is crucial for the maximum torques generated by these actuators to align. Therefore, I imposed a hard constraint on the maximum torque in the torque-actuated case, restricting it to the maximum physiological muscle force achievable by the models under consideration. Although it may be technically feasible to increase the maximum torque within a technical system, such an adjustment would compromise the fairness of comparing underlying morphologies. Theoretically, other control features such as the maximum speed or average torque of the torque actuator could also be aligned with the muscle morphology. In my thesis, however, I specifically focused on aligning only the maximum torque, as exemplified in Contribution IV-V. The reason behind this choice was that this only changes the action-space of the actuator, whereas imposing other constraints such as maximum speed or average torque would also change the actuator behavior, and therefore the morphology, itself. This deliberate choice allows the idealized torque actuators to serve as an upper performance boundary: For example, the torque actuators are able to instantaneously generate any desired force, which is not possible for the muscle actuators that only slowly change their output due to the activation dynamics and the dependency on the kinematics. This also has advantages for the torque actuators, for example for the high-jumping case in Contribution V: Here, a strong and fast motion is required to launch the body upwards, which is solved much faster in the torque case - though it has to be noted, that we did not consider any stability requirements. Including an additional speed limit would therefore also worsen the upper performance bound of the torque actuator. Nevertheless, it is worth noting that for other research questions other sensory limitations, such as sensory conduction velocities (More et al., 2010; More and Donelan, 2018) or the trade-off between energy and information (Niven and Laughlin, 2008) observed in biological systems, as well as matching maximum speed or average torque, could be taken into account.

Fourth, to make more generally applicable statements about the underlying morphology, it is important to consider a wide range of **evaluation criteria**. In this thesis, the focus was on the control effort (contribution IV), data efficiency in the learning process, robustness towards hyperparameter variations and the robustness towards unknown and unlearned perturbations (contribution V). Other criteria that have been investigated are stability and robustness, energy efficiency, precision, cost, performance and many more (see also Section 2.4). These criteria might be taken into consideration either individually or depend on a combination of different criteria. Which criteria are selected for comparison might depend on the task for which the morphology is used.

Finally, closely linked with the previous point, it is important to consider the **task** for which a specific morphology is used. While this thesis investigated the benefits of muscle-actuated motion in terms of control effort and learning for a wide range of reaching and locomotion tasks, the focus was always on anthropomorphic movement objectives. Similar to the concept of ecological niches, an optimal morphology might only be optimal for a specific task. For example, a morphology that is optimal for human-like tasks might not be optimal for industrial tasks such as welding, pick and place or packaging. This is why it is important to consider the task(s) for which a specific morphology is used. This itself, however, might of course also be used as an evaluation criterion: General-purpose systems are desirable, and typically the performance should not only be good enough to perform isolated tasks but rather be adaptable to coordinate several functions in order to traverse unstructured environments (Toda, 1962; Gilday and Iida, 2022).

About the importance of modeling muscle-tendon dynamics As was shown in this thesis, muscle-tendon dynamics are beneficial for controlling and learning biological movements. Additionally, including muscle-tendon dynamics in the study of human motor control and biomechanics is crucial because the choice of modeling simplification impacts the conclusions drawn about motor control. While the choice of simplifying models is often driven by the need to reduce computational complexity, it is important to consider the implications of these simplifications on the conclusions drawn about motor control.

My findings, presented in this thesis, align with existing literature, where similar findings have been presented. For instance, in Contribution I, I demonstrated that using a macroscopic model formulation of the muscles' dynamics leads to a change in the arm kinematics, particularly the tangential velocities. This is closely in line with the outcomes discussed in Pinter et al. (2012) where they compared different types of actuator models - ranging from a torque-driven model and second-order linear mass-spring-damper system to a musculoskeletal model. They demonstrated that the responses to perturbations vary and are significantly different depending on the level of detail used to model the underlying actuator. Therefore, both of our studies demonstrate in different ways that the actuator morphology has a large influence on the movement and if the macroscopic muscle characteristics are neglected, inadequate conclusions about motor control are drawn.

Similar, recent works using predictive simulations have shown that muscle-tendon dynamics are required to achieve human-like motion (Wang et al., 2012; Miller et al., 2012b), and it has been stated that torque-driven models exhibit distinct behavior under the same optimal control assumption compared to muscle-driven models (McErlain-Naylor et al., 2021). This insight is directly applied in Contribution II, where a muscle-driven model is directly employed to generate human-like motions for designing an assistive device. Using this model instead of generating torque speed profiles without muscle dynamics allows for the direct incorporation of natural constraints such as movement speed, muscle fatigue, and muscle strength.

Furthermore, I together with the co-authors showed in Contribution V that including muscle dynamics improves stability and balancing tasks. Here, muscle actuators result in more robust controllers that generalize effectively across perturbations and transfer tasks, such as adding unknown weights to the arm or applying external forces at the hip joint during squatting and hopping tasks. Similar to this, Van Wouwe et al. (2022) showed that including muscle dynamics improves the predictions of human standing balance because muscle co-contraction is predicted as a result of a minimal effort strategy. While I did not conduct a direct investigation of muscle co-contraction in my thesis, it was still demonstrated that muscle dynamics improves the stability against perturbations in various movements.

However, simply including muscle dynamics might not be enough if the elasticity of the tendon is neglected: It is well known that assuming rigid tendons in muscle-driven simulations speeds up the computational time but leads to inaccurate predictions of muscle co-contraction (De Groote et al., 2016). This simplification is especially crucial for motions where the elasticity of tendons is used to store energy such as in high-force motions e.g. in running (Hicks et al., 2015). Additionally, the removal of serial tendon elasticity, as shown by Miller et al. (2012a) leads to a reduction in achievable maximum sprinting speed. Yet, the importance of tendon elasticity in learning new behaviors from scratch remains an open question. Our experiments, thus far, have not definitively confirmed nor denied its significance: Contribution V, demonstrates the benefits of muscle dynamics in learning new behaviors, although two different muscle models were employed: In the Demoa muscle model visco-elastic, passive tendon characteristics are included, which are neglected in the MuJoCo muscle model. Therefore, the role of tendon elasticity in the learning process remains uncertain.

Exploring other specific factors that might contribute to the learning advantages such as the nonlinear force-length, nonlinear force-velocity, activation dynamics, and the nonlinear routing of the muscle-tendon unit were however investigated in several ablation studies shown in Fig. 18 and 23 in the supplementary material of Contribution V. Notably, switching off the nonlinear force-velocity relation has the strongest impact of all aforementioned properties, resulting in poorer learning performance than even the torque actuator performance. Secondly, we added low-pass filters akin to a simplified muscle activation dynamics function to the torque actuation scheme, however, this did not significantly improve the learning performance. However, is important to note that implementing a more complex muscle activation function such as the Hatze activation dynamics (Hatze, 1977; Rockenfeller et al., 2015; Rockenfeller and Günther, 2018) is not possible in the torque actuated case as this function is dependent on the muscle length. Furthermore, the intricate interplay of these muscle properties complicates isolating the significance of each individual property.

Scenarios where muscle-tendon dynamics are not advantageous While this thesis and the literature in the previously mentioned section support the idea that muscle-tendon dynamics is beneficial for the control and learning of biological movements, it is important to note that this is not always the case. Traditionally, in robotics, the interface between an actuator and its load has been made as stiff as possible. Choosing a high interface stiffness has the benefit of maximizing the bandwidth (Pratt et al., 1997). Additionally, conventional actuators such as linear or rotary electrical motors are able to provide high power with fast response times (Chen et al., 2021) which made them highly successful in classical industry tasks for centuries. Therefore, this thesis does not claim that muscle-like actuators are *always* beneficial, but rather for anthropomorphic tasks that require stability and robustness. In the following, I discuss three exemptions where muscle actuators are not beneficial:

In Haeufle et al. (2020b), I together with the co-authors showed that neural information load for point-reaching and walking tasks is reduced if muscle dynamics are included compared to ideal torque actuators. This can be easily understood if one considers that a single constant control input leads to a dynamic movement trajectory while using muscle dynamics, and therefore, this corresponds to the lowest possible control effort $I_{\text{min}} = 0$. A similar hypothetical scenario can be constructed for the torque actuator: If one considers a single-joint pendulum that should produce a constant end effector force, this can be generated by a single torque actuation signal. On the other hand, using muscle dynamics in this scenario would require a continuous adaptation of the muscle activation signal due to the nonlinearities, leading to a higher information load.

The second exemption shows that while I demonstrated in Wochner et al. (2022b) that learning with muscle-like actuators is beneficial in terms of data-efficiency and robustness, there are some tasks where this does not hold true: In tasks that require fast and strong motions such as the high-jumping tasks, the learning is improved when using torque actuators. This can be explained by the fact that in this case I only optimized for a swift motion that launches the system into the air, and not for a stable landing. This leads to an almost instantaneous, maximum torque output that is not possible with muscle-like actuators.

Finally, while most examples in this thesis are solved by forward dynamics, it has been shown that if synthetic reference trajectories should be replicated by different actuator morphologies, the muscle actuators might not lead to faster learning (Peng and Van De Panne, 2017). Note, that in fact the idealized torque actuator always acts as an upper performance bound due to the ability to instantaneously generate any desired torque. However, while (Peng and Van De Panne, 2017) showed that this is beneficial for learning the replication of artificial trajectories, this might not necessarily hold true for human-like movements, which is the focus of this thesis. Additionally, I showed that the muscle actuators are beneficial for learning new behaviors and also showed this for more complex 3D models (see contribution V, Wochner et al. (2022b)).

Limitations of the modeling and control approach Although I showed that muscle-actuated motion has various benefits, there are still some limitations that should be considered.

First, the muscle model mainly used in this thesis (Günther et al., 2007; Haeufle et al., 2014a) neglects some muscle characteristics that may enhance stability. For example, it has been reported that muscles exhibit short-range muscular stiffness that helps to resist against lengthening at the start of a movement (Rack and Westbury, 1974). Furthermore, it has been shown in experiments with running guinea fowls that the history-dependent force production in muscles plays an important role to counteract unexpected drops in terrain (Daley et al., 2009). Including these properties might further improve the stability of the system.

Second, the human arm (Appendix A) and full body model (Appendix B) that I mainly used in this thesis, have various simplifications. The musculoskeletal arm model is restricted to the planar motion of the arm. This can be justified for the investigated point-reaching tasks (Wochner et al., 2020) because the analysis of the experimental data revealed that the recorded movement mostly lay along the para-sagittal plane. In the full body model, I included 8 controllable joints (ankle, knee, hip, lumbar and cervical spine joint) and two arms with passively actuated joints. This is a simplification of the human body which has 244 kinematic degrees of freedom (Morecki et al., 1984). Additionally, each joint was actuated using only the elementary biological drive of two muscle-tendon units set up in an agonistic way (Schmitt et al., 2019). Therefore, several biological muscles are represented as lumped muscles neglecting their individual contributions. Furthermore, biarticular muscles which span across multiple joints were not included. While this simplification is justified for the investigated research question of whether muscle properties are beneficial for control and learning in robotics, it is important to note that this model might be too simplistic to investigate the complexity and variability of human movement. However, including biarticular muscles might further support our findings because it has been shown that biarticular muscles provide stability for example by securing the zigzag configuration of the leg (see also Sec. 2.4).

Finally, also limitations regarding the assumptions of the control scheme need to be discussed. In this thesis, I assume that human motion can be explained by an underlying optimality principle expressed as a mathematical cost function (Wochner et al., 2020). While there is evidence to support this assumption, and we can make use of it to control robots in a human-like manner, it is difficult to falsify this assumption (Berret et al., 2019). Arbitrarily complex cost functions with composite costs can always be constructed to fit any fixed set of data. Using Occam's razor principle or testing generalization across tasks can increase confidence in the validity of the cost function. Additionally, it has been argued that motor control is just “good enough” (Loeb, 2012) or habitual (De Rugy et al., 2012) instead of being truly optimal. This remains an open debate and while there is evidence to support the hypothesis that in novel situations individuals converge towards habitual behaviors, the question remains whether this is just a question of adaption time or if there is a fundamental difference between optimal and habitual behaviors. Moreover, similar to our findings that incorporating muscle dynamics alters the conclusions drawn about optimality, including more morphological aspects of biophysical systems such as neural structures could further improve our understanding of human movement.

Outlook and first steps in these directions This thesis gives the basis towards furthering our understanding of human movement. More specifically, it gives insights into understanding healthy biological movement for both voluntary as well as reflexive movements in both upper- and lower-body movements. Predicting healthy movement is crucial in order to discern the movement patterns from *pathological conditions* affecting the motion. These pathological conditions range from impairments of the muscle-tendon system, e.g., due to diseases such as muscular dystrophy or injuries such as tendon ruptures, to impairments of the nervous system itself, e.g., due to diseases such as Parkinson's disease or injuries such as spinal cord injuries. In all these cases, the movement is affected, necessitating continuous adaptation of the control system to the new circumstances. Additionally, the complex interplay between the control system and the underlying musculoskeletal system is impaired by aging, affecting us all. Mechanistically, this might lead to a decrease in muscle strength (Goodpaster et al., 2006; Delmonico et al., 2009), altered muscle stiffness and activation dynamics (Lim et al., 2019; Pavan et al., 2020), changes in joint stiffness (Blanpied and Smidt, 1993) and increased neural signal delays (Rivner et al., 2001). Using predictive simulations, these effects can be studied in a controlled environment as shown e.g. in Song and Geyer (2018), where evidence was presented that mainly the loss of muscle strength and contraction speed leads to observed changes in gait patterns such as reduced walking speed and economy. Some of these mechanistic effects were also shown in this thesis (Wochner et al., 2022a), where our experimental data revealed, for instance, that elderly individuals exhibit longer latency times measured by the EMG signal compared to younger individuals. As a first step toward modeling this, the sensitivity of the reflex controller was adjusted, as presented. Nevertheless, more detailed investigations are required to model pathological diseases, regarding both the control system and the musculoskeletal system.

Moreover, the knowledge gained in this thesis can be used to develop *personalized rehabilitation strategies*. Recent research has shown that the fusion of video- and IMU data for human motion tracking, coupled with biomechanical modeling, can be utilized to predict the movement of healthy individuals (Pearl et al., 2022). This knowledge can be leveraged to devise personalized rehabilitation strategies for individuals with impaired movements, such as patients suffering from osteoarthritis. Typically, a therapeutic rehabilitation strategy involving a 5° toe-in walking gait is employed to hinder the further progression of knee osteoarthritis (Shull et al., 2013). While their proof-of-concept fusion method (Pearl et al., 2022) shows promising outcomes, it can be further extended based on this thesis by using full 3D muscle-driven simulations in conjunction with dynamic optimization. This approach offers the advantage of not only using standardized therapeutic toe-in strategies but also tailoring rehabilitation strategies to individual patients based on their individual muscle recruitment patterns.

Further, improving the quality of life for people with disabilities or pathologies can be achieved using *exoskeletons and prostheses*. Exoskeletons are wearable devices that support the wearer in performing tasks that would otherwise be difficult or impossible due to their impaired mobility. In this thesis, methods are proposed for tailoring the design of an electrical machine to individual users (Waldhof et al., 2022). This customization can be used to design exoskeletons that are more efficient and more robust. Additionally, these exoskeletons can be controlled using the same control strategies as the biological system (Wochner et al., 2020). This approach offers the advantage of predicting more human-like movements that potentially feels more natural to the wearer. Moreover, I showed that the control signal can be significantly reduced while still generating stable and dynamic movements. Although the concept of control effort was initially used only as an analysis tool for comparing actuators, it may also have implications for driving neural prostheses based on functional electrical stimulation. Existing evidence suggests that a very high stimulation frequency can lead to fatigue (Rongsawad and Ratanapinunchai, 2018). Exploring whether the concept of minimizing information can also be applied to control neural prostheses is an open question for future work. Additionally, a significant challenge that persists is how to predict and integrate the user's intended movement as the next most probable action into the exoskeleton's movement.

Finally, the knowledge gained in this thesis can be used to *design and control robots* that are more efficient and robust. Specifically, it is proposed to include properties of the biological morphology such as the nonlinear properties of the muscle-tendon system to improve robustness and learning capabilities (Wochner et al., 2022b). This can be implemented in two different ways: Muscle characteristics such as the force-length-velocity relation and low-pass filter characteristics can be simulated and integrated into low-level control layers applied to torque-controlled robotic systems. Alternatively, novel soft robotic actuators, such as artificial muscles (Klute et al., 2002; Tondu, 2012; Wolfen et al., 2018), have been developed to mimic the muscle-tendon system. In contrast, researchers have recently also powered a biohybrid robot by an antagonistic pair of skeletal muscle tissues (Morimoto et al., 2018). These in vitro constructed cells can be selectively actuated through electric fields, where the voltage leads to muscle contractions. Testing these various actuators in combination with the proposed control strategies is a promising direction for future work. Furthermore, although not the primary focus of this thesis, simplifying control and reducing computational demands in terms of data-efficiency is a very first step towards creating more sustainable robots. Integrating bioinspired morphology, such as muscle-like properties, might increase energetic sustainability. This might lead to more energy-efficient robots which has been identified as a large challenge ahead for robotics (Mazzolai and Laschi, 2020).

Bibliography

W. Abend, E. Bizzi, and P. Morasso. Human arm trajectory formation. *Brain: a journal of neurology*, 105(Pt 2):331–348, 1982.

M. Ackermann and A. J. Van den Bogert. Optimality principles for model-based prediction of human gait. *Journal of biomechanics*, 43(6):1055–1060, 2010.

M. A. Adams and P. Dolan. Spine biomechanics. *Journal of biomechanics*, 38(10):1972–1983, 2005.

M. A. Adams, N. Bogduk, K. Burton, and P. Dolan. *The Biomechanics of Back Pain-E-Book.* Elsevier health sciences, 2012.

R. M. Alexander. Energy-saving mechanisms in walking and running. *Journal of experimental biology*, 160(1):55–69, 1991.

R. M. Alexander. *Principles of animal locomotion.* Princeton University Press, 2003.

R. M. Alexander, G. Maloiy, R. Ker, A. Jayes, and C. Warui. The role of tendon elasticity in the locomotion of the camel (camelus dromedarius). *Journal of Zoology*, 198(3):293–313, 1982.

A. Ali, V. Fontanari, W. Schmoelz, and S. K. Agrawal. Systematic review of back-support exoskeletons and soft robotic suits. *Frontiers in bioengineering and biotechnology*, 9:765257, 2021.

K. An, K. Takahashi, T. Harrigan, and E. Chao. Determination of muscle orientations and moment arms. *Journal of biomechanical engineering*, 106(3):280–282, 1984.

A. E. Anderson, B. J. Ellis, and J. A. Weiss. Verification, validation and sensitivity studies in computational biomechanics. *Computer methods in biomechanics and biomedical engineering*, 10(3):171–184, 2007.

F. C. Anderson and M. G. Pandy. A dynamic optimization solution for vertical jumping in three dimensions. *Computer methods in biomechanics and biomedical engineering*, 2(3): 201–231, 1999.

F. C. Anderson and M. G. Pandy. Dynamic optimization of human walking. *J. Biomech. Eng.*, 123(5):381–390, 2001a.

F. C. Anderson and M. G. Pandy. Static and dynamic optimization solutions for gait are practically equivalent. *Journal of biomechanics*, 34(2):153–161, 2001b.

W. Associates, Y. Springs, O. A. R. Project, S. A. Scientific, and T. I. Office. *Anthropometric source book*, volume 1024. National Aeronautics and Space Administration, Scientific and Technical , 1978.

S. K. Au, H. Herr, J. Weber, and E. C. Martinez-Villalpando. Powered ankle-foot prosthesis for the improvement of amputee ambulation. In *2007 29th annual international conference of the IEEE engineering in medicine and biology society*, pages 3020–3026. IEEE, 2007.

G. Aumüller, G. Aust, J. Engele, J. Kirsch, G. Maio, and A. Mayerhofer. *Duale Reihe Anatomie*. Thieme Stuttgart, 2017. ISBN 9783132417526.

G. Averta, C. Della Santina, G. Valenza, A. Bicchi, and M. Bianchi. Exploiting upper-limb functional principal components for human-like motion generation of anthropomorphic robots. *Journal of NeuroEngineering and Rehabilitation*, 17(1):1–15, 2020.

A. Bayer, S. Schmitt, M. Günther, and D. Haeufle. The influence of biophysical muscle properties on simulating fast human arm movements. *Computer methods in biomechanics and biomedical engineering*, 20(8):803–821, 2017.

S. M. Beeman, A. R. Kemper, M. L. Madigan, C. T. Franck, and S. C. Loftus. Occupant kinematics in low-speed frontal sled tests: Human volunteers, hybrid iii atd, and pmhs. *Accident Analysis & Prevention*, 47:128–139, 2012.

N. Bernstein. The co-ordination and regulation of movements. *The co-ordination and regulation of movements*, 1966.

B. Berret, I. Delis, J. Gaveau, and F. Jean. Optimality and modularity in human movement: from optimal control to muscle synergies. *Biomechanics of anthropomorphic systems*, pages 105–133, 2019.

A. A. Biewener and T. J. Roberts. Muscle and tendon contributions to force, work, and elastic energy savings: a comparative perspective. *Exercise and sport sciences reviews*, 28 (3):99–107, 2000.

E. Bizzi and V. C. Cheung. The neural origin of muscle synergies. *Frontiers in computational neuroscience*, 7:51, 2013.

P. Blanpied and G. L. Smidt. The difference in stiffness of the active plantarflexors between young and elderly human females. *Journal of gerontology*, 48(2):M58–M63, 1993.

S. S. Blemker, D. S. Asakawa, G. E. Gold, and S. L. Delp. Image-based musculoskeletal modeling: applications, advances, and future opportunities. *Journal of Magnetic Resonance Imaging: An Official Journal of the International Society for Magnetic Resonance in Medicine*, 25(2):441–451, 2007.

R. Blickhan, A. Seyfarth, H. Geyer, S. Grimmer, H. Wagner, and M. Günther. Intelligence by mechanics. *Philosophical Transactions of the Royal Society A: Mathematical, Physical and Engineering Sciences*, 365(1850):199–220, 2007.

E. Burdet, R. Osu, D. W. Franklin, T. E. Milner, and M. Kawato. The central nervous system stabilizes unstable dynamics by learning optimal impedance. *Nature*, 414(6862): 446–449, 2001.

V. Caggiano, H. Wang, G. Durandau, M. Sartori, and V. Kumar. Myosuite–a contact-rich simulation suite for musculoskeletal motor control. *arXiv preprint arXiv:2205.13600*, 2022.

P. M. Carter, C. A. Flannagan, M. P. Reed, R. M. Cunningham, and J. D. Rupp. Comparing the effects of age, bmi and gender on severe injury (ais 3+) in motor-vehicle crashes. *Accident Analysis & Prevention*, 72:146–160, 2014.

G. Cavagna and M. Kaneko. Mechanical work and efficiency in level walking and running. *The Journal of physiology*, 268(2):467–481, 1977.

S. E. Chang, T. Pesek, T. R. Pote, J. Hull, J. Geissinger, A. A. Simon, M. M. Alemi, and A. T. Asbeck. Design and preliminary evaluation of a flexible exoskeleton to assist with lifting. *Wearable Technologies*, 1:e10, 2020.

Y. Chen, Y. Yang, M. Li, E. Chen, W. Mu, R. Fisher, and R. Yin. Wearable actuators: An overview. *Textiles*, 1(2):283–321, 2021.

A. H. Cohen and P. Wallén. The neuronal correlate of locomotion in fish: fictive swimming induced in an in vitro preparation of the lamprey spinal cord. *Experimental brain research*, 41(1):11–18, 1980.

S. H. Collins, M. Wisse, and A. Ruina. A three-dimensional passive-dynamic walking robot with two legs and knees. *The International Journal of Robotics Research*, 20(7):607–615, 2001.

R. D. Crowninshield and R. A. Brand. A physiologically based criterion of muscle force prediction in locomotion. *Journal of biomechanics*, 14(11):793–801, 1981.

M. A. Daley, A. Voloshina, and A. A. Biewener. The role of intrinsic muscle mechanics in the neuromuscular control of stable running in the guinea fowl. *The Journal of physiology*, 587(11):2693–2707, 2009.

M. Damsgaard, J. Rasmussen, S. T. Christensen, E. Surma, and M. De Zee. Analysis of musculoskeletal systems in the anybody modeling system. *Simulation Modelling Practice and Theory*, 14(8):1100–1111, 2006.

F. De Groote and A. Falisse. Perspective on musculoskeletal modelling and predictive simulations of human movement to assess the neuromechanics of gait. *Proceedings of the Royal Society B*, 288(1946):20202432, 2021.

F. De Groote, A. Van Campen, I. Jonkers, and J. De Schutter. Sensitivity of dynamic simulations of gait and dynamometer experiments to hill muscle model parameters of knee flexors and extensors. *Journal of biomechanics*, 43(10):1876–1883, 2010.

F. De Groote, A. L. Kinney, A. V. Rao, and B. J. Fregly. Evaluation of direct collocation optimal control problem formulations for solving the muscle redundancy problem. *Annals of biomedical engineering*, 44:2922–2936, 2016.

A. De Rugy, G. E. Loeb, and T. J. Carroll. Muscle coordination is habitual rather than optimal. *Journal of Neuroscience*, 32(21):7384–7391, 2012.

W. Decker, B. Koya, W. Pak, C. D. Untaroiu, and F. S. Gayzik. Evaluation of finite element human body models for use in a standardized protocol for pedestrian safety assessment. *Traffic injury prevention*, 20(sup2):S32–S36, 2019.

M. J. Delmonico, T. B. Harris, M. Visser, S. W. Park, M. B. Conroy, P. Velasquez-Mieyer, R. Boudreau, T. M. Manini, M. Nevitt, A. B. Newman, and B. H. Goodpaster. Longitudinal study of muscle strength, quality, and adipose tissue infiltration. *The American journal of clinical nutrition*, 90(6):1579–1585, 2009.

S. L. Delp, J. P. Loan, M. G. Hoy, F. E. Zajac, E. L. Topp, and J. M. Rosen. An interactive graphics-based model of the lower extremity to study orthopaedic surgical procedures. *IEEE Transactions on Biomedical engineering*, 37(8):757–767, 1990.

S. L. Delp, F. C. Anderson, A. S. Arnold, P. Loan, A. Habib, C. T. John, E. Guendelman, and D. G. Thelen. Opensim: open-source software to create and analyze dynamic simulations of movement. *IEEE transactions on biomedical engineering*, 54(11):1940–1950, 2007.

I. Delvolvé, P. Branchereau, R. Dubuc, and J.-M. Cabelguen. Fictive rhythmic motor patterns induced by nmda in an in vitro brain stem–spinal cord preparation from an adult urodele. *Journal of Neurophysiology*, 82(2):1074–1077, 1999.

C. L. Dembia, N. A. Bianco, A. Falisse, J. L. Hicks, and S. L. Delp. Opensim moco: Musculoskeletal optimal control. *PLOS Computational Biology*, 16(12):e1008493, 2020.

M. Desmurget and S. Grafton. Forward modeling allows feedback control for fast reaching movements. *Trends in cognitive sciences*, 4(11):423–431, 2000.

DIN 33402-2:2005-12. Ergonomics - human body dimensions - part 2: Values, December 2005.

P. Dolan and M. Adams. The relationship between emg activity and extensor moment generation in the erector spinae muscles during bending and lifting activities. *Journal of biomechanics*, 26(4-5):513–522, 1993.

D. Driess, H. Zimmermann, S. Wolfen, D. Suissa, D. Haeufle, D. Hennes, M. Toussaint, and S. Schmitt. Learning to Control Redundant Musculoskeletal Systems with Neural Networks and SQP: Exploiting Muscle Properties. *ICRA 2018 (accepted)*, 2018.

F. Dzeladini, J. Van Den Kieboom, and A. Ijspeert. The contribution of a central pattern generator in a reflex-based neuromuscular model. *Frontiers in human neuroscience*, 8:371, 2014.

A. Erdemir, S. McLean, W. Herzog, and A. J. van den Bogert. Model-based estimation of muscle forces exerted during movements. *Clinical biomechanics*, 22(2):131–154, 2007.

M. Eriten and H. Dankowicz. A rigorous dynamical-systems-based analysis of the self-stabilizing influence of muscles. *Journal of biomechanical engineering*, 131(1):011011, 2009.

A. Falisse, S. Van Rossom, I. Jonkers, and F. De Groote. Emg-driven optimal estimation of subject-specific hill model muscle–tendon parameters of the knee joint actuators. *IEEE Transactions on Biomedical Engineering*, 64(9):2253–2262, 2016.

A. Falisse, G. Serrancolí, C. L. Dembia, J. Gillis, I. Jonkers, and F. De Groote. Rapid predictive simulations with complex musculoskeletal models suggest that diverse healthy and pathological human gaits can emerge from similar control strategies. *Journal of The Royal Society Interface*, 16(157):20190402, 2019.

F. Fischer, M. Bachinski, M. Klar, A. Fleig, and J. Müller. Reinforcement learning control of a biomechanical model of the upper extremity. *Scientific Reports*, 11(1):1–15, 2021.

P. M. Fitts. The information capacity of the human motor system in controlling the amplitude of movement. *Journal of experimental psychology*, 47(6):381, 1954.

T. Flash and N. Hogan. The coordination of arm movements: an experimentally confirmed mathematical model. *Journal of neuroscience*, 5(7):1688–1703, 1985.

D. W. Franklin, G. Liaw, T. E. Milner, R. Osu, E. Burdet, and M. Kawato. Endpoint stiffness of the arm is directionally tuned to instability in the environment. *Journal of Neuroscience*, 27(29):7705–7716, 2007.

D. W. Franklin, E. Burdet, K. P. Tee, R. Osu, C.-M. Chew, T. E. Milner, and M. Kawato. Cns learns stable, accurate, and efficient movements using a simple algorithm. *Journal of neuroscience*, 28(44):11165–11173, 2008.

B. J. Fregly. A conceptual blueprint for making neuromusculoskeletal models clinically useful. *Applied Sciences*, 11(5):2037, 2021.

K. Fukushima. Neocognitron: A self-organizing neural network model for a mechanism of pattern recognition unaffected by shift in position. *Biological cybernetics*, 36(4):193–202, 1980.

R. J. Full and D. E. Koditschek. Templates and anchors: neuromechanical hypotheses of legged locomotion on land. *Journal of experimental biology*, 202(23):3325–3332, 1999.

B. A. Garner and M. G. Pandy. The obstacle-set method for representing muscle paths in musculoskeletal models. *Computer methods in biomechanics and biomedical engineering*, 3 (1):1–30, 2000.

B. A. Garner and M. G. Pandy. Estimation of musculotendon properties in the human upper limb. *Annals of biomedical engineering*, 31:207–220, 2003.

T. Geijtenbeek. Scone: Open source software for predictive simulation of biological motion. *Journal of Open Source Software*, 4(38):1421, 2019.

T. Geijtenbeek, A. J. Van Den Bogert, B. J. Van Basten, and A. Egges. Evaluating the physical realism of character animations using musculoskeletal models. In *MIG*, pages 11–22. Springer, 2010.

K. G. Gerritsen, A. J. van den Bogert, M. Hulliger, and R. F. Zernicke. Intrinsic muscle properties facilitate locomotor controla computer simulation study. *Motor control*, 2(3): 206–220, 1998.

H. Geyer and H. Herr. A muscle-reflex model that encodes principles of legged mechanics produces human walking dynamics and muscle activities. *IEEE Transactions on neural systems and rehabilitation engineering*, 18(3):263–273, 2010.

H. Geyer, A. Seyfarth, and R. Blickhan. Positive force feedback in bouncing gaits? *Proceedings of the Royal Society of London. Series B: Biological Sciences*, 270(1529):2173–2183, 2003.

K. Ghazi-Zahedi, D. F. Haeufle, G. Montúfar, S. Schmitt, and N. Ay. Evaluating morphological computation in muscle and dc-motor driven models of hopping movements. *Frontiers in Robotics and AI*, 3:42, 2016.

K. Ghazi-Zahedi, J. Rieffel, S. Schmitt, and H. Hauser. Recent trends in morphological computation. *Frontiers in Robotics and AI*, page 159, 2021.

K. Gilday and F. Iida. Intelligent soft hands and benchmarking towards general-purpose robotic manipulation. In *IOP Conference Series: Materials Science and Engineering*, volume 1261, page 012010. IOP Publishing, 2022.

T. Gollisch and M. Meister. Eye smarter than scientists believed: neural computations in circuits of the retina. *Neuron*, 65(2):150–164, 2010.

B. H. Goodpaster, S. W. Park, T. B. Harris, S. B. Kritchevsky, M. Nevitt, A. V. Schwartz, E. M. Simonsick, F. A. Tylavsky, M. Visser, and A. B. Newman. The loss of skeletal muscle strength, mass, and quality in older adults: the health, aging and body composition study. *The Journals of Gerontology Series A: Biological Sciences and Medical Sciences*, 61(10): 1059–1064, 2006.

A. Gordon, A. F. Huxley, and F. Julian. The variation in isometric tension with sarcomere length in vertebrate muscle fibres. *The Journal of physiology*, 184(1):170–192, 1966.

J. C. Gordon, N. C. Holt, A. Biewener, and M. A. Daley. Tuning of feedforward control enables stable muscle force-length dynamics after loss of autogenic proprioceptive feedback. *Elife*, 9:e53908, 2020.

A. Graevemeyer. Im Fall des Fallens. *c't Magazin für Computertechnik, Heise Zeitschriftenverlag GmbH & Co. KG*, 1:142–145, 2023. URL `https://www.heise.de/select/ct/2023/1/2229907140264063595`.

M. Günther. *Computersimulationen zur Synthetisierung des muskulär erzeugten menschlichen Gehens unter Verwendung eines biomechanischen Mehrkörpermodells.* PhD thesis, Eberhard-Karls-Universität zu Tübingen, 1997.

M. Günther and H. Ruder. Synthesis of two-dimensional human walking: a test of the λ-model. *Biological cybernetics*, 89(2):89–106, 2003.

M. Günther, S. Schmitt, and V. Wank. High-frequency oscillations as a consequence of neglected serial damping in hill-type muscle models. *Biological cybernetics*, 97(1):63–79, 2007.

D. Haeufle, M. Günther, A. Bayer, and S. Schmitt. Hill-type muscle model with serial damping and eccentric force–velocity relation. *Journal of biomechanics*, 47(6):1531–1536, 2014a.

D. Haeufle, M. Günther, G. Wunner, and S. Schmitt. Quantifying control effort of biological and technical movements: an information-entropy-based approach. *Physical Review E*, 89 (1):012716, 2014b.

D. F. Haeufle, K. Stollenmaier, I. Heinrich, S. Schmitt, and K. Ghazi-Zahedi. Morphological computation increases from lower-to higher-level of biological motor control hierarchy. *Frontiers in Robotics and AI*, 7:511265, 2020a.

D. F. Haeufle, I. Wochner, D. Holzmüller, D. Driess, M. Günther, and S. Schmitt. Muscles reduce neuronal information load: quantification of control effort in biological vs. robotic pointing and walking. *Frontiers in Robotics and AI*, 7:77, 2020b.

D. F. B. Haeufle, M. Günther, A. Bayer, and S. Schmitt. Hill-type muscle model with serial damping and eccentric force-velocity relation. *Journal of Biomechanics*, 47(6):1531–1536, 2014c. ISSN 18732380. doi: 10.1016/j.jbiomech.2014.02.009.

M. Hammer, M. Günther, D. Haeufle, and S. Schmitt. Tailoring anatomical muscle paths: a sheath-like solution for muscle routing in musculoskeletal computer models. *Mathematical biosciences*, 311:68–81, 2019.

M. L. Handford and M. Srinivasan. Energy-optimal human walking with feedback-controlled robotic prostheses: a computational study. *IEEE Transactions on Neural Systems and Rehabilitation Engineering*, 26(9):1773–1782, 2018.

G. G. Handsfield, C. H. Meyer, J. M. Hart, M. F. Abel, and S. S. Blemker. Relationships of 35 lower limb muscles to height and body mass quantified using mri. *Journal of biomechanics*, 47(3):631–638, 2014.

C. M. Harris and D. M. Wolpert. Signal-dependent noise determines motor planning. *Nature*, 394(6695):780, 1998.

H. Hatze. A myocybernetic control model of skeletal muscle. *Biological cybernetics*, 25(2): 103–119, 1977.

F. Heinen, M. E. Lund, J. Rasmussen, and M. de Zee. Muscle–tendon unit scaling methods of hill-type musculoskeletal models: An overview. *Proceedings of the Institution of Mechanical Engineers, Part H: Journal of Engineering in Medicine*, 230(10):976–984, 2016.

W. Herzog, L. Read, and H. Ter Keurs. Experimental determination of forcelength relations of intact human gastrocnemius muscles. *Clinical Biomechanics*, 6(4):230–238, 1991.

J. L. Hicks, T. K. Uchida, A. Seth, A. Rajagopal, and S. L. Delp. Is my model good enough? best practices for verification and validation of musculoskeletal models and simulations of movement. *Journal of biomechanical engineering*, 137(2), 2015.

A. V. Hill. The heat of shortening and the dynamic constants of muscle. *Proceedings of the Royal Society of London. Series B-Biological Sciences*, 126(843):136–195, 1938.

N. Hogan. Adaptive control of mechanical impedance by coactivation of antagonist muscles. *IEEE Transactions on automatic control*, 29(8):681–690, 1984a.

N. Hogan. Impedance control: An approach to manipulation. In *1984 American control conference*, pages 304–313. IEEE, 1984b.

K. W. Hollander, R. Ilg, T. G. Sugar, and D. Herring. An Efficient Robotic Tendon for Gait Assistance. *Journal of Biomechanical Engineering*, 128(5):788–791, 03 2006. ISSN 0148-0731. doi: 10.1115/1.2264391. URL `https://doi.org/10.1115/1.2264391`.

P. Holmes, R. J. Full, D. Koditschek, and J. Guckenheimer. The dynamics of legged locomotion: Models, analyses, and challenges. *SIAM review*, 48(2):207–304, 2006.

K. G. Holt, J. Hamill, and R. O. Andres. Predicting the minimal energy costs of human walking. *Medicine and science in sports and exercise*, 23(4):491–498, 1991.

S. Hong, D. Han, K. Cho, J. S. Shin, and J. Noh. Physics-based full-body soccer motion control for dribbling and shooting. *ACM Transactions on Graphics (TOG)*, 38(4):1–12, 2019.

M. G. Hoy, F. E. Zajac, and M. E. Gordon. A musculoskeletal model of the human lower extremity: the effect of muscle, tendon, and moment arm on the moment-angle relationship of musculotendon actuators at the hip, knee, and ankle. *Journal of biomechanics*, 23(2): 157–169, 1990.

D. H. Hubel and T. N. Wiesel. Receptive fields and functional architecture of monkey striate cortex. *The Journal of physiology*, 195(1):215–243, 1968.

C. Hubicki, J. Grimes, M. Jones, D. Renjewski, A. Spröwitz, A. Abate, and J. Hurst. Atrias: Design and validation of a tether-free 3d-capable spring-mass bipedal robot. *The International Journal of Robotics Research*, 35(12):1497–1521, 2016.

D. R. Hume, A. Navacchia, P. J. Rullkoetter, and K. B. Shelburne. A lower extremity model for muscle-driven simulation of activity using explicit finite element modeling. *Journal of biomechanics*, 84:153–160, 2019.

M. Hutter, C. Gehring, D. Jud, A. Lauber, C. D. Bellicoso, V. Tsounis, J. Hwangbo, K. Bodie, P. Fankhauser, M. Bloesch, et al. Anymal-a highly mobile and dynamic quadrupedal robot. In *2016 IEEE/RSJ international conference on intelligent robots and systems (IROS)*, pages 38–44. IEEE, 2016.

F. Iida and R. Pfeifer. Sensing through body dynamics. *Robotics and Autonomous Systems*, 54(8):631–640, 2006.

A. J. Ijspeert and A. Crespi. Online trajectory generation in an amphibious snake robot using a lamprey-like central pattern generator model. In *Proceedings 2007 IEEE International Conference on Robotics and Automation*, pages 262–268. IEEE, 2007.

A. J. Ijspeert, A. Crespi, D. Ryczko, and J.-M. Cabelguen. From swimming to walking with a salamander robot driven by a spinal cord model. *science*, 315(5817):1416–1420, 2007.

A. Ikkala and P. Hämäläinen. Converting biomechanical models from opensim to mujoco. In *Converging Clinical and Engineering Research on Neurorehabilitation IV: Proceedings of the 5th International Conference on Neurorehabilitation (ICNR2020), October 13–16, 2020*, pages 277–281. Springer, 2022.

M. Ishikawa, P. V. Komi, M. J. Grey, V. Lepola, and G.-P. Bruggemann. Muscle-tendon interaction and elastic energy usage in human walking. *Journal of applied physiology*, 99 (2):603–608, 2005.

M. Iwamoto and Y. Nakahira. Development and validation of the total human model for safety (thums) version 5 containing multiple 1d muscles for estimating occupant motions with muscle activation during side impacts. *Stapp car crash journal*, 59:53, 2015.

Y. Jiang, T. Van Wouwe, F. De Groote, and C. K. Liu. Synthesis of biologically realistic human motion using joint torque actuation. *ACM Transactions On Graphics (TOG)*, 38 (4):1–12, 2019.

C. T. John, F. C. Anderson, J. S. Higginson, and S. L. Delp. Stabilisation of walking by intrinsic muscle properties revealed in a three-dimensional muscle-driven simulation. *Computer methods in biomechanics and biomedical engineering*, 16(4):451–462, 2013.

E. Joos, F. Péan, and O. Goksel. Reinforcement learning of musculoskeletal control from functional simulations. In *International Conference on Medical Image Computing and Computer-Assisted Intervention*, pages 135–145. Springer, 2020.

K. Junius, M. Moltedo, P. Cherelle, C. Rodriguez-Guerrero, B. Vanderborght, and D. Lefeber. Biarticular elements as a contributor to energy efficiency: biomechanical review and application in bio-inspired robotics. *Bioinspiration & biomimetics*, 12(6):061001, 2017.

M. Kawato. Internal models for motor control and trajectory planning. *Current opinion in neurobiology*, 9(6):718–727, 1999.

M. Kelly. An introduction to trajectory optimization: How to do your own direct collocation. *SIAM Review*, 59(4):849–904, 2017.

R. Kent, M. Trowbridge, F. J. Lopez-Valdes, R. H. Ordoyo, and M. Segui-Gomez. How many people are injured and killed as a result of aging? frailty, fragility, and the elderly risk-exposure tradeoff assessed via a risk saturation model. In *Annals of advances in automotive medicine/Annual Scientific Conference*, volume 53, page 41. Association for the Advancement of Automotive Medicine, 2009.

Ł. Kidziński, S. P. Mohanty, C. F. Ong, Z. Huang, S. Zhou, A. Pechenko, A. Stelmaszczyk, P. Jarosik, M. Pavlov, S. Kolesnikov, et al. Learning to run challenge solutions: Adapting reinforcement learning methods for neuromusculoskeletal environments. In *The NIPS'17 Competition: Building Intelligent Systems*, pages 121–153. Springer, 2018.

Ł. Kidziński, C. Ong, S. P. Mohanty, J. Hicks, S. Carroll, B. Zhou, H. Zeng, F. Wang, R. Lian, H. Tian, et al. Artificial intelligence for prosthetics: Challenge solutions. In *The NeurIPS'18 Competition*, pages 69–128. Springer, 2020.

Y. Kim, Y. Jung, W. Choi, K. Lee, and S. Koo. Similarities and differences between musculoskeletal simulations of opensim and anybody modeling system. *Journal of Mechanical Science and Technology*, 32:6037–6044, 2018.

D. A. Kistemaker, A. K. J. Van Soest, and M. F. Bobbert. Is equilibrium point control feasible for fast goal-directed single-joint movements? *Journal of Neurophysiology*, 95(5): 2898–2912, 2006.

D. A. Kistemaker, A. J. K. Van Soest, J. D. Wong, I. Kurtzer, and P. L. Gribble. Control of position and movement is simplified by combined muscle spindle and Golgi tendon organ feedback. *Journal of Neurophysiology*, 109(4):1126–1139, 2013. ISSN 0022-3077. doi: 10.1152/jn.00751.2012.

S. Kitazaki and M. Griffin. A modal analysis of whole-body vertical vibration, using a finite element model of the human body. *Journal of Sound and Vibration*, 200(1):83 – 103, 1997. ISSN 0022-460X. doi: https://doi.org/10.1006/jsvi.1996.0674.

C. Kleinbach, O. Martynenko, J. Promies, D. F. Haeufle, J. Fehr, and S. Schmitt. Implementation and validation of the extended hill-type muscle model with robust routing capabilities in ls-dyna for active human body models. *Biomedical engineering online*, 16: 1–28, 2017.

G. K. Klute, J. M. Czerniecki, and B. Hannaford. Artificial muscles: Actuators for biorobotic systems. *The International Journal of Robotics Research*, 21(4):295–309, 2002.

T. Komura, Y. Shinagawa, and T. L. Kunii. Creating and retargetting motion by the musculoskeletal human body model. *The visual computer*, 16:254–270, 2000.

N. Konow and T. J. Roberts. The series elastic shock absorber: tendon elasticity modulates energy dissipation by muscle during burst deceleration. *Proceedings of the Royal Society B: Biological Sciences*, 282(1804):20142800, 2015.

A. S. Koopman, M. Näf, S. J. Baltrusch, I. Kingma, C. Rodriguez-Guerrero, J. Babič, M. P. de Looze, and J. H. van Dieën. Biomechanical evaluation of a new passive back support exoskeleton. *Journal of Biomechanics*, 105:109795, 2020.

A. D. Kuo. A least-squares estimation approach to improving the precision of inverse dynamics computations. 1998.

V. La Barbera, F. Pardo, Y. Tassa, M. Daley, C. Richards, P. Kormushev, and J. Hutchinson. Ostrichrl: A musculoskeletal ostrich simulation to study bio-mechanical locomotion. *arXiv preprint arXiv:2112.06061*, 2021.

F. Lacquaniti, Y. P. Ivanenko, and M. Zago. Patterned control of human locomotion. *The Journal of physiology*, 590(10):2189–2199, 2012.

E. Le Flao, M. Brughelli, P. A. Hume, and D. King. Assessing head/neck dynamic response to head perturbation: a systematic review. *Sports Medicine*, 48:2641–2658, 2018.

Y. LeCun, B. Boser, J. Denker, D. Henderson, R. Howard, W. Hubbard, and L. Jackel. Handwritten digit recognition with a back-propagation network. *Advances in neural information processing systems*, 2, 1989.

S. Lee, M. Park, K. Lee, and J. Lee. Scalable muscle-actuated human simulation and control. *ACM Transactions On Graphics (TOG)*, 38(4):1–13, 2019.

S.-H. Lee and D. Terzopoulos. Heads up! biomechanical modeling and neuromuscular control of the neck. In *ACM SIGGRAPH 2006 Papers*, pages 1188–1198. 2006.

Y. Lee, S. Kim, and J. Lee. Data-driven biped control. In *ACM SIGGRAPH 2010 papers*, pages 1–8. 2010.

G. Legnani, F. Casolo, P. Righettini, and B. Zappa. A homogeneous matrix approach to 3d kinematics and dynamics - i. theory. *Mechanism and Machine Theory*, 31(5):573 – 587, 1996.

F. Liao, F. Zhou, and Y. Chai. Neuromorphic vision sensors: Principle, progress and perspectives. *Journal of Semiconductors*, 42(1):013105, 2021.

J.-Y. Lim, S. J. Choi, J. J. Widrick, E. M. Phillips, and W. R. Frontera. Passive force and viscoelastic properties of single fibers in human aging muscles. *European journal of applied physiology*, 119:2339–2348, 2019.

D. G. Lloyd and T. F. Besier. An emg-driven musculoskeletal model to estimate muscle forces and knee joint moments in vivo. *Journal of biomechanics*, 36(6):765–776, 2003.

D. G. Lloyd, T. S. Buchanan, and T. F. Besier. Neuromuscular biomechanical modeling to understand knee ligament loading. *Medicine and science in sports and exercise*, 37(11): 1939–1947, 2005.

G. Loeb. Control implications of musculoskeletal mechanics. In *Proceedings of 17th international conference of the engineering in medicine and biology society*, volume 2, pages 1393–1394. IEEE, 1995.

G. E. Loeb. Optimal isnt good enough. *Biological cybernetics*, 106:757–765, 2012.

K. Manal and T. S. Buchanan. An electromyogram-driven musculoskeletal model of the knee to predict in vivo joint contact forces during normal and novel gait patterns. *Journal of biomechanical engineering*, 135(2), 2013.

O. V. Martynenko, I. Wochner, L. V. Nölle, E. H. Alfaro, S. Schmitt, C. Mayer, A. Mishra, P. Ghosh, R. K. Chitteti, J. Weber, et al. Comparison of the head-neck kinematics of different active human body models with experimental data. *Ircobi Proceedings*, 2021.

M. A. Mat Dzahir and S.-i. Yamamoto. Recent trends in lower-limb robotic rehabilitation orthosis: Control scheme and strategy for pneumatic muscle actuated gait trainers. *Robotics*, 3(2):120–148, 2014.

B. Mazzolai and C. Laschi. A vision for future bioinspired and biohybrid robots. *Science robotics*, 5(38):eaba6893, 2020.

S. A. McErlain-Naylor, M. A. King, and P. J. Felton. A review of forward-dynamics simulation models for predicting optimal technique in maximal effort sporting movements. *Applied Sciences*, 11(4):1450, 2021.

M. A. McEvoy and N. Correll. Materials that couple sensing, actuation, computation, and communication. *Science*, 347(6228):1261689, 2015.

T. McGeer. Passive walking with knees. In *Proceedings., IEEE International Conference on Robotics and Automation*, pages 1640–1645. IEEE, 1990.

T. McGeer et al. Passive dynamic walking. *Int. J. Robotics Res.*, 9(2):62–82, 1990.

R. McNeill Alexander. Energetics and optimization of human walking and running: the 2000 raymond pearl memorial lecture. *American journal of human biology*, 14(5):641–648, 2002.

N. Mehrabi, R. Sharif Razavian, B. Ghannadi, and J. McPhee. Predictive simulation of reaching moving targets using nonlinear model predictive control. *Frontiers in computational neuroscience*, 10:143, 2017.

N. Mehrabi, M. H. Schwartz, and K. M. Steele. Can altered muscle synergies control unimpaired gait? *Journal of biomechanics*, 90:84–91, 2019.

L. Meszaros-Beller, M. Hammer, J. M. Riede, P. Pivonka, J. P. Little, and S. Schmitt. Effects of geometric individualisation of a human spine model on load sharing: neuro-musculoskeletal simulation reveals significant differences in ligament and muscle contribution. *Biomechanics and Modeling in Mechanobiology*, pages 1–26, 2023.

B. Michaud and M. Begon. biorbd: A c++, python and matlab library to analyze and simulate the human body biomechanics. *Journal of Open Source Software*, 6(57):2562, 2021.

B. Michaud, F. Bailly, E. Charbonneau, A. Ceglia, L. Sanchez, and M. Begon. Bioptim, a python framework for musculoskeletal optimal control in biomechanics. *IEEE Transactions on Systems, Man, and Cybernetics: Systems*, 2022.

R. H. Miller, B. R. Umberger, and G. E. Caldwell. Limitations to maximum sprinting speed imposed by muscle mechanical properties. *Journal of biomechanics*, 45(6):1092–1097, 2012a.

R. H. Miller, B. R. Umberger, J. Hamill, and G. E. Caldwell. Evaluation of the minimum energy hypothesis and other potential optimality criteria for human running. *Proceedings of the Royal Society B: Biological Sciences*, 279(1733):1498–1505, 2012b.

D. Mitrovic, S. Klanke, R. Osu, M. Kawato, and S. Vijayakumar. A computational model of limb impedance control based on principles of internal model uncertainty. *PloS one*, 5 (10):e13601, 2010.

L. Modenese, E. Ceseracciu, M. Reggiani, and D. G. Lloyd. Estimation of musculotendon parameters for scaled and subject specific musculoskeletal models using an optimization technique. *Journal of biomechanics*, 49(2):141–148, 2016.

H. L. More and J. M. Donelan. Scaling of sensorimotor delays in terrestrial mammals. *Proceedings of the Royal Society B*, 285(1885):20180613, 2018.

H. L. More, J. R. Hutchinson, D. F. Collins, D. J. Weber, S. K. Aung, and J. M. Donelan. Scaling of sensorimotor control in terrestrial mammals. *Proceedings of the Royal Society B: Biological Sciences*, 277(1700):3563–3568, 2010.

A. Morecki, J. Ekiel, and K. Fidelus. *Cybernetic systems of limb movements in man, animals, and robots*. Prentice Hall, 1984.

Y. Morimoto, H. Onoe, and S. Takeuchi. Biohybrid robot powered by an antagonistic pair of skeletal muscle tissues. *Science robotics*, 3(18):eaat4440, 2018.

C. T. Moritz and C. T. Farley. Passive dynamics change leg mechanics for an unexpected surface during human hopping. *Journal of Applied Physiology*, 97(4):1313–1322, 2004.

F. Mörl, T. Siebert, S. Schmitt, R. Blickhan, and M. Günther. Electro-Mechanical Delay in Hill-Type Muscle Models. *Journal of Mechanics in Medicine and Biology*, 12(05):1250085, 2012. ISSN 0219-5194. doi: 10.1142/s0219519412500856.

F. Mörl, M. Günther, J. M. Riede, M. Hammer, and S. Schmitt. Loads distributed in vivo among vertebrae, muscles, spinal ligaments, and intervertebral discs in a passively flexed lumbar spine. *Biomechanics and modeling in mechanobiology*, 19:2015–2047, 2020.

M. Murray, L. Mollinger, G. Gardner, and S. Sepic. Kinematic and emg patterns during slow, free, and fast walking. *Journal of Orthopaedic Research*, 2(3):272–280, 1984.

NASA. *Anthropometric Source Book, Volume I-III.* NASA Anthropometry Project, 1978.

L. M. Nashner and J. F. Peters. Dynamic posturography in the diagnosis and management of dizziness and balance disorders. *Neurologic clinics*, 1990.

L. M. Nashner, F. O. Black, and C. Wall. Adaptation to altered support and visual conditions during stance: patients with vestibular deficits. *Journal of Neuroscience*, 2(5):536–544, 1982.

R. R. Neptune, D. J. Clark, and S. A. Kautz. Modular control of human walking: a simulation study. *Journal of biomechanics*, 42(9):1282–1287, 2009.

C. D. Newgard and K. J. McConnell. Differences in the effectiveness of frontal air bags by body size among adults involved in motor vehicle crashes. *Traffic injury prevention*, 9(5): 432–439, 2008.

J. E. Niven and S. B. Laughlin. Energy limitation as a selective pressure on the evolution of sensory systems. *Journal of Experimental Biology*, 211(11):1792–1804, 2008.

F. Nori and R. Frezza. A control theory approach to the analysis and synthesis of the experimentally observed motion primitives. *Biological cybernetics*, 93(5):323–342, 2005.

J. Östh, K. Brolin, and D. Bråse. A human body model with active muscles for simulation of pretensioned restraints in autonomous braking interventions. *Traffic injury prevention*, 16(3):304–313, 2015.

W. Pak. *Development and Validation of Human Body Finite Element Models for Pedestrian Protection*. PhD thesis, Virginia Tech, 2019.

S. Pankoke and A. Siefert. *Virtual simulation of static and dynamic seating comfort in the development process of automobiles and automotive seats: Application of finite-element-occupant-model CASIMIR*. SAE International Warrendale, PA, 2007.

J. H. Park. Impedance control for biped robot locomotion. *IEEE Transactions on Robotics and Automation*, 17(6):870–882, 2001.

C. Paul. Morphological computation: A basis for the analysis of morphology and control requirements. *Robotics and Autonomous Systems*, 54(8):619–630, 2006.

C. Paul, H. Yokoi, and K. Matsushita. Design and control of humanoid robot locomotion with passive legs and upper body actuation. In *International Symposium on Robotics*, 2003.

P. Pavan, E. Monti, M. Bondí, C. Fan, C. Stecco, M. Narici, C. Reggiani, and L. Marcucci. Alterations of extracellular matrix mechanical properties contribute to age-related functional impairment of human skeletal muscles. *International Journal of Molecular Sciences*, 21(11):3992, 2020.

O. D. Pearl, S. Shin, A. Godura, S. Bergbreiter, and E. Halilaj. Fusion of video and inertial sensing data via dynamic optimization of a biomechanical model. *bioRxiv*, pages 2022–11, 2022.

X. B. Peng and M. Van De Panne. Learning locomotion skills using deeprl: Does the choice of action space matter? In *Proceedings of the ACM SIGGRAPH/Eurographics Symposium on Computer Animation*, pages 1–13, 2017.

R. Pfeifer and J. Bongard. *How the body shapes the way we think: a new view of intelligence.* MIT press, 2006.

P. Pigeon, L. Yahia, and A. G. Feldman. Moment arms and lengths of human upper limb muscles as functions of joint angles. *Journal of Biomechanics*, 29(10):1365–1370, oct 1996. ISSN 00219290. doi: 10.1016/0021-9290(96)00031-0.

I. J. Pinter, A. J. Van Soest, M. F. Bobbert, and J. B. Smeets. Conclusions on motor control depend on the type of model used to represent the periphery. *Biological cybernetics*, 106: 441–451, 2012.

C. Pizzolato, D. G. Lloyd, M. Sartori, E. Ceseracciu, T. F. Besier, B. J. Fregly, and M. Reggiani. Ceinms: A toolbox to investigate the influence of different neural control solutions on the prediction of muscle excitation and joint moments during dynamic motor tasks. *Journal of biomechanics*, 48(14):3929–3936, 2015.

G. A. Pratt and M. M. Williamson. Series elastic actuators. In *Proceedings 1995 IEEE/RSJ International Conference on Intelligent Robots and Systems. Human Robot Interaction and Cooperative Robots*, volume 1, pages 399–406. IEEE, 1995.

G. A. Pratt, M. M. Williamson, P. Dillworth, J. Pratt, and A. Wright. Stiffness isn't everything. In *Experimental Robotics IV: The 4th International Symposium, Stanford, California, June 30–July 2, 1995*, pages 253–262. Springer, 1997.

B. I. Prilutsky and V. M. Zatsiorsky. Optimization-based models of muscle coordination. *Exercise and sport sciences reviews*, 30(1):32, 2002.

I. P. A. Putra, J. Iraeus, R. Thomson, M. Y. Svensson, A. Linder, and F. Sato. Comparison of control strategies for the cervical muscles of an average female head-neck finite element model. *Traffic injury prevention*, 20(sup2):S116–S122, 2019.

W. Qin, R. Tao, L. Sun, and K. Dong. Muscle-driven virtual human motion generation approach based on deep reinforcement learning. *Computer Animation and Virtual Worlds*, 33(3-4):e2092, 2022.

C. C. Raasch and F. E. Zajac. Locomotor strategy for pedaling: muscle groups and biomechanical functions. *Journal of neurophysiology*, 82(2):515–525, 1999.

P. M. Rack and D. Westbury. The short range stiffness of active mammalian muscle and its effect on mechanical properties. *The Journal of physiology*, 240(2):331–350, 1974.

H. Ralston. Energetics of human walking. *Neural control of locomotion*, pages 77–98, 1976.

J. Rasmussen, M. Damsgaard, and M. Voigt. Muscle recruitment by the min/max criteriona comparative numerical study. *Journal of biomechanics*, 34(3):409–415, 2001.

J. Rasmussen, M. Damsgaard, E. Surma, S. T. Christensen, M. De Zee, and V. Vondrak. Anybody-a software system for ergonomic optimization. In *Fifth world congress on structural and multidisciplinary optimization*, volume 4, 2003.

S. Reschechtko and J. A. Pruszynski. Stretch reflexes. *Current Biology*, 30(18):R1025–R1030, 2020.

M. H. Rivner, T. R. Swift, and K. Malik. Influence of age and height on nerve conduction. *Muscle & nerve*, 24(9):1134–1141, 2001.

T. J. Roberts and E. Azizi. The series-elastic shock absorber: tendons attenuate muscle power during eccentric actions. *Journal of Applied Physiology*, 109(2):396–404, 2010.

D. W. Robinson, J. E. Pratt, D. J. Paluska, and G. A. Pratt. Series elastic actuator development for a biomimetic walking robot. In *1999 IEEE/ASME International Conference on Advanced Intelligent Mechatronics (Cat. No. 99TH8399)*, pages 561–568. IEEE, 1999.

R. Rockenfeller and M. Günther. Inter-filament spacing mediates calcium binding to troponin: A simple geometric-mechanistic model explains the shift of force-length maxima with muscle activation. *Journal of Theoretical Biology*, 454:240–252, 2018. ISSN 10958541. doi: 10.1016/j.jtbi.2018.06.009.

R. Rockenfeller, M. Günther, S. Schmitt, and T. Götz. Comparing different muscle activation dynamics using sensitivity analysis. *CoRR*, 2014.

R. Rockenfeller, M. Günther, S. Schmitt, and . Götz, Thomas. Comparative sensitivity analysis of muscle activation dynamics. *Computational and Mathematical Methods in Medicine*, 2015:1–16, 2015. doi: 10.1155/2015/585409.

K. Rongsawad and J. Ratanapinunchai. Effects of very high stimulation frequency and wide-pulse duration on stimulated force and fatigue of quadriceps in healthy participants. *Annals of rehabilitation medicine*, 42(2):250–259, 2018.

E. A. Rückert and G. Neumann. Stochastic optimal control methods for investigating the power of morphological computation. *Artificial Life*, 19(1):115–131, 2013.

T. Rupp, W. Ehlers, N. Karajan, M. Günther, and S. Schmitt. A forward dynamics simulation of human lumbar spine flexion predicting the load sharing of intervertebral discs, ligaments, and muscles. *Biomechanics and modeling in mechanobiology*, 14:1081–1105, 2015.

M. Sartori, M. Maculan, C. Pizzolato, M. Reggiani, and D. Farina. Modeling and simulating the neuromuscular mechanisms regulating ankle and knee joint stiffness during human locomotion. *Journal of neurophysiology*, 114(4):2509–2527, 2015.

D. J. Saxby, B. A. Killen, C. Pizzolato, C. Carty, L. Diamond, L. Modenese, J. Fernandez, G. Davico, M. Barzan, G. Lenton, et al. Machine learning methods to support personalized neuromusculoskeletal modelling. *Biomechanics and Modeling in Mechanobiology*, 19: 1169–1185, 2020.

S. Schmitt. demoa-base: A Biophysics Simulator for Muscle-driven Motion, 2022. URL `https://doi.org/10.18419/darus-2550`.

S. Schmitt, M. Günther, and D. F. Häufle. The dynamics of the skeletal muscle: A systems biophysics perspective on muscle modeling with the focus on hill-type muscle models. *GAMM-Mitteilungen*, 42(3):e201900013, 2019.

P. Schumacher, D. Häufle, D. Büchler, S. Schmitt, and G. Martius. Dep-rl: Embodied exploration for reinforcement learning in overactuated and musculoskeletal systems. *arXiv preprint arXiv:2206.00484*, 2022.

A. Seth, J. L. Hicks, T. K. Uchida, A. Habib, C. L. Dembia, J. J. Dunne, C. F. Ong, M. S. DeMers, A. Rajagopal, M. Millard, et al. Opensim: Simulating musculoskeletal dynamics and neuromuscular control to study human and animal movement. *PLoS computational biology*, 14(7):e1006223, 2018.

A. Seyfarth, H. Geyer, R. Blickhan, S. Lipfert, J. Rummel, Y. Minekawa, and F. Iida. Running and walking with compliant legs. *Fast Motions in Biomechanics and Robotics: Optimization and Feedback Control*, pages 383–401, 2006.

M. A. Sherman, A. Seth, and S. L. Delp. What is a moment arm? calculating muscle effectiveness in biomechanical models using generalized coordinates. In *International Design Engineering Technical Conferences and Computers and Information in Engineering Conference*, volume 55973, page V07BT10A052. American Society of Mechanical Engineers, 2013.

P. B. Shull, A. Silder, R. Shultz, J. L. Dragoo, T. F. Besier, S. L. Delp, and M. R. Cutkosky. Six-week gait retraining program reduces knee adduction moment, reduces pain, and improves function for individuals with medial compartment knee osteoarthritis. *Journal of Orthopaedic Research*, 31(7):1020–1025, 2013.

A. Siefert, S. Pankoke, and H.-P. Wölfel. Virtual optimisation of car passenger seats: Simulation of static and dynamic effects on drivers seating comfort. *International Journal of Industrial Ergonomics*, 38(5-6):410–424, 2008.

G. P. Siegmund, J. R. Brault, and D. D. Chimich. Do cervical muscles play a role in whiplash injury? *Journal of Whiplash & Related Disorders*, 1(1):23–40, 2002.

P. Slade, M. J. Kochenderfer, S. L. Delp, and S. H. Collins. Personalizing exoskeleton assistance while walking in the real world. *Nature*, 610(7931):277–282, 2022.

J. Sobotta. *Atlas der Anatomie des Menschen*, volume 3. Elsevier Health Sciences, 2010.

S. Soffe and A. Roberts. Tonic and phasic synaptic input to spinal cord motoneurons during fictive locomotion in frog embryos. *Journal of Neurophysiology*, 48(6):1279–1288, 1982.

M. H. Sohn, D. M. Smith, and L. H. Ting. Effects of kinematic complexity and number of muscles on musculoskeletal model robustness to muscle dysfunction. *Plos one*, 14(7): e0219779, 2019.

S. Song and H. Geyer. A neural circuitry that emphasizes spinal feedback generates diverse behaviours of human locomotion. *The Journal of physiology*, 593(16):3493–3511, 2015.

S. Song and H. Geyer. Predictive neuromechanical simulations indicate why walking performance declines with ageing. *The Journal of physiology*, 596(7):1199–1210, 2018.

S. Song, Ł. Kidziński, X. B. Peng, C. Ong, J. Hicks, S. Levine, C. G. Atkeson, and S. L. Delp. Deep reinforcement learning for modeling human locomotion control in neuromechanical simulation. *Journal of NeuroEngineering and Rehabilitation*, 18(1):1–17, 2021.

A. Sproewitz, R. Moeckel, J. Maye, and A. J. Ijspeert. Learning to move in modular robots using central pattern generators and online optimization. *The International Journal of Robotics Research*, 27(3-4):423–443, 2008.

A. Spröwitz, A. Tuleu, M. Vespignani, M. Ajallooeian, E. Badri, and A. J. Ijspeert. Towards dynamic trot gait locomotion: Design, control, and experiments with cheetah-cub, a compliant quadruped robot. *The International Journal of Robotics Research*, 32(8):932–950, 2013.

M. Srinivasan and A. Ruina. Computer optimization of a minimal biped model discovers walking and running. *Nature*, 439(7072):72–75, 2006.

K. Stollenmaier, I. S. Rist, F. Izzi, and D. F. Haeufle. Simulating the response of a neuromusculoskeletal model to assistive forces: implications for the design of wearables compensating for motor control deficits. In *2020 8th IEEE RAS/EMBS International Conference for Biomedical Robotics and Biomechatronics (BioRob)*, pages 779–784. IEEE, 2020.

D. R. Suissa. *Modeling, Control and Optimization in Human Motor Control: A Simulation Study of a Physiological Human Arm.* Master thesis, University of Stuttgart, 2017.

G. Taga, Y. Yamaguchi, and H. Shimizu. Self-organized control of bipedal locomotion by neural oscillators in unpredictable environment. *Biological cybernetics*, 65(3):147–159, 1991.

M. Toda. The design of a fungus-eater: A model of human behavior in an unsophisticated environment. *Behavioral Science*, 7(2):164–183, 1962.

E. Todorov and M. I. Jordan. Smoothness maximization along a predefined path accurately predicts the speed profiles of complex arm movements. *Journal of Neurophysiology*, 80(2): 696–714, 1998.

E. Todorov, T. Erez, and Y. Tassa. Mujoco: A physics engine for model-based control. In *2012 IEEE/RSJ international conference on intelligent robots and systems*, pages 5026–5033. IEEE, 2012.

B. Tondu. Modelling of the mckibben artificial muscle: A review. *Journal of Intelligent Material Systems and Structures*, 23(3):225–253, 2012.

M. C. Tresch and A. Jarc. The case for and against muscle synergies. *Current opinion in neurobiology*, 19(6):601–607, 2009.

U. Trinler, H. Schwameder, R. Baker, and N. Alexander. Muscle force estimation in clinical gait analysis using anybody and opensim. *Journal of biomechanics*, 86:55–63, 2019.

M. J. van der Horst, J. Thunnissen, R. Happee, R. Van Haaster, and J. Wismans. The influence of muscle activity on head-neck response during impact. *SAE transactions*, pages 4003–4023, 1997.

M. M. van der Krogt, L. Bar-On, T. Kindt, K. Desloovere, and J. Harlaar. Neuromusculoskeletal simulation of instrumented contracture and spasticity assessment in children with cerebral palsy. *Journal of neuroengineering and rehabilitation*, 13(1):1–11, 2016.

R. Q. van der Linde. Design, analysis, and control of a low power joint for walking robots, by phasic activation of mckibben muscles. *IEEE transactions on robotics and automation*, 15(4):599–604, 1999.

R. Van Ham, T. G. Sugar, B. Vanderborght, K. W. Hollander, and D. Lefeber. Compliant actuator designs. *IEEE Robotics & Automation Magazine*, 16(3):81–94, 2009.

G. v. van Ingen Schenau, M. Bobbert, and R. Rozendal. The unique action of bi-articular muscles in complex movements. *Journal of anatomy*, 155:1, 1987.

A. J. van Soest and M. F. Bobbert. The contribution of muscle properties in the control of explosive movements. *Biological cybernetics*, 69(3):195–204, 1993.

T. Van Wouwe, L. H. Ting, and F. De Groote. An approximate stochastic optimal control framework to simulate nonlinear neuro-musculoskeletal models in the presence of noise. *PLOS Computational Biology*, 18(6):e1009338, 2022.

B. Vanderborght, A. Albu-Schäffer, A. Bicchi, E. Burdet, D. G. Caldwell, R. Carloni, M. Catalano, O. Eiberger, W. Friedl, G. Ganesh, et al. Variable impedance actuators: A review. *Robotics and autonomous systems*, 61(12):1601–1614, 2013.

H. Wagner and R. Blickhan. Stabilizing function of skeletal muscles: an analytical investigation. *Journal of theoretical biology*, 199(2):163–179, 1999.

M. Waldhof, I. Wochner, K. Stollenmaier, N. Parspour, and S. Schmitt. Design and scaling of exoskeleton power units considering load cycles of humans. *Robotics*, 11(5):107, 2022.

S. M. Walker and G. R. Schrodt. I segment lengths and thin filament periods in skeletal muscle fibers of the rhesus monkey and the human. *The Anatomical Record*, 178(1):63–81, 1974.

J. R. Walter, M. Günther, D. F. Haeufle, and S. Schmitt. A geometry-and muscle-based control architecture for synthesising biological movement. *Biological cybernetics*, pages 1–31, 2021.

J. R. Walter, I. Wochner, M. Jacob, K. Stollenmaier, P. Lerge, and S. Schmitt. allmin: A Reduced Human All-Body Model, 2022. URL `https://doi.org/10.18419/darus-2982`.

H. Wang, V. Caggiano, G. Durandau, M. Sartori, and V. Kumar. Myosim: Fast and physiologically realistic mujoco models for musculoskeletal and exoskeletal studies. In *2022 International Conference on Robotics and Automation (ICRA)*, pages 8104–8111. IEEE, 2022.

J. M. Wang, S. R. Hamner, S. L. Delp, and V. Koltun. Optimizing locomotion controllers using biologically-based actuators and objectives. *ACM Transactions on Graphics (TOG)*, 31(4):1–11, 2012.

A. White. Clinical biomechanics of the spine. *Clinical biomechanics of the spine*, 1990.

T. L. Wickiewicz, R. R. Roy, P. L. Powell, and V. R. Edgerton. Muscle architecture of the human lower limb. *Clinical Orthopaedics and Related Research®*, 179:275–283, 1983.

C. Winby, D. Lloyd, and T. Kirk. Evaluation of different analytical methods for subject-specific scaling of musculotendon parameters. *Journal of biomechanics*, 41(8):1682–1688, 2008.

D. A. Winter. *Biomechanics and motor control of human movement*. John Wiley & Sons, 2009.

D. A. Winter and H. Yack. Emg profiles during normal human walking: stride-to-stride and inter-subject variability. *Electroencephalography and clinical neurophysiology*, 67(5): 402–411, 1987.

M. Wisse and J. Van Frankenhuyzen. Design and construction of mike; a 2-d autonomous biped based on passive dynamic walking. *Adaptive motion of animals and machines*, pages 143–154, 2006.

I. Wochner and S. Schmitt. arm26: A Human Arm Model, 2022. URL `https://doi.org/10.18419/darus-2871`.

I. Wochner, D. Driess, H. Zimmermann, D. F. Haeufle, M. Toussaint, and S. Schmitt. Optimality principles in human point-to-manifold reaching accounting for muscle dynamics. *Frontiers in computational neuroscience*, 14:38, 2020.

I. Wochner, L. V. Nölle, O. V. Martynenko, and S. Schmitt. 'Falling heads': investigating reflexive responses to head–neck perturbations. *Biomedical engineering online*, 21(1):1–23, 2022a.

I. Wochner, P. Schumacher, G. Martius, D. Büchler, S. Schmitt, and D. F. Haeufle. Learning with muscles: Benefits for data-efficiency and robustness in anthropomorphic tasks. *Conference on Robot Learning, CoRL*, 2022b.

S. Wolfen, J. Walter, M. Günther, D. F. Haeufle, and S. Schmitt. Bioinspired pneumatic muscle spring units mimicking the human motion apparatus: benefits for passive motion range and joint stiffness variation in antagonistic setups. In *2018 25th International Conference on mechatronics and machine vision in practice (M2VIP)*, pages 1–6. IEEE, 2018.

D. M. Wolpert, R. C. Miall, and M. Kawato. Internal models in the cerebellum. *Trends in cognitive sciences*, 2(9):338–347, 1998.

D. M. Wolpert, Z. Ghahramani, and J. R. Flanagan. Perspectives and problems in motor learning. *Trends in cognitive sciences*, 5(11):487–494, 2001.

R. J. Wood. Design, fabrication, and analysis of a 3dof, 3cm flapping-wing mav. In *2007 IEEE/RSJ international conference on intelligent robots and systems*, pages 1576–1581. IEEE, 2007.

J.-c. Wu and Z. Popović. Terrain-adaptive bipedal locomotion control. *ACM Transactions on Graphics (TOG)*, 29(4):1–10, 2010.

T. Xu, X. Sheng, T. Zhang, H. Liu, X. Liang, A. Ding, et al. Development and validation of dummies and human models used in crash test. *Applied bionics and biomechanics*, 2018, 2018.

S.-H. Yeo, J. Verheul, W. Herzog, and S. Sueda. Numerical instability of hill-type muscle models. *Journal of the Royal Society Interface*, 20(199):20220430, 2023.

Y. Yesilevskiy, W. Yang, and C. D. Remy. Spine morphology and energetics: how principles from nature apply to robotics. *Bioinspiration & biomimetics*, 13(3):036002, 2018.

K. Zahedi and N. Ay. Quantifying morphological computation. *Entropy*, 15(5):1887–1915, 2013.

K. Zahedi, N. Ay, and R. Der. Higher coordination with less controla result of information maximization in the sensorimotor loop. *Adaptive Behavior*, 18(3-4):338–355, 2010.

F. E. Zajac, R. R. Neptune, and S. A. Kautz. Biomechanics and muscle coordination of human walking: Part i: Introduction to concepts, power transfer, dynamics and simulations. *Gait & posture*, 16(3):215–232, 2002.

A. Zhang, I. G. Ramirez-Alpizar, K. G. Esclasse, O. Stasse, and K. Harada. Humanoid walking pattern generation based on model predictive control approximated with basis functions. *Advanced Robotics*, 33(9):454–468, 2019.

M. Ziegler, F. Iida, R. Pfeifer, et al. Cheap underwater locomotion: roles of morphological properties and behavioural diversity. In *International Conference on Climbing and Walking Robots, CLAWAR, Karlsruhe*, 2006.

I. Contribution 1: Optimality Principles in human point-to-manifold reaching accounting for muscle dynamics

frontiers
in Computational Neuroscience

ORIGINAL RESEARCH
published: 15 May 2020
doi: 10.3389/fncom.2020.00038

Optimality Principles in Human Point-to-Manifold Reaching Accounting for Muscle Dynamics

***Isabell Wochner*[1]**, *Danny Driess*[2], *Heiko Zimmermann*[3], *Daniel F. B. Haeufle*[4], *Marc Toussaint*[2] *and Syn Schmitt*[1]**

[1] Institute for Modelling and Simulation of Biomechanical Systems, University of Stuttgart, Stuttgart, Germany, [2] Machine Learning and Robotics Lab, University of Stuttgart, Stuttgart, Germany, [3] Khoury College of Computer Sciences, Northeastern University, Boston, MA, United States, [4] Hertie Institute for Clinical Brain Research, and Werner Reichard Centre for Integrative Neuroscience, University of Tübingen, Tübingen, Germany

Human arm movements are highly stereotypical under a large variety of experimental conditions. This is striking due to the high redundancy of the human musculoskeletal system, which in principle allows many possible trajectories toward a goal. Many researchers hypothesize that through evolution, learning, and adaption, the human system has developed optimal control strategies to select between these possibilities. Various optimality principles were proposed in the literature that reproduce human-like trajectories in certain conditions. However, these studies often focus on a single cost function and use simple torque-driven models of motion generation, which are not consistent with human muscle-actuated motion. The underlying structure of our human system, with the use of muscle dynamics in interaction with the control principles, might have a significant influence on what optimality principles best model human motion. To investigate this hypothesis, we consider a point-to-manifold reaching task that leaves the target underdetermined. Given hypothesized motion objectives, the control input is generated using Bayesian optimization, which is a machine learning based method that trades-off exploitation and exploration. Using numerical simulations with Hill-type muscles, we show that a combination of optimality principles best predicts human point-to-manifold reaching when accounting for the muscle dynamics.

Keywords: neuro-musculoskeletal model, motor control, optimality principles, hierarchical control, biomechanics, biorobotics, Bayesian optimization

Edited by:
Florentin Wörgötter,
University of Göttingen, Germany

Reviewed by:
Thomas Wennekers,
University of Plymouth,
United Kingdom
Sebastian Herzog,
Max Planck Society (MPG), Germany

****Correspondence:***
Isabell Wochner
isabell.wochner@
simtech.uni-stuttgart.de

Received: *01 October 2019*
Accepted: *14 April 2020*
Published: *15 May 2020*

Citation:
Wochner I, Driess D, Zimmermann H, Haeufle DFB, Toussaint M and Schmitt S (2020) Optimality Principles in Human Point-to-Manifold Reaching Accounting for Muscle Dynamics. Front. Comput. Neurosci. 14:38. doi: 10.3389/fncom.2020.00038

1. INTRODUCTION

Goal-directed arm movement has been studied extensively in neuroscience with the aim of deriving a predictive model of human and animal movements (e.g., Bizzi et al., 1984; Flash and Hogan, 1985; Harris and Wolpert, 1998; Campos and Calado, 2009). It is widely accepted that the central nervous system (CNS) selects a specific movement to follow an optimal path, which minimizes certain costs to achieve the movement goal (Todorov and Jordan, 2002; Franklin and Wolpert, 2011). Still, it is unclear which criterion of optimality is chosen by the CNS while generating and controlling the motion. For point-to-point reaching tasks, several different isolated optimality criteria have been proposed, such as e.g., minimum hand jerk (Flash and Hogan, 1985), minimum torque change (Uno et al., 1989), minimum energy (Alexander, 1997), and minimum variance (Harris and Wolpert, 1998). In a more recent work, Berret et al. (2011b) used kinematic input data and reconstructed the optimality function for point-to-manifold movements in humans. Such point-to-manifold movements are interesting, as they allow for a richer set of solutions as compared to point-to-point movements (de Rugy et al., 2012; Kistemaker et al., 2014; Mehrabi et al., 2017). Berret et al. (2011b) found that only a combined cost function minimizing mechanical energy consumption and movement jerk (maximizing smoothness) allows to reasonably predict the trajectories of point-to-manifold movements.

In the study of Berret et al. (2011b), muscle forces acting on the respective joints are lumped to one joint torque per each joint. While this assumption is supported by the idea that muscles are grouped together to produce joint torque forming synergies of muscles (e.g., d'Avella et al., 2003), it neglects the contribution of the individual muscle to joint torque generation. Similar, in a very recent study by Oguz et al. (2018), free-space reaching motions were investigated by using joint torques representing muscle contractions. Both studies do not take into account the interaction of the individual, non-linear muscle dynamics with the non-linear dynamics of the skeleton. However, it is known that muscles with their characteristic activation dynamics, non-linearities, elasticities, and antagonistic setup contribute to the characteristics of biological movement (van Soest and Bobbert, 1993; Daley et al., 2009; Schmitt et al., 2019) which has consequences for the interpretation of the underlying motor control principles (Pinter et al., 2012). Thus, the question is whether individual muscle dynamics play a significant role in the optimality of motion generation and control for point-to-manifold tasks? More precisely, in comparison with Berret et al. (2011b) the question is, whether or not the composite optimality function found, still holds true, if muscle dynamics are considered, explicitly?

In this contribution, a neuro-musculoskeletal arm model (Bayer et al., 2017; Driess et al., 2018; Stollenmaier et al., 2020) is used to simulate arm movements. Point-to-manifold experiments are investigated numerically. The underlying control policy to generate arm movements is synthesized using different isolated, well-known optimality principles and combinations thereof. Due to the complexity of the movement apparatus, the optimality of a given control policy can only be evaluated by performing a simulation. Therefore, we propose to use Bayesian optimization as a sample efficient technique to optimize the cost function corresponding to a chosen optimality principle. Bayesian optimization uses a probabilistic surrogate model of the cost function to automatically trade-off exploitation and exploration according to a utility function. Thus, it can be interpreted as a form of reinforcement learning similar to the natural process in animal learning.

The purpose of this study is to investigate whether previously proposed cost functions allow to reproduce experimental data of human point-to-manifold movements. The novelty of our work is the use of a neuro-musculoskeletal model to synthesize optimal movement considering both isolated and combined cost functions and investigate the contribution of individual muscle dynamics in point-to-manifold movements.

2. METHODS

Different optimality principles are applied to a two-joint biophysical arm model with six muscles, represented by Hill-type muscles (Günther et al., 2007; Haeufle et al., 2014), to investigate free endpoint movements. A point-to-manifold scenario is set up to distinguish between various cost functions. The arm movement is generated by finding a static, open-loop muscle stimulation set for all included muscle, using the selected optimality principle, to reach the manifold from a given, fixed starting point. Thus, let ξ be a trajectory of features (e.g., joint positions, velocities, torques, etc.) that is obtained by simulating an arm movement as a function of the static muscle stimulation u. The trajectory evolves solely from the dynamics of the musculoskeletal system. The optimization problem for the specified cost function J reads as

$$\min_{u \in \mathcal{U}} J(\xi(u)) \tag{1}$$

where $\mathcal{U} = [0,1]^n$ denotes the space of n possible muscle stimulations (in our case $n = 6$). Testing a new muscle stimulation involves the computationally expensive simulation of the arm system since no closed-form expression for $\xi(u)$ exists. To address this challenge, we propose to find muscle stimulations in a sample efficient way via Bayesian optimization.

In the following, the single components of the workflow, namely the neuro-musculoskeletal arm model, the formulation of the optimality principles as cost functions, and Bayesian optimization are described. Furthermore, the general setup is shown.

2.1. Setup

Point-to-manifold experiments are more suitable to distinguish between different cost functions than point-to-point experiments, as shown by Berret et al. (2011b). To validate the predictions of our model, we resort to previously published experimental data from Berret et al. (2011a). In this study, subjects were asked to point with a one-shot movement to a bar placed in front of them with closed eyes. In contrast to typical point-to-point experiments, the endpoint on the bar was not defined a priori but is freely chosen by the subjects. The numerical setup is established accordingly by placing the neuro-musculoskeletal arm model in front of a vertical bar, as visualized in **Figure 1**. The bar represents the target manifold in front of the subject at a distance of 85% of the total arm length ($L = l_1 + l_2$, where l_1 and l_2 denote upper arm and forearm lengths, respectively). Every simulation starts from the same given set point with zero initial velocities and an arm posture of $\varphi = 90^\circ$ for the elbow and $\psi = 0^\circ$ for the shoulder angle. This initial condition can be seen in **Figure 1**, the angles are defined in **Figure 2**. These values are chosen to mimic the experimental setup from Berret et al. (2011b). The initial condition for the muscles was chosen to minimize the sum of muscle stimulation to resemble a relaxed starting position (Bayer et al., 2017). Applying an open-loop stimulation $u \in \mathcal{U}$ then results in the execution of a dynamic movement. The trajectory and endpoint equilibrium position depend on the chosen stimulation u.

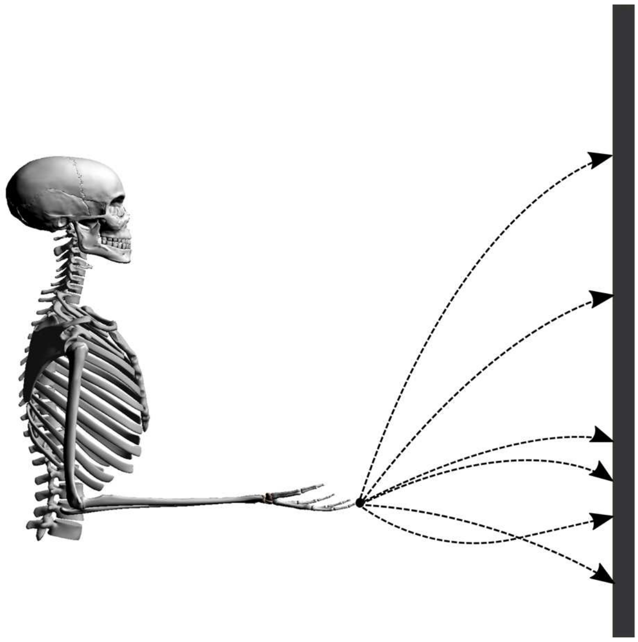

FIGURE 1 | Illustration of the setup. Possible trajectories of the finger tip from the start position to the bar are shown in dashed lines.

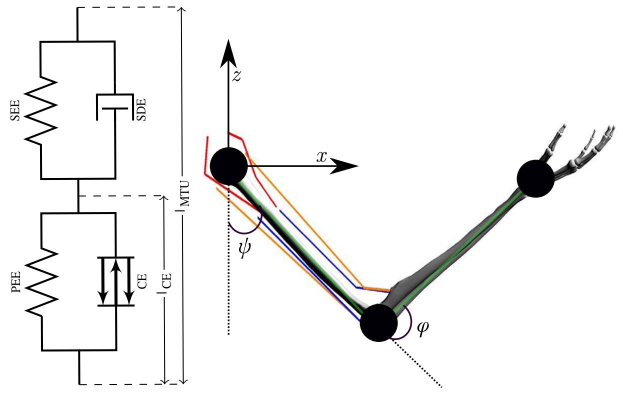

FIGURE 2 | The numerical model of a human arm. The six muscles are modeled as lumped Hill-type muscles depicted on the left (figure adapted from Haeufle et al., 2014). On the right, the kinematic chain (green lines) with the two joints and the joint angles ψ and φ is shown. Red lines depict the two monoarticular shoulder muscles (ante- and retroversion), orange lines the two biarticular ones and blue lines represent the two monoarticular elbow muscles (flexor and extensor).

2.1.1. Point-to-Manifold

We define the point-to-manifold scenario for our study as follows:

$$\begin{aligned} x(0) &= x_0, & \dot{x}(0) &= 0, \\ z(0) &= z_0, & \dot{z}(0) &= 0, \\ x(T) &= x^{\star}, & \dot{x}(T) &= 0, \\ z(T)&: \text{arbitrary} & \dot{z}(T) &= 0. \end{aligned} \tag{2}$$

Here, x and z are the hand positions in the respective directions for the starting time $t = 0$ and the movement duration $t = T$, $\dot{x}$ and $\dot{z}$ denote the time derivatives of these quantities. Furthermore, $x^{\star}$ stands for the desired horizontal end position. Note, that in contrast to point-to-point movements, here the desired z position is a random goal point within the manifold spanned by the z axis.

2.2. Musculoskeletal Model

The numerical arm model consists of two segments representing the upper and lower arm, which are driven by six muscles, two monoarticular muscles each for the shoulder and the elbow joint, as well as two biarticular muscles acting on both joints (Driess et al., 2018, see **Supplementary Material** for more details). The parameters are based on previous publications (Kistemaker et al., 2007; Bayer et al., 2017). The upper body is fixed in space, and a hinge joint connects the two segments. The limitation to planar movements is justified, as it has been shown in the analysis of experimental data that the movements mostly lay along the para-sagittal plane (Berret et al., 2011a). The dynamics of the skeletal system are modeled as rigid bodies solving the Euler-Lagrange equation

$$M(\theta)\ddot{\theta} + C(\theta, \dot{\theta}) = F(\theta, \dot{\theta}, t), \tag{3}$$

where $M(\theta)$ is the mass matrix, $\theta = [\varphi, \psi]$ contains the elbow and shoulder angle, respectively, $C(\theta, \dot{\theta})$ consists of the centrifugal, gravitational and Coriolis forces and F denotes all components of the muscle-tendon forces acting on the arm. Muscle forces acting on the segments are predicted by Hill-type muscle models (Haeufle et al., 2014). This means that the muscle-tendon unit (MTU) is modeled with spring-damper elements consisting of four components (**Figure 2**): a contractile element (CE) modeling the force-length and force-velocity properties of active muscle fibers, a parallel elastic element (PEE), a serial elastic element (SEE), and a serial damping element (SDE). The underlying non-linear dynamics of the muscle model can be formulated as follows

$$\dot{l}_{\mathrm{CE}} = f_v(l_{\mathrm{CE}}, l_{\mathrm{MTU}}, \dot{l}_{\mathrm{MTU}}, a) \tag{4a}$$

$$F_{\mathrm{MTU}} = f_f(l_{\mathrm{MTU}}, \dot{l}_{\mathrm{MTU}}, a, l_{\mathrm{CE}}, \dot{l}_{\mathrm{CE}}). \tag{4b}$$

Here, the first-order differential equation describes the contraction dynamics of the contractile element $\dot{l}_{\mathrm{CE}}$, which is integrated in the calculation of the force of the muscle-tendon unit F_{MTU}. The muscle's force depends on the current contraction state of the muscle l_{CE}, the length of the muscle-tendon unit l_{MTU}, and the muscle activity a. The relation between a neural stimulation signal u and the muscle activity a is a complex biochemical process which is approximated here by Hatze's model of activation dynamics (Hatze, 1977). Thus, the muscle activity a, which represents the free calcium ion concentration in the muscle, can be predicted with a first-order differential equation

$$\dot{a} = f_a(a, l_{\mathrm{CE}}, u). \tag{5}$$

To generate the stimulation signal $u \in [0,1]^6$, an open-loop controller is implemented, which ensures that the simulated arm movements always terminate in a static equilibrium with a vanishing net joint moment (Bayer et al., 2017). The stimulations u are selected based on the chosen optimality principle with Bayesian optimization.

Performing a forward dynamic simulation with this arm model results in a feature matrix $\xi(u)$

$$\xi(u) = \Big(\theta_i(t), \dot{\theta}_i(t), \ddot{\theta}_i(t), \dddot{\theta}_i(t), x(t), z(t), \dddot{x}(t), \dddot{z}(t), \tau_i(t), \dot{\tau}_i(t), u\Big)_{t=0}^{T} \quad \text{for } i = 1, 2. \tag{6}$$

The single components of $\xi(u)$ are trajectories in time t and represent different physical quantities, such as the joint angles $\theta = [\varphi, \psi]$, the hand position in x- and z-direction, the torques τ_1 and τ_2 (acting on the two joints, elbow and shoulder, respectively) and time derivatives of these quantities. Note that all the results are shown for a non-fixed movement duration T (if not otherwise mentioned). This is due to the fact that open-loop muscle stimulations were found, which ensured that a steady state is always reached at the end of the arm movement. Therefore, the simulation was set up such that the model simulates until the arm velocity drops below a threshold value (10^{-4} m/s) and then terminates because the equilibrium state is reached.

2.3. Optimality Principles

Several cost functions have been proposed in the literature to investigate human arm movement with optimality principles. The most common ones are presented and compared here. Based on the evaluated state variables (i.e., components of feature matrix ξ), they are divided into five general groups. First, we consider *kinematic models*, e.g., the minimum-jerk model in joint and Cartesian-space coordinates (Flash and Hogan, 1985; Wada et al., 2001) and the minimum angle acceleration model (Ben-Itzhak and Karniel, 2008). They penalize high-order derivatives which in turn maximize the smoothness as introduced by Todorov and Jordan (1998). Historically, the minimum-jerk model was one of the most influential theories in motor control theory which was able to reproduce many of the experimental observations in real-human movements. However, kinematic models do not take anatomical constraints or non-linear arm characteristics into account. Therefore, *dynamic models* were proposed. In the literature, two cost variables are formulated at the dynamic level, namely the minimum torque (Nelson, 1983) and the minimum torque change model (Uno et al., 1989; Nakano et al., 1999). Although it might not seem intuitively important to optimize the torque change in biological systems, it was argued that the minimization of wear and tear on the musculoskeletal system is desired. On the contrary, the necessity of energy efficiency in the biological system is evident. Therefore, *energetic models* were proposed. One approach could be to minimize the metabolic energy consumed by the muscles, which is not considered here. Instead, the total absolute work was formulated as a cost function which is related to the mechanical energy (Berret et al., 2008). Alternatively, a more robotic approach, such as minimizing the control effort, can be used. Typically, using *control effort models* helps to handle redundancies. In this case, the amount of motor neuron activity is optimized by penalizing the sum of the squared muscle activations (Guigon et al., 2007). Furthermore, the class of *hybrid models* combines several single optimality principles. This work specifically focuses on the hybrid cost function proposed by Berret et al. (2011a) and Hilt et al. (2016). This model combines an energy term with a smoothness expression (e.g., angle jerk) and is able to predict free-endpoint arm movements. Our hypothesis was that due to the use of muscle dynamics, an additional term for the hybrid cost function might be necessary. We propose to include the control effort term (see J_{JEE} in **Table 1**) as it is the only single cost function term that directly affects muscle dynamics by taking the muscle stimulations into account. An overview of the cost functions used in this study is given in **Table 1**.

2.3.1. External Task Constraint

To ensure that the task constraints of pointing to a vertical bar are fulfilled, the desired end position is imposed. This is done by extending the cost function with an additional term. The total cost function is then defined as

$$J_{\mathrm{total}} = ||x_T - x^{\star}||^2 + 0.01 \cdot J_{\mathrm{opt}} \tag{7}$$

where x_T denotes the reached x-position of the hand in equilibrium and $x^{\star}$ stands for the desired horizontal end position (location of the bar). Note that the relation between the task constraint and the chosen optimality principle has the same magnitude as suggested by Li and Todorov (2007).

2.4. Finding Muscle Stimulations via Bayesian Optimization

As discussed in section 2, the goal is to find static muscle stimulations $u \in \mathcal{U} \subset \mathbb{R}^6$ that, when applied to the neuro-musculoskeletal system, minimize the specified cost function J. However, no analytical form of J, i.e., no gradient in particular, is known, instead, J can only be queried for specific choices of u, which involves the computationally expensive forward dynamic simulation of the system, cf. section 2.2. Therefore, the optimization procedure is an episodic process that seeks for an optimal set of muscle stimulations based on the information gathered so far. In this way, there are parallels between the situation in the present work and real-world motor learning tasks, where humans improve their skills by trial and error (Taube et al., 2008).

Bayesian optimization (Brochu et al., 2010) addresses these problems in a sample efficient manner, by learning a probabilistic surrogate model of the cost function $u \mapsto J(\xi(u))$ based on collected data $\mathcal{D}_n = \left\{(u_i, J(\xi(u_i)))\right\}_{i=1}^{n}$ obtained from n previous episodes. (The cost function model can be interpreted as an internal model of a biological system.)

A common choice for the probabilistic surrogate model are so-called Gaussian processes (Rasmussen and Williams, 2004),

TABLE 1 | Cost functions as proposed in literature.

Optimality principle	Mathematical description
Angle acceleration (Ben-Itzhak and Karniel, 2008)	$J_{\mathrm{ACC}} = \int_0^T \left(\ddot{\varphi}^2 + \ddot{\psi}^2\right) dt$
Hand jerk (Flash and Hogan, 1985)	$J_{\mathrm{HJ}} = \int_0^T \left(\dddot{x}^2 + \dddot{z}^2\right) dt$
Angle jerk (Wada et al., 2001)	$J_{\mathrm{AJ}} = \int_0^T \left(\dddot{\varphi}^2 + \dddot{\psi}^2\right) dt$
Torque (Nelson, 1983)	$J_{\mathrm{T}} = \int_0^T \left(\tau_1^2 + \tau_2^2\right) dt$
Torque change (Uno et al., 1989; Nakano et al., 1999)	$J_{\mathrm{TC}} = \int_0^T \left(\dot{\tau_1}^2 + \dot{\tau_2}^2\right) dt$
Energy (Berret et al., 2008)	$J_{\mathrm{EN}} = \int_0^T \left(\lvert\dot{\varphi} \cdot \tau_1\rvert + \lvert\dot{\psi} \cdot \tau_2\rvert\right) dt$
Effort (Guigon et al., 2007)	$J_{\mathrm{EFF}} = \sum_{i=1}^{6} u_i^2$
Hybrid jerk and energy (Berret et al., 2011a; Hilt et al., 2016)	$J_{\mathrm{JE}} = \int_0^T \left(\lvert\dot{\varphi} \cdot \tau_1\rvert + \lvert\dot{\psi} \cdot \tau_2\rvert\right) dt + 10^{-3} \cdot \int_0^T \left(\dddot{\varphi}^2 + \dddot{\psi}^2\right) dt$
Hybrid jerk, energy, and effort	$J_{\mathrm{JEE}} = \int_0^T \left(\lvert\dot{\varphi} \cdot \tau_1\rvert + \lvert\dot{\psi} \cdot \tau_2\rvert\right) dt + 10^{-3} \cdot \int_0^T \left(\dddot{\varphi}^2 + \dddot{\psi}^2\right) dt + \sum_{i=1}^{6} u_i^2$

which describe the probability density of $J(\xi(u))$ given the current dataset $\mathcal{D}_n$ as a Gaussian distribution

$$P(J(\xi(u))|\mathcal{D}_n) = \mathcal{N}(J(\xi(u))|\mu_n(u), \sigma_n^2(u)) \tag{8}$$

with mean $\mu_n(u) = \kappa(u)^T \left(K_n + \varepsilon^2 I_n\right)^{-1} y_n$ and variance $\sigma_n^2(u) = k(u,u) - \kappa_n(u)^T \left(K_n + \varepsilon^2 I_n\right)^{-1} \kappa_n(u)$, where $\kappa_n(u) = \left(k(u, u_i)\right)_{i=1}^n$, $K_n = \left(k(u_i, u_j)\right)_{i,j=1}^n$, $y_n = \left(J(\xi(u_i))\right)_{i=1}^n$. In this work, we use the common squared exponential kernel $k\colon \mathcal{U} \times \mathcal{U} \to \mathbb{R}$ with $k(u, u') = \alpha \exp\left(-\gamma \left\lVert u - u' \right\rVert_2^2\right)$. The choice of the kernel and its hyperparameters encodes the correlation between data points and thereby the complexity/smoothness of the surrogate model. In this case, the hyperparameters are the length scale $\gamma \in \mathbb{R}$ and signal variance $\alpha \in \mathbb{R}$.

Based on the information encoded in the Gaussian process model, Bayesian optimization selects the next query point u_{n+1} for the next episode by maximizing an acquisition function a

$$u_{n+1} = \underset{u \in \mathcal{U}}{\operatorname{argmax}}\, a(u; \mathcal{D}_n). \tag{9}$$

In the vicinity of the already collected stimulations, the model has high certainty, reflected in a low variance $\sigma_n^2(u_{n+1})$. This knowledge can be exploited by querying the cost function at a point of high certainty and low predicted cost. However, there might be unexplored regions in $\mathcal{U}$ with low costs that the current model is unaware of, i.e., has high uncertainty. This trade-off between exploring $\mathcal{U}$ and minimizing J based on the current information in the probabilistic model is formalized in the upper confident bound acquisition function

$$a_{\mathrm{UCB}}(u; \mathcal{D}_n) = \beta \sigma_n(u) - \mu_n(u), \tag{10}$$

where $\beta \in \mathbb{R}$ controls this exploration/exploitation tradeoff.

In all experiments, the tradeoff parameter was $\beta = 0.01$, the kernel hyperparameters α, l were optimized with L-BFGS by maximizing the data likelihood. The dataset was initialized with 10 random muscle stimulations sampled uniformly in $\mathcal{U}$. The optimization of the acquisition function was also performed with L-BFGS using 30 random restarts, again uniformly sampled in $\mathcal{U}$. The algorithm terminates after a fixed number of iterations (maxIter), in this case, after 600 iterations, which seems to be a good choice for this problem setting, as shown in section 3.3.

The pseudo-code of this algorithm is shown in **Table 2**. Bayesian optimization has empirically been shown to be a sample efficient method for optimizing black-box cost functions, e.g., in real world robotic applications (Marco et al., 2016; Drieß et al., 2017).

3. RESULTS

3.1. Predicted Trajectories

Our neuro-musculoskeletal model predicts eight different trajectories, one for each optimality principle. The first eight subplots in **Figures 3A–H** show the best five simulated trajectories corresponding to the five best u of each cost function, which were found using Bayesian optimization. The last plot on the lower right in **Figure 3I**, shows the recorded experimental data for 17 subjects as collected by Berret et al. (2011a). Note, that the data was post-processed in the same way as in the paper from Berret et al. (2011a): The signals were low-pass filtered using a digital fifth-order Butterworth filter at a cutoff frequency of 10 Hz. Furthermore, the on- and offset of the movement were defined at the time points where the linear tangential velocity of the fingertip exceeded 5% of its peak velocity, and respectively dropped below. The graphs show that the predicted finger paths differ for the different optimality principles (subplots **Figures 3A–H**). This is not surprising as, in contrast to typical point-to-point tasks, the point-to-manifold experiment allows more freedom. Another point to be mentioned is the similarity between the angle acceleration model (**Figure 3A**), the hand jerk model (**Figure 3B**), the angle jerk model (**Figure 3C**), and the torque change model (**Figure 3E**). This behavior can be explained by the fact that all four models maximize the smoothness of

TABLE 2 | Bayesian optimization algorithm.

Algorithm

```
initialize data set $\mathcal{D}_0$ with 10 random samples
    for n = 1,2,...,maxIter do
        select muscle stimulation $u_n \in \mathbb{R}^6$ by optimizing the acquisition function $a_{\mathrm{UCB}}$
        $u_n = \arg\max_{u \in \mathcal{U}} a_{\mathrm{UCB}}(u; \mathcal{D}_{n-1})$
        Run dynamic simulation of musculoskeletal system to obtain $\xi(u_n)$
        Evaluate the cost function $J(\xi(u_n))$
        Augment the data $\mathcal{D}_n = \mathcal{D}_{n-1} \cup \{(u_n, J(\xi(u_n)))\}$
        Update Gaussian process model of the cost function
end for
```

movements. **Figure 3D** displays the results using the torque model. Based on this optimality principle, the arm points more or less on a straight path toward the bar and predicts a much lower endpoint on the bar compared to the experimental data. Similar to the torque model, the energy model predicts a lower endpoint on the bar (**Figure 3F**). Furthermore, the general curvature is different to the experimental data. Instead of having a concave trajectory as shown in the experimental data, the energy model predicts trajectories which first drop downwards, before pointing forward. It is also interesting to observe the effort model (**Figure 3G**) for which the simulated trajectory first falls strongly and then points upwards to the bar. Therefore, this model is the only one which predicts a lower endpoint on the bar than the original start point. As prioritized by the cost function, this model uses the lowest muscle activations to control the movement in comparison to all other model predictions. However, none of the optimality principles with a single cost term reproduces the experimental trajectories as well as the hybrid model J_{JE}.

Similar to the results of Berret et al. (2011a), our model can predict biological behavior more realistically with the hybrid model (**Figure 3H**) in comparison to all single-cost optimality principles. For the hybrid model, the endpoint, as well as the general curvature, match the experimental data well (c.f. **Figure 3I**). For the comparison between the simulated and the experimental trajectories, it is still an open question in motor control how to define a metric that includes all important movement features (Gielen, 2009). One metric, which was proposed by Berret et al. (2011a), is a sum of measuring the Cartesian and curvature errors between the simulated and the experimental trajectories. They discussed that based on human intuition, it is important to include both the shape of the path and the endpoint position. Due to this metric, we analyzed all the endpoints and curvatures of the simulated trajectories visually, as shown in **Figure 3**. Furthermore, we performed a quantitative analysis, where we computed the endpoint error on the bar and the maximum signed curvature error as a measure of convexity or concavity of a trajectory. The results of this quantitative analysis are shown in the **Table S1** and **Figure S2**. To summarize this analysis, looking at both trajectory metrics, the hybrid jerk and energy model has the lowest error compared to the experimental data for all cost functions presented in **Figure 3**.

To conclude, the results presented above show the behavior of different single cost functions. None of them is able to match both the curvature and the endpoint of the experimental data well. The predicted trajectory of the hybrid jerk and energy model is the closest to real human behavior w.r.t. the endpoint error and curvature error, which is the reason why this cost function is investigated in more detail in the following.

3.2. Influence of Muscle Stimulations on Tangential Velocities

So far, only the position trajectory has been analyzed and discussed. The next step is to investigate whether the hybrid model (jerk and energy) is also able to predict other kinematic features, such as the tangential velocity correctly. This is shown in **Figure 4**. On the left, the experimental tangential velocities (again 17 subjects) are shown in comparison to the velocity curves of the model with the best trajectory prediction, i.e., the hybrid model J_{JE} (solid blue line in **Figure 4B**). It is striking that both the peak as well as the general curvature, are significantly different. This is contrary to the results of Berret et al. (2011a), where the hybrid model was able to match the experimental velocities well. An explanation for these differences could be that in our study, muscle stimulations are used as control variables instead of controlling the torques directly. Another point is that the movement duration was not restricted. Previous investigations (e.g., Gribble and Ostry, 2000; Kistemaker et al., 2006; Shadmehr, 2010; Berret et al., 2011a; Pinter et al., 2012) usually fixed the movement duration. To show how this affects the results, we additionally implemented a limitation of the movement duration to 1 s, which corresponds to the experimental movement duration. This was done by terminating the simulation after 1 s. To ensure that the velocity at the endpoint is still zero, an additional term was added to the external task constraint in J_{total}. Restricting the movement duration also takes into account that slow movements are favored by the jerk model due to the fact that the jerk cost approaches zero for an infinite movement duration. However, this restriction still leads to a right-skewness in the curvature of the predicted tangential velocities, as shown in **Figure 4B** (dashed red line). Consequently, the difference in modeling the arm by including muscle dynamics was taken into consideration. As mentioned previously (section 2.2), the Hatze activation function was used for modeling the activation

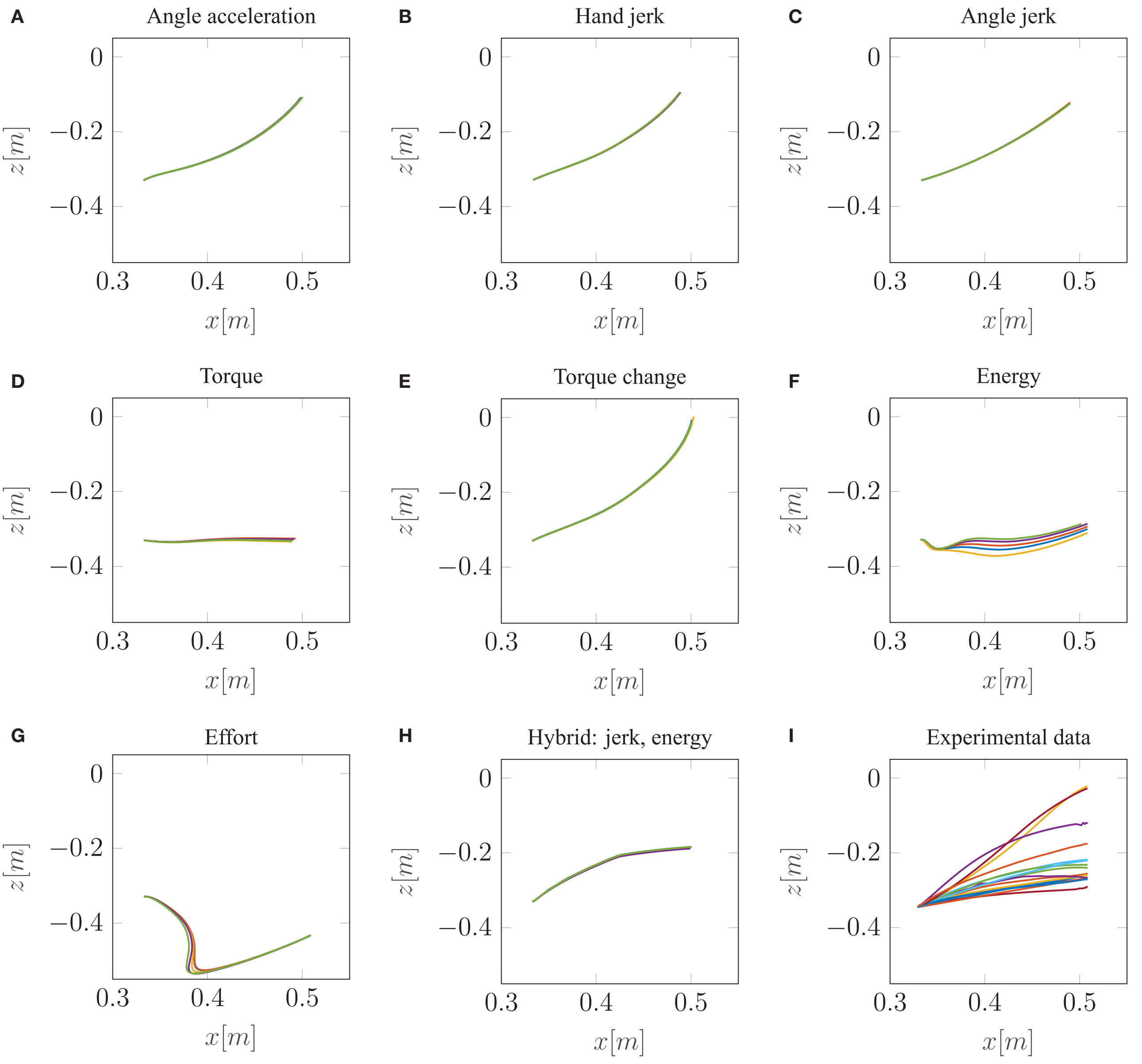

FIGURE 3 | The best five predicted trajectories for the fingertip movement ending on the bar are shown. Eight different cost functions are compared with the experimental trajectories, in analogy to the metric of Berret et al. (2011a), which is based on Cartesian (endpoint of trajectory) and curvature errors (see section 3.1).

dynamics of the muscles. This function has the property that high muscle stimulations only need a short time to reach peak activity, while the time to decrease is longer (Rockenfeller et al., 2015; Bayer et al., 2017). Indeed, some of the chosen muscle activations based on the hybrid model are very high, e.g., the monoarticular anteversion shoulder muscle (MSA) is activated with $u = 1$. This explains the strong asymmetrical behavior of the tangential velocity (**Figure 4B**).

This is in line with our hypothesis, as mentioned above in section 2.3 that it is necessary to restrict the search space by selecting low activated muscle stimulations. Therefore, we proposed to add an effort term to the hybrid cost function, which favors a small sum of squared muscle stimulations (J_{JEE}, last row of **Table 1**). This additional term directly affects and takes the muscle dynamics into account. As shown with the J_{JEE} line (orange) in **Figure 4C**, this leads to movements with a realistic bell-shaped velocity curve with a peak velocity of $0.85\,m/s$. This is comparable to experimental data. All other tangential velocities shown in **Figure 4C** have smaller peak velocities and show more right-skewness in their velocity profiles compared to both the experimental data and the J_{JEE} function. Furthermore, **Figure 5** shows that the predicted finger path of the new cost function J_{JEE} is similar to the experimental results regarding two significant movement features: the Cartesian error (endpoint of

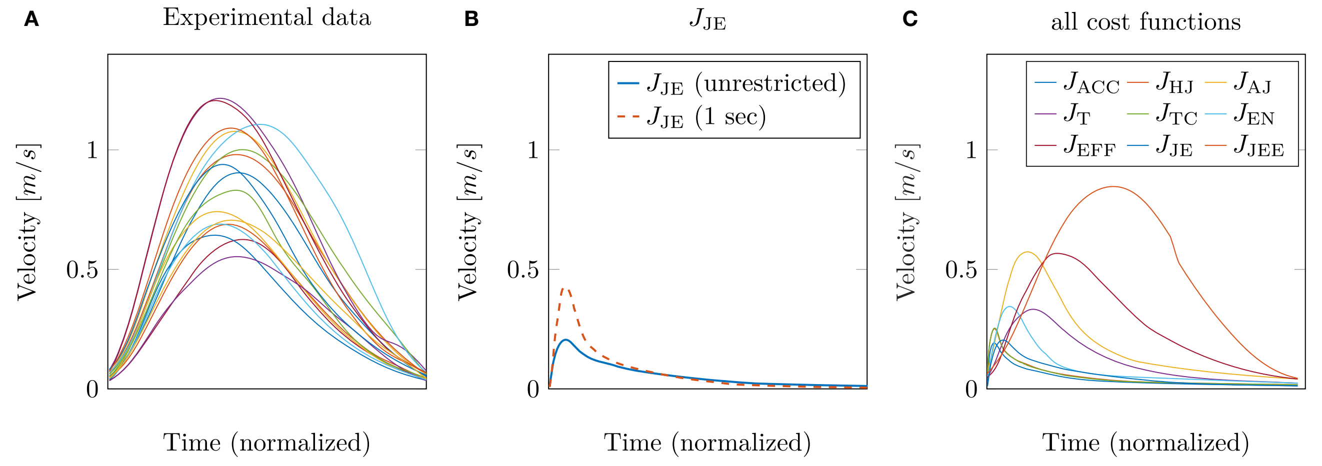

FIGURE 4 | (A) The experimentally measured tangential velocities of 17 subjects are compared to the simulated velocities using **(B)** the hybrid J_{JE} model and **(C)** all cost functions including the extended hybrid J_{JEE} model (1 s) for the best prediction.

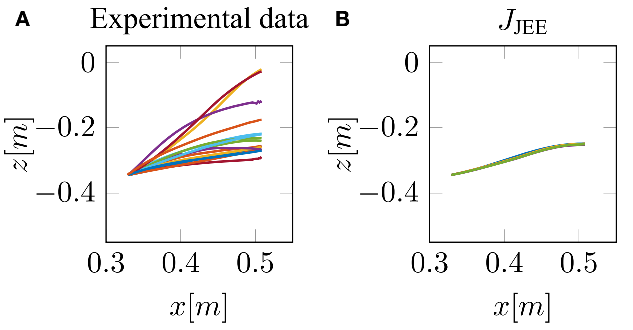

FIGURE 5 | Comparison between the experimental trajectories and the new cost function J_{JEE}.

the trajectory) and the general curvature error (based on the metric of Berret et al., 2011a). Taken these two movement features together with the movement features of the velocity curve (see **Figure 4C**: bell-shaped profile and peak velocity matches), this supports our hypothesis that the additional effort term should be included in the cost function J_{JEE}. In addition, we performed a quantitative analysis for the two trajectory movement criteria (as mentioned above) and for two velocity movement criteria for all cost function including the final proposed cost function J_{JEE}. The quantitative analysis of the velocity profiles consists of the peak velocity error and the skewness error (measuring bell-shapedness or left- or right-skewness) in comparison to the experimental data. The results are shown in **Table S1** and **Figure S2**. For all movement criteria, the J_{JEE} cost function has either the lowest or a very small error compared to the other presented models.

Summed up, the results show that our model can predict biological behavior more realistically if the muscle activation is taken into account.

3.3. Performance of Bayesian Optimization

The performance of Bayesian optimization in comparison to random testing was investigated. The reason for this is to show that the optimization is better than simply randomly sampling the search space of $u \in \mathcal{U} \subset \mathbb{R}^6$. The results for all cost functions were similar, therefore, they are shown using the example of the hybrid model (J_{JE}). To do so, three test runs were performed using random testing (each run with 600 iterations) and then compared to three test runs using Bayesian optimization (each run with 600 iterations). The resulting cost function J_{total} for both cases is shown with boxplots in **Figure 6**. It can be stated that the median of J_{total}, indicated by the red central line, for random testing (left side) is significantly higher compared to using Bayesian optimization (right side). Furthermore, the 25th to 75th percentiles, also called the interquartile ranges (IQR), are in different magnitudes as indicated by the blue boxes. In this case, the maximum whisker length w is 1.5 times the IQR. This means that points are classified as outliers if they are greater than $q3 + w \cdot (q3 - q1)$ or less than $q1 - w \cdot (q3 - q1)$, where $q1$ and $q3$ are the 25th and 75th percentiles of all drawn observations. It is interesting to note that most points classified as outliers in the Bayesian optimization case (shown as orange crosses) are still part of the interquartile range in the case of random testing. Additionally, it can be shown that the mean values of the two test scenarios are from different populations by using a statistical hypothesis test with the Student's t-distribution. The H_0-hypothesis that the two test runs have an equal mean value is rejected with a significance level of $\alpha = 0.01$. Therefore, it can be stated that Bayesian optimization is better than random testing for sampling muscle activations under the consideration of different optimality principles.

Furthermore, we evaluated how the absolute cost value of the best evaluation changes over the iterations for thirty repeated runs. The mean and the standard deviation of this evaluation is shown in **Figure 7**. The absolute cost value drops at the beginning and then settles on a mean value of around 8.09e−5. Note, that we would not expect the absolute cost value to go to zero, because the movement has a cost and rather converges toward a finite value. Furthermore, the absolute value of the standard deviation

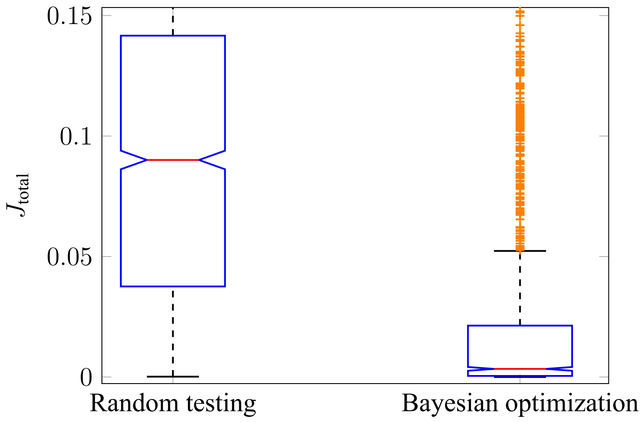

FIGURE 6 | Performance of Bayesian optimization. The total error using random testing (left boxplot) is compared to using Bayesian optimization (right boxplot). The median of all observations is shown with a central red line, and the blue boxes represent the 25th to 75th percentile. The tested muscle activations sampled by Bayesian optimization result in a significantly lower error compared to randomly drawn stimulations.

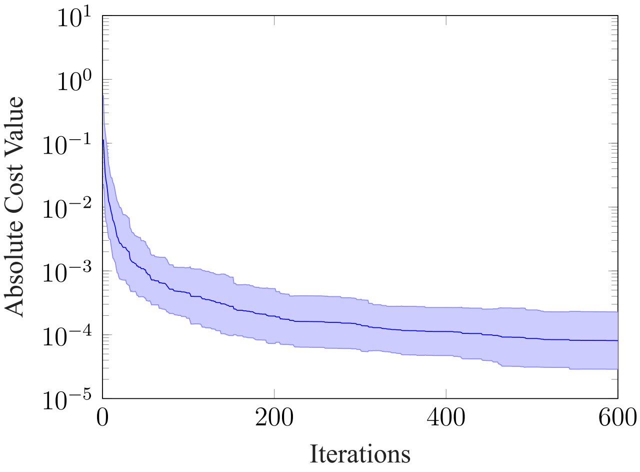

FIGURE 7 | Absolute cost value of the best observation. Plotting the mean and the standard deviation (shaded area) for 30 repeated runs.

(shown as the shaded area) narrows down, the more iterations are performed.

4. DISCUSSION

In this study, we hypothesized that a combination of optimality principles determines human point-to-manifold reaching and that the muscle dynamics have an influence on the investigation of optimality. For this purpose, we applied several cost functions to a forward dynamics simulation of a muscle-driven arm model. The cost functions are minimized using Bayesian optimization, which searches for optimal open-loop muscle stimulations. We showed that a mixed cost function minimizing mechanical work, jerk, and neuronal stimulation effort simultaneously can replicate the participants' behavior in this task much better than any other of the investigated single cost criteria (**Figure 3**).

In the human arm, all sources of mechanical energy to drive the movement lie in the muscle-tendon unit (MTU). All actions of the MTU are triggered by motor commands of the central nervous system (CNS) sent directly to the individual muscle fiber within the MTU over neural pathways. Additionally, the MTU sends sensory signals back to the CNS. Thus, the MTU is the crucial link between the neuronal communication of the CNS and the physical interaction within the body's structure and the environment. In literature, several authors highlight the contribution of muscle properties to the control of motion, e. g., in jumping (van Soest and Bobbert, 1993), hopping (Haeufle et al., 2010), animal running (Daley et al., 2009). For studying neuroscience, however, it is still unclear which features to include into a mathematical model of a biological motion system. Pinter et al. (2012) compared arm models with actuators of different levels of detail – from a plain torque generator to a model actuated by four macroscopic Hill-type MTUs. They demonstrated that the response to perturbations varies and conclusions on control concepts may be inadequate if the macroscopic muscle characteristics are not considered. The findings of this work are in line with the literature. By using an arm model including individual muscles and, at least, a macroscopic model formulation of the muscles' dynamics, the arm kinematics change, significantly. We are not the first to mention that the choice of the used biophysical model and its level of detail to study motion generation and control is sensible as mentioned above, however, we recommend to include explicit formulations of the muscles' dynamics (Kistemaker et al., 2014; Mehrabi et al., 2017). For example, the velocity profile of the arm kinematics changed dramatically (**Figure 4**), just by accounting for appropriate muscle stimulations in the cost function.

In combination with these Hill-type muscles, we used an open-loop control approach to investigate optimality principles. This means no trajectories were planned, nor did we perform an inverse dynamics calculation (internal inverse model). Furthermore, open-loop control, in this case, means no sequence of muscle activations was used because setting only one set of scalar muscle stimulations is sufficient to produce trajectories (**Figures 3**, **5**). This is different from some of the previous investigations (e.g., Kawato et al., 1987; Wolpert et al., 1995; Todorov and Jordan, 2002; Berret et al., 2011a) where closed-loop control or inverse simulations were used to analyze different cost functions. We think the assumption that feedback does not play a large role in this experiment is justified (Shadmehr et al., 2010; Oguz et al., 2018) because the participants had closed eyes without any external perturbations. Furthermore, the lack of feedback corrections means that the controller also acts as a planner (internal forward model) because it predicts the arm motion for a selected control signal. Summed up, we showed that it is possible to generate trajectories and investigate optimality with a simple open-loop control (see **Figure 3**).

Another important aspect of the controller is not only investigating optimality but also fulfilling the task, in this case, point-to-manifold reaching. Point-to-manifold reaching allows discriminating between cost functions which is shown in **Figure 3**. This is important because other tasks, like the intensely studied point-to-point reaching task, may result in similar behavior for different cost functions resulting in the conclusion that cost functions may be interchangeable (Nelson, 1983; Kistemaker et al., 2014; Spiers et al., 2016). Tasks like point-to-manifold reaching with a more openly defined target have a higher potential for revealing differences in the optimality principles as they result in different trajectories. This was also discussed by Berret et al. (2011a) where they showed, as a proof of concept, that hand jerk and torque change cost functions are much more distinguishable in point-to-manifold than in point-to-point reaching. Furthermore, we performed point-to-point simulations with a similar setup described above from the point-to-manifold simulations (see **Figure S1**). As shown there, almost all criteria predict the two typical movement features for point-to-point reaching movements: straight paths and bell-shaped speed profiles similar to previous findings in the literature (e.g., Abend et al., 1982; Flash and Hogan, 1985; Harris and Wolpert, 1998; Todorov, 2004). This makes it almost impossible to decide which cost function is the true one based on the given task since they all have a good theoretical basis and predict very similar trajectories. Therefore, it can be stated that conclusions on optimality principles depend, at least partly, on the chosen task.

Using this openly defined task, we showed that a combination of smoothness, energy, and effort seems to be a good choice as optimality principle for selecting a trajectory (**Figure 5**). Many arguments have been made to give an understanding of why each of the single cost criteria gives an advantage to the survival of the fittest (for an overview see Todorov, 2004). It is often argued that while energy is a limited resource in our system, it is important to minimize its consumption (Hatze and Buys, 1977; Alexander, 1997; Berret et al., 2008), whereas smoothness can be interpreted as a measure of the prevention of self-injuries of the musculoskeletal system (Todorov and Jordan, 1998). A combination of these two principles was already proposed by Berret et al. (2011a). However, we found that by including muscle dynamics, the cost function needs to be adapted, as well. If muscle stimulation represents a physiological signal, like the muscle membrane potential in our case, we found that the interpretation of control effort is more plausible and physiologically valid. Therefore, including the cost of muscle stimulation into the cost function (J_{JEE}, last row of **Table 1**) is not only necessary but allows for a more realistic search for the underlying optimality principles, as well. Additionally, such an enhanced cost function allows for an implicit integration of earlier findings regarding movement optimality, such as reduction of noise (Harris and Wolpert, 1998), because noise scales with the control signal. Furthermore, it was mentioned by McKay and Ting (2012) that similar muscle activity patterns are predicted by cost functions, such as reduction of signal-dependent noise compared to the minimization of control effort. This would further support our findings. Concluding, a combination of these cost functions is reasonable, and evidence for this combination is shown in this work (see **Figure 5**).

Considering this influence of the muscles on the selection of the optimality principle, the question arises if other implicit aspects also have an influence? In this study, we showed that transferring a real task to a valid simulation task also leaves some other parameters open to be set, such as movement duration (see **Figure 4**). It is unclear how the non-specific task requirement of pointing fast is translated into a quantitatively measured time. Some authors (e.g., Tanaka et al., 2006) argued that movement duration is minimized under the constraint that the endpoint accuracy of the movement is still good enough based on Fitts's law (Fitts, 1954). However, in this openly defined target we used in this work, the accuracy is not given explicitly, which in turn makes it difficult to set a movement end time. Therefore, we first choose an open subset of possible solutions by simulating the movement until an equilibrium endpoint is reached. However, we have seen that restricting the movement duration from an equilibrium endpoint to 1 s, consequently, also changed the tangential velocities. Setting this new end time which is closer to the experimental movement durations, affected the simulated tangential velocities such that they matched the experimental ones better (**Figure 4**). This shows that it is not clear how implicit task aspects, such as time are incorporated in the biological structure nor how they can be modeled.

Another point which is important for investigating muscle-actuated synthesized movement is that not only the initial angles or initial end-effector position determine the system state but rather the pre-activation of the muscles needs to be included as well. In another study by Bayer et al. (2017), it was shown that the pre-activation of the muscles has a strong effect on the maximum movement velocity. Therefore, we chose the minimum sum of muscle stimulations as the initial condition. This can be interpreted as a "relaxed" starting state. Taken this together with the previously discussed time aspect (**Figure 4**), we want to emphasize that through external factors or non-specific task requirements, the arm movement control is changed. In this context, by external factors, we mean both the environment as well as the given task. Here, the environment includes, e.g., external perturbations, joint limits, obstacle avoidance, and many more. Both the environment and the given task can influence the movement features, such as speed and movement duration, accuracy, distance and amplitude, noise and the initial condition. Connecting these points, this supports the hypothesis that optimality is a restricted function in the domain of task and environment.

DATA AVAILABILITY STATEMENT

The datasets generated for this study are available on request to the corresponding author.

AUTHOR CONTRIBUTIONS

IW, SS, and MT: project concept. IW: numerical experiments. IW and SS: analyzed the data. IW, DD, HZ, DH, and SS: contributed methods/code. IW, DD, HZ, DH, MT, and SS: wrote the paper.

FUNDING

This work was funded by the Baden-Württemberg Stiftung in the scope of the NEUROROBOTICS project DeepControl granted to MT and SS. DH was supported by the Ministry of Science, Research and the Arts Baden-Württemberg (Az: 33-7533-30-20/7/2). Additional support was received by the Deutsche Forschungsgemeinschaft (DFG, German Research Foundation) under Germany's Excellence Strategy—EXC 2075-390740016 (SimTech) and EXC 310 granted to SS and MT. We acknowledge support by Open Access Publishing Fund of University of Stuttgart.

ACKNOWLEDGMENTS

We thank Katrin Stollenmaier for preparing the **Supplementary Material** (Stollenmaier et al., 2020) describing the arm model (Arm26). Furthermore, we thank Bastien Berret for providing the experimental data.

SUPPLEMENTARY MATERIAL

The Supplementary Material for this article can be found online at: https://www.frontiersin.org/articles/10.3389/fncom.2020.00038/full#supplementary-material

The Supplementary Material for this article describes the Arm26 model which was used in this study (Stollenmaier et al., 2020). Furthermore, it contains results for point-to-point simulations to show the advantage of using a more openly defined task, such as the point-to-manifold task. Additionally, we performed a quantitative analysis comparing four movement features of the results for all cost functions with the experimental data.

REFERENCES

Abend, W., Bizzi, E., and Morasso, P. (1982). Human arm trajectory formation. *Brain* 105, 331–348. doi: 10.1093/brain/105.2.331

Alexander, R. M. (1997). A minimum energy cost hypothesis for human arm trajectories. *Biol. Cybern*. 76, 97–105. doi: 10.1007/s004220050324

Bayer, A., Schmitt, S., Günther, M., and Haeufle, D. (2017). The influence of biophysical muscle properties on simulating fast human arm movements. *Comput. Methods Biomech. Biomed. Eng*. 20, 803–821. doi: 10.1080/10255842.2017.1293663

Ben-Itzhak, S., and Karniel, A. (2008). Minimum acceleration criterion with constraints implies bang-bang control as an underlying principle for optimal trajectories of arm reaching movements. *Neural Comput*. 20, 779–812. doi: 10.1162/neco.2007.12-05-077

Berret, B., Chiovetto, E., Nori, F., and Pozzo, T. (2011a). Evidence for composite cost functions in arm movement planning: an inverse optimal control approach. *PLoS Comput. Biol*. 7:e1002183. doi: 10.1371/journal.pcbi.1002183

Berret, B., Chiovetto, E., Nori, F., and Pozzo, T. (2011b). Manifold reaching paradigm: how do we handle target redundancy? *J. Neurophysiol*. 106, 2086–2102. doi: 10.1152/jn.01063.2010

Berret, B., Darlot, C., Jean, F., Pozzo, T., and Papaxanthis, Charalambos Gauthier, J. P. (2008). The inactivation principle: mathematical solutions minimizing the absolute work and biological implications for the planning of arm movements. *PLoS Comput. Biol*. 4:e1000194. doi: 10.1371/journal.pcbi.1000194

Bizzi, E., Accornero, N., Chapple, W., and Hogan, N. (1984). Posture control and trajectory formation during arm movement. *J. Neurosci*. 4, 2738–2744. doi: 10.1523/JNEUROSCI.04-11-02738.1984

Brochu, E., Cora, V. M., and December, F. (2010). A tutorial on bayesian optimization of expensive cost functions, with application to active user modeling and hierarchical reinforcement learning. *arXiv* 1012.2599.

Campos, F., and Calado, J. (2009). Approaches to human arm movement control–a review. *Annu. Rev. Control* 33, 69–77. doi: 10.1016/j.arcontrol.2009.03.001

Daley, M. A., Voloshina, A., and Biewener, A. A. (2009). The role of intrinsic muscle mechanics in the neuromuscular control of stable running in the guinea fowl. *J. Physiol*. 587, 2693–2707. doi: 10.1113/jphysiol.2009.171017

d'Avella, A., Saltiel, P., and Bizzi, E. (2003). Combinations of muscle synergies in the construction of a natural motor behavior. *Nat. Neurosci*. 6, 300–308. doi: 10.1038/nn1010

de Rugy, a., Loeb, G. E., and Carroll, T. J. (2012). Muscle coordination is habitual rather than optimal. *J. Neurosci*. 32, 7384–7391. doi: 10.1523/JNEUROSCI.5792-11.2012

Drieß, D., Englert, P., and Toussaint, M. (2017). "Constrained bayesian optimization of combined interaction force/task space controllers for manipulations," in *Proceedings of the International Conference on Robotics and Automation (ICRA)* (Singapore). doi: 10.1109/ICRA.2017.7989111

Driess, D., Zimmermann, H., Wolfen, S., Suissa, D., Haeufle, D., Hennes, D., et al. (2018). "Learning to control redundant musculoskeletal systems with neural networks and SQP: exploiting muscle properties," in *Proceedings of the International Conference on Robotics and Automation (ICRA)* (Brisbane, QLD). doi: 10.1109/ICRA.2018.8463160

Fitts, P. M. (1954). The information capacity of the human motor system in controlling the amplitude of movement. *J. Exp. Psychol*. 47:381. doi: 10.1037/h0055392

Flash, T., and Hogan, N. (1985). The coordination of arm movements: an experimentally confirmed mathematical model. *J. Neurosci*. 5, 1688–1703. doi: 10.1523/JNEUROSCI.05-07-01688.1985

Franklin, D. W., and Wolpert, D. M. (2011). Computational mechanisms of sensorimotor control. *Neuron* 72, 425–442. doi: 10.1016/j.neuron.2011.10.006

Gielen, S. (2009). "Review of models for the generation of multi-joint movements in 3-D," in *Advances in Experimental Medicine and Biology*, ed D. Sternad (Boston, MA: Springer), 523–550. doi: 10.1007/978-0-387-77064-2_28

Gribble, P. L., and Ostry, D. J. (2000). Compensation for loads during arm movements using equilibrium-point control. *Exp. Brain Res*. 135, 474–482. doi: 10.1007/s002210000547

Guigon, E., Baraduc, P., and Desmurget, M. (2007). Computational motor control: redundancy and invariance. *J. Neurophysiol*. 97, 331–347. doi: 10.1152/jn.00290.2006

Günther, M., Schmitt, S., and Wank, V. (2007). High-frequency oscillations as a consequence of neglected serial damping in hill-type muscle models. *Biol. Cybern*. 97, 63–79. doi: 10.1007/s00422-007-0160-6

Haeufle, D., Günther, M., Bayer, A., and Schmitt, S. (2014). Hill-type muscle model with serial damping and eccentric force-velocity relation. *J. Biomech*. 47, 1531–1536. doi: 10.1016/j.jbiomech.2014.02.009

Haeufle, D. F. B., Grimmer, S., and Seyfarth, A. (2010). The role of intrinsic muscle properties for stable hopping-stability is achieved by the force-velocity relation. *Bioinspir. Biomim*. 5:16004. doi: 10.1088/1748-3182/5/1/016004

Harris, C. M., and Wolpert, D. M. (1998). Signal-dependent noise determines motor planning. *Nature* 394:780. doi: 10.1038/29528

Hatze, H. (1977). A myocybernetic control model of skeletal muscle. *Biol. Cybern*. 25, 103–119. doi: 10.1007/BF00337268

Hatze, H., and Buys, J. D. (1977). Energy-optimal controls in the mammalian neuromuscular system. *Biol. Cybern*. 27, 9–20. doi: 10.1007/BF00357705

Hilt, P., Berret, B., Papaxanthis, C., Stapley, P. J., and Pozzo, T. (2016). Evidence for subjective values guiding posture and movement coordination in a free-endpoint whole-body reaching task. *Sci. Rep*. 6:23868. doi: 10.1038/srep23868

Kawato, M., Furukawa, K., and Suzuki, R. (1987). A hierarchical neural-network model for control and learning of voluntary movement. *Biol. Cybern*. 57, 169–185. doi: 10.1007/BF00364149

Kistemaker, D., a., Van Soest, A. J., and Bobbert, M. F. (2006). Is equilibrium point control feasible for fast goal-directed single-joint movements? *J. Neurophysiol.* 95, 2898–2912. doi: 10.1152/jn.00983.2005

Kistemaker, D. A., Soest, A. J. K. V., and Bobbert, M. F. (2007). A model of open-loop control of equilibrium position and stiffness of the human elbow joint. *Biol. Cybern.* 96, 341–350. doi: 10.1007/s00422-006-0120-6

Kistemaker, D. A., Wong, J. D., and Gribble, P. L. (2014). The cost of moving optimally: kinematic path selection. *J. Neurophysiol.* 112, 1815–1824. doi: 10.1152/jn.00291.2014

Li, W., and Todorov, E. (2007). Iterative linearization methods for approximately optimal control and estimation of non-linear stochastic system. *Int. J. Control* 80, 1439–1453. doi: 10.1080/00207170701364913

Marco, A., Hennig, P., Bohg, J., Schaal, S., and Trimpe, S. (2016). "Automatic LQR tuning based on Gaussian process global optimization," in *Proceedings of the International Conference on Robotics and Automation (ICRA)* (Stockholm: IEEE). doi: 10.1109/ICRA.2016.7487144

McKay, J. L., and Ting, L. H. (2012). Optimization of muscle activity for task-level goals predicts complex changes in limb forces across biomechanical contexts. *PLoS Comput. Biol.* 8:e1002465. doi: 10.1371/journal.pcbi.1002465

Mehrabi, N., Sharif Razavian, R., Ghannadi, B., and McPhee, J. (2017). Predictive simulation of reaching moving targets using nonlinear model predictive control. *Front. Comput. Neurosci.* 10:143. doi: 10.3389/fncom.2016.00143

Nakano, E., Imamizu, H., Osu, R., Uno, Y., Gomi, H., Yoshioka, T., et al. (1999). Quantitative examinations of internal representations for arm trajectory planning: minimum commanded torque change model. *J. Neurophysiol.* 81, 2140–2155. doi: 10.1152/jn.1999.81.5.2140

Nelson, W. L. (1983). Physical principles for economies of skilled movements. *Biol. Cybern.* 147, 135–147. doi: 10.1007/BF00339982

Oguz, O. S., Zhou, Z., Glasauer, S., and Wollherr, D. (2018). An inverse optimal control approach to explain human arm reaching control based on multiple internal models. *Sci. Rep.* 8:5583. doi: 10.1038/s41598-018-23792-7

Pinter, I. J., van Soest, A. J., Bobbert, M. F., and Smeets, J. B. J. (2012). Conclusions on motor control depend on the type of model used to represent the periphery. *Biol. Cybern.* 106, 441–451. doi: 10.1007/s00422-012-0505-7

Rasmussen, C. E., and Williams, C. K. I. (2004). *Gaussian Processes for Machine Learning*. Berlin; Heidelberg: Springer.

Rockenfeller, R., Günther, M., Schmitt, S., and Götz, T. (2015). Comparative sensitivity analysis of muscle activation dynamics. *Comput. Math. Methods Med.* 2015, 1–16. doi: 10.1155/2015/585409

Schmitt, S., Günther, M., and Häufle, D. F. (2019). The dynamics of the skeletal muscle: a systems biophysics perspective on muscle modeling with the focus on hill-type muscle models. *GAMM Mitteil.* 42:e201900013. doi: 10.1002/gamm.201900013

Shadmehr, R. (2010). From equilibrium point to optimal control. *Motor Control* 14, 1–6. doi: 10.1123/mcj.14.3.e25

Shadmehr, R., Smith, M. A., and Krakauer, J. W. (2010). Error correction, sensory prediction, and adaptation in motor control. *Annu. Rev. Neurosci.* 33, 89–108. doi: 10.1146/annurev-neuro-060909-153135

Spiers, A., Khan, S. G., and Herrmann, G. (2016). *Biologically Inspired Control of Humanoid Robot Arms*. Cham: Springer International Publishing.

Stollenmaier, K., Ilg, W., and Haeufle, D. F. B. (2020). Predicting perturbed human arm movements in a neuro-musculoskeletal model to investigate the muscular force response. *Front. Bioeng. Biotechnol.* 8:308. doi: 10.3389/fbioe.2020.00308

Tanaka, H., Krakauer, J. W., and Qian, N. (2006). An optimization principle for determining movement duration. *J. Neurophysiol.* 95, 3875–3886. doi: 10.1152/jn.00751.2005

Taube, W., Gruber, M., and Gollhofer, A. (2008). Spinal and supraspinal adaptations associated with balance training and their functional relevance. *Acta Physiol.* 193, 101–116. doi: 10.1111/j.1748-1716.2008.01850.x

Todorov, E. (2004). Optimality principles in sensorimotor control. *Nat. Neurosci.* 7, 907–915. doi: 10.1038/nn1309

Todorov, E., and Jordan, M. I. (1998). Smoothness maximization along a predefined path accurately predicts the speed profiles of complex arm movements. *J. Neurophysiol.* 80, 696–714. doi: 10.1152/jn.1998.80.2.696

Todorov, E., and Jordan, M. I. (2002). Optimal feedback control as a theory of motor coordination. *Nat. Neurosci.* 5:1226. doi: 10.1038/nn963

Uno, Y., Kawato, M., and Suzuki, R. (1989). Formation and control of optimal trajectory in human multijoint arm movement. *Biol. Cybern.* 61, 89–101. doi: 10.1007/BF00204593

van Soest, A. J., and Bobbert, M. F. (1993). The contribution of muscle properties in the control of explosive movements. *Biol. Cybern.* 69, 195–204. doi: 10.1007/BF00198959

Wada, Y., Kaneko, Y., Nakano, E., Osu, R., and Kawato, M. (2001). Quantitative examinations for multi joint arm trajectory planning-using a robust calculation algorithm of the minimum commanded torque change trajectory. *Neural Netw.* 14, 381–393. doi: 10.1016/S0893-6080(01)00026-0

Wolpert, D. M., Ghahramani, Z., and Jordan, M. I. (1995). An internal model for sensorimotor integration. *Science* 269, 1880–1882. doi: 10.1126/science.7569931

Conflict of Interest: The authors declare that the research was conducted in the absence of any commercial or financial relationships that could be construed as a potential conflict of interest.

II. Contribution 2: Design and Scaling of Exoskeleton Power Units Considering Load Cycles of Humans

robotics

Article

Design and Scaling of Exoskeleton Power Units Considering Load Cycles of Humans

Marcel Waldhof [1,]*, Isabell Wochner [2], Katrin Stollenmaier [2], Nejila Parspour [1] and Syn Schmitt [2]

[1] Institute of Electrical Energy Conversion, University of Stuttgart, 70569 Stuttgart, Germany
[2] Institute of Modelling and Simulation of Biomechanical Systems, University of Stuttgart, 70569 Stuttgart, Germany
* Correspondence: marcel.waldhof@iew.uni-stuttgart.de; Tel.: +49-711-695-67666

Abstract: Exoskeletons are powerful tools for aiding humans with pathological conditions, in dangerous environments or in manually exhausting tasks. Typically, they are designed for specific maximum scenarios without taking into account the diversity of tasks and the individuality of the user. To address this discrepancy, a framework was developed for personalizing an exoskeleton by scaling the components, especially the electrical machine, based on different simulated human muscle forces. The main idea was to scale a numerical arm model based on body mass and height to predict different movements representing both manual labor and daily activities. The predicted torques necessary to produce these movements were then used to generate a load/performance cycle for the power unit design. Considering these torques, main operation points of this load cycle were defined and a reference power unit was scaled and optimized. Therefore, a scalability model for an electrical machine is introduced. This individual adaptation and scaling of the power unit for different users leads to a better performance and a lighter design.

Keywords: axial flux machine; exoskeletons; human arm model; multiphase electrical machines; permanent magnet machines; personalization

Citation: Waldhof, M.; Wochner, I.; Stollenmaier, K.; Parspour, N.; Schmitt, S. Design and Scaling of Exoskeleton Power Units Considering Load Cycles of Humans. *Robotics* **2022**, *11*, 107. https://doi.org/10.3390/robotics11050107

Academic Editor: Ming Xie

Received: 25 August 2022
Accepted: 29 September 2022
Published: 8 October 2022

1. Introduction

The application areas of exoskeletons are as wide-ranging as the requirements for the drive units. In medical environments, exoskeletons can be used for the rehabilitation of motor-impaired patients, for one, or permanently to compensate for muscle/neurological diseases. In addition to medical applications, exoskeletons are also employed in industrial environments. Here, they support workers during heavy activities in order to counteract long-term damage to the body. In [1,2], the usage of exoskeletons in industrial environments is investigated, and displays an increase in productivity. Smets [3] shows the challenges of this practice in his study. He states that a "one for all solution" is not effective because the different requirements of the users cannot be met to the same extent and thus the use of the exoskeletons by workers is negated. In addition, the weight and comfort of the exoskeletons are brought up as major criteria. The classic design process of exoskeleton power units focuses on maximum loads, whereas the interaction with the human force component is neglected. This leads to an oversizing of the drivetrain and thus to a high weight. This problem was also stated in a recent review of the design of current upper limb exoskeletons by Gull et al. [4]. More specifically, they defined the still unsolved challenge of designing novel exoskeletons based on neuro-musculoskeletal models. In the following, we present some of the earlier studies that investigated human- and task-centered approaches to more accurately design the drive system and the exoskeleton.

Shao et al. [5] optimized the design of a three-DOF cable-driven upper arm exoskeleton by minimizing the force exerted on a numerical arm model. Using this optimization based on the mechanical arm model, they were able to ensure that one representative user could perform all motions over a large range of motion, though the muscle dynamics were neglected. Zhou et al. [6] proposed a method used to optimize the design of robotic exoskeletons using simulations of a musculoskeletal arm model to addresses the individual requirements of the user. Here, they optimized the stiffnesses of a simplistic exoskeleton based on linkages arranged as a parallelogram at the example of a generic arm model driven by recorded human motion data. Zoss [7] also used clinical gait data (CGA) to design a lower body exoskeleton. Using these data for a scaled generic human in combination with a simple power analysis, they showed that appropriately sized electric actuators could be chosen, leading to a decrease in power consumption, with the disadvantage of being twice as heavy as the original actuation. To overcome this drawback of overdimensioned actuators, Toxiri et al. [8] focus on a specific use case of the exoskeleton and generate the requirements for the drive system based on this by including an elastic element acting to the mechanical in parallel. Calanca [9] uses both of the different requirements and adapts his drive systems with commercially available components for the gearbox and electric drives to better fit the drive systems to the user. All of these approaches show a significant increase in the user's acceptance of using the exoskeletons, but they still do not adequately meet the user's individual needs. Most of the presented approaches require real human motion data to drive the biomechanical model, which has the disadvantage of novel and potentially dangerous tasks not being able to be tested virtually a priori. Furthermore, all of them optimized the exoskeletons design for one generic biomechanical model. Therefore, typically, only one or two design variables could be optimized, whereas a greater fine-tuning of the drive system requires individual scaling of the electric machine.

In [10,11], a general approach for scaling electromagnetic systems is presented. Pries further shows that an electric machine can be scaled with a constant parameter. This approach is refined in [12,13]. It scales the outer diameter as well as the active length of an electric drive via parameters and optimizes it to the driving cycle of electric mobility. This shows a significant increase in efficiency as well as torque density. Seok [14] gives a similar approach, where he scales the outer diameter and axial length of the motor for a legged robot. This approach shows a good adaption to the desired task, but is still limited to a few geometric motor parameters. A major remaining challenge in scaling is the production of the drive in quantities of one. However, many concepts of additive manufacturing for electric drives have been presented recently that can solve this challenge [15–17].

It has been found that, in order to create an individual exoskeleton for the individual user, the physiology of the user must be recorded and taken into account. Furthermore, the performed task has to be investigated and then the drive system has to be scaled according to these requirements in order to generate a drive system that is as light and efficient as possible.

This personalized design process, which is currently unknown to the author in the literature, shall be further examined in this approach. For this purpose, a scalable human arm model shall be created, which represents the individual user's exoskeleton requirements. Finally, a novel scaling model of a drive unit is presented in order to implement an individual drive. The purpose of this study is to optimize the design process for personalized exoskeletons to reduce the weight and increase the power density of exoskeletons. To this end, the unique body dimensions of each person and the required task are considered. In a first step, the body dimensions were used as the input for a scalable human model (see Section 2.2) to generate the occurring forces for the desired task. Therefore, the total height l_B and mass m_B of the body was measured. To define the task trajectory, the entire movement was split up into sub-movements with a defined start and target angles of the elbow and the shoulder joint. Resulting torques were analyzed and used to generate a load cycle for the power unit design (see Section 2.5). The defined main operation points, in addition to user-dependent constraints such as mass and size, were used to scale a reference power unit for the specialized needs (see Section 2.6). In Figure 1, a schematic overview of the design process and the structure of this paper is given.

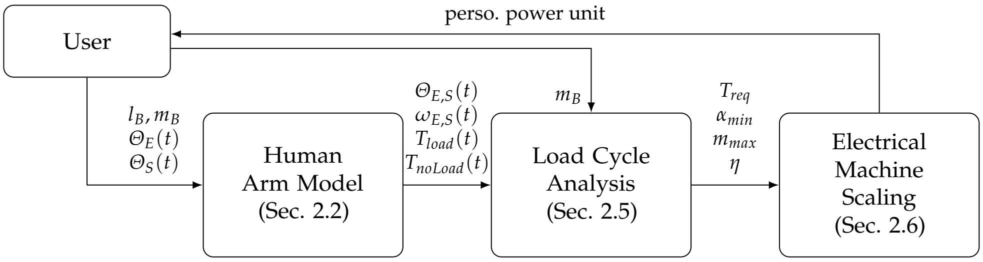

Figure 1. Schematic overview of the design method in this approach.

The novelty of this work is the combined virtual prototyping environment coupling the forward dynamic simulation of different scaled musculoskeletal arm models with the scaling of the electrical machine. To this end, a novel scaling model for a geometrical scaled drive unit is introduced.

Use Case

The design approach introduced in this paper was demonstrated by the example of an upper body exoskeleton, more specifically, on the elbow power unit. As a representation of a human model, an arm model with a shoulder and elbow joint was used to predict movement parameters necessary for the power unit design. The power unit scalability model was introduced for an axial flux machine; in particular, five geometric parameters of the axial flux machine were scaled, and this model was verified on a five-phase air-cored case study. Further, the general approach should be applicable to any exoskeleton with any electrical machine design used for the support of different body parts. However, the applied constraints and feasibility were specified on this case study. The study case of the air-cored machine allows us to neglect the iron core losses and non-linear effects of iron in the machine.

2. Materials and Methods

2.1. Definition of Movement

To demonstrate that the power unit is designed for a representative biological movement range of the arm, the following movement matrix is defined. Consider both flexion and extension movements for one- and two-joint movements with different velocities in three different conditions: without additional weight (no load), lifting a fixed weight (2.5 kg) and a scaled weight (100% arm weight). In total, this represents eight different cases shown in Table 1 and visualized in Figure 2. The chosen angle deviation is 90° for both the shoulder Θ_S and the elbow joint Θ_E in the two-joint movement in order to include a wide range of motion.

Table 1. Movement matrix.

Cases	Start to Target Angle [Θ_E, Θ_S]				Mov. Duration	DoF
A	[00°,00°]	to	[−90°,−90°]	flex.	1.2 s	two joints
B	[−90°,−90°]	to	[00°,00°]	ext.	1.2 s	two joints
C	[00°,00°]	to	[00°,−90°]	flex.	1.2 s	one joint
D	[00°,−90°]	to	[00°,00°]	ext.	1.2 s	one joint
E	[00°,00°]	to	[−90°,−90°]	flex.	0.6 s	two joints
F	[−90°,−90°]	to	[00°,00°]	ext.	0.6 s	two joints
G	[00°,00°]	to	[00°,−90°]	flex.	0.6 s	one joint
H	[00°,−90°]	to	[00°,00°]	ext.	0.6 s	one joint

Furthermore, a target position of 90° for both joints is a typical position in manual labor such as overhead drilling [1,2], which is a potential application for this exo power unit. Another potential use case is exos in rehabilitation, where single-joint movements are often performed in typical exercises [18]. All cases include representations of typical daily activities; for instance, opening a door or carrying objects. Apart from joint angle configuration, movement speed and movement duration typically have a crucial influence on biomechanical parameters such as torque. Therefore, two typical movement durations were selected to represent both faster (0.6 s) and slower (1.2 s) movements [19,20].

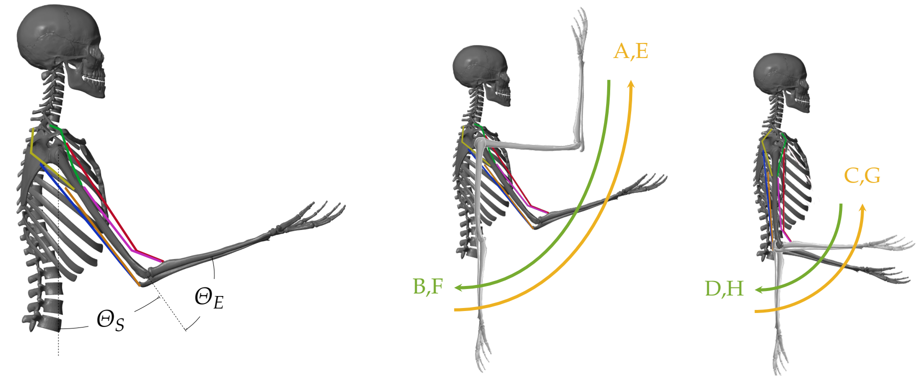

(**a**) Arm joint angles in deg (**b**) Two degrees of freedom (**c**) One degree of freedom

Figure 2. Visualization of arm model with the considered movement matrix. In (**a**), the defined angles are shown. (**b**,**c**) show the start and target positions of the movements as well as the controlled trajectory.

2.2. Arm Model

Modeling the lifting movement, the "Arm26" model as described in [21] was used. It consists of two joints (elbow and shoulder) and six muscles, modeled as Hill-type muscles (see Figure 2a). Here, each joint was actuated with two monoarticular muscles, as well as two biarticular muscles. The dynamics of the skeletal system were modeled as rigid bodies solving the Euler–Lagrange equation. Furthermore, the muscle model consisted of an extended Hill-type muscle model with a more realistic eccentric force–velocity relation and serial damping as shown in [22,23]. The routing of the muscle path around the joints was accomplished using deflection ellipses as described in [24] and we included nonlinear activation dynamics according to [25]. For a more detailed description, we refer to the supplementary material of [21]. Additionally, physiological joint limits were included as linear one-sided spring-damper elements. Note that the arm model was implemented using Matlab®/Simulink® version 2018a with the Simscape Multibody™ environment.

It was scaled for three different human sizes: F05, M50, M95. These model sizes are typically used in biomechanical studies, e.g., in car occupant models [26] and pedestrian safety models [27,28] among others. The reason behind this is because the range between the 5th percentile female and the 95th percentile male (in both size and weight) represents 90% of the population. The total body height l_B and total body mass m_B used in this study were taken from [29] as shown in Table 2.

Table 2. Total height and weight for three typical human percentiles commonly used in ergonomic studies.

Description	Unit	F05	M50	M95
total height l_B	m	1.535	1.750	1.855
total weight m_B	kg	52.000	79.000	100.000

2.3. Scaling Approach

For scaling a musculoskeletal model, three sets of parameters need to be modified: first, the geometry of the model, including segment lengths, segment masses, centers of mass and moments of inertia, needs to be scaled. These quantities were scaled linearly based on the total height of the considered person l_B and the total body mass m_B. The linear scaling factors used for the "Arm26" model were taken from Winter et al. [30].

The second set of parameters that were scaled includes all muscle lengths, i.e., muscle attachment points relative to the bones (muscle origin, insertion and deflection points), as well as the muscle-length-dependent parameters $l^{\mathrm{CE,opt}}$ and $l^{\mathrm{SEE,0}}$. These were scaled proportionally to the segment lengths and used the "Arm26" model as reference [21].

Finally, the maximum isometric force $F_{\max}$ of all muscles needs to be scaled. Since this force is linearly related to physiological cross-sectional area (PCSA), the PCSA was scaled instead. This cross-sectional area PCSA can, in turn, be scaled dependent on the total body mass m_B [31]. Notably, all parameters can be scaled depending on the total body height l_B and mass m_B. Although statistical parameters (as given in [29]) were used for these two quantities, they can easily be exchanged for subject-specific modifications.

2.4. Control

As desired movement trajectory, a minimum jerk trajectory with a fifth-order polynomial was implemented to ensure a smooth trajectory in accordance with [32]. This higher-level input Θ_E^{des}(t) was then transformed into a triphasic stimulation pattern $u(t)$ using the pattern search algorithm in Matlab® (as described in [33]). The assumption to use a triphasic stimulation pattern as in [33] is justified because, during fast point-to-point movements, three phases in the muscle surface electromyogram (EMG) patterns are typically observed [34,35]. This corresponds to an acceleration phase where mostly the agonist muscles are active, which is followed by a braking phase of the antagonistic muscles, until the arm is kept in the desired end position in the final phase. Based on this muscle stimulation, a forward-dynamic simulation of the arm model was performed.

2.5. Load Cycle Analysis

The necessary torque $T_{load,opt}$ to perform the actions in time was specified by a dynamic simulation based on classical mechanics with an inverse dynamics approach. This theoretical torque curve was compared to the results of the human arm model, from which, the required supporting torque of the power unit was calculated.

To generate load profiles for the electrical machine, the required movement was simulated with and without additional load. To the user, the movement with an added weight should feel comparable to an unloaded movement. This signifies that the movement velocity should be equal to the optimal unloaded movement velocity ω_{opt}.

$$T_{req} = T_{load,opt} - k_{per}\, T_{load} - (1 - k_{per})\, T_{noLoad} \tag{1}$$

$$\omega_{req} = \omega_{opt} \tag{2}$$

The support torque is individually adjustable. The constant k_{per} describes the power factor of the person. If k_{per} is set to one, the person will take the full load of the load cycle, which means that there will be no support of the drive unit. If the constant is zero, the weighted movement will feel like the unloaded movement. However, independent of k_{per}, the difference in the torque curves is supported to match the optimal trajectory. In Figure 3, exemplary torque curves are visualized. More torque curves are presented in the Appendix A (c.f. Figures A1–A4). The torque–speed plane was then calculated with (1) and (2) and presented in Figure 4 for three different people for movement A with 100% additional arm weight.

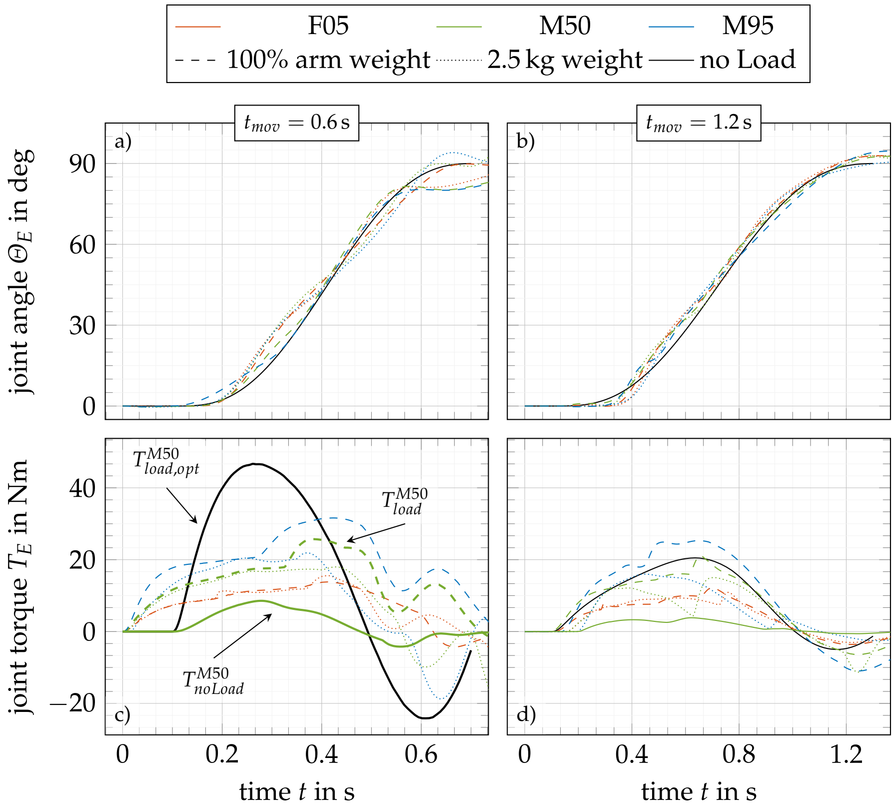

Figure 3. Simulated load cycle comparison for the movements, case A and E (see Table 1), with different movement durations t_{mov} and loads m_{load}. The solid black line shows the optimal trajectory and torque curve $T_{load,opt}$ of the M50 with 100% arm weight. In (**a**,**b**) the joint angles of the elbow and in (**c**,**d**) the resulting torque in the elbow joint during the performed task are presented. Further, in (**c**), exemplary for M50, the torque curves used in (1) are marked.

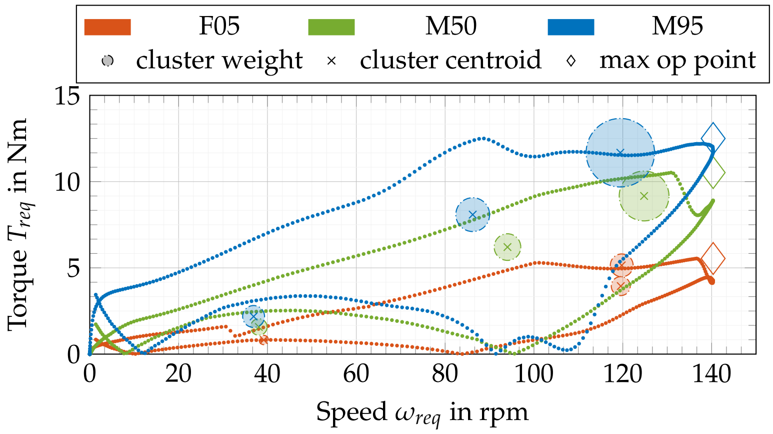

Figure 4. Clustering result for all persons for case A with the relative weight of 100% arm weight and a support of $k_{per} = 0.5$. The cluster centroids with their statistical weight. The size of the cluster weight circle shows how many points and how much loss power are grouped in this cluster, statistically related to the number of all points and total loss power of the load cycle. The maximum operation point later is used as EM design point.

To ensure that all requirements were met, the maximum operating point (maximum speed, maximum torque) was used as the design point for calculating the electric machine. In addition to the maximum operating point, all other operating points are also relevant for the optimum design of the drive, since the loss energy varies in each one, respectively. In this context, partial load points may occur more frequently in a load cycle, where a high efficiency would be desirable. To optimize the overall efficiency over the course of a load cycle, the efficiency has to be considered at each stage thereof. Determining these is very computationally and time consuming for variable electric machines during optimization. Consequently, a reduction of these points needs to be considered. Data downsampling alone could lead to a loss of information about the cycle, which is not recommended. For data reduction, cluster algorithms are a promising approach. Various methods of analyzing driving cycles are presented in the literature [36,37]. Besides the thorough knowledge of experts used to generate relevant operating points, the k-means machine learning algorithm is superior to other algorithms mentioned there. This algorithm generates a centroid by using the Euclidian distance for a given number of clusters under consideration of different similarity constraints [38].

In this approach, in addition to the torque/speed characteristic and considering the physical behavior in the cluster algorithm, the power dissipation was chosen as a supplemental constraint. In robotic applications, especially in this case study, the amount of copper losses is dominant and calculated with

$$P_{L,C} = \frac{m}{k_T^2} R_{ph} \, {T_{req}}^2 \,. \tag{3}$$

Here, the phase resistance R_{ph}, the number of phases m and the torque constant k_T of the reference motor were used. Based on the clustering results with three clusters (Figure 4), the elaborated points can be used for electrical machine scaling instead of using all data points. Furthermore, the clusters were weighted based on the time of the cycle within the cluster multiplied by the copper losses related to the total loss power.

2.6. Power Unit Design

2.6.1. Reference Machine

The reference power unit (PU) in this approach consisted of a yokeless double-sided axial flux machine (AFM). In [39], the AFM was geometrically compared to other motor topologies, such as radial and transversal flux machines [40]. The result shows that the AFM is beneficial over other topologies for torque production in flat application fields. The AFM was connected to a harmonic drive gear (HD) by a toothed belt. The optimal gear ratio was designed in accordance with [41], where the stator current of the electrical machine considering a known LC was minimized. This leads to a total gear reduction of $i_G = 235$, on average, for different load cycles. The gear ratio is quite high for dynamic applications. This leads to some issues in back drivability of the system, which can be handled through compensating control algorithms. The gear ratio is adaptable and not necessarily fixed for the scaling approach.

Finally, this leads to a design torque of $T_{AFM} = 180\,\text{mNm}$ of the AFM. The DC-Link voltage of the reference machine was set to 48 V. Stator housing and coil holders, presented in Figure 5, are made of 3D-printed PLA. Hence, small adjustments in geometry scaling are easily implementable.

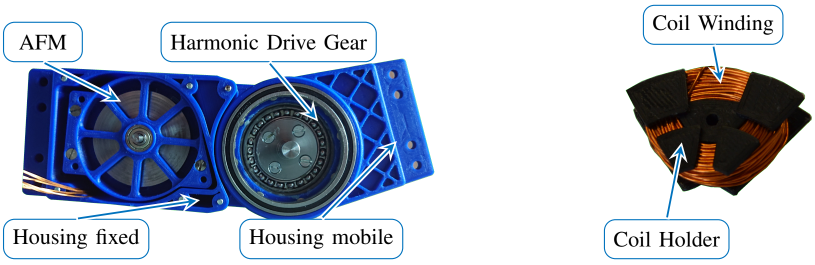

(**a**) (**b**)

Figure 5. Reference power unit design prototype. (**a**) Power unit for an elbow. All housing components are made of 3D-printed PLA. (**b**) 3D-printed coil holders with winding.

2.6.2. Scaling Approach

Figure 6 shows the considered geometry and introduces the geometrical scaling parameters. The general topology was set to a five-phase machine with a stator pole pair number of one. To increase the winding factor, a rotor pole pair number of three was chosen.

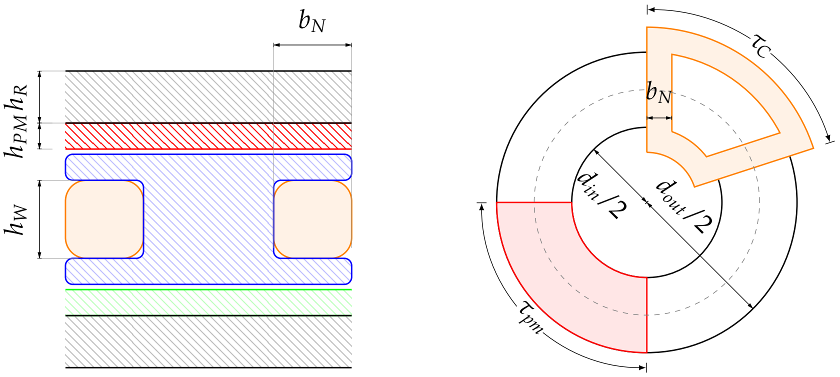

(**a**) (**b**)

Figure 6. Geometry drawings of yokeless double-sided axial flux machine with relevant design parameters. The outer diameter of the AFM is expressed by d_{out}. The ratio between the inner diameter and the outer diameter is expressed through k_D. The winding area is defined through the height h_W and the width b_N. The coil width is defined with τ_C. The winding is implemented parallel along radial direction. The heights of the permanent magnets h_{PM} and the width τ_{pm} are shown. The rotor height is given with h_R. (**a**) Cut view on the middle radius. (**b**) Top view.

The scaling approach utilized in this paper was based on analytical functions that are presented in literature [42,43]. This means varying the machine parameters to a certain extent around the reference machine design. The general scaling law can be given for x as product of x_0, the considered value of the reference machine and c_x, the scaling factor of x. Rearranging this leads to the desired relationship

$$c_x = \frac{x}{x_0}. \tag{4}$$

Further, x can be set to every parameter of the electrical machine and can be defined as $x = f(d_{out}, k_D, h_W, \ldots)$. Applying (4) to every parameter leads to the general model

$$c_x = f(c_{d_{out}}, c_{k_D}, c_{h_W}, \ldots)\,. \tag{5}$$

The general scaling law in (5) can basically be applied to all of the output quantities. For some relationships, it is convenient to introduce so-called auxiliary constants. These will be abbreviated with f_x and depend solely on values of the reference machine and physical, material or other auxiliary constants.

In the following, an example for the torque is given. The torque is calculated as

$$T_{AFM} = \frac{\pi}{4}\,\zeta_{w,\nu}\,\hat{B}_\delta\,A_{AFM}\,{d_{out}}^3\,(k_D - {k_D}^3). \tag{6}$$

The winding factor $\zeta_{w,\nu}$, the flux density $\hat{B}_\delta$ and the current density A_{AFM} are given. In case of the torque equation, the scaling model is defined as

$$c_T = \frac{T_{AFM}}{T_0} = c_{el}\,c_{magn}\,c_{geom}. \tag{7}$$

For a better understanding of the scaling influences, they can be grouped into electrical, magnetic and geometrical dependencies. In this paper, the geometrical scaling is investigated. Geometrical cross-dependencies to magnetical and electrical scaling are considered. The scaling parameters are defined as $\lambda = (c_{d_{out}}, c_{k_D}, c_{h_W}, c_{b_N}, c_{h_{PM}})^T$. Further, it is implicated that the electrical and magnetic load of the electrical machine should be constant. In other words, the winding scheme, magnet topology, etc., are fixed. In terms of the magnetic flux density $\hat{B}_\delta$ in the air gap, there is a geometric relationship between the height of the permanent magnet h_{PM} and the height of the winding h_W. This dependency leads to additional constraints that are considered for the solution of the problem. In (8), (see following page) the torque scaling model is given. Important parts in this equation are the scaling factors for the winding factor $c_{\zeta_1}(\lambda)$ and the edge leakage factor $c_{k_L}(\lambda)$.

The winding factor is investigated in [44]. The scaling behavior was simplified to the carrier wave of the system on the centered radius in this case. Then, the trigonometric functions were mapped to a third grade Taylor polynomial, which maps the function with less than one percent error.

The leakage factor contemplates the edge effects of the permanent magnets on the outer and inner radius of the machine. Furthermore, the shortcut effects between the permanent magnets are taken into account. This factor is based on an average area reduction of the permanent magnet, thus leading to a reduction in the magnetic flux density in the air gap.

In addition, torque c_T, speed c_ω, mass c_m, acceleration c_α and efficiency c_η are defined as necessary values for scaling in personalization for exo drives. The detailed model functions are given in (8) to (12).

The exemplary design area generated from the model (Figure 7) depends on the first three geometric scaling factors of λ. All other scaling factors are kept constant for visualization.

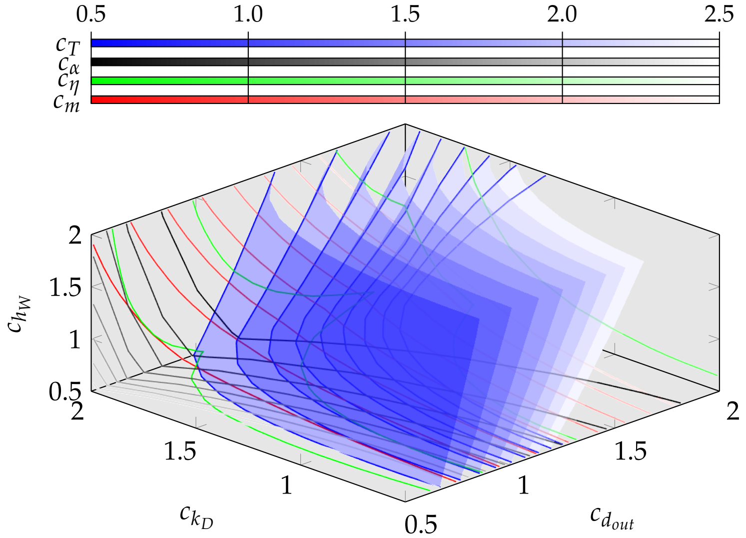

Figure 7. Model dependency on three exemplary different scale factors. The iso-surfaces visualize the scaling of the torque. The contour lines in the axes limit show the scaling for all model outputs.

The model provides the opportunity to generate these design areas for all different kinds of scaling factors. To solve the model for the load cycles as defined in Section 2.5, the intersubsection points of these scaling functions must be identified.

$$c_T = c_N\, c_I\, c_{\zeta_1}\, c_{k_L}\, \frac{c_{Br}}{1 + f_\delta \left(\frac{f_{\delta 0}\, c_\delta + f_{h_{PS0}}\, c_{h_{PS}} + f_{h_{W0}}\, c_{h_W}}{c_{h_{PM}}} - 1 \right)}\, {c_{d_{out}}}^2 \left(f_{K2} + (1 - f_{K2})\, {c_{k_D}}^2 \right) \tag{8}$$

$$c_\omega = \frac{c_{U_i}}{c_N\, c_{\zeta_1}\, c_{k_L}\, \frac{c_{Br}}{1+f_\delta \left(\frac{f_{\delta 0}\, c_\delta + f_{h_{PS0}}\, c_{h_{PS}} + f_{h_{W0}}\, c_{h_W}}{c_{h_{PM}}} - 1 \right)}\, {c_{d_{out}}}^2 \left(f_{K2} + (1 - f_{K2})\, {c_{k_D}}^2 \right)} \tag{9}$$

$$c_\alpha = \frac{c_T}{\frac{{c_{d_{out}}}^4}{1+f_{\Theta_1}} \left(c_{h_R} + \frac{c_{h_{PM}}}{f_{\Theta_2}} \left(1 - {c_{k_D}}^4 \left(1 - \frac{1}{f_{K4}} \right) \right) \right)} \tag{10}$$

$$c_m = \frac{{c_{d_{out}}}^2}{\frac{1}{f_{m_1}} + f_{m_2}\, (1 - f_{\alpha_2}) + f_F + 1} \left(\frac{c_{h_R}}{f_{m_1}} + \left(f_{K2} + (1 - f_{K2})\, {c_{k_D}}^2 \right) \left(c_{h_{PM}}\, f_{m_2}\, (1 - f_{\alpha_2}) + c_{h_{PS}}\, f_F + c_{h_W} \right) \right) \tag{11}$$

$$c_\eta = \frac{c_T\, c_n}{f_{P_{mech0}}\, c_T\, c_n + f_{P_{Cu0}}\, \frac{{c_N}^2 {c_I}^2}{c_{k_{Cu}}\, c_{h_W}\, c_{b_N}} \left(\left(f_{P_{Cu1}} - f_{P_{Cu2}}\, c_{k_D} \right) c_{d_{out}} - f_{P_{Cu3}}\, c_{b_N} \right)} \tag{12}$$

2.6.3. Solving

The model equations are solved with the Levenberg–Marquardt algorithm, which is based on the least-square algorithm method. The solvability strongly depends on the initial points. Therefore, a multi-start algorithm is used to check a wide range of initial points. A pre-calculated geometrically feasibility check of the initial points restricts the solver to start only with feasible initial points. The solution is based on the following equations. From the load cycle analysis, in combination with the individual body requirements of the user, minimal needed values are identifiable. Therefore, the maximum needed torque $T_{max,req}$ (see (13)) and the minimum necessary acceleration $\alpha_{min,req}$ (see (15)) that fulfil the load cycle are determined. Depending on the user, a maximum weight $m_{max,user}$ of the electrical machine is chosen (see (14)).

$$c_T(\lambda) - {}^{T_{req}}/{}_{T_0} = 0 \tag{13}$$

$$c_m(\lambda) - {}^{m_{max,user}}/{}_{m_0} \leq 0 \tag{14}$$

$${}^{\alpha_{min,req}}/{}_{\alpha_0} - c_\alpha(\lambda) \leq 0 \tag{15}$$

Only in the case of the demanded torque is a strict maximum bond given. For the acceleration and mass, soft maximum and minimum bonds are given. In other words, only the necessary torque should be exactly achieved. Should it be possible through scaling to achieve a lighter motor than the permissible weight or more dynamics as the demanded acceleration for a higher efficiency, the solver can choose this solution. This leads to a better performance of the solver.

2.6.4. Constraints

An important part of scaling definitions is to define the feasible possibilities of the model. Therefore, the following constraints are examined.

For the geometric feasibility, the maximum possible assembly space for the power unit is considered, as well as the space constraint at the inner radius of the AFM. Here, the width of the winding slot has to be small enough to fit two times within the pole pitch of the AFM:

$$\frac{c_{b_N}}{c_{d_{out}}\, c_{k_D}} - \frac{d_{out}\, k_D}{2\, b_N}\, \underbrace{\frac{\pi}{m}}_{f_1} < 0\,. \tag{16}$$

Under consideration of a parallel slot opening over the machine diameter, the factor f_1 has to be adapted to

$$f_1 = \sin({}^{\pi}/{}_{m}). \tag{17}$$

As mentioned in [39], the double-sided AFM is beneficial over a radial flux machine (RFM) if the assembly space factor c_{AR} is smaller than one. Therefore,

$$\frac{{c_x}^2 f_{AR1} - c_x f_{AR2} + f_{x2}}{{c_x}^3 c_{k_D} \left(f_{K2} - (f_{K2} - 1)\, {c_{k_D}}^2\right)} - \frac{1}{f_{AR_0}} < 0\,, \tag{18}$$

is defined, where c_x describes the ratio between the outer diameter and the active length in terms of the machine geometry.

Besides the geometric constraints, thermal constraints were implemented as well. The thermal behavior of the AFM was controlled through the maximum allowed current line density. In air-cooled electrical machines, a current line density of 5–10 $\mathrm{A/mm^2}$ is recommended. For short time operations, a current line density of $J_{max} = 30\,\mathrm{A/mm^2}$ is permissible [45]. The following constraint is given to

$$\frac{c_N\, c_I}{c_{k_{Cu}}\, c_{b_N}\, c_{h_W}} - \frac{J_{max}}{J_0} < 0. \tag{19}$$

Figure 8 shows a design map for an exemplarily designed load cycle (case A) of M50 person. The blue surface shows all scaling combinations that match the torque requirement. Some of the above-mentioned constraints and model equations are displayed as intersubsection lines of the constraint surfaces on the constant torque surface. A further design criterion is the efficiency of the scaled machine. The scaling influence on the efficiency is shown as a contour plot on the constant torque plane. In this case, the efficiency is rising equally to the slot height c_{h_W}. Based on these findings, the most efficient scaled machine on the intersubsection lines of (14) and (16) of the possible variants was chosen (see blue dot).

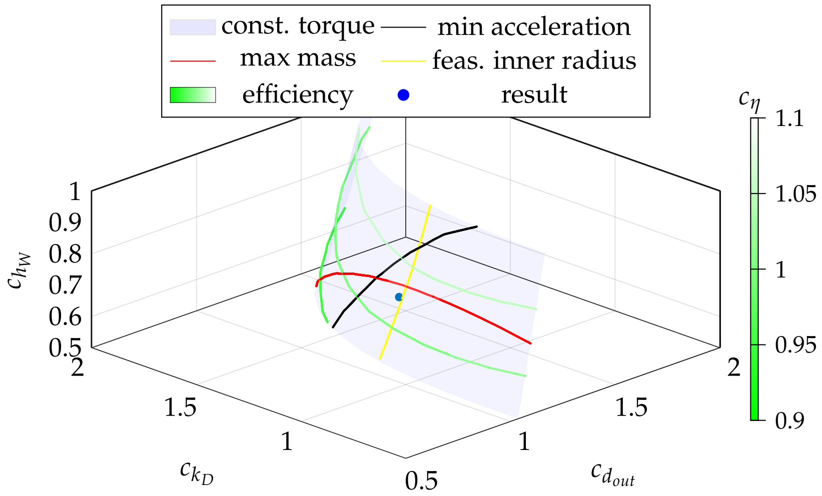

Figure 8. Solution map for the elbow power unit of a M50 at the movement case A.

2.6.5. Validation

The model validation is accomplished in two steps: At first, the influences of the scaling parameters are proven by a three-dimensional FEA simulation. Secondly, the reference power unit is built up as a first prototype (see Figure 5) to validate the FEA simulation as well as the analytical model. The measurements are performed on a motor test bench where constant operating points, as well as the earlier mentioned reference load cycle, are implementable. For the speed characteristic, the induced voltage in open circuit operation mode is validated, which indicates the right electromagnetic behavior. For torque and performance validation, the motor is controlled as presented in [46]. Detailed results are given in Table 3 and can be observed as matching very well.

Table 3. Result comparison from the analytical model (AM), 3D finite element analysis (FEA) and measurements of the prototype (PT).

Parameter	**Unit**	**AM**	**FEA**	**PT**
Torque T_{AFM}	mNm	180.80	178.90	176.20
Ind. Voltage U_i	$^{\mathrm{mV}}/_{\mathrm{rpm}}$	1.54	1.49	1.49
Mass m_{ref}	g	156.15	156.35	157.20
Efficiency η [1]	%	62.49	62.25	61.90

[1] at $n = 3000\,\mathrm{rpm}$, $\hat{i}_1 = 5\,\mathrm{A}$.

The differences between prototype and FEA simulation are in all values under 1.5%. The maximum deviation between analytical model and prototype is 3.2%, which is acceptable under the assumptions at hand.

3. Results

For the discussion of the results, an exemplary load cycle consisting of the movements "ABCD" and "EFGH" was investigated. Further, the slow load cycle will be called "slc", and the fast one "flc".

3.1. Influences of Movement

The movement velocity has the largest impact on the load cycle and the requirements of the power unit, as shown in Figure 9a. With a decrease in the movement time, dynamic effects are dominating and the torque necessary to compensate the inertia is rising. In the case of the M95 person, the needed torque rises from 10.11 Nm to 22.81 Nm. This corresponds to an increase of 125.6%. Furthermore, the power unit speed scales up linearly to the movement velocity. This means that two completely different design points are necessary for the PU designs. Figure 9b shows the difference in the load cycle for different weights. It should be noted that the course of the load cycle remains similar whereas the maximum needed torque scales up linearly. To check the type of movement in Figure 9c,d, movements with different degrees of freedom are shown. In Figure 9c, it is notable that the design point is nearly independent of the movement. On the other hand, the course of the load cycles is different. The cluster points of the single joint movement are shifted into a low speed range, which changes the load cycle efficiency, so the electrical machine has to be adapted. In Figure 9d, the same movements are visualized, only with a shorter duration. In the case of the M95 person, the difference in the demanded torque is between 108% in the slow movement (s. Figure 9c) and 242% in the fast movement (s. Figure 9d). The cross effect to the movement speed is dominant. Further, the cluster points are shifted into a region with higher torques. It can be confirmed, as known in mechatronic systems, that both the type of movement and the speed of movement should be considered in combination and, more precisely, a task-defined load cycle is necessary.

3.2. Influences of Person

Based on the torque–speed profiles, differences caused by the individual person are also noticeable in Figure 9. Due to the different body dimensions, the same activities require different load forces. The comparison of a fixed weight with the weight adjusted to the body mass does not show any differences for the F05 person, whereas the requirements almost double for the M95 person. Figure 9a shows that the dynamic effects also upscale depending on the body dimensions. As mentioned above, concerning the M95 person, the torque demand increases by 125.6%, and, in the case of the F05 person, by 50%. Furthermore, the simulation shows that the model of the F05 woman cannot lift heavy loads smoothly due to a reduced maximum force in the muscles. This leads to the conclusion that the personalized body dimension will lead to the optimal consideration of the demanded torques.

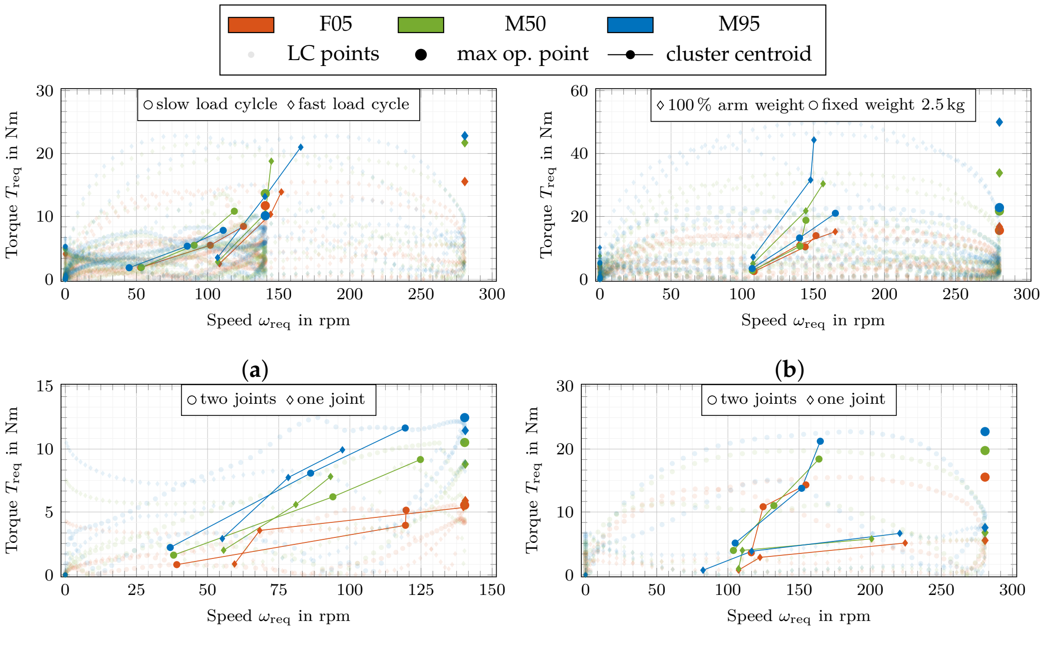

(**a**) (**b**)

(**c**) (**d**)

Figure 9. Comparison of load cycle data based on several criteria. Besides the load cycle data points (low opacity in background), the cluster centroids of the k-means algorithm are displayed. The cluster weight is not further visualized. As electrical machine design point, the maximum operation point is used. (**a**) Load profiles slc and flc with a fixed weight of 2.5 kg. (**b**) flc with fixed load at 2.5 kg and referred load at 100% arm weight. (**c**) Movements of case A vs. C with an additional load of 100% arm weight. (**d**) Movements of case E vs. G with an additional fixed weight of 2.5 kg.

3.3. Power Unit Scaling

To quantify the benefit of scaling the power modules to the personal needs of the user objectively, the mass of the power module was used as a benchmark characteristic. The mass of the reference motor was compared to the scaled versions. To consider differences in the efficiency of the modules, an additional accumulator mass was calculated. Here, the difference in loss energy over 1000 performed cycles is referred to as the energy density $e = 180\,\frac{\mathrm{Wh}}{\mathrm{kg}}$ ($\widehat{=}\,648\,\frac{\mathrm{Ws}}{\mathrm{g}}$) of a lithium-ion accumulator. The formula is given as

$$\Delta m_{add} = m_{sc} + n_{cyc}\,\frac{E_{V,cu,sc} - E_{V,cu,ref}}{e} - m_{ref}. \tag{20}$$

If this additional mass m_{add} is smaller than zero, the scaled machine for the considered load cycle is advantageous.

The mass saving of the scaled machines in comparison to the reference machine is given in Table 4. In the case of the slc performed by the F05 person, a mass of 46.7 g is saved. This leads to a reduction of 29.4% of the AFM mass compared to the reference design. Comparing the load cycle slc to flc for the M95 person, the weight saving is 28.4%. Moreover, it needs to be mentioned that the reference power unit could not meet all torque demands. This would lead to a new reference design with additional weight in the case of a standardized solution, which, in turn, leads to more weight saving in other cases. This indicates that the introduced scaling approach is highly beneficial.

Table 4. Weight differences between the reference machine and scaled electrical machines for exemplary load cycles with different load weights and a total number of cycles $n_{cyc} = 1000$.

Load Cycle	Person	m_{load} [g]	η_{LC} [%]	Δm_{add} [g]
slc	F05	2.5	33.8	−46.7
	M50	2.5	43.8	−44.3

Table 4. *Cont.*

Load Cycle	Person	m_{load} [g]	η_{LC} [%]	Δm_{add} [g]
	M95	2.5	37.9	−39.6
	F05	2.6	30.9	−40.5
	M50	3.95	49.2	−25.7
	M95	5	57.6	−9.7
flc	F05	2.5	51.3	−32.2
	M50	2.5	67.2	−15.8
	M95	2.5	74.2	6.8
	F05	2.6	52.4	−28.7
	M50 [1]	3.95	73.4	14.5
	M95 [1]	5	77.8	42.63

[1] Reference machine does not fulfil all maximum requirements.

4. Discussion and Conclusions

In this paper, a methodology for the individual design of exoskeleton drive units for user- and task-dependent applications was presented. This approach merged a scalable biomechanical human model and a scalable electromagnetic and mechanical model of an electrical machine.

With the scalable human model, forces from arbitrary tasks with different loads are predictable. Thereby, necessary forces for the drive unit design were generated. Alternatively, these forces could be generated from experimental data using an inverse dynamics method, which avoids the model assumptions and limitations presented in [21]. A clear advantage of our method compared to this is that we can easily scale an exoskeleton for different participants based only on the height and weight of the participant. Therefore, we can avoid time-expansive and costly lab measurements.

The analysis of the simulated load cycles shows clear dependencies of the performed task. Among other parameters, the movement speed has a strong influence on the load cycle. In addition, a clear difference is apparent by scaling the human model. Here, in the case of the same movement and load, the force difference between the 5th percentile woman and the 95th percentile man was simulated to 46% related to F05.

Based on these generated forces, a reference elbow power unit was adapted by using the electrical machine scaling model, introduced here in order to meet the exact requirements of the user. The model varies geometrical parameters of the electrical machine to fit the requirements in torque, mass and acceleration. Commercially available motors are not suitable in terms of construction space and power class. Ill-fitting motors cause an oversizing of the power unit, which will lead to additional weight. The typical power density in exoskeleton electrical machines is at 200–300 W/kg. An off-the-shelf motor that meets the performance characteristics introduced here is given a motor weight of 850 g [47]. This is more than five times the weight of the presented reference motor in this journal. Further, the construction space fits in the outer diameter but the axial length of the commercial motor is three times higher, which does not fit in the construction space. Off-the-shelf motors are often limited in scaling and only configurable via a modular system, which is realized by adjusting the active length or the number of windings. The double-sided axial flux machine introduced here, in combination with the additive manufacturing, is easily adaptable to the individual user needs. This scaling leads to a smaller motor weight that saves up to 30% compared to the reference motor. In summary, it can be stated that the scaling presented here enables a significant improvement for the personalization of the electrical machine.

The biomechanical and analytical motor model were validated through experimental data, separately. The measurements used for the biomechanical model are presented in previous investigations [21]. The analytical motor model was validated by a prototype and measurements in this journal. The deviation between the calculation and measurements is below 3.2%, which shows a good suitability of the model. Combined experiments are planned in future research. For a collaborative validation of the approach, a comprehensive ergonomics study with several people wearing a reference exoskeleton on the one hand and a personalized exoskeleton on the other hand is necessary. In this way, objective results on the suitability of the approach can be obtained. These experiments can be realized in future projects.

In addition, the convergence of the biomechanical simulation was used to show which loads can be performed by specific groups of people. Here, it could be observed that the F05 person could not handle as large loads as the M50 or M95 person. This is due to the restricted muscle forces in the model. Thus, in future research, it would be interesting to create a closed coupling between a human and electromechanical model in order to handle heavier loads. Further, human movements can reach speeds of up to 0.2 s for am elbow flexion of 90 degrees. The simulation shows that the actual power unit is not able to support those movement speeds. In ongoing research, the power unit is optimized for such scenarios.

In summary, it is evident that the drive design is improved by the framework presented here and that a lighter design of the exo power unit is possible under consideration of the individual needs of the user and demands of the task.

Supplementary Materials: The following supporting information can be downloaded at: https://www.mdpi.com/article/10.3390/robotics11050107/s1.

Author Contributions: Methodology, software and validation, M.W., I.W., K.S.; supervision and discussion, M.W., I.W., K.S., N.P. and S.S. All authors have read and agreed to the published version of the manuscript.

Funding: The research leading to this publication has received funding from the High-Performance Center Mass Personalization in Stuttgart (https://www.masspersonalization.de/, accessed on 24 August 2022), which was supported by the Ministry of Science, Research and the Arts Baden-Württemberg [Az: 32-7542.2-500/55/3]. Further I. Wochner and S. Schmitt were funded by Deutsche Forschungsgemeinschaft (DFG, German Research Foundation) under Germany's Excellence Strategy—EXC 2075—390740016. We acknowledge the support by the Stuttgart Center for Simulation Science (SimTech).

Conflicts of Interest: The authors declare no conflict of interest.

Abbreviations

The following abbreviations are used in this manuscript:

AFM	Axial Flux Machine
EM	Electrical Machine
EMG	Muscle Surface Electromyogram
exo	Exoskeleton
FEM	Finite Element Method
HD	Harmonic Drive Gear
LC	Load Cycle
PCSA	Physiological Cross-sectional Area
PU	Power Unit
RFM	Radial Flux Machine

Appendix A. Flexion Movement Load Cycles

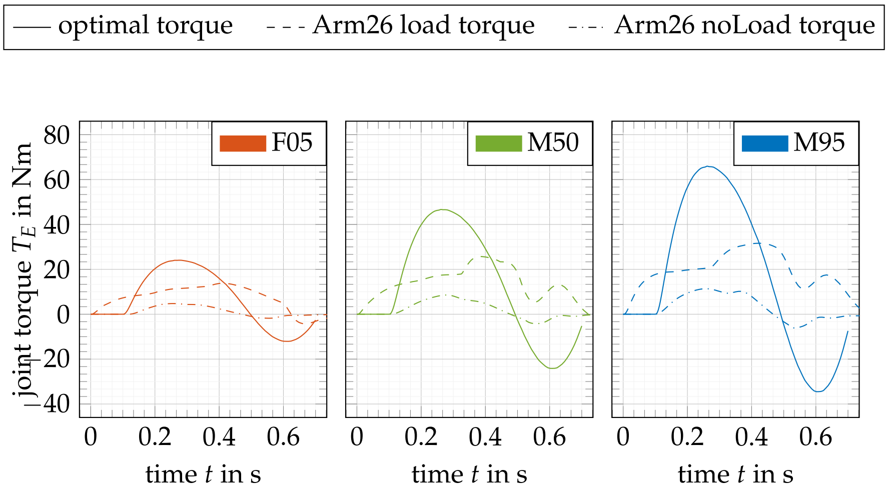

Figure A1. Load profiles for all 3 individuals for $m = 100\%$ arm weight and case E.

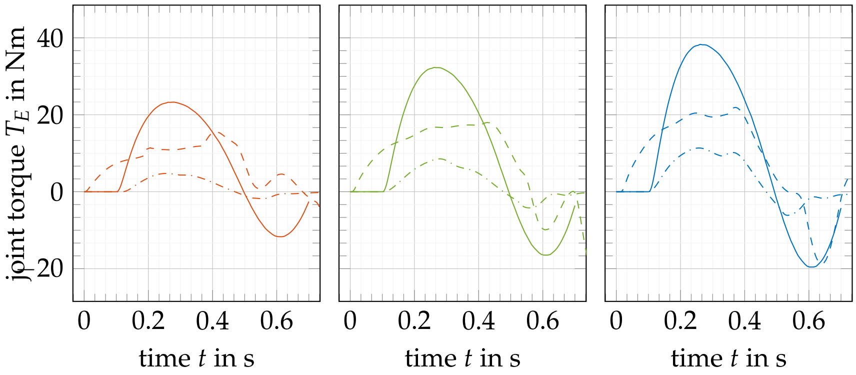

Figure A2. Load profiles for all 3 individuals for $m = 2.5$ kg and case E.

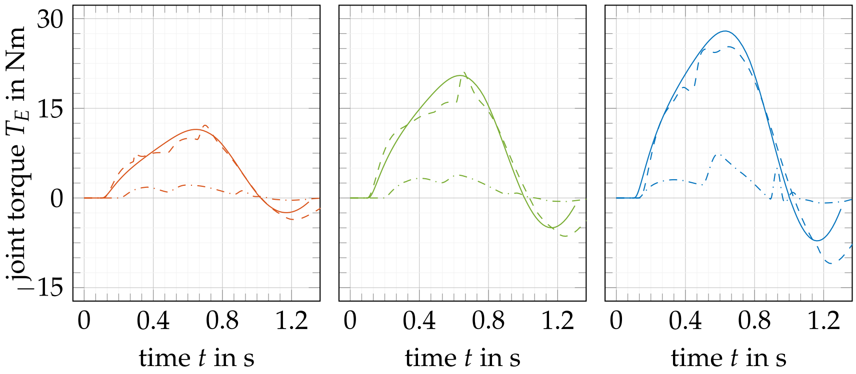

Figure A3. Load profiles for all 3 individuals for $m = 100\%$ arm weight and case A.

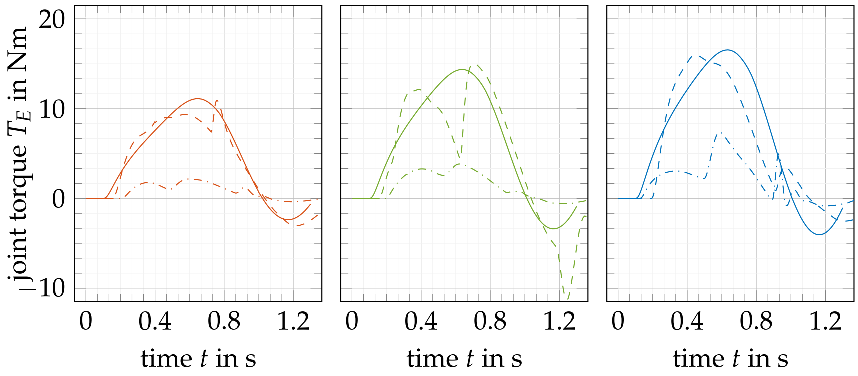

Figure A4. Load profiles for all 3 individuals for $m = 2.5$ kg and case A.

References

1. Sylla, N.; Bonnet, V.; Colledani, F.; Fraisse, P. Ergonomic contribution of ABLE exoskeleton in automotive industry. *Int. J. Ind. Ergon.* **2014**, *44*, 475–481. [CrossRef]
2. van Engelhoven, L.; Poon, N.; Kazerooni, H.; Barr, A.; Rempel, D.; Harris-Adamson, C. Evaluation of an adjustable support shoulder exoskeleton on static and dynamic overhead tasks. *Proc. Hum. Factors Ergon. Soc. Annu. Meet.* **2018**, *62*, 804–808. [CrossRef]
3. Smets, M. A Field Evaluation of Arm-Support Exoskeletons for Overhead Work Applications in Automotive Assembly. *IISE Trans. Occup. Ergon. Hum. Factors* **2019**, *7*, 192–198. [CrossRef]
4. Gull, M.A.; Bai, S.; Bak, T. A review on design of upper limb exoskeletons. *Robotics* **2020**, *9*, 16. [CrossRef]
5. Shao, Z.F.; Tang, X.; Yi, W. Optimal design of a 3-DOF cable-driven upper arm exoskeleton. *Adv. Mech. Eng.* **2014**, *6*, 157096. [CrossRef]
6. Zhou, L.; Li, Y.; Bai, S. A human-centered design optimization approach for robotic exoskeletons through biomechanical simulation. *Robot. Auton. Syst.* **2017**, *91*, 337–347. [CrossRef]
7. Zoss, A.; Kazerooni, H. Design of an electrically actuated lower extremity exoskeleton. *Adv. Robot.* **2006**, *20*, 967–988. [CrossRef]
8. Toxiri, S.; Calanca, A.; Poliero, T.; Caldwell, D.G.; Ortiz, J. Actuation Requirements for Assistive Exoskeletons: Exploiting Knowledge of Task Dynamics. In *Wearable Robotics: Challenges and Trends*; Biosystems & Biorobotics; Carrozza, M.C., Micera, S., Pons, J.L., Eds.; Springer: Cham, Switzerland, 2019; Volume 22, pp. 381–385. [CrossRef]
9. Calanca, A.; Toxiri, S.; Costanzi, D.; Sartori, E.; Vicario, R.; Poliero, T.; Di Natali, C.; Caldwell, D.G.; Fiorini, P.; Ortiz, J. Actuation Selection for Assistive Exoskeletons: Matching Capabilities to Task Requirements. *IEEE Trans. Neural Syst. Rehabil. Eng. A Publ. IEEE Eng. Med. Biol. Soc.* **2020**, *28*, 2053–2062. [CrossRef]
10. Pries, J.; Hofmann, H. Magnetic and thermal scaling of electric machines. *Int. J. Veh. Des.* **2013**, *61*, 219. [CrossRef]
11. Hsieh, K.T.; Kim, B.K. One kind of scaling relations on electromechanical systems. *IEEE Trans. Magn.* **1997**, *33*, 240–244. [CrossRef]
12. Zhou, K.; Ivanco, A.; Filipi, Z.; Hofmann, H. Finite-Element-Based Computationally Efficient Scalable Electric Machine Model Suitable for Electrified Powertrain Simulation and Optimization. *IEEE Trans. Ind. Appl.* **2015**, *51*, 4435–4445. [CrossRef]
13. Stipetic, S.; Zarko, D.; Popescu, M. Scaling laws for synchronous permanent magnet machines. In Proceedings of the 2015 Tenth International Conference on Ecological Vehicles and Renewable Energies (EVER), Monte Carlo, Monaco, 31 March–2 April 2015; IEEE: Piscataway, NJ, USA, 2015; pp. 1–7. [CrossRef]
14. Seok, S.; Wang, A.; Otten, D.; Kim, S. Actuator design for high force proprioceptive control in fast legged locomotion. In Proceedings of the 2012 IEEE/RSJ International Conference on Intelligent Robots and Systems, Vilamoura-Algarve, Portugal, 7–12 October 2012; IEEE: Piscataway, NJ, USA, 2012. [CrossRef]
15. Wrobel, R.; Mecrow, B. Additive Manufacturing in Construction of Electrical Machines—A Review. In Proceedings of the 2019 IEEE Workshop on Electrical Machines Design, Control and Diagnosis (WEMDCD), Athens, Greece, 22–23 April 2019; Volume 1, pp. 15–22. [CrossRef]
16. Tiismus, H.; Kallaste, A.; Vaimann, T.; Rassolkin, A.; Belahcen, A. Technologies for Additive Manufacturing of Electrical Machines. In Proceedings of the 2019 20th International Conference of Young Specialists on Micro/Nanotechnologies and Electron Devices (EDM), Erlagol, Russia, 29 June–3 July 2019; pp. 651–655. [CrossRef]
17. Kallaste, A.; Vaimann, T.; Rassalkin, A. Additive Design Possibilities of Electrical Machines. In Proceedings of the 2018 IEEE 59th International Scientific Conference on Power and Electrical Engineering of Riga Technical University (RTUCON), Riga, Latvia, 12–13 November 2018; pp. 1–5. [CrossRef]
18. Huang, J.; Huo, W.; Xu, W.; Mohammed, S.; Amirat, Y. Control of Upper-Limb Power-Assist Exoskeleton Using a Human-Robot Interface Based on Motion Intention Recognition. *IEEE Trans. Autom. Sci. Eng.* **2015**, *12*, 1257–1270. [CrossRef]
19. Yamasaki, H.; Tagami, Y.; Fujisawa, H.; Hoshi, F.; Nagasaki, H. Interaction torque contributes to planar reaching at slow speed. *Biomed. Eng. Online* **2008**, *7*, 27. [CrossRef]
20. Wang, C.; Xiao, Y.; Burdet, E.; Gordon, J.; Schweighofer, N. The duration of reaching movement is longer than predicted by minimum variance. *J. Neurophysiol.* **2016**, *116*, 2342–2345. [CrossRef]

21. Stollenmaier, K.; Ilg, W.; Haeufle, D.F.B. Predicting Perturbed Human Arm Movements in a Neuro-Musculoskeletal Model to Investigate the Muscular Force Response. *Front. Bioeng. Biotechnol.* **2020**, *8*, 308. [CrossRef]
22. Günther, M.; Schmitt, S.; Wank, V. High-frequency oscillations as a consequence of neglected serial damping in Hill-type muscle models. *Biol. Cybern.* **2007**, *97*, 63–79. [CrossRef]
23. Haeufle, D.; Günther, M.; Bayer, A.; Schmitt, S. Hill-type muscle model with serial damping and eccentric force-velocity relation. *J. Biomech.* **2014**, *47*, 1531–1536. [CrossRef]
24. Hammer, M.; Günther, M.; Haeufle, D.; Schmitt, S. Tailoring anatomical muscle paths: A sheath-like solution for muscle routing in musculoskeletal computer models. *Math. Biosci.* **2019**, *311*, 68–81. [CrossRef] [PubMed]
25. Hatze, H. A myocybernetic control model of skeletal muscle. *Biol. Cybern.* **1977**, *25*, 103–119. [CrossRef]
26. Pankoke, S.; Siefert, A. *Virtual Simulation of Static and Dynamic Seating Comfort in the Development Process of Automobiles and Automotive Seats: Application of Finite-Element-Occupant-Model CASIMIR*; SAE International: Warrendale, PA, USA, 2007. [CrossRef]
27. Decker, W.; Koya, B.; Pak, W.; Untaroiu, C.D.; Gayzik, F.S. Evaluation of finite element human body models for use in a standardized protocol for pedestrian safety assessment. *Traffic Inj. Prev.* **2019**, *20*, S32–S36. [CrossRef]
28. Pak, W. Development and Validation of Human Body Finite Element Models for Pedestrian Protection. Ph.D. Thesis, Virginia Tech, Blacksburg, VA, USA, 2019.
29. DIN e.V. (publ.) (DIN 33402-2:2005-12, 2005): Ergonomics—Human Body Dimensions, Part 2: Values. 2005. Available online: https://www.beuth.de/en/standard/din-33402-2/84092742 (accessed on 24 August 2022).
30. Winter, D.A. *Biomechanics and Motor Control of Human Movement*; John Wiley & Sons: Hoboken, NJ, USA, 2009.
31. Handsfield, G.G.; Meyer, C.H.; Hart, J.M.; Abel, M.F.; Blemker, S.S. Relationships of 35 lower limb muscles to height and body mass quantified using MRI. *J. Biomech.* **2014**, *47*, 631–638. [CrossRef] [PubMed]
32. Flash, T.; Hogan, N. The coordination of arm movements: An experimentally confirmed mathematical model. *J. Neurosci.* **1985**, *5*, 1688–1703. [CrossRef] [PubMed]
33. Stollenmaier, K.; Rist, I.S.; Izzi, F.; Haeufle, D.F. Simulating the response of a neuro-musculoskeletal model to assistive forces: Implications for the design of wearables compensating for motor control deficits. In Proceedings of the 2020 8th IEEE RAS/EMBS International Conference for Biomedical Robotics and Biomechatronics (BioRob), New York, NY, USA, 29 November–1 December 2020; IEEE: Piscataway, NJ, USA, 2020; pp. 779–784.
34. Wierzbicka, M.M.; Wiegner, A.W.; Shahani, B.T. Role of agonist and antagonist muscles in fast arm movements in man. *Exp. Brain Res.* **1986**, *63*, 331–340. [CrossRef] [PubMed]
35. Kistemaker, D.A.; Van Soest, A.K.J.; Bobbert, M.F. Is equilibrium point control feasible for fast goal-directed single-joint movements? *J. Neurophysiol.* **2006**, *95*, 2898–2912. [CrossRef]
36. Gunther, S.; Ulbrich, S.; Hofmann, W. Driving cycle-based design optimization of interior permanent magnet synchronous motor drives for electric vehicle application. In Proceedings of the International Symposium on Power Electronics, Electrical Drives, Automation and Motion (SPEEDAM), Ischia, Italy, 18–20 June 2014; IEEE: Piscataway, NJ, USA, 2014; pp. 25–30. [CrossRef]
37. Salameh, M.; Brown, I.P.; Krishnamurthy, M. Fundamental Evaluation of Data Clustering Approaches for Driving Cycle-Based Machine Design Optimization. *IEEE Trans. Transp. Electrif.* **2019**, *5*, 1395–1405. [CrossRef]
38. Selim, S.Z.; Ismail, M.A. K-means-type algorithms: A generalized convergence theorem and characterization of local optimality. *IEEE Trans. Pattern Anal. Mach. Intell.* **1984**, *6*, 81–87. [CrossRef]
39. Waldhof, M.; Echle, A.; Parspour, N. A Novel Drive Train Concept for Personalized Upper Body Exoskeletons with a Multiphase Axial Flux Machine. In Proceedings of the 2019 IEEE International Electric Machines & Drives Conference (IEMDC), San Diego, CA, USA, 12–15 May 2019; IEEE: Piscataway, NJ, USA, 2019; pp. 2160–2166. [CrossRef]
40. Keller, M.; Müller, S.; Parspour, N. Design of a transverse flux machine as joint drive for an articulated six-axis robot arm. In Proceedings of the 2016 International Symposium on Power Electronics, Electrical Drives, Automation and Motion (SPEEDAM), Capri, Italy, 22–24 June 2016; pp. 849–854. [CrossRef]
41. Bartlett, H.L.; Lawson, B.E.; Goldfarb, M. Optimal Transmission Ratio Selection for Electric Motor Driven Actuators With Known Output Torque and Motion Trajectories. *J. Dyn. Syst. Meas. Control* **2017**, *139*, 43. [CrossRef]
42. Hanselman, D.C. *Brushless Permanent-Magnet Motor Design*; McGraw-Hill: New York, NY, USA, 1994.
43. Gieras, J.F.; Wang, R.J.; Kamper, M.J. *Axial Flux Permanent Magnet Brushless Machines*, 2nd ed.; Springer: New York, NY, USA, 2008.
44. Kamper, M.J.; Wang, R.J.; Rossouw, F.G. Analysis and Performance of Axial Flux Permanent-Magnet Machine with Air-Cored Nonoverlapping Concentrated Stator Windings. *IEEE Trans. Ind. Appl.* **2008**, *44*, 1495–1504. [CrossRef]
45. Rosu, M.; Zhou, P.; Lin, D.; Ionel, D.M.; Popescu, M.; Blaabjerg, F.; Rallabandi, V.; Staton, D. *Multiphysics Simulation by Design for Electrical Machines, Power Electronics and Drives*; IEEE Press Series on Power Engineering; Wiley: Hoboken, NJ, USA, 2018; Volume 66.
46. Waldhof, M.; Parspour, N. Torque Ripple Minimization in Exoskeleton Drives with Multiphase Electrical Machines by Current Harmonic Injection. In Proceedings of the 2020 International Conference on Electrical Machines (ICEM), Gothenburg, Sweden, 23–26 August 2020; Volume 1, pp. 2152–2158. [CrossRef]
47. Maxon-Motor-GmbH. Available online: https://www.maxongroup.de/maxon/view/category/motor?etcc_cu=onsite&etcc_med_onsite=Product&etcc_cmp_onsite=ECXSPEEDProgramm&etcc_plc=Overview-Page-brushless-DC-Motors&etcc_var=[de]#de#_d_&target=filter&filterCategory=ECX (accessed on 21 March 2022).

III. Contribution 3: Falling Heads: investigating reflexive responses to head-neck perturbations

Wochner *et al. BioMedical Engineering OnLine* (2022) 21:25
https://doi.org/10.1186/s12938-022-00994-9

BioMedical Engineering
OnLine

RESEARCH Open Access

'Falling heads': investigating reflexive responses to head–neck perturbations

Isabell Wochner*, Lennart V. Nölle, Oleksandr V. Martynenko and Syn Schmitt

*Correspondence: isabell.wochner@simtech.uni-stuttgart.de
Institute for Modelling and Simulation of Biomechanical Systems, Stuttgart Center for Simulation Science, University of Stuttgart, Stuttgart, Germany

Abstract

Background: Reflexive responses to head–neck perturbations affect the injury risk in many different situations ranging from sports-related impact to car accident scenarios. Although several experiments have been conducted to investigate these head–neck responses to various perturbations, it is still unclear why and how individuals react differently and what the implications of these different responses across subjects on the potential injuries might be. Therefore, we see a need for both experimental data and biophysically valid computational Human Body Models with bio-inspired muscle control strategies to understand individual reflex responses better.

Methods: To address this issue, we conducted perturbation experiments of the head–neck complex and used this data to examine control strategies in a simulation model. In the experiments, which we call 'falling heads' experiments, volunteers were placed in a supine and a prone position on a table with an additional trapdoor supporting the head. This trapdoor was suddenly released, leading to a free-fall movement of the head until reflexive responses of muscles stopped the downwards movement.

Results: We analysed the kinematic, neuronal and dynamic responses for all individuals and show their differences for separate age and sex groups. We show that these results can be used to validate two simple reflex controllers which are able to predict human biophysical movement and modulate the response necessary to represent a large variability of participants.

Conclusions: We present characteristic parameters such as joint stiffness, peak accelerations and latency times. Based on this data, we show that there is a large difference in the individual reflexive responses between participants. Furthermore, we show that the perturbation direction (supine vs. prone) significantly influences the measured kinematic quantities. Finally, 'falling heads' experiments data are provided open-source to be used as a benchmark test to compare different muscle control strategies and to validate existing active Human Body Models directly.

Keywords: Reflex behaviour, Head–neck perturbations, Motor control, Musculoskeletal model, 3D finite element modelling, Muscle modelling

Background

Head and neck injuries, such as traumatic brain injuries, concussions and whiplash-associated disorders, can occur in a multitude of scenarios varying from traffic accidents and physical assaults to sports and recreation-related collisions. The main point they have in common is that they are induced by biomechanical forces such as contact or inertial forces that are transmitted to the brain, head or upper body. The resulting injuries are widely recognized as a significant public health concern [3, 61]. Hence, it is critical to identify individual risk factors for such injuries to understand the causes and develop injury prevention strategies.

Previous studies investigating head–neck responses to perturbations conducted experiments with different methodological setups, including load dropping, release and direct impacts to the head–neck complex [29, 42, 47, 56, 67, 72]. One of these methods, the release experiment, was proposed by Ito et al. [29, 30]. They introduced this new technique for studying responses in neck muscles by exposing the head to a sudden onset of a free fall under its own weight. Using this method, they compared normal and labyrinthine-defective subjects in the supine position (extension of the head) and demonstrated that reflex responses contribute significantly to head-righting. Investigations of another research group by Portero et al. [54–56] examined the response to a similar release experiment, including preloads in both flexion and extension positions. They focused on assessing the musculotendinous stiffness of the head–neck segment but only in the first 30 ms after the acceleration peak to avoid altered kinematics due to reflexive contributions. For a general overview of experimental studies with regard to head–neck perturbations, we refer to the systematic review of Le Flao et al. [42]. As a conclusion, they requested future studies to include neck muscle latency [ms], neck stiffness [Nm/rad], linear accelerations [g] and rotational head accelerations [rad/s^2] due to their potential use in assessing concussion risks.

These concussion risks are related to linear and rotational head accelerations as prevailing injury theories provided in literature [19, 60, 81] suggest. However, the magnitude of force needed to cause these injuries cannot be studied in ethically justifiable experiments. Computer simulations using musculoskeletal models provide an alternative assessment tool, additionally used in this study.

These simulations allow us to estimate the forces and moments within the body, while varying muscle activations and control strategies. To ensure that the predicted response during simulation studies using biomechanical models is biophysically valid, both correct muscle modelling, as well as bio-inspired control strategies, are crucial. Several studies [26, 57, 66] state that the muscles' reaction alters the head kinematics and therefore, the influence of cervical muscles and their control strategy on the head–neck response can be significant.

In this contribution, we want to study this influence by presenting the results of 'falling heads' experiments in a supine and prone position to investigate the individual responses to head–neck perturbations. Additionally, we mimicked this experimental setup in numerical simulations. Based on these setups, we quantify the kinematic, dynamic and neuronal response to head–neck perturbations and pose the question of how human diversity (such as biological sex and age) affects these quantities. Furthermore, we use the numerical model to answer the question whether and how the biomechanical response is affected by changes of the neuronal state (e.g. sensitivity to the stretching of the muscle).

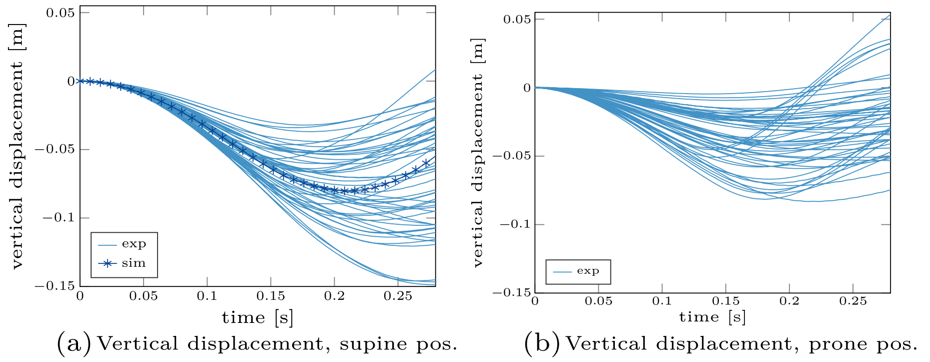

Fig. 1 Vertical displacement of 'falling heads' experiment. The vertical displacement of the supine (**a**) and prone (**b**) position is shown for all participants and all trials (light blue solid lines). For the supine case, we additionally show the simulation trajectory (as dark blue line with asterisks)

The purpose of this study is to give insights in understanding individual head–neck responses to perturbations and to provide a comprehensive data set as open-source[1] which can be directly used as a benchmark setup to compare and validate different models and controllers. The novelty of our work is twofold: first, we use a similar 'falling heads' setup as proposed by Ito et al. [29, 30] but with two different force directions (flexion and extension) and for a larger number of healthy participants with different ages and sexes. Second, we build up a numerical model with the same setup and compare potential muscle reflex controller strategies to experimental findings.

Results

Kinematic, neuronal and dynamic characteristics of the reflex response

In this section, we present the main results in a condensed form. First, vertical displacement curves of all participants extracted from the video data are shown in Fig. 1. Additionally, the simulation curve for the supine case is given in Fig. 1a as a comparison value. Three things can be noted from the presented results: first, the range of the maximal falling height varies between participants (in the range between 3.2–14.9 cm for the supine case). Second, the participants tend to fall less in the prone case (range between 0.5–8.3 cm, Fig. 1b) compared to the supine case. This difference is significant ($p < 0.01$), for a detailed overview of the statistical analysis we refer to Additional file 1: Table E3 the supplementary material E. Third, the simulated supine experiment shows a good agreement with the experiments with regard to the displacement and can predict similar head-fall kinematics in terms of both the maximum displacement as well as the general slope and timing.

The difference between peak displacements in the supine and the prone cases shows a similar trend for the peak accelerations and time to peak accelerations. An overview of all mean and standard deviations for the peak accelerations is given in Table 1. Both, the linear peak acceleration and the time to linear peak acceleration are higher in the supine compared to the prone case ($p < 0.01$). These values are comparable to literature values

---

[1] The dataset for the electromyographic (EMG) data is available at https://doi.org/10.18419/darus-1038 and the dataset for the kinematic trajectories can be found at https://doi.org/10.18419/darus-1132.

Table 1 Peak accelerations (given as mean ± standard deviation)

	Supine	Prone
Peak lin. acc.	-0.7 ± 0.1 g	-0.5 ± 0.2 g
Time to peak lin. acc.	44.0 ± 3.5 ms	36.4 ± 2.5 ms
Peak rot. acc.	62.4 ± 11.5 rad/s^2	44.0 ± 18.2 rad/s^2
Time to peak rot. acc.	52.1 ± 10.1 ms	57.8 ± 12.1 ms

Table 2 EMG latency times (given as mean ± standard deviation)

	Supine	Prone
SCM	33.4 ± 17.6 ms	31.5 ± 12.1 ms
Trapezius	49.0 ± 19.7 ms	43.8 ± 13.5 ms

of similar experiments, e.g. Ito et al. [29, 30] who reported linear mean peak acceleration values of 0.76–1.2 g for the supine case (for the healthy participants). The same tendency of greater peak acceleration in the supine case can also be seen for the rotational accelerations ($p < 0.01$). The same increase between peak accelerations during forced flexion (prone case) and forced extension (supine case) is also reported in the literature [47, 72]. They report smaller absolute values (in the range of 12.8–36.2 rad/s^2); however, they also had smaller flexion and extension angles due to a different experimental setup.

These kinematic characteristics are partly influenced by the latency time of the muscles contributing to reflexive behaviour in response to the perturbation. The mean and standard deviations for the detected EMG onset for both muscles (*SCM* and *trapezius*) are given in Table 2. The range of latency times in this study was 17.67–86.67 ms which is comparable to previously reported values of 18.6–88.0 ms for quick-release or load-dropping studies [7, 14, 29, 30, 47, 63, 72]. Furthermore, it can be noted that the *SCM* is activated faster than the *trapezius* in both cases which is also reported in Corna et al. [7], Ito et al. [30].

The effective stiffness represents the combination of these kinematic and neuronal reflex responses. We show this stiffness plotted over the change of torque in Fig. 2. The absolute values are comparable to previous studies which reported 22 Nm/rad [67] or a range between 22.6–41.3 Nm/rad [72]. Furthermore, we see an increase of the effective stiffness for an increase in torque as also supported by Portero et al. [55, 56].

Age and sex differences

Typically, age and sex are investigated as covariates influencing the dynamic response to head and neck perturbations. Hence, we present the experimental results split up into three age groups and two sexes in the following.

The differences for these covariates for the vertical displacement curves are shown in Fig. 3. The panels on the left (Fig. 3a, c) show the trajectories for the different sexes with different colours, the panels on the right (Fig. 3b, d) the ones for the age groups, respectively. Based on these results, we can note two things: first, male participants fall a shorter distance than female participants in the supine position. In the prone position, this behaviour is reversed (not significant, ($p = 0.07$). A detailed overview of the statistical analysis is given in Additional file 1: Table E4 regarding the covariate sex and

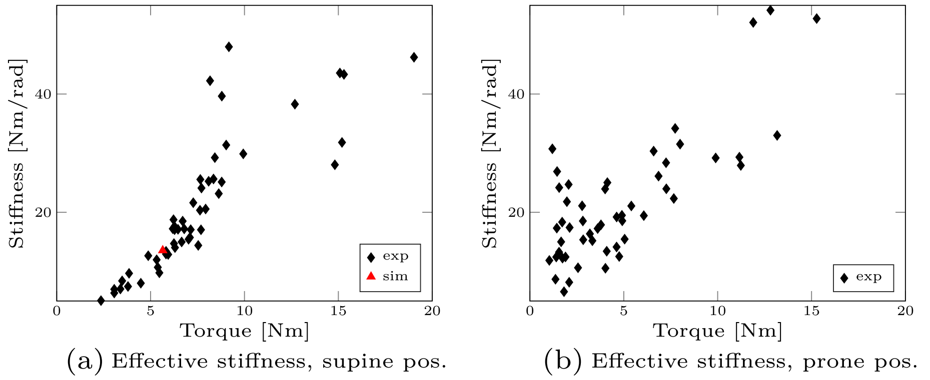

(a) Effective stiffness, supine pos. (b) Effective stiffness, prone pos.

Fig. 2 Effective stiffness. The effective stiffness of the supine position (**a**) and the prone position (**b**) is shown for all participants and all trials (black diamonds). For the supine case, we additionally show the simulation value (red triangle)

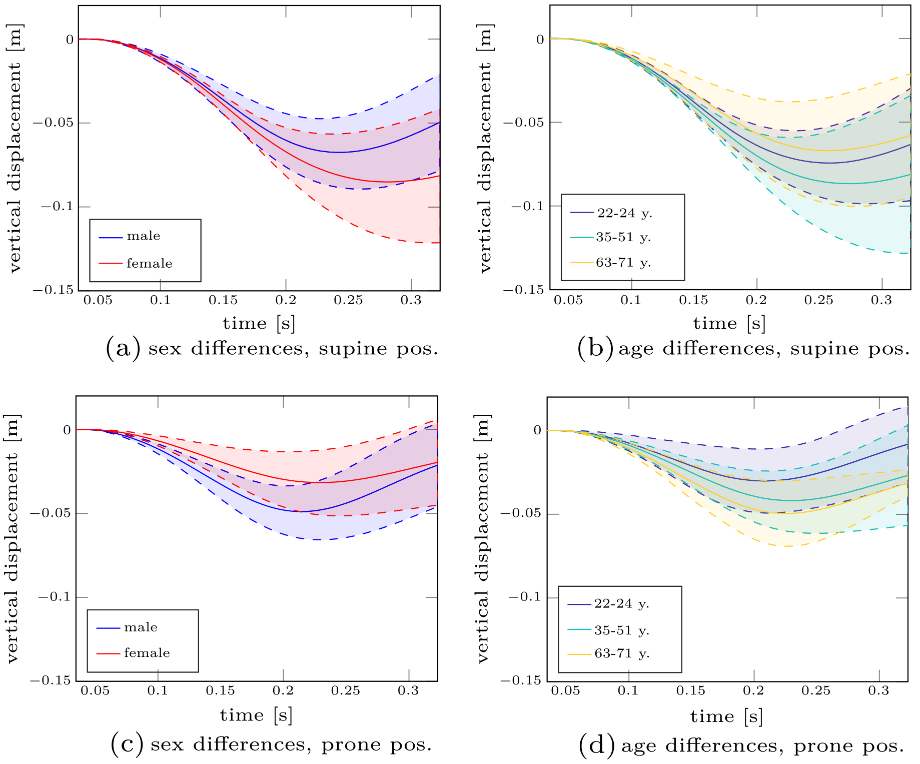

(a) sex differences, supine pos. (b) age differences, supine pos.

(c) sex differences, prone pos. (d) age differences, prone pos.

Fig. 3 Differences in vertical displacement for different ages and sexes. Experimental vertical displacement trajectories for both the supine (**a**, **b**) and the prone position (**c**, **d**) are shown. The differences of age and sex are highlighted with different colours

Additional file 1: Table E5 regarding the covariate age in the supplementary material E). Second, in the supine position, elderly (63–71 years) people fall less strongly compared to younger people, in the prone position, this behaviour is also reversed.

We can observe similar trends dependent on the force direction for the peak acceleration values. An overview of all acceleration values split up into different sex and age groups is given in Table 3. Two main points can be emphasized here: first, for the elderly

Table 3 Subgroup-specific peak accelerations (given as mean ± standard deviation)

	Age groups			**Sex**	
	22–24 years	**36–51 years**	**63–71 years**	**Male**	**Female**
Peak lin. acc., supine	− 0.75 ± 0.1 g	0.79 ± 0.1 g	− 0.66 ± 0.2 g	− 0.71 ± 0.2 g	− 0.77 ± 0.1 g
Time to peak lin. acc., supine	45.8 ± 2.5 ms	43.6 ± 2.9 ms	41.4 ± 2.7 ms	42.2 ± 2.9 ms	45.2 ± 2.7 ms
Peak rot. acc., supine	67.7 ± 6.0 rad/s^2	64.3 ± 5.6 rad/s^2	50.3 ± 13.8 rad/s^2	57.2 ± 13.5 rad/s^2	66.0 ± 6.2 rad/s^2
Time to peak rot. acc., supine	52.7 ± 7.6 ms	53.7 ± 13.7 ms	48.8 ± 4.4 ms	49.3 ± 5.9 ms	54.1 ± 11.2 ms
Peak lin. acc., prone	− 0.43 ± 0.3 g	− 0.51 ± 0.2 g	− 0.62 ± 0.2 g	− 0.65 ± 0.2 g	− 0.40 ± 0.2 g
Time to peak lin. acc., prone	36.7 ± 1.9 ms	35.6 ± 2.1 ms	37.0 ± 2.2 ms	36.4 ± 2.6 ms	36.4 ± 1.7 ms
Peak rot. acc., prone	38.7 ± 20.2 rad/s^2	43.5 ± 13.7 rad/s^2	53.0 ± 17.4 rad/s^2	54.7 ± 14.5 rad/s^2	36.1 ± 15.3 rad/s^2
Time to peak rot. acc., prone	54.0 ± 10.3 ms	63.8 ± 6.1 ms	55.6 ± 12.7 ms	58.5 ± 9.9 ms	57.4 ± 10.8 ms

people both the peak linear and the peak rotational acceleration, as well as the time to peak acceleration, have the smallest value in the supine case. However, this behaviour is reversed in the prone case. Here, both the peak linear and rotational accelerations have the highest values compared to the other age groups. Second, the exact opposite applies to the women participating in this study compared to the male participants. The peak linear and rotational acceleration, as well as the time to peak, is higher in the supine case. In contrast to this, the peak linear and rotational acceleration of female participants is smaller compared to male participants in the prone case.

In contrast to this force-directional dependency, the latency times (the difference between the perturbation and muscle onset) show similar trends for both force directions. They are shown as bar plots in Fig. 4 where the mean value is shown as a red square and the standard deviation as black bars. Based on the age and sex subgroups, we can see that elderly people have higher latency times (mean value is 1.3–2.2 times higher compared to the 36–51 years old, significant for SCM ($p < 0.05$)). Further, we can state that men seem to have higher latency times than women. Even though there might be a slight bias (only men were in the oldest age group), these findings are in accordance with the literature [14, 72].

In-depth force analysis

As a result of calculating the inverse dynamics, we show the calculated net moment M_{net} plotted over the angular displacement for a representative participant (participant 4) in Fig. 5. The three different curves correspond to the separate trials. It can be seen that

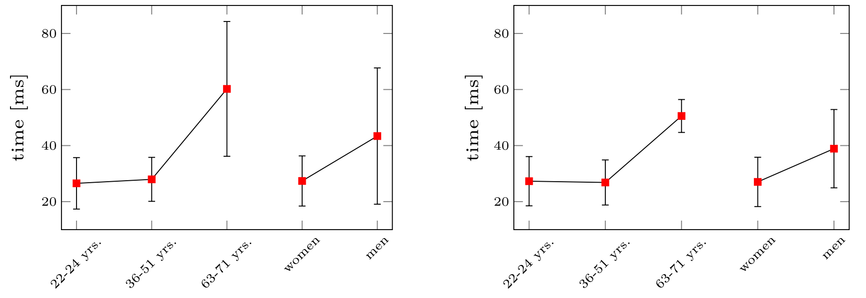

(a) Latency times for SCM, supine pos. (b) Latency times for SCM, prone pos.

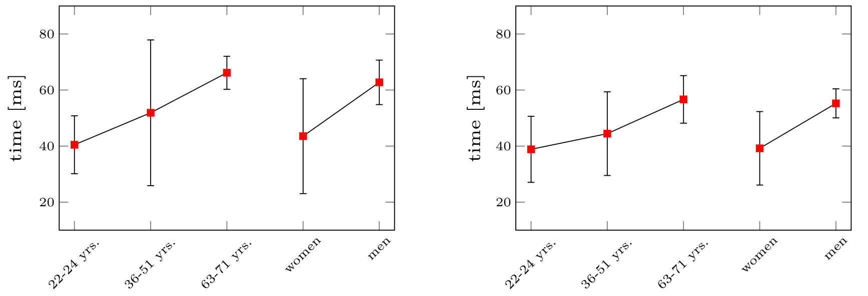

(c) Latency times for *trapezius*, supine pos. (d) Latency times for *trapezius*, prone pos.

Fig. 4 Experimental latency times. The latency times for the *SCM* and *trapezius* muscles in both the supine (**a**, **c**) and prone position (**b**, **d**) are shown. The mean and standard deviation were calculated for different age and sex groups

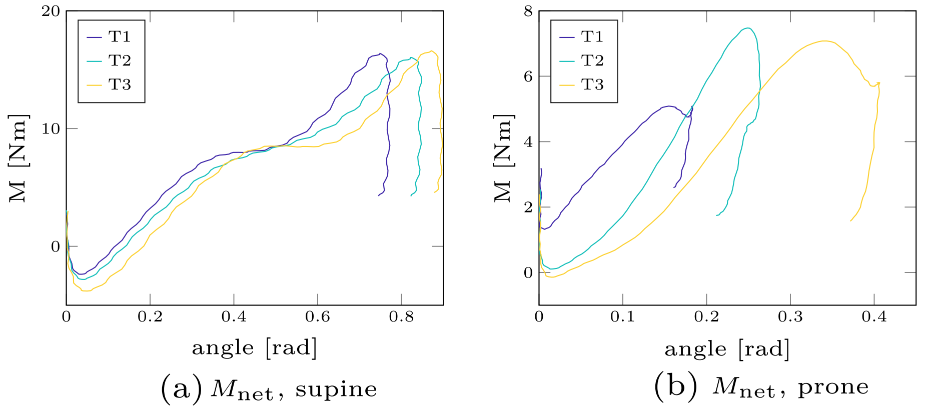

(a) M_{net}, supine (b) M_{net}, prone

Fig. 5 Experimental net moment. The net moment M_{net} plotted over the angle is shown here for a representative participant (participant 4), in both experiments (supine and prone position). The different colours represent the three separate trials

the slope is almost linear in the beginning, which is comparable to previous studies [54–56]. Furthermore, we see a hysteresis at the end of the torque–displacement curve in our experiments: the torque increases at first for increasing angular displacement, then reaches a maximum torque and displacement value and then gets smaller for decreasing displacement. For an overview of all torque–displacement curves for each participant, we refer to the two figures for the supine and prone case in Additional file 1: Supplementary material A. Based on these figures, one can conclude that the overall curve characteristics are similar within participants and especially in between trials.

As a second result, we compare the three different dynamic quantities resulting from Eq. (6) for the experimental as well as the simulated data in Fig. 6. We show the experimental results for participant 17 because both the height and weight have similar values compared to the simulation model. Several points can be noted here: first, the peak force in the vertical direction F_y is more than three times higher than in horizontal direction F_x. Second, both the peak forces as well as the general force curve over time are roughly similar in both experiment and simulation. Finally, the simulation model is able to predict the linear increase of moment over angle in the beginning and has a similar peak moment as in the experiments. There are some discriminable differences between

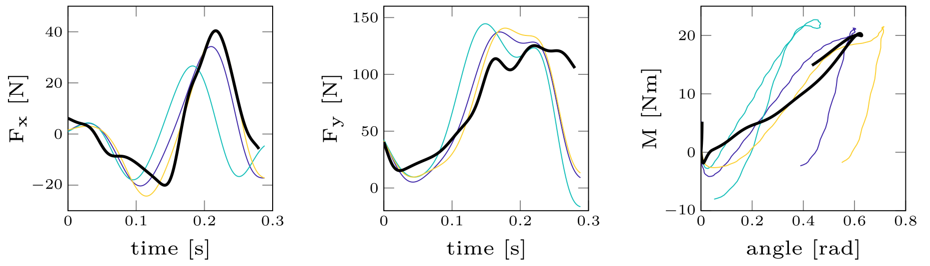

(a) F_x (b) F_y (c) M_{net}

Fig. 6 Dynamic quantities. Comparison of different dynamic quantities for both the experimental results (participant 17, all three trials, displayed in colour) and the simulation result (displayed in black) the simulation and experimental results, e.g. the hysteresis behaviour at the end of the torque–displacement curve where the decrease in torque for a decreasing displacement is less than in the experiments. However, these differences are less pronounced than the observed variations between participants (e.g. as shown in the torque–angle curves in Additional file 1: supplementary material A of all participants).

Controller variation in the simulation

We varied the reflex control parameter ω representing the strain threshold to see how this influences the prediction of human reflexive movement. The results for the vertical and rotational displacement are shown in Fig. 7a, c, respectively. Note, that the vertical displacement of Marker 2 from the experiments corresponds to the head centre of gravity of the model as their position are roughly aligned. Based on the figures, we can see that thresholds ω between $3 - 10\%$ fit the experimental corridor well (standard deviation shown as a grey area). The other thresholds predict trajectories which lie outside the standard deviation, but still show similarities to trajectories of real participants (shown as dashed grey lines). Besides, we see that for smaller reflex thresholds the peak displacement is less pronounced, which in turn reduces both the linear and rotational peak accelerations. Furthermore, we can state that the trajectory predicted using the reflex controller with a threshold of 5% has the smallest L2-error compared to the experimental mean trajectory.

Therefore, we used this threshold for a comparison with the lambda controller and computed comparable k_p values (an exemplary transformation from reflex to lambda control parameters is shown in Additional file 1: supplementary material B). The

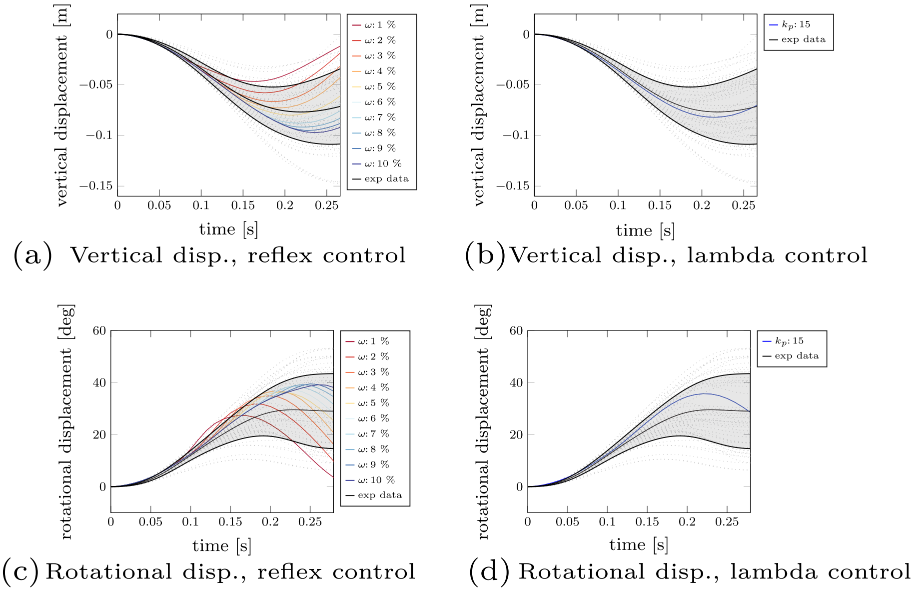

Fig. 7 Results of controller variation. Simulation results showing the vertical and rotational displacement trajectories for both the reflex controller (**a**, **c**) and the lambda controller (**b**, **d**). In comparison to the simulation results (displayed in colour), the mean value of the experimental data is shown with a black solid line, the standard deviation of the experimental data is shown as a grey area and all experimental trajectories are shown as dashed grey lines

predicted vertical and rotational displacements using the lambda controller are shown in Fig. 7b, d. It can be seen that the predicted trajectory is close to the experimental mean trajectory.

Discussion

In this study, we characterized the reflexive response to head–neck perturbations using a 'falling heads' experiment (as shown in Fig. 8). For this purpose, we extracted kinematic (displacements, accelerations), dynamic (stiffness) as well as neuronal (EMG latencies) quantities from the experimental data and compared them both to literature data as well as to our simulation results. We demonstrated that our results fit well with the data found in literature. Furthermore, we showed that a different behaviour for the supine case (extension) compared to the prone case (flexion) is observable: we see less vertical displacement (see Fig. 1), smaller peak accelerations (see Table 1) and a faster response in terms of EMG latency time (see Table 2) in the prone case. The reason for this difference is the muscles' ability to generate a more significant extension moment compared to flexion, as reported in the literature [74]. This larger extension strength over flexion has two main reasons: first, the postural role of extensor musculature and second, the apparent muscle mass difference between posterior and anterior muscles of the cervical spine [32, 71]. This finding might have direct implications for the evaluation of concussion and whiplash-associated-disorder risks because if the force is applied from a different direction (frontal versus back), the peak linear and rotational accelerations values are reduced as shown in Table 1.

Age and/or sex are typically used to cluster people in groups for a more structured discussion of the results of biomechanical studies. In the present study, the comparison of the results, distinguished by age or sex revealed differences (Figs. 3, 4; Table 3), however most of them were *not* statistically significant (see also Additional file 1: Suppl. Material S5). Therefore, we want to stimulate a broader discussion of how to group people according to the mentioned attributes in general. Traditionally, as was done to analyse the data in this contribution, age groups are defined to account for younger, middle-aged and more elderly people, while sex groups separate women and men. This subgrouping inevitably implies the study results to be dependent on the number of days lived since birth or the biological sex. However, we ask whether this is always appropriate? From an ergonomics perspective, grouping along biological sex and age is appropriate, because it can be easily determined and, thus, is a trivial and valid task. It enables to correlate generic characteristics with the respective groups [69]. Correlation of demographic characteristics such as height and weight with, for example, biological sex also holds for our experimental data (see Table 4). Such a correlation even allows to guess, for example, whether sizes of seats or doors fit most people or a special group of people (e.g. elderly, [35]) or how to design work places [28, 59]. Undoubtedly, ageing affects individual system properties, like muscle torque, velocity and power [39]. In this sense, the classical grouping is appropriate. From a biomechanics standpoint, it is key to understand the underlying cause of experimental observations, e.g. forces or torques. In living systems, these forces or torques depend on the current state of the respective system. For example, how often a ligament has been stretched close to its individual failure strain. In this case,

Table 4 Demographic characteristics for participants ($n = 17$), given as mean ± standard deviation

	Age groups			**Sex**	
	22–24 years ($n = 7$)	**36–51 years ($n = 6$)**	**63–71 years ($n = 4$)**	**Male ($n = 7$)**	**Female ($n = 10$)**
Age [years]	22.4 ± 0.8	44.7 ± 6.4	66.5 ± 3.4	51.9 ± 20.7	32.8 ± 11.9
Weights [kg]	65.6 ± 9.5	60.0 ± 11.6	68.5 ± 8.4	72.0 ± 8.6	58.9 ± 7.5
Height [m]	1.70 ± 0.06	1.69 ± 0.08	1.78 ± 0.01	1.78 ± 0.03	1.67 ± 0.03
BMI [kg/m^2]	22.6 ± 3.3	20.9 ± 2.1	21.8 ± 2.8	22.6 ± 2.5	21.3 ± 2.9
Sex [#m, #f]	2 m, 5 f	1 m, 5 f	4 m, 0 f	7 m, 0 f	0 m, 10 f

number of stretches close to failure and *individual failure parameter* are two important values to determine the ligament's state. It might turn out that a neck ligament of a 90-year old man is in the same degenerated state relative to its initial state when this very person was 20 years old—say 90% degenerated, compared to a 60-year-old woman who gave birth to five children. So in this hypothetic example, a grouping into age or biological sex does not seem appropriate to understand causes of potentially different head kinematics. Related research fields such as clinical biomechanics have proposed similar ideas, where they suggested to group cervical spines according to biological age, e.g. [75]. They characterize biological age as degeneration of ligaments among other factors rather than relying on chronological age. Another interesting approach comes from the field of computer vision, where they take body shapes into account to create and scale human body models [44]. This overcomes the need to scale digital human body models solely based on height, weight and biological sex. The advent of these digital human body models allows to generate synthetic compositions of humans. Already five decades ago, three-dimensional, mathematical models of the human body emerged [21]. The core idea of representative segments for which individual body parameters are determined based on data regression remained but was improved over time [9, 11, 76, 80]. There have even been attempts to account for age [24, 31]. It seems now is the right time to start understanding individual contributions of degenerated (aged) and subject-specific body parts on functional characteristics like joint angle progression. Therefore, we would like to encourage research towards finding new concepts to distinguish humans based on causal dependencies of forces and torques around joints and age (degeneration). As we have stated above, this paragraph intends to stimulate the discussion. We see a need to find more appropriate grouping, but unfortunately have no solution yet. However, we hypothesize to group people and scale human body models according to attributes such as, e.g. body shape, degeneration, and fitness, among others. Therefore, we conclude that current grouping might be inappropriate and attenuate our findings with respect to the subgroups presented in this study (see Sect. 2.2).

Experimental validation of active Human Body models (AHBMs) raises significant challenges as one needs to validate both the human body's passive and active mechanical characteristics and its subsystems. To ensure this validation process, various studies are focusing both on the whole body [12, 15, 27] and subsystems [8]. However, there is a clear need to explore the passive and active behaviour of the neck region required [64].

Our study offers force (Fig. 5) and dynamic (Fig. 6) data from the experiment and simulation for this specific region. A recent work where such force data were directly used to improve a digital human body model is the study of Mörl et al. [51]. Here, they demonstrated how a similar stiffness calculation could be used directly to adjust their lumbar spine model values taken from well-established literature sources of ligament and passive muscle stiffness to fit the experimentally measured stiffness. Similarly, researchers could take our data to improve their neck models. Furthermore, our data set could be used to validate and compare existing control strategies. In our model, we only used two stretch-based reflex controllers, however, recently a more sophisticated control approach for a multi-body head–neck model was proposed by Zheng et al. [82] where the vestibular reflex was additionally included. This reflex is modulated by sensing the disturbed head motion (linear acceleration and angular velocity) by the vestibular organs in the inner ear (both the semicircular canals and the otoliths) [36]. Therefore, the main purpose of the dataset presented here (available with open-source access), is to serve as a benchmark test for both passive neck properties, but also for different muscle control strategies in the same model and its implementations in various codes. We believe that the outcome and the experimental data of this study will help to improve existing and to develop potentially better AHBMs.

Initially, we posed the question how the biomechanical reflex response changes, if we vary the neuronal state in the simulation. Therefore, two muscle length feedback controllers were used to run a 'falling heads' simulation with varied controller variables (threshold ω and spindle feedback gain k_p, respectively) to represent the sensitivity of the neuronal state to the perturbation. Based on these simulations, we postulate that we are able to synthesize biophysically valid human movement with our control approach (as shown in Fig. 7). This is in line with the literature, where various authors [26, 57, 58] showed that including muscle activations helps to improve the agreement of experimental and simulated responses by decreasing the acceleration of the head. Furthermore, we showed that we are able to modulate the response using simple control parameter adjustments (see Fig. 7a, c). On the one hand, this modulation of the response can be used to represent a large variability of participants. On the other hand, it shows how a higher sensitivity of the neuronal state (in term of reflex thresholds) helps in reducing acceleration peaks. Whether these reflex thresholds are set explicitly like this by the nervous system as a result of an optimization function for unexpected perturbations, e.g. to minimize these accelerations peaks, stress or in general injury risks, was not investigated in this study. However, previous work showed that by using optimization principles it is possible to explain and predict voluntary movement, e.g. for walking [1, 50], eye movements [22], standing from a chair [53], and point-to-manifold reaching [78]. Whether such an optimization function is also adapted for unexpected perturbations, should be explored in further work. Independent of which optimization criterion is used, future work can directly exploit the correlation between a reduction in peak acceleration and the sensitivity of the neuronal state to develop better injury prevention strategies. This means that if mechanisms are applied to prepare humans to upcoming events (e.g. by sound signals), they can pre-tune their reflex gains accordingly, which in turn might reduce potential injury risks.

Conclusions

In this study, we present novel experimental data in a 'falling heads' setup in order to investigate individual reflexive responses to head–neck perturbations. We extracted several biomechanical parameters such as joint stiffness, peak acceleration and latency times based on this data.

Analysing this data, we show that there is a large difference in the individual reflexive responses between participants, e.g. for the peak falling height. Furthermore, we show that the perturbation direction has a significant influence on the kinematic quantities (e.g. peak linear and rotational acceleration) which is not reflected in the EMG latency times. Finally, we show that the musculoskeletal simulations with a reflex controller provide comparable results to the experiments. The setup of these numerical simulations is simple, making them an ideal candidate for future validation requirements in virtual testing procedures.

Concluding, a novel experimental dataset for head–neck perturbations including two different force directions (flexion and extension) for a larger number of healthy participants with different ages and sexes) is now available open-source. This experimental dataset can be used as a benchmark test to improve, compare and develop better human body models and muscle control strategies.

Methods

We conducted experiments in which relaxed volunteers were placed on a table in a supine and a prone position to investigate the individual responses to head–neck perturbations. The subject's head was supported by a trapdoor, which was suddenly released. This action resulted in a free-fall movement of the head until the subject reacted to the perturbation by developing a force in the antagonistic muscles, leading to the deceleration of the falling head. We recorded the kinematic trajectory of the head and the electromyographic (EMG) signal of the *sternocleidomastoideus* and the *trapezius* muscles to investigate this reflexive behaviour. Furthermore, we performed simulations matching the supine experiments using the academic THUMSv5 model [33] including Hill-type muscles activated using two different threshold-based reflex controllers. For both scenarios (real-world experiment and simulation), we performed an inverse dynamics analysis to determine the underlying force interactions, give an estimate for the stiffness values and use this data to validate the used human body model. The methods are described in further detail in the following.

Participants

Seventeen subjects volunteered to participate in the experiment (7 males, with an age range of 22–71 years). All of them were healthy. The demographic characteristics of all participants are given in Table 4. To investigate whether age or sex influenced the reflexive behaviour in this experimental setup, we divided the experimental data for some of the analysis into three age groups and two sexes (male, female) as shown in Table 4. Written informed consent was obtained from each participant in the study, which was approved by the ethics committee of the Karl-Franzens-University of Graz (reference number: 39/67/63 ex 2014/15). In addition, we certify that all methods were carried out in accordance with all applicable institutional and governmental regulations concerning the ethical use of human volunteers and in accordance with the Helsinki declaration during the course of this research.

'Falling heads' experiment

An illustration of the conducted 'falling heads' experiments is shown in Fig. 8. Participants were placed on a table first in the supine and then the prone position. The head was supported by a trap door, which was unexpectedly released by an electromagnet at irregular intervals. In the supine position, it was ensured that the T1 vertebrae was placed directly on the edge of the table. They were not restrained, however, in the supine position, arms were placed on the abdomen of the participants and in the prone position, arms were placed such that they hang quietly in an angle of 90° to the horizontal line (armpits directly on the table's edge). Furthermore, the boundary conditions were adapted to account for the different anthropometries of the participants by manipulating the position and height of the table to ensure two things: first, that the edge of the table was parallel and on the same height as the trapdoor. Secondly, to adjust the gap between the table and the trapdoor such that head was always placed on the same marked position on the foam of the trapdoor. In the prone position, this position was equivalent to placing the forehead to nasal bone on the trapdoor. The trapdoor was not moved due to calibration reasons. For every participant, the experiment was repeated three times in each position. The free fall would gently brake by the cushioned trapdoor after a maximum angle deviation of 40° to avoid any injuries (if the participants did not react before that). The subjects were encouraged to relax between each drop. Relaxation was also checked based on the level of EMG activity. To ensure that the recorded kinematics and the EMG signal are synchronized, we included a hardware trigger (by breaking the power circuit) which releases the trapdoor, starts the recording of the camera and sets a trigger index in the EMG signal.

Kinematic analysis

Head and neck kinematics were recorded using a HCC-1000 camera and HCC Control software (VDS Vosskühler GmbH/Germany) at a sampling rate of 462 fps. Three markers were recorded to detect both translational as well as rotational movements of the head. Volunteers were asked to wear a swimming cap in order to place the markers better and to avoid that they are obscured by hair. Marker 1 was positioned close to the eyes

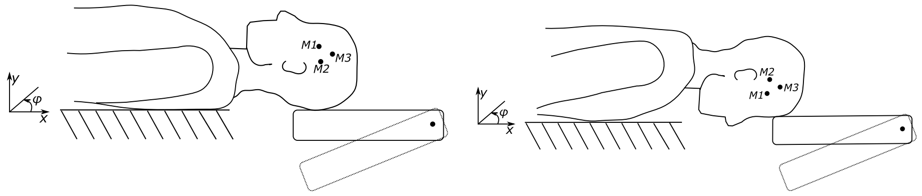

(a) supine (b) prone

Fig. 8 Sketch of the volunteer placement. The volunteer were placed in supine (**a**) and prone (**b**) position. The participant's head was supported by a trapdoor released at the start of the experiment. The three recorded markers are labelled as M1, M2 and M3 in the figure. Here, $\varphi = 0$ represents the starting position, where the head is at rest on the *sphenoid* bone. Marker 2 was positioned in sight line with a distance of 4 cm to Marker 1 and corresponds to the head centre of gravity projection in the sagittal plane. Finally, Marker 3 was attached such that all three markers formed an equilateral triangle as shown in the sketch in Fig. 8. The motion analyses were performed with custom software written in Matlab® (Mathworks, Natick, MA, USA) based on the recorded marker positions.[2] From these recorded trajectories, we calculated displacements, velocities and accelerations and processed the signals with a Butterworth low-pass filter (cut-off frequency 15 Hz; fourth-order).

Electromyographic analysis

Muscle activation was monitored using surface EMG of the *sternocleidomastoideus (SCM)* muscle and the *trapezius* muscle. The EMG activity was recorded at 1000 Hz using myoResearch software (Noraxon/USA). The placement of the electrodes at the *trapezius* muscle was done according to SENIAM guidelines [23]: the electrode pair was placed in the middle of the line between the spinous process of the 7th cervical vertebra and the acromion. The electrodes for the *sternocleidomastoideus (SCM)* muscle were placed over the middle part of the SCM muscle according to Sheykholeslami et al. [65]. All electrodes were attached parallel to the muscle fibre orientation at a distance of 20 mm. The reference electrode was fixed on the acromion. Volunteers were asked to relax their muscles before the onset of the movement. To measure the time delay between the release of the trapdoor and the first muscle activation, we used a threshold-based EMG onset detection method [43], which is a combination of two other methods [4, 25]. The main idea is to use the full-wave rectified EMG signal y_k to compute a test function g_k and to define the muscle activity onset t_0 as the point of time when this test function exceeds a threshold value. This threshold value is specified as a multiple h of standard deviations. As a rule of the algorithm, at least $T1$ samples should be higher than the threshold value, while allowing for $T2$ samples to fall below this value. The algorithm is summarized below [68]:

$$t_0 = \min_{k \leq W}(g_k \leq h) - W + 1, \tag{1}$$

$$g_k = \frac{1}{\hat{\sigma}_0}\left(\frac{1}{W}\sum_{i=k-W+1}^{k} y_k - \hat{\mu}_0\right). \tag{2}$$

Here, W denotes the width of the fixed-size sliding test window, k the current time, and $\hat{\mu}_0$ and $\hat{\sigma}_0$ the mean and standard deviation of the M initial samples of y_k, respectively. Five parameters need to be chosen for the onset detection: the number of initial samples M, the number of multiple standard deviations to calculate the threshold h, the window size W, the minimum number of samples above the threshold $T1$ and the number of samples which are allowed to fall below the threshold in this period, $T2$. Detected latency times t_0 smaller than 10 ms or larger than 100 ms were considered as invalid. The lower value was chosen because due to the conduction times of the action potential propagation and the central delay of the involved synapses [41], the muscles cannot be

---

[2] The postprocessing code is available at https://doi.org/10.18419/darus-2526.

activated instantaneously. The upper value was chosen because we are only interested in the reflex activation and all latency times larger than 100 ms were considered to be a voluntary reaction. We justify this restriction interval because previous studies found neck muscle latencies in response to perturbations to be in the range of 18.6–88 ms [7, 14, 29, 30, 47, 63, 72].

An optimization algorithm with two objective criteria was utilized to find the five necessary parameters for the neck reflex latency. The first criterion ensures that the optimized parameters minimize the number of invalid latency times t_0. Additionally, the second criterion tries to find parameters which minimize the standard deviation σ of latency times between trials for each subject. Such an approach allowed us to find parameter values as objectively as possible without having to rely on expert opinions.

We define the entire objective criterion ε as:

$$\varepsilon_1 = \sum_{i=1}^{n}\sum_{j=1}^{m}(t_0(i,j) < 10) \vee (t_0(i,j) > 100), \tag{3}$$

$$\varepsilon_2 = \sum_{i=1}^{n}\sigma(t_0(i,j)), \text{ with } j = 1\ldots m, \tag{4}$$

$$\varepsilon = w \cdot \varepsilon_1 + \varepsilon_2. \tag{5}$$

Here, n denotes the number of subjects (in our case $n = 17$) and m the number of trials (in our case $m = 3$). We chose a weighting factor $w = 100$ to emphasize the importance of detecting as many valid latency times as possible. The objective function was minimized using the *surrogateopt* algorithm in Matlab® (Mathworks, Natick, MA, USA).

Inverse dynamics analysis

We formulate the equations of motions for the head–neck segment to extract the joint torque M_{net} exerted on the head–neck segment by the trunk segment at the connecting joint. Previous studies modelled the head–neck system as a rigid inverted pendulum with a fixed centre of rotation [55, 67]. For our analysis, we had to extend their approach because the investigated head movement in our study is a combination of translation and rotation. For the rigid head–neck segment as part of an open chain in the sagittal x-y-plane, the following three equations of motion apply [17, 76]:

$$F_x = m\ddot{x}, \tag{6}$$

$$F_y = m(\ddot{y} - g), \tag{7}$$

$$M_{\text{net}} = I\ddot{\varphi} - r_xF_y + r_yF_x. \tag{8}$$

The force F_y acting in the vertical axis is dependent on the gravitational acceleration g. We estimate the head–neck mass m based on [76] as 8.1% of the total subject's mass. We calculate the moment of inertia I about the centre of mass (based on data from [76]) and scaled accordingly with the total subject's mass and height. The vectors r_x and r_y represent the distance between the bone centre of mass (COM) to the centre of joint rotation. The perturbing force $(m \cdot g)$ was delayed by 4 ms to take into account that the detachment of the head from the trapdoor does not happen instantaneously (alternatively a contact force at $t = 0$ could be defined). This delay was determined by comparison of the onset of the perturbing force and the measured head acceleration traces and adjusting the delay accordingly. We use this model and the calculated torque to estimate neck stiffness for the first 150 ms following perturbation onset similar to the study of Simoneau et al. [67]. This stiffness is called effective neck stiffness because it represents a combination of intrinsic and reflexive components. We calculate this stiffness for the first 150 ms as a linear approximation, i.e. the change in torque versus change in angle [56]:

$$S = \frac{\Delta M_{\text{net}}}{\Delta \varphi}. \tag{9}$$

Note that there are various approaches to calculate joint stiffness. Many of them are more complicated comparing to the proposed one. For example, one can include initial rest angle, damping, shifts of rest length and nonlinearities to calculate leg stiffness [6, 16]. Such methods allow making statements about the underlying biomechanical structures. However, we chose this somewhat reduced approach to enable a comparison of our absolute values to similar neck stiffness calculations done by Simoneau et al. [67] and Portero et al. [56].

Simulations

We compared the experiments of the supine case to simulations of the head-fall setup. There are two main computational methods used for simulations with human body models: Multibody (MB) Dynamics and Finite Element (FE) Analysis and the current study utilizes the latter. Among the most advanced FE Active Human Body Models (AHBMs) with muscle elements and a controller integrated into the whole body we can name the Global Human Body Models Consortium (GHBMC) [10], Total HUman Model for Safety (THUMS) [33, 34], SAFER A-HBM [40], THUMS TUC-VW AHBM [70, 79] and the AHBM developed during the joint collaboration of Mercedes-Benz AG and University of Stuttgart [49, 52]. A detailed comparison of these models and muscle control strategies used is given in Additional file 1: Table D2 in the supplementary material D. For our simulations, we used the THUMS v5 AM50 Occupant Model Academic Version [33] using the FE simulation software LS-DYNA. This model is driven by Hill-type muscles which are activated using two different threshold-based stretch reflex controllers. Please note, that there exist more sophisticated controllers (e.g. [82] for a MB model) which account also for the vestibular reflex which is modulated due to linear acceleration and angular velocity. Our model modifications and the necessary repositioning to replicate the experimental setup, are described in the following.

Positioning of the model

The model was repositioned according to the experimental setup shown in Fig. 8. All the parts, not related to the head, neck or torso regions were removed. Besides, translational and rotational constraints were introduced to the pelvis and abdomen. The gravitational load was applied according to the new model orientation. The table was implemented using a planar rigid wall supporting the lower back of the model. Furthermore, a second rigid plane was implemented to model the trapdoor supporting the head–neck complex. To ensure that the model starts in a planar equilibrium, we let the model settle due to the gravitational acceleration. Then, after this pre-simulation, the model was considered identical to the initial position of the volunteers and the second rigid plane was released to simulate the release of the trapdoor.

Modification of the muscles

In the standard version of the THUMS v5 model, muscles are modelled with a material named *MAT_MUSCLE (*MAT_156) [46]. Recently, a new Hill-type muscle material with a more realistic eccentric force–velocity relation and serial damping [18, 20] was implemented in LS-DYNA as a user-defined material which was named the extended Hill-type muscle model (EHTM) [37, 38, 48]. It shows a better material model accuracy compared to the standard muscle model *MAT_MUSCLE (*MAT_156) used in LS-DYNA [37, 77]. Therefore, in order to make the THUMS v5 more biophysically valid, we replaced the *MAT_MUSCLE material by this user-defined EHTM material for all muscles defined in the head–neck region (see Appendix A of THUMS v5 documentation [73]). Corresponding *MAT_MUSCLE parameters were converted into the EHTM parameters according to the procedure described in the supplementary material C. Note, that such a conversion is not unambiguous because the new muscle material requires at least one additional parameter, e.g. the ratio between the optimal fibre length l_{opt} or the tendon slack length $l_{\mathrm{SEE,0}}$ (can be taken from literature). Similar to [62], we define this ratio as:

$$m_{\mathrm{ratio}} = \frac{l_{\mathrm{opt}}}{l_{\mathrm{opt}} + l_{\mathrm{SEE,0}}}. \tag{10}$$

Using the assumption that the original muscle length $l_0 = l_{\mathrm{opt}} + l_{\mathrm{SEE,0}}$, we can then directly calculate the missing values of the model (abbreviated with mdl) based on the literature data (abbreviated with lit):

$$l_{\mathrm{opt,\,mdl}} = m_{\mathrm{ratio,lit}} \cdot l_{0,\mathrm{mdl}}, \tag{11}$$

$$l_{\mathrm{SEE,0,mdl}} = l_{0,\mathrm{mdl}} - l_{\mathrm{opt,\,mdl}}. \tag{12}$$

This a valid assumption for a normal upright state [62], which we have for the head–neck muscles. It should be mentioned here, that in the special case of $m_{\mathrm{ratio}} = 1$, we directly set the tendon slack length $l_{\mathrm{SEE,0}}$ to 1 mm. As literature source for m_{ratio}, we used values taken from [5]. The neck muscle parameters we used in this study are provided open-source.[3] Note, that we excluded the *digastricus*, the *mylohyoideus* and the *stylohyoideus* muscles from the simulation model. This was done because they are mainly responsible for lifting the jaw or tongue, which is not relevant for the investigated movement in this

---

[3] The neck muscle data set is available at https://doi.org/10.18419/darus-1145.

Table 5 Reflex controller algorithm (adapted from [38])

```
Reflex Controller for muscle $i$
initialize muscle stimulation $u_i = 0$.
initialize strain $\varepsilon_i = 0$
if time $t > t_{\text{old}}$ + delay $\tau$ do
    calculate strain $\varepsilon_i = \frac{l_{\text{CE,i}}(t_{\text{old}}) - l_{\text{CE,ref,i}}}{l_{\text{CE,ref,i}}}$.
    if strain $\varepsilon_i >$ threshold $\omega$
        activate reflex: set stimulation $u_i = 1$.
    else if strain $\varepsilon_i > 0$ and stimulation $u_i = 1$ do
        keep reflex activated: stimulation $u_i = 1$.
    else do
        deactivate reflex: set stimulation $u_i = 0$.
    end if
end if
```

study. Besides, the specific parameters for these muscles were not available in Borst et al. [5].

Muscle reflex controller

A dedicated reflex controller was proposed and included in the user-defined EHTM material model to determine the muscle stimulation u_i based on the current strain [13, 38, 48]. The latest improved open-source code version is made available.[4] The proposed reflex controller is a stretch-based muscle length controller, which activates every *i*th muscles with 100% stimulation u_i as soon as a particular strain threshold ω is exceeded. The detailed description of the controller's logic is given in Table 5 (adapted from [38]). Three parameters can be defined prior to the simulation: the delay time τ, the reference length of the contractile element $l_{\text{CE,ref}}$ and the threshold ω. For the 'falling heads' setup, we chose the initial lengths of the contractile element after settling on the table as reference lengths $l_{\text{CE,ref}}$ because they correspond to the relaxed state of the participants lying on the table. Previous studies [13, 26] reported to use a delay value of 25 ms, which is why we chose this value for τ. The threshold ω was varied between 1 and 10% because this range has a good agreement (small L2-error) with the experimental data (see also Fig. 7). As we show later in the Results section, the reflex threshold 5% has the smallest L2-error compared to the mean of the experimental data. Therefore, the simulation results are shown only for this curve if not stated otherwise.

Muscle lambda controller

As an alternative to the reflex controller, there also exists a neural feedback controller [2] based on the muscle fibre length of the contractile element (CE) l_i^{CE}. The stimulation signal u_i^{lambda} is calculated as follows:

$$u_i^{\text{lambda}} := \frac{k_p}{l^{\text{CE,opt}}}(l_i^{\text{CE}}(t) - \lambda_i). \tag{13}$$

---

[4] The EHTM code and manual are available at https://doi.org/10.18419/darus-1144.

With this, a sensory feedback mechanism can be described, because u_i^{lambda} depends on the difference between the currently desired fibre length of the contractile element λ_i and the actual CE fibre length l_i^{CE}. The difference is weighted by a muscle spindle feedback gain k_p and the optimal CE fibre length $l^{\text{CE,opt}}$.

Abbreviations

AHBM: Active human body model; *CE*: Contractile element; *EHTM*: Extended Hill-type muscle model; *EMG*: Electromyographic; *FE*: Finite element; *GHBMC*: Global human body consortium; *MB*: Multibody; *SCM*: Sternocleidomastoideus; *THUMS*: Total human model for safety.

Supplementary Information

The online version contains supplementary material available at https://doi.org/10.1186/s12938-022-00994-9.

Additional file 1: S1 Appendix. Inverse Dynamics Analysis: Moment of all participants. We show two figures containing the resulting moment of the inverse dynamics analysis for all participants for the supine and prone case. **S2 Appendix**. Transformation between muscle reflex and lambda controller. We present a more detailed explanation how the parameters between the reflex and lambda controller can be transformed. **S3 Appendix**. A guideline for parameters conversion from *MAT_MUSCLE to the EHTM. We give a more detailed guideline how the material parameters from the LS-DYNA *MAT_MUSCLE material can be converted to parameters for the Extended Hill-Type Material used in this study. **S4 Appendix**. Overview of Finite Element Active Human Body Models. A detailed comparison of the currently existing FE Active Human Body Models and their muscle control strategies is given in this table. **S5 Appendix**. Statistical analysis of the experimental data. A detailed statistical analysis based on the t-test with all p-values for comparing the three covariates force-direction, biological sex, and age is given.

Acknowledgements

The authors thank Tim Messerschmidt and Michael Weiß for preparing and conducting the experiments under the supervision of Syn Schmitt, and Lorena Lantella and Meike Rudlaff for the initial analysis and method setup for the EMG analysis. Furthermore, we would like to thank Michael Günther for helpful discussions, experimental data analysis supervision and comprehensive support. We also like to acknowledge the initial integration of the reflex and lambda controllers into the user-defined EHTM model version 2 done by Fabian Kempter and Christian Kleinbach. This study was part of a larger study conducted under the guidance of Philipp Huber at the Karl-Franzens-University of Graz, for which we would like thank him. Finally, we thank Emma Larsson, Johan Davidson, Jens Weber and Atul Mishra who provided AHBM images for Additional file 1: Suppl. Material S4.

Authors contributions

IW: conceptualization, methodology, software, validation, formal analysis, investigation, data curation, writing—original draft, writing—review and editing, visualization, supervision. LVN: software, data curation, writing—review and editing. OVM: software, writing—review and editing, supervision, project administration, funding acquisition. SS: conceptualization, resources, writing—review and editing, supervision, project administration, funding acquisition. All authors read and approved the final manuscript.

Funding

Open Access funding enabled and organized by Projekt DEAL. This work was supported by the EU Horizon 2020 research and innovation program under grant agreement No. 768947 "OSCCAR" and by the Deutsche Forschungsgemeinschaft (DFG, German Research Foundation) under Germany's Excellence Strategy - EXC 2075 - 390740016 (SimTech) and EXC 310. This document reflects only the author's view, the Innovation and Networks Executive Agency (INEA) is not responsible for any use that may be made of the information it contains.

Availability of data and materials

The experimental data sets are available at https://doi.org/10.18419/darus-1038 (EMG data) and https://doi.org/10.18419/darus-1132 (trajectory data). The postprocessing scripts for the kinematic and the inverse dynamics analysis are available at https://doi.org/10.18419/darus-2526. The neck muscle parameters we used in this study are also provided open-source: They are available at https://doi.org/10.18419/darus-1145. The improved code of the muscle material (EHTM) is available at https://doi.org/10.18419/darus-1144.

Declarations

Ethics approval and consent for publication

Written informed consent was obtained from each participant in the study, which was approved by the ethics committee of the Karl-Franzens-University of Graz (reference number: 39/67/63 ex 2014/15). In addition, we certify that all methods were carried out in accordance with all applicable institutional and governmental regulations concerning the ethical use of human volunteers and in accordance with the Helsinki declaration during the course of this research.

Competing interests

The authors declare that the research was conducted in the absence of any commercial or financial relationships that could be construed as a potential conflict of interest.

Received: 22 December 2021 Accepted: 29 March 2022

References

1. Anderson FC, Pandy MG. Dynamic optimization of human walking. J Biomech Eng. 2001;123(5):381–90.
2. Bayer A, Schmitt S, Günther M, et al. The influence of biophysical muscle properties on simulating fast human arm movements. Comput Methods Biomech Biomed Engin. 2017;20(8):803–21. https://doi.org/10.1080/10255842.2017.1293663.
3. Bener A, Rahman YSA, Mitra B. Incidence and severity of head and neck injuries in victims of road traffic crashes: In an economically developed country. Int Emerg Nurs. 2009;17(1):52–9.
4. Bonato P, D'Alessio T, Knaflitz M. A statistical method for the measurement of muscle activation intervals from surface myoelectric signal during gait. IEEE Trans Biomed Eng. 1998;45(3):287–99.
5. Borst J, Forbes PA, Happee R, et al. Muscle parameters for musculoskeletal modelling of the human neck. Clin Biomech. 2011;26(4):343–51.
6. Brughelli M, Cronin J. A review of research on the mechanical stiffness in running and jumping: methodology and implications. Scandinavian journal of medicine & science in sports. 2008;18(4):417–26.
7. Corna S, Ito Y, Von Brevern M, et al. Reflex (unloading) and (defensive capitulation) responses in human neck muscle. J Physiol. 1996;496(2):589–96.
8. Davidsson J. Volunteer shoulder range of motion and stiffness: data for evaluation of crash test dummies and human body models. In: IRCOBI Conference 2013, Gothenburg, Sweden, IRC-13-30; 2013. p. 230–244.
9. de Leva P. Adjustments to zatsiorsky-seluyanov's segment inertia parameters. J Biomech. 1996;29(9):1223–30. https://doi.org/10.1016/0021-9290(95)00178-6.
10. Devane K, Johnson D, Gayzik FS. Validation of a simplified human body model in relaxed and braced conditions in low-speed frontal sled tests. Traffic Injury Prevention. 2019;1–6. https://doi.org/10.1080/15389588.2019.1655733.
11. Dumas R, Chèze L, Verriest JP. Adjustments to mcconville et al. and young et al. body segment inertial parameters. J Biomech. 2007;40(3):543–53. https://doi.org/10.1016/j.jbiomech.2006.02.013.
12. Ejima S, Zama Y, Ono K, et al. Prediction of pre-impact occupant kinematic behavior based on the muscle activity during frontal collision. In: The 21th International Technical Conference on the Enhanced Safety of Vehicles (ESV), 09-0913; 2009. https://www-esv.nhtsa.dot.gov/Proceedings/21/09-0193.pdf
13. Feller L, Kleinbach C, Fehr J, et al. Incorporating muscle activation dynamics into the global human body model. In: Proceedings of the IRCOBI conference, Malaga, Spain; 2016.
14. Foust DR, Chaffin DB, Snyder RG, et al. Cervical range of motion and dynamic response and strength of cervical muscles. SAE Transactions. 1973;3222–34.
15. Ghaffari G, Brolin K, Pipkorn B, et al. Passenger muscle responses in lane change and lane change with braking maneuvers using two belt configurations: Standard and reversible pre-pretensioner. Traffic Inj Prev. 2019;20(sup1):S43–51. https://doi.org/10.1080/15389588.2019.1634265.
16. Günther M, Blickhan R. Joint stiffness of the ankle and the knee in running. J Biomech. 2002;35(11):1459–74.
17. Günther M, Sholukha VA, Kessler D, et al. Dealing with skin motion and wobbling masses in inverse dynamics. Journal of Mechanics in Medicine and Biology. 2003;3(03n04):309–35.
18. Günther M, Schmitt S, Wank V. High-frequency oscillations as a consequence of neglected serial damping in hill-type muscle models. Biol Cybern. 2007;97(1):63–79.
19. Guskiewicz KM, Mihalik JP. Biomechanics of sport concussion: quest for the elusive injury threshold. Exerc Sport Sci Rev. 2011;39(1):4–11.
20. Haeufle D, Günther M, Bayer A, et al. Hill-type muscle model with serial damping and eccentric force-velocity relation. J Biomech. 2014;47(6):1531–6.
21. Hanavan EP Jr. A mathematical model of the human body. Tech. rep., AIR FORCE AEROSPACE MEDICAL RESEARCH LAB WRIGHT-PATTERSON AFB OH; 1964.
22. Harris CM, Wolpert DM. Signal-dependent noise determines motor planning. Nature. 1998;394(6695):780–4.
23. Hermens HJ, Freriks B, Merletti R, et al. European recommendations for surface electromyography. Roessingh research and development. 1999;8(2):13–54.
24. Ho Hoang KL, Mombaur K. Adjustments to de leva-anthropometric regression data for the changes in body proportions in elderly humans. J Biomech. 2015;48(13):3732–6. https://doi.org/10.1016/j.jbiomech.2015.08.018.
25. Hodges PW, Bui BH. A comparison of computer-based methods for the determination of onset of muscle contraction using electromyography. Electroencephalogr Clin Neurophysiol. 1996;101(6):511–9.
26. van der Horst MJ, Thunnissen J, Happee R, et al. The influence of muscle activity on head-neck response during impact. SAE transactions. 1997;4003–23.
27. Huber P, Kirschbichler S, Prüggler A, et al. Passenger kinematics in braking, lane change and oblique driving maneuvers. In: Proceedings of the IRCOBI Conference, Lyon, France; 2015. p. 783–802. http://www.ircobi.org/wordpress/downloads/irc15/pdf_files/89.pdf
28. Imrhan SN. Muscular strength in the elderly - implications for ergonomic design. Int J Ind Ergon. 1994;13(2):125–38. https://doi.org/10.1016/0169-8141(94)90079-5.
29. Ito Y, Corna S, Von Brevern M, et al. Neck muscle responses to abrupt free fall of the head: comparison of normal with labyrinthine-defective human subjects. J Physiol. 1995;489(3):911–6.

30. Ito Y, Corna S, von Brevern M, et al. The functional effectiveness of neck muscle reflexes for head-righting in response to sudden fall. Exp Brain Res. 1997;117(2):266–72.
31. Jensen RK, Fletcher P. Distribution of mass to the segments of elderly males and females. J Biomech. 1994;27(1):89–96. https://doi.org/10.1016/0021-9290(94)90035-3.
32. Jordan A, Mehlsen J, Bülow PM, et al. Maximal isometric strength of the cervical musculature in 100 healthy volunteers. Spine. 1999;24(13):1343.
33. Kato D, Nakahira Y, Iwamoto M. A study of muscle control with two feedback controls for posture and reaction force for more accurate prediction of occupant kinematics in low-speed frontal impacts. In: Proceedings of the 25th International technical conference on the enhanced safety of vehicles (ESV), Detroit, USA; 2017.
34. Kato D, Nakahira Y, Atsumi N, et al. Development of human-body model thums version 6 containing muscle controllers and application to injury analysis in frontal collision after brake deceleration. In: Proceedings of the International IRCOBI Conference. IRCOBI Council, Athens, Greece; 2018. http://www.ircobi.org/wordpress/downloads/irc18/pdf-files/32.pdf
35. Kelly P, Kroemer K. Anthropometry of the elderly: Status and recommendations. Hum Factors. 1990;32:571–95. https://doi.org/10.1177/001872089003200506.
36. Keshner E. Vestibulocollic and cervicocollic control. Encyclopedia of neuroscience. 2009;4220–4.
37. Kleinbach C, Martynenko O, Promies J, et al. Implementation and validation of the extended hill-type muscle model with robust routing capabilities in ls-dyna for active human body models. Biomed Eng Online. 2017;16(1):109.
38. Kleinbach CG. Simulation of occupant kinematics using active human body models. Dissertation, Universität Stuttgart, Düren; 2019.
39. Lanza IR, Towse TF, Caldwell GE, et al. (2003) Effects of age on human muscle torque, velocity, and power in two muscle groups. J Appl Physiol. 1985;95(6):2361–9. https://doi.org/10.1152/japplphysiol.00724.2002.
40. Larsson E, Iraeus J, Fice J, et al. Active human body model predictions compared to volunteer response in experiments with braking, lane change, and combined manoeuvres. In: Proceedings of the International IRCOBI Conference. IRCOBI Council, Florence, Italy; 2019. p. 349–369, http://www.ircobi.org/wordpress/downloads/irc19/pdf-files/50.pdf
41. Latash ML. Neurophysiological basis of movement. Human Kinetics; 2008.
42. Le Flao E, Brughelli M, Hume PA, et al. Assessing head/neck dynamic response to head perturbation: a systematic review. Sports Med. 2018;48(11):2641–58.
43. Lidierth M. A computer based method for automated measurement of the periods of muscular activity from an emg and its application to locomotor emgs. Electroencephalogr Clin Neurophysiol. 1986;64(4):378–80.
44. Loper M, Mahmood N, Romero J, et al. Smpl: A skinned multi-person linear model. ACM transactions on graphics (TOG). 2015;34(6):1–16.
45. LSTC. LS-DYNA R9.0 Keyword User's Manual Volume I. 08/29/16 (r:7883); 2016a. http://www.lstc.com/download/manuals
46. LSTC. LS-DYNA R9.0 Keyword User's Manual Volume II Material Models. 08/31/16 (r:7893); 2016b. http://www.lstc.com/download/manuals
47. Mansell J, Tierney RT, Sitler MR, et al. Resistance training and head-neck segment dynamic stabilization in male and female collegiate soccer players. J Athl Train. 2005;40(4):310.
48. Martynenko O, Kempter F, Kleinbach C, et al. Integrated physiologically motivated controller for the open-source extended Hill-type muscle model in LS-DYNA. In: Proceedings of the International IRCOBI Conference. IRCOBI Council, Athens, Greece; 2018. p. 239–241, http://www.ircobi.org/wordpress/downloads/irc18/pdf-files/35.pdf
49. Martynenko OV, Neininger FT, Schmitt S. Development of a hybrid muscle controller for an active finite element human body model in LS-DYNA capable of occupant kinematics prediction in frontal and lateral maneuvers. In: Proceedings of the 26th International Technical Conference on the Enhanced Safety of Vehicles (ESV), Eindhoven, Netherlands; 2019. p. 1–12, https://www-esv.nhtsa.dot.gov/Proceedings/26/26ESV-000215.pdf
50. Meyer AJ, Eskinazi I, Jackson JN, et al. Muscle synergies facilitate computational prediction of subject-specific walking motions. Frontiers in bioengineering and biotechnology. 2016;4:77.
51. Mörl F, Günther M, Riede JM, et al. Loads distributed in vivo among vertebrae, muscles, spinal ligaments, and intervertebral discs in a passively flexed lumbar spine. Biomechanics and modeling in mechanobiology; 2020.
52. Öztürk A, Mayer C, Kumar H, et al. A step towards integrated safety simulation through pre-crash to in-crash data transfer. In: Proceedings of the 26th International Technical Conference on the Enhanced Safety of Vehicles (ESV), Eindhoven, Netherlands, 2019; p. 1–10, http://www-esv.nhtsa.dot.gov/Proceedings/26/26ESV-000257.pdf
53. Pandy M, Garner B, Anderson F. Optimal control of non-ballistic muscular movements: a constraint-based performance criterion for rising from a chair. J Biomech Eng. 1995;1117:15–26.
54. Portero R, Quaine F, Cahouet V, et al. In vivo neck musculo-tendinous stiffness in response to quick-releases. In: 6th World Congress of Biomechanics (WCB 2010). August 1-6, 2010 Singapore, Springer; 2010. p. 593–596.
55. Portero R, Lecompte J, Thoumie P, et al. Musculo-tendinous stiffness of the in vivo head-neck segment in response to quick-releases: A reproducibility study. Isokinet Exerc Sci. 2011;19(1):7–12.
56. Portero R, Quaine F, Cahouet V, et al. Musculo-tendinous stiffness of head-neck segment in the sagittal plane: An optimization approach for modeling the cervical spine as a single-joint system. J Biomech. 2013;46(5):925–30.
57. Putra IPA, Iraeus J, Thomson R, et al. Comparison of control strategies for the cervical muscles of an average female head-neck finite element model. Traffic Inj Prev. 2019;20(sup2):S116–22.
58. Reynier KA, Alshareef A, Sanchez EJ, et al. The effect of muscle activation on head kinematics during non-injurious head impacts in human subjects. Annals of Biomedical Engineering. 2020;1–12.
59. Roper K, Yeh D. Ergonomic solutions for an aging workforce. J Facil Manag. 2007;5:172–8. https://doi.org/10.1108/14725960710775054.
60. Rowson S, Duma SM, Beckwith JG, et al. Rotational head kinematics in football impacts: an injury risk function for concussion. Ann Biomed Eng. 2012;40(1):1–13.
61. Rubiano AM, Carney N, Chesnut R, et al. Global neurotrauma research challenges and opportunities. Nature. 2015;527(7578):S193–7.

62. Rupp T, Ehlers W, Karajan N, et al. A forward dynamics simulation of human lumbar spine flexion predicting the load sharing of intervertebral discs, ligaments, and muscles. Biomech Model Mechanobiol. 2015;14(5):1081–105.
63. Schmidt JD, Guskiewicz KM, Blackburn JT, et al. The influence of cervical muscle characteristics on head impact biomechanics in football. Am J Sports Med. 2014;42(9):2056–66.
64. Shelat C, Ghosh P, Chitteti R, et al. "Relaxed" HBM – an Enabler to Pre-Crash Safety System Evaluation. In: Proceedings of the IRCOBI Conference, Malaga, Spain; 2016.
65. Ki S, To M, Kaga K. The effect of sternocleidomastoeid electrode location on vestibular evoked myogenic potential. Auris Nasus Larynx. 2001;28(1):41–3.
66. Siegmund GP, Brault JR, Chimich DD. Do cervical muscles play a role in whiplash injury? Journal of Whiplash & Related Disorders. 2002;1(1):23–40.
67. Simoneau M, Denninger M, Hain TC. Role of loading on head stability and effective neck stiffness and viscosity. J Biomech. 2008;41(10):2097–103.
68. Staude G, Flachenecker C, Daumer M, et al. (2001) Onset detection in surface electromyographic signals: a systematic comparison of methods. EURASIP Journal on Advances in Signal Processing. 2001;2:867,853.
69. Strasser H. The "art of aging" from an ergonomics viewpoint-wisdoms on age. Occup Ergon. 2017;13(S1):1–24.
70. Sugiyama T, Weber J, Sandoz B, et al. Validation of a reactive finite element human body model under moderate lateral loading. In: Proceedings of the 7th International Symposium: Human Modeling and Simulation in Automotive Engineering, Berlin, Germany; 2018.
71. Suryanarayana L, Kumar S. Quantification of isometric cervical strength at different ranges of flexion and extension. Clin Biomech. 2005;20(2):138–44.
72. Tierney RT, Sitler MR, Swanik CB, et al. Gender differences in head-neck segment dynamic stabilization during head acceleration. Med Sci Sports Exerc. 2005;37(2):272–9.
73. Toyota. User's Guide of Computational Human Model THUMS®: AM50 Occupant Model Academic Version 5.02. Toyoto Motor Corporation, Toyota Central R&D Labs. Inc.; 2017.
74. Vasavada AN, Li S, Delp SL. Three-dimensional isometric strength of neck muscles in humans. Spine. 2001;26(17):1904–9.
75. Wierzbicki V, Pesce A, Marrocco L, et al. How old is your cervical spine? cervical spine biological age: a new evaluation scale. Eur Spine J. 2015;24(12):2763–70.
76. Winter DA. Biomechanics and motor control of human movement. USA:Wiley; 2009.
77. Wochner I, Endler CA, Schmitt S, et al. Comparison of controller strategies for active human body models with different muscle materials. In: IRCOBI Conference Proceedings; 2019. http://www.ircobi.org/wordpress/downloads/irc19/pdf-files/30.pdf
78. Wochner I, Driess D, Zimmermann H, et al. Optimality principles in human point-to-manifold reaching accounting for muscle dynamics. Front Comput Neurosci. 2020;14:38.
79. Yigit E. Reaktives FE-Menschmodell im Insassenschutz. Springer Fachmedien Wiesbaden. 2018. https://doi.org/10.1007/978-3-658-21226-1.
80. Zatsiorsky V, Seluyanov V, Chugunova L. Methods of determing mass-inertial characteristics of human body segments. In: Chernyi G, Regirer S, editors. Contemporary Problems of Biomechnics. CRC Press; 1990. p. 272–91.
81. Zhang L, Yang KH, King AI. A proposed injury threshold for mild traumatic brain injury. J Biomech Eng. 2004;126(2):226–36.
82. Zheng Z, Mo F, Liu T, et al. A novel neuromuscular head-neck model and its application on impact analysis. IEEE Trans Neural Syst Rehabil Eng. 2021;29:1394–402.

Publisher's Note

IV. Contribution 4: Muscles reduce neuronal information load: quantification of control effort in biological vs. robotic pointing and walking

frontiers
in Robotics and AI

ORIGINAL RESEARCH
published: 24 June 2020
doi: 10.3389/frobt.2020.00077

Muscles Reduce Neuronal Information Load: Quantification of Control Effort in Biological vs. Robotic Pointing and Walking

Daniel F. B. Haeufle[1,2]*, **Isabell Wochner**[3,4], **David Holzmüller**[5,6], **Danny Driess**[5,7], **Michael Günther**[3] **and Syn Schmitt**[3,4]

[1] Hertie Institute for Clinical Brain Research, University of Tübingen, Tübingen, Germany, [2] Center for Integrative Neuroscience, University of Tübingen, Tübingen, Germany, [3] Institute for Modelling and Simulation of Biomechanical Systems, University of Stuttgart, Stuttgart, Germany, [4] Stuttgart Center for Simulation Science, University of Stuttgart, Stuttgart, Germany, [5] Machine Learning and Robotics Lab, University of Stuttgart, Stuttgart, Germany, [6] Institute for Stochastics and Applications, University of Stuttgart, Stuttgart, Germany, [7] Max-Planck Institute for Intelligent Systems, Stuttgart, Germany

OPEN ACCESS

Edited by:
Thrishantha Nanayakkara,
Imperial College London,
United Kingdom

Reviewed by:
Leonardo Abdala Elias,
State University of Campinas, Brazil
Cosimo Della Santina,
Massachusetts Institute of
Technology, United States

***Correspondence:**
Daniel F. B. Haeufle
daniel.haeufle@uni-tuebingen.de

Specialty section:
This article was submitted to
Soft Robotics,
a section of the journal
Frontiers in Robotics and AI

Received: 10 November 2019
Accepted: 07 May 2020
Published: 24 June 2020

Citation:
Haeufle DFB, Wochner I, Holzmüller D,
Driess D, Günther M and Schmitt S
(2020) Muscles Reduce Neuronal
Information Load: Quantification of
Control Effort in Biological vs. Robotic
Pointing and Walking.
Front. Robot. AI 7:77.
doi: 10.3389/frobt.2020.00077

It is hypothesized that the nonlinear muscle characteristic of biomechanical systems simplify control in the sense that the information the nervous system has to process is reduced through off-loading computation to the morphological structure. It has been proposed to quantify the required information with an information-entropy based approach, which evaluates the minimally required information to control a desired movement, i.e., control effort. The key idea is to compare the same movement but generated by different actuators, e.g., muscles and torque actuators, and determine which of the two morphologies requires less information to generate the same movement. In this work, for the first time, we apply this measure to numerical simulations of more complex human movements: point-to-point arm movements and walking. These models consider up to 24 control signals rendering the brute force approach of the previous implementation to search for the minimally required information futile. We therefore propose a novel algorithm based on the pattern search approach specifically designed to solve this constraint optimization problem. We apply this algorithm to numerical models, which include Hill-type muscle-tendon actuation as well as ideal torque sources acting directly on the joints. The controller for the point-to-point movements was obtained by deep reinforcement learning for muscle and torque actuators. Walking was controlled by proprioceptive neural feedback in the muscular system and a PD controller in the torque model. Results show that the neuromuscular models consistently require less information to successfully generate the movement than the torque-driven counterparts. These findings were consistent for all investigated controllers in our experiments, implying that this is a system property, not a controller property. The proposed algorithm to determine the control effort is more efficient than other standard optimization techniques and provided as open source.

Keywords: muscle, control effort, morphological computation, reinforcement leaning, reflexes during walking, information entropy, torque actuator

1. INTRODUCTION

To generate dynamic movements, biological and technical systems actively process information by sensing their state and deriving control signals. The part of the system that performs this active information processing is typically termed *controller*. A controller has to deal with the dynamics characteristics of the controlled system, e.g., the neuronal delays, and the muscular elasticities and nonlinearities in biological systems or the ideally linear torque characteristics in technical systems. While—from a classical engineering point of view—muscular elasticities and nonlinearities complicate the implementation of an adequate controller, several studies show that they are beneficial for the generation of movements in terms of robustness against perturbations (van Soest and Bobbert, 1993; Gerritsen et al., 1998; Wagner and Blickhan, 1999, 2003; Eriten and Dankowicz, 2009; van der Krogt et al., 2009; Haeufle et al., 2010, 2012; John et al., 2013). Examinations of the control of point-to-point movements in the human arm (Pinter et al., 2012; Kambara et al., 2013; Bayer et al., 2017; Stollenmaier et al., 2020; Wochner et al., 2020) as well as in a frog's leg (Giszter et al., 1993), suggest that the neuronal system explicitly relies on the visco-elastic characteristics of the muscles to stabilize a specific posture or to generate smooth dynamic trajectories from jerky control signals.

When discussing the potential contribution of morphology to control, researchers use conjectures like "reduce the control effort" (Blickhan et al., 2007) or "simplify control" (Full and Koditschek, 1999; Holmes et al., 2006) to suggest that less information has to be processed by the biological controller, i.e., the nervous system, during the movement due to the specific morphology. This part is then performed by the morphology, in the sense of "morphological computation" (Paul, 2006; Zahedi and Ay, 2013; Ghazi-Zahedi et al., 2016). A quantitative analysis of the information processing benefit that is gained by these characteristics of the biological system in direct comparison to (technical) systems with different characteristics is possible. For this purpose, we have proposed to measure the minimally required information to generate a movement, i.e., the *control effort* (Haeufle et al., 2014b). Applied to a simplified model of human hopping—with only one actuator and one mechanical degree of freedom—this approach showed that the muscle properties allow reducing the control effort almost by a factor of 20 in comparison to an ideal torque generator model-driven by a PD controller (Haeufle et al., 2014b). This and the existing evidence for muscular benefits in control suggests that relief of effort for the nervous control system may be engraved into muscle design, and may, in other words, have been one of several basic design criteria during the evolution of biological muscle. We, therefore, hypothesize that control effort is relevant in different and more complex movements.

To study this, we here extend the quantification of control effort to more complex movements as, e.g., human point-to-point arm movements and human walking, which is the first novelty of this paper. To determine control effort in complex musculo-skeletal or robotic models with many control signals, we propose a new algorithm (provided online), which is the second novelty of this paper. We applied this algorithm to two existing musculo-skeletal models: one for arm movements (Driess et al., 2018; Stollenmaier et al., 2020), and one for planar walking (Geyer and Herr, 2010). For each model, a "robotic" version equipped with ideal torque generators was deployed (in analogy to "MOM" in van Soest and Bobbert, 1993). To obtain the controller for point-to-point arm movements, we considered deep reinforcement learning methods. Walking was controlled with proprioceptive neural feedback as well as a PD controller.

2. A SUMMARY OF THE APPROACH TO QUANTIFY CONTROL EFFORT

The measure of *control effort* previously introduced (Haeufle et al., 2014b) quantifies the minimal information required to generate a specific movement. The basis for this is the quantification of the information of the control signals—i.e., sensor signals and actuator command signals—based on SHANNON's information entropy (Shannon and Weaver, 1949). In a nutshell, the idea is to change the resolution of discretized control signals to reduce their information content. If the discretization is too coarse, the movement breaks down. The coarsest resolution where the movement still works represents the minimal information and is termed *control effort*. In the following, we will briefly summarize the concept.

We start with defining parameters for the discretization of the control signals: Each control signal $u_i(t)$ (with $i \in \{1, \ldots, N_u\}$ and N_u the number of control signals) is discretized. Discretization limits the number of possible sensor measurement values to n_i (amplitude resolution) and the number of repeated measurements during the movement to m_i (time resolution). Both are positive natural numbers $n_i \in \mathbb{N}_1$ and $m_i \in \mathbb{N}_1$ (excluding 0). Each pair (n_i, m_i) represents the overall resolution of a specific signal u_i. The vector

$$\mathbf{r} = (n_1, m_1, n_2, m_2, \ldots, n_i, m_i, \ldots, n_{N_u}, m_{N_u}) \in \mathcal{R} \tag{1}$$

is the vector containing all amplitude and time resolution parameters. It has $2N_u$ elements. The set of possible parameter vectors is $\mathcal{R} := \mathbb{N}_1^{2N_u}$, the set of all possible vectors of length $2N_u$ with positive natural numbers.

The information of these control signals can then be calculated by (see also Appendix A):

$$I(\mathbf{r}) = \sum_{i=1}^{N_u} m_i \log_2 n_i \quad . \tag{2}$$

with $I : \mathbb{N}_1^{2N_u} \rightarrow \mathbb{R}$. This is a simple monotonic function, which depends on the resolution parameter vector. By reducing the values in $\mathbf{r}$, i.e., lowering the resolution, the information is reduced.

By reducing the information in the control signal, the movement performance will deteriorate and eventually break down. As an example: if the sensor resolution on the elbow joint position is reduced, the deviation from the target position will eventually increase. To quantify this, we define a performance function $P : \mathbb{N}_1^{2N_u} \rightarrow \mathbb{R}$. This performance function is movement specific and will be specified later (see sections 4.1.2, 4.2.2).

Finding the minimally required information, i.e., the *control effort*, is, thus, a constrained optimization problem of the form

$$\begin{aligned} \min_{\mathbf{r}\in\mathcal{R}} \quad & I(\mathbf{r}) \\ \text{subject to} \quad & P(\mathbf{r}) \leq 0 \end{aligned} \tag{3}$$

The cost function $I(\mathbf{r})$ is cheap to evaluate and straight-forward to optimize. Evaluating the constraint $P(\mathbf{r})$, however, requires the simulation of a movement which is computationally expensive.

3. NEW ALGORITHM TO QUANTIFY CONTROL EFFORT

In the publication, where we proposed the approach to quantify control effort, we searched for the minimal information by brute force (Haeufle et al., 2014b). This was possible due to the small number of control signals ($N_u \leq 3$). For more complex movements with many signals (as investigated here) such an approach needs to be replaced by a systematic optimization. As stated above, it is a constrained optimization problem with a very simple cost function, but a computationally expensive Boolean constraint (movement succeeded or failed), which is additionally stochastic in the presence of motor noise in the investigated arm movements. This prohibits the calculation of a derivative, even by numerical methods. Therefore, all constrained optimization techniques that rely on a gradient of the constraint are not applicable. As the cost function is computationally cheap, it should always be evaluated first and it should be avoided to calculate the constraint function for parameter sets for which it is already clear that the cost is larger than for the currently best parameter set. This makes it difficult to apply algorithms that rely on surrogate functions (e.g., SGHO), as the objective would become very unsteady, also due to the Boolean constraint (a failed movement would be interpreted as a very high cost). Direct search methods seem therefore appropriate (e.g., dual annealing, differential evolution, pattern search). Furthermore, we know two important aspects of our optimization problem: our cost function is monotonically decreasing and if the resolution becomes to coarse, the movement will break down. Thus, we expect a clear border above which the constraint is fulfilled and below it is not. With this knowledge, we can specifically tailor the optimization to minimize the costly calculation of the constraint function. We, therefore, developed a direct search approach that is specifically designed for our optimization problem (Equation 3). The algorithm is based on the pattern search concept, a class of derivative-free direct search algorithms (Todorov and Jordan, 2003; Lewis et al., 2000; Rios and Sahinidis, 2013). In the following, we will describe the concept of the algorithm. Its algorithmic details are given in the Appendix B and the algorithm can be found online at https://github.com/daniel-haeufle/Control_Effort_Optim_Algorithm.

3.1. Outline of the Algorithm

In every iteration of the algorithm, a new set of parameters $\mathbf{r} \in \mathcal{R}$ is selected (polled), evaluated, and the results are compared to the previous best solution (Algorithm 1, Appendix B.1). The key step of the optimization algorithm is the selection (polling) of new parameter sets $\mathbf{r}$.

The initial guess of the parameter set $\mathbf{r}_{\text{init}}$ has to be with high values for time and amplitude resolution n_i and m_i, almost resembling numerically continuous signals. With the high resolution parameters, $\mathbf{r}_{\text{init}}$ fulfills the constraint function $P(\mathbf{r})$. Therefore, it becomes the currently best parameter set in the first iteration: $\mathbf{r} = \mathbf{r}_{\text{init}}$.

Starting from this initial guess, the pattern search algorithm searches for a better solution by exploratory moves (polling) in the parameter space by sampling the function in the vicinity of the currently best parameter set $\mathbf{r}$. Polling is performed by iteratively adding a specified set D of vectors $\mathbf{d}_l \in D$ (the *pattern*), multiplied by a current mesh size vector $\mathbf{m} \in \mathbb{R}^{2N_u}$ to the currently best solution as

$$\mathbf{r}_{\text{test}} = \mathbf{r} - \mathbf{m} \odot \mathbf{d}_l \tag{4}$$

(where $\odot$ represents the element wise multiplication of the two vectors). The mesh size vector basically contains one "scaling factor" for each resolution parameter (entry in $\mathbf{r}$). In general, the mesh size vector is reduced (scaled by 0.5) if no better solution is found in the evaluated parameter space and increased (scaled by 2) if a better solution is found. This represents an adaptive search step width (mesh size). For a very helpful overview of the approach of pattern search algorithms, we refer the reader to Torczon (1997).

Our algorithm employs three different polling methods, which differ by the pattern vectors D.

3.1.1. Phase 1: Rapid Parallel Reduction of Resolution in All Signals

The first phase is an initial rough sweep where all signals are treated equally. Polling is done by a bisection search method working uniformly on all entries of $\mathbf{r}$, i.e., the pattern of this first phase D_1 contains only one vector

$$\bar{\mathbf{d}} = (1, 1, \ldots, 1). \tag{5}$$

By adapting the mesh size as described above, this results in a global bisection algorithm acting in parallel on all entries of $\mathbf{r}$. The bisection search algorithm is shown in Algorithm 2, Appendix B.2. The benefit of phase 1 is that the performance function needs to be evaluated only a few times to identify a first rough performance limit, even for models with a high number of control signals.

3.1.2. Phase 2: Pattern Search

The more thorough sweep of the second phase is more closely inspired by pattern search algorithms. The pattern D_2 consists of the vectors $\mathbf{d}_l := e_l$, where $e_l = (0, \ldots, 0, 1, 0, \ldots, 0)$ is the l-th unit vector. It is motivated by the fact that the cost function is monotonically decreasing for each entry. Thus, with this set, the algorithm only polls in the direction of reduced cost $I(\mathbf{r})$ saving a lot of computational time to less specific search patterns. The vectors $\mathbf{d}_l$ represent a linearly independent basis and only modify each variable individually. This is fine for most cases, but may cause the optimization to converge to an undesired local minimum. To reduce this risk, we added a set of vectors $\{\bar{\mathbf{d}}_l\}$ in case the previous poll did not reveal any new and better solution. These vectors were constructed such that they had a positive value of 0.5 added to the entry of the previous successful polling direction: $\bar{\mathbf{d}}_l = \mathbf{d}_l + (0, \ldots, 0.5, \ldots, 0)$. Let us say the previous successful poll modified the second entry of $\mathbf{r}$. Then, the additional polling vectors would look like this:

$$\begin{aligned}\bar{\mathbf{d}}_1 &= (1, -0.5, 0, \ldots, 0)\\ \bar{\mathbf{d}}_2 &= (0, 0.5, 0, \ldots, 0)\\ \bar{\mathbf{d}}_l &= (0, -0.5, \ldots, 1, \ldots, 0)\\ \bar{\mathbf{d}}_{2N_u} &= (0, -0.5, 0, \ldots, 1)\,.\end{aligned}$$

These additional vectors represent linear combinations and allow the optimization algorithm to go "back" in one parameter to get out of a local minimum.

Please note: the mesh size vector $\mathbf{m}$ is also adapted as in phase 1. The algorithm for phase 2 is shown in Algorithm 3 Appendix B.3.

3.1.3. Phase 3: Check Local Neighborhood and Calculate Error

The third and final phase is used to scan the local neighborhood of $\mathbf{r}_{\text{best}}$ for better solutions and, at the same time, to calculate the error ΔI_{opt}. We allow for three simultaneously changed entries in $\mathbf{r}$ as linear combinations of the vectors in the pattern D_2 to find potentially better solutions. For this systematic sweep, the mesh size vector is not adapted anymore. It is simply a vector of ones. This is shown in Algorithm 4, Appendix B.4. In principle, allowing more than three non-zero entries in d may further improve the found vector $\mathbf{r}$. However, this would come with a high computational cost.

3.2. Optimal Result: Control Effort I_{min}

At the end of the third phase, $\mathbf{r}_{\text{opt}} = \mathbf{r}$ represents the best parameter vector found by the algorithm. With this, we calculate the control effort, which is the actual information content (Equation 15, **Appendix A**) of all signals

$$I_{\text{min}} = I^{\text{Sh}}(\mathbf{r}_{\text{opt}}) \tag{6}$$

$$= \sum_{i=1}^{N_u} \sum_{j=1}^{n_i} p_{ji}^{\text{opt}} \log_2 p_{ji}^{\text{opt}} \quad . \tag{7}$$

This is the minimally required information content of all control signals to generate the desired movement, i.e., still fulfilling the performance constraint $P(\mathbf{r}) = 0$. We identify this minimal information as control effort and symbolize it with I_{min}.

Please note that during the optimization, we assumed equal distribution of the signal values u_{ji} in the range $u_i^{\text{min}} \leq u_{ji} \leq u_i^{\text{max}}$ with $j = 1, \ldots, n_i$. Therefore, the probabilities were assumed to be $p_{ji} = 1/n_i$. The cost function of the optimization is based on this assumption and therefore requires no computationally expensive simulation to evaluate the cost function. However, the actual probability $p_{ji} = p(u_i(t) = u_{ji})$ that a signal $u_i(t)$ has the value u_{ji} at time t differs from the original assumption. Therefore, the actual information at the optimal solution differs too. The real probabilities were estimated from the recorded control signals of the optimal walking simulation (p_{ji}^{opt}) using (Equation 7).

3.3. Error Estimation

We want to quantify the amount of error that we make by confining the components $\mathbf{r}$ to integer values. To this end, our search algorithm calculates an error ΔI_{opt} specifying the maximum information reduction that can be achieved by reducing a single entry of $\mathbf{r}_{\text{opt}}$ by one. Specifically, we define

$$\Delta I_{\text{opt}} := \max_{l \in \{1, \ldots, 2N_u\}} I(\mathbf{r}_{\text{opt}}) - I(\mathbf{r}_{\text{opt}} - e_l). \tag{8}$$

For small ΔI_{opt}, we thus expect the discretization of $\mathbf{r}$ to only have little effect on the continuous information $I_{\text{min}} \in [0, \infty)$.

4. CONTROL EFFORT IN TYPICAL HUMAN MOVEMENT TASKS

This study hypothesized that reduced control effort for muscle models over torque actuators found in a simplified hopping model (Haeufle et al., 2014b) is also present in more realistic models of human movements. To test this, we applied the measure described above to biologically plausible models of human point-to-point arm movements and human walking. The models we employed for this study (or very similar ones) have been previously used to study motor control phenomena, where muscle characteristics play a role. Such arm models were used to investigate hypotheses on the control of fast arm movements (Kistemaker et al., 2006), motor learning to compensate for loads during arm movements (Gribble and Ostry, 2000), or the reaction to external forces (Stollenmaier et al., 2020). The walking model was originally used to demonstrate that level walking could be generated by simple reflex control schemes in the spinal cord and does not necessarily require central planning or pattern generators (Geyer and Herr, 2010). It reproduces human muscle activity patterns, joint torques, and kinematics quite well.

In both cases, muscle-driven models were the starting point. For comparison, we derived torque-driven models by stripping these models of all muscular dynamics and considering direct torque actuators in the joints. This resulted in a total of six different cases for which we quantified control effort: two different movements with three different scenarios to quantify control effort each. The two movements were goal-directed (pointing) arm movements and level walking. The three different scenarios to quantify control effort were the following (**Figure 1**)

- STIM: discretization of the motor signals stimulating the muscles (controller output) in the neuromuscular model.
- SENS: discretization of the sensor signals fed back to the controller (its input) in the neuromuscular model.
- TORQUE: discretization of the motor signals (controller output) fed to ideal torque generators.

STIM and SENS represent the biological, neuromuscular system. TORQUE represents the robotic, technical system. In the

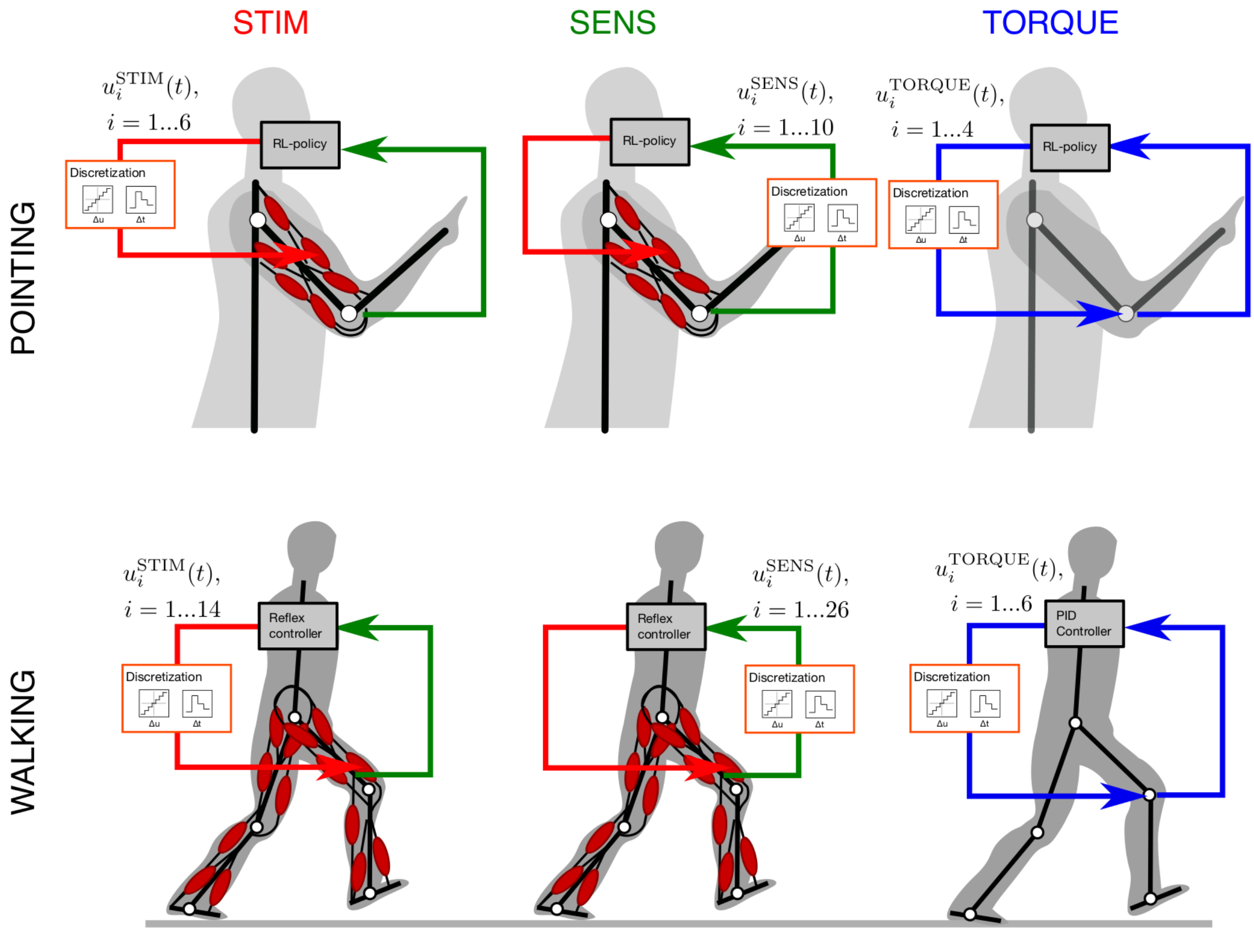

FIGURE 1 | Schematics of the study design: the two movements investigated in this study are goal-directed pointing movements (POINTING) and periodic level walking (WALKING). The pointing movements were simulated with a model consisting of two rigid bodies (upper and lower arm) connected by two hinge joints (based on Stollenmaier et al., 2020). The walking model has seven rigid bodies (two legs with foot, shank, thigh and a single head-arms-trunk segment), all connected by six hinge joints (based on Geyer and Herr, 2010). The muscle-driven models considered nonlinear visco-elastic muscle characteristics and muscular activation dynamics, six muscles in the pointing, 14 in the walking model. The torque-driven models use ideal torque actuators in each hinge joint. The control policy in the pointing models (RL policy) is derived by reinforcement learning. Walking in the muscle-driven model is generated by a reflex-based neural control scheme (Geyer and Herr, 2010) and by a PID controller in the torque-actuator model. To determine *control effort*, the control signals are discretized in amplitude (Δu_i) and time (Δt_i). In the STIM and TORQUE scenario, this discretization is applied to the output of the controller, i.e., the muscular control signals or the torque signals, respectively. In the SENS scenario, the input to the controller is discretized, i.e., the proprioceptive sensor signals.

following, we compare control effort for biological and technical systems in the same movement task.

4.1. Movement 1: Pointing

4.1.1. Models

The first movement investigated was a point-to-point arm motion simulated with a 2D arm model (Driess et al., 2018; Stollenmaier et al., 2020). The task is to reach a certain goal position, which also defines the performance criterion P and is described in section 4.1.2 below. The arm model consists of two segments representing the upper and lower arm, which are connected by the elbow and shoulder joint to the fixed shoulder (Driess et al., 2018).

We considered two different ways to generate the actuation torques at the joints: First, a muscle-driven arm model using six Hill-type muscle-tendon units—four monoarticular and two biarticular muscles—that produce torques through nonlinear moment arms. The model of the muscle-tendon units considers the nonlinear force-length-velocity characteristics of the muscle fibers, the nonlinear elasticity of the tendon (Haeufle et al., 2014a), and the biochemical processes leading from neuronal stimulation to muscle force (Hatze, 1977). With this, it considers the visco-elastic and low-pass filter properties of muscles, which are considered to be important for stabilizing movements (Gerritsen et al., 1998; Haeufle et al., 2010; Pinter et al., 2012; John et al., 2013). The details and the parameters of the model can be found in **Supplementary Material** (**Data set 1**).

As a second model to generate the actuation torques, we simply considered two ideal torque actuators that act directly on the joints of the arm.

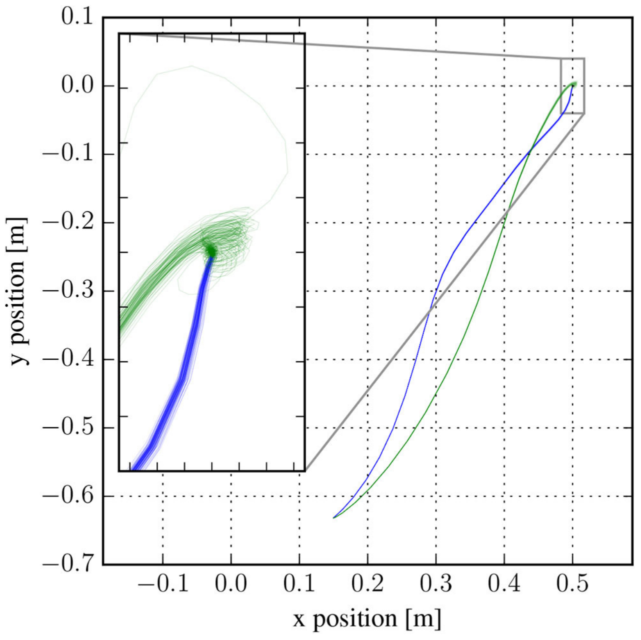

FIGURE 2 | Overlay of 100 sampled trajectories of the end-effector position in the best trained models for the muscle-driven arm (green) and the torque-driven arm (blue). The end-effector moves from its initial position (lower left) to its goal (0.5, 0). Noise in the trajectories arises from noise in the controller (policy) $\pi(a_t|s_t)$. The data shown here was generated without delay in the control loop for both models.

In both cases, we used a deep reinforcement learning (RL) algorithm to obtain a controller for reaching a certain goal position. Details about the RL algorithms can be found in Appendix C. We use Deep RL since it bears parallels to biological learning (Neftci and Averbeck, 2019), and the task is simple enough so that we can find good controllers using such a very general learning scheme. The goal of the RL algorithm is to find a policy π which maps an observation (related to the state of the arm model) to an action (the control input), hence a closed loop controller, such that the expected sum of rewards $\mathbb{E}\left(\sum_{t=1}^{T} r_t\right)$ is maximized. A high reward here corresponds to a low deviation from the target position and low applied muscle activations resp. torques. See Appendix C for a proper mathematical definition of these terms.

In our case, the simulation is interrupted every 10 ms in order to get a new control input. We do this for a fixed number $T \in \mathbb{N}$ of iterations. In each of the T iterations, the simulation yields a state s_t. From the state, we compute an observation $o_t = f(s_t)$. A given policy π then yields a probability distribution $\pi(a_t|o_t)$ from which an action a_t is sampled. This action either corresponds to (normalized) muscle stimulations or to torques. Due to the sampling of the probability distribution, this action has small stochasticity included, similar to motor noise. A fixed reward function R is used to compute a reward $r_t = R(s_t, a_t)$. Using the action a_t as a control input, another 10 ms of movement is simulated and the next state $s_{t+1} = S(s_t, a_t)$ is obtained.

Note that the same RL algorithm was used to learn policies for both models (muscle- and torque-driven arm), but the dimensions of the action and observation spaces differ among these models (cf. Appendix C). By construction of this RL algorithm, the distributions $\pi(a_t|o_t)$ are Gaussian, i.e., the output of the policy always contains additive Gaussian noise with non-zero variance. More specifically,

$$\pi(a_t|o_t) = \mathcal{N}\left(a_t|\mathrm{NN}(o_t), \mathrm{diag}(e^{2s_1}, \ldots, e^{2s_{d_a}})\right),$$

i.e., a_t follows a Gaussian distribution with mean given by a learnable neural network applied to o_t and a diagonal covariance matrix with learnable parameters $s_1, \ldots, s_{d_a}$, where d_a is the dimension of a_t. While the RL algorithm can adapt the variance of the noise during training, Faisal et al. (2008) suggest that humans can also manage to reduce noise in the nervous system by various complicated mechanisms that cannot easily be modeled or are not yet fully understood. **Figure 2** shows that the generated trajectories still contain remaining noise, especially toward the end of the muscle-arm trajectory.

Another difference between the muscle- and torque-driven arm is that we trained and tested the control policy for the muscle-driven model with a delay for sensor signals of 30 ms similar to the electromechanical delay (Mörl et al., 2012; Rockenfeller and Günther, 2016) in human muscles (De Vlugt et al., 2006), i.e., using $o_t = f(s_{t-3})$. We did not consider any control signal delays in our torque-driven model(s) as such delays can be neglected in real-world technical systems that employ torque drives.

4.1.2. Nonlinear Constraint: Movement Performance for Pointing

For pointing movements, we selected as performance criterion P the accuracy of pointing to a specific point in space. For each poll, five simulation runs were performed to ensure that the stochasticity of the controller does not affect the result. Accordingly, it was checked as a first part of the criterion P whether the arm model's "finger" trajectory ended up in a circle around the desired end goal x_{goal} with radius 2.5 cm:

$$(x_{\mathrm{goal}} - x(t_{\mathrm{end}}))^2 + (y_{\mathrm{goal}} - y(t_{\mathrm{end}}))^2 < (2.5\,\mathrm{cm})^2. \tag{9}$$

Note, that the mean over the five simulation runs was taken for the end position of the trajectories $x(t_{\mathrm{end}})$ and $y(t_{\mathrm{end}})$ to account for the effect of movement variability. The second part of P is necessary to ensure that the "finger" not only passes through the target but actually holds this position. Therefore, it was checked whether both angle velocities $\dot{q}_i$ (again averaged) were smaller than a certain threshold:

$$\dot{q}_i < 0.15\,\mathrm{rad/s}, \qquad \text{with } i = 1, 2. \tag{10}$$

Only if both criteria were fulfilled, the poll was considered successful, which gives a conditional expression for the performance criterion as follows:

$$P(\mathbf{r}) = \begin{cases} 0, & \text{if Equation (9) and Equation (10) are true} \\ 1, & \text{otherwise.} \end{cases}$$

4.2. Movement 2: Walking

4.2.1. Models

The second movement investigated in this study was human walking as "defined" by the performance criterion P described in section 4.2.2 below. For this, we resorted to an existing neuromuscular model (Geyer and Herr, 2010). It is a multi-body model with seven segments and hinge-joints in the ankle, knee, and hip. It is actuated by 14 Hill-type muscle-tendon complex models. The muscular control is based on neuronal reflex pathways processing in total 24 proprioceptive signals with biologically realistic neuronal delays. Such a control concept is inspired by the presence of mono-synaptic reflex pathways in the spinal cord, which could explain the low-level implementation of the rhythmic pattern generation of level walking (see Geyer and Herr, 2010, for more details). In forward-dynamic simulations, this model predicts robust walking patterns with strikingly realistic kinematics, ground reaction forces, and muscular activities.

Like for the arm model, we derived a technical model, which, in our case, is a torque-driven model without muscle-tendon characteristics and without neuronal control. This model had the same anthropometrics as the neuromuscular walking model. However, the joint torques for each of the six joints were generated based on PD controllers enforcing the joint kinematics φ_i^{ref} recorded from a reference simulation using the neuromuscular model (Geyer and Herr, 2010):

$$u_i^{\mathrm{TORQUE}} = k_P(\varphi_i - \varphi_i^{\mathrm{ref}}) + k_D(\dot{\varphi}_i - \dot{\varphi}_i^{\mathrm{ref}}),$$

with $i = 1 \ldots 6$ for the six joints (2x ankle, 2x knee, 2x hip). This represents a typical low-level control implementation in classical robotics. We here ignore all potential higher-level planning contributions and replace them with the recorded kinematics as the desired trajectory. This is, therefore, equivalent to the level of investigation in the reflex-driven neuromuscular model.

The joint torque was limited to 1.5 times the maximum active values generated by the muscles in the neuromuscular reference simulation. Two sets of feedback gain parameters k_P and k_D, one for stance and one for swing phase were determined in simulations with very fine discretization ($n = 10^{15}$ and $m = 10^{15}$) by a pattern search algorithm (Matlab (R) global optimization toolbox, with random initial conditions). We will show the results for the two best control parameter sets (CP2 and CP10).

The multi-body dynamics of both models are implemented in SimMechanics 1st generation within Matlab(R), SimulinkTM version 2016a. The differential equations are solved with a variable step solver (ode23s stiff/Mod. Rosenbrock) with relative and absolute tolerance of 10^{-3} and 10^{-4}, respectively. After an initial phase of approximately 5 s, the model's walking pattern is fairly repetitive. Therefore, all evaluations were done on the interval $t \in [5\,\mathrm{s}, 10\,\mathrm{s}]$.

4.2.2. Nonlinear Constraint: Movement Performance for Walking

The nonlinear constraint for the walking model was a combination of a criterion for a desired walking speed and a second one for "not falling": From the continuous walking simulation, we can estimate the typical walking speed of the head-arms-trunk (HAT) segment with linear regression to $\dot{x}_{\mathrm{HAT,cont.}} = 1.33\,\mathrm{ms}^{-1}$. The first criterion for the performance limit is for the x-coordinate of the HAT segment x_{HAT} to stay within 6% to this walking speed:

$$\frac{\left|\dot{x}_{\mathrm{HAT,cont.}} - \dot{x}_{\mathrm{HAT}}(t)\right|}{\dot{x}_{\mathrm{HAT,cont.}}(t)} < 0.06 \qquad (11)$$

The second criterion—not falling—is simply described by the vertical position of the HAT segment y_{HAT}. Simulation tests showed that if the condition

$$y_{\mathrm{HAT}}(t) > 1.24\,\mathrm{m} \qquad (12)$$

is violated, the model is falling and not walking anymore.

If at least one of these criteria is violated, the simulation stops (at t_{stop}) and the performance is the time difference to the desired simulation time

$$P(\mathbf{r}) = T - t_{\mathrm{stop}}. \qquad (13)$$

The optimization constraint

$$P(\mathbf{r}) = 0 \qquad (14)$$

thus only allows for parameter sets which generate walking patterns not violating the above two conditions during the entire simulation time $T = 10\,\mathrm{s}$.

4.3. Discretization of Signals to Determine Control Effort

In principle, it is not clear which signals need to be discretized to determine control effort. At first sight, all output signals of the controller which directly control the actuators—the muscle stimulation or the joint torque signals—seem the obvious choice. However, also the sensor signals provide important information to the system, so it could also be argued that all input signals to the controller need to be discretized (Haeufle et al., 2014b). Here, we tested three scenarios (**Figure 1**).

4.3.1. Discretize Muscle Stimulations (STIM)

In the first scenario, we discretized the muscle stimulations both in time and amplitude for all muscles with the algorithm given above. These discretized muscle stimulations u_i^{STIM} are then used as an input signal to each muscle. Because the muscles can be activated between 0 and 100%, we set $u_i^{\mathrm{STIM,min}} = 0$ and $u_i^{\mathrm{STIM,max}} = 1$ respectively, as well as the duration of the movement $T^{\mathrm{POINTING}} = 1\,\mathrm{s}$ for the pointing movements and $T^{\mathrm{WALKING}} = 5\,\mathrm{s}$. The time and amplitude resolution parameters m_i and n_i of each of the stimulation signals u_i^{STIM} were then varied with the algorithm described above.

4.3.2. Discretize Proprioceptive Sensor Signals (SENS)

In the second scenario, all proprioceptive sensor signals $u_i^{\mathrm{SENS}}(t)$ are discretized in the neuromuscular models (**Figure 1**). Here the minimum u_i^{min} and maximum u_i^{max} signal values were determined from a not discretized reference simulation. As above, the duration was $T^{\text{POINTING}} = 1\,\text{s}$ and $T^{\text{WALKING}} = 5\,\text{s}$ and the signal resolution parameters were optimized for minimal information with the algorithm above.

4.3.3. Discretize Torque Actuations (TORQUE)

In the third scenario, we discretized the control signals for the torque-driven system $u_i^{\text{TORQUE}}(t)$ (**Figure 1**). For the POINTING movement, we set $u_i^{\text{min}} = -20\,\text{Nm}$ and $u_i^{\text{max}} = 20\,\text{Nm}$ to approximately match the capacities of the muscles in the arm model. For the WALKING movement, the minimum u_i^{min} and maximum u_i^{max} signal values were determined from a not discretized reference simulation and the durations were again $T^{\text{POINTING}} = 1\,\text{s}$ and $T^{\text{WALKING}} = 5\,\text{s}$. The signal resolution parameters were optimized for minimal information with the algorithm above.

5. RESULTS

The control effort, i.e., the minimally required information I_{min} to generate pointing and walking movements, is lower in the neuromuscular models STIM and SENS as compared to the TORQUE model (**Figures 3A,B**).

In the pointing movements, the control effort is lowest for the STIM scenario ($I_{\text{min}}^{\text{STIM}} = 67.5\,\text{bit/s}$), where the information is reduced in the output of the controller. The control policy derived by reinforcement learning (RL), however, does not allow to reduce the information as much on the input side (SENS) as on the output side (STIM), resulting in almost three-fold higher control effort ($I_{\text{min}}^{\text{SENS}} = 222.5\,\text{bit/s}$). The torque model requires the most information, resulting in an almost four-fold higher control effort ($I_{\text{min}}^{\text{TORQUE}} = 310.3\,\text{bit/s}$).

In the walking model, the control effort for the STIM and SENS scenarios are quite similar and both about half of the best TORQUE model (**Figure 3B** and **Table 1**). The second best (CP2) PID controller parameters require double the amount of information than the best parameters (CP10).

The discretization—introduced to reduce the information content of the control signals—modifies the walking pattern. In the STIM and SENS scenarios, the parameters $\mathbf{r}_{\text{opt}}$ (minimal information solution) result in slower walking patterns than in the reference solution (**Figure 4**). In the TORQUE scenario, the parameters $\mathbf{r}_{\text{opt}}$ result in strong oscillations in the joint torques (**Figure 5**).

To demonstrate the reduction in information by changing the resolution parameters n_i and m_i to lower values (more coarse), we give the results for the different stages of the optimization algorithm (**Table 1**). The algorithm started with an initial guess of $n_i = 10^{15}$ and $m_i = 10^{15}$, resulting in high initial information content I_0 of the control signals which is about two orders of magnitude larger than the optimal result. This initial guess is highest for the SENS model as this model discretizes all 24 sensor signals—the highest number of signals investigated in this study. Therefore, I_0 is naturally high. Also, the number of required iterations is high, especially in the third stage, due to the high number of possible linear combinations checked in this stage. However, at the end of the third stage, the control effort I_{min} of the SENS model is the lowest.

In this study (**Figure 3A**), the model scenarios STIM and SENS were trained and tested with a sensor delay ($\delta t = 30\,\text{ms}$ in pointing and $\delta t = 5\ldots20\,\text{ms}$ in walking), representing the unavoidable neuronal delay (More et al., 2010) in biology, while the torque model had zero delay representing a modern technical solution. To investigate the influence of sensor delays on control effort in some more depth, we additionally trained

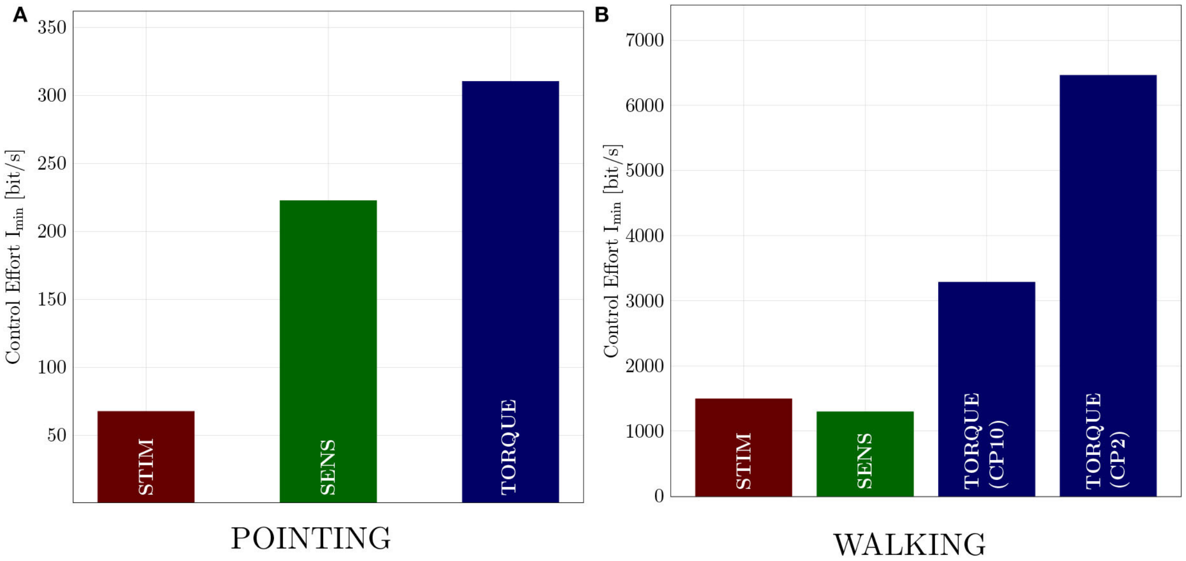

FIGURE 3 | Control effort of **(A)** POINTING movements and **(B)** WALKING. In general, the control effort of walking is higher than the control effort of pointing movements. For both movements, the two neuromuscular models STIM and SENS require less information to generate the motion than the torque-driven model.

TABLE 1 | Control effort of walking as determined with the adapted pattern search algorithm at the different stages of the optimization.

Model	Number of control signals N_u	Initial I I_0 [*kbit*/*s*]	I stage 1 I_1 [*kbit*/*s*]	I stage 2 I_2 [*kbit*/*s*]	Control effort $I_{\min}$ [*kbit*/*s*]	Optim. error ΔI_{opt} [*kbit*/*s*]
STIM	14	688	3.48 #16	2.68 #611	1.49 #21,715	0.0016
SENS	24	1,229	7.74 #16	1.88 #3,275	1.29 #67,953	0.0063
TORQUE (CP10)	6	295	295 #16	3.54 #527	3.28 #209	0.0002
TORQUE (CP2)	6	295	220 #16	7.84 #590	6.46 #434	0.0060

Also given are the number of iterations # for each stage of the optimization. [*kbit/s*] *means* [10^3 *bit/s*].

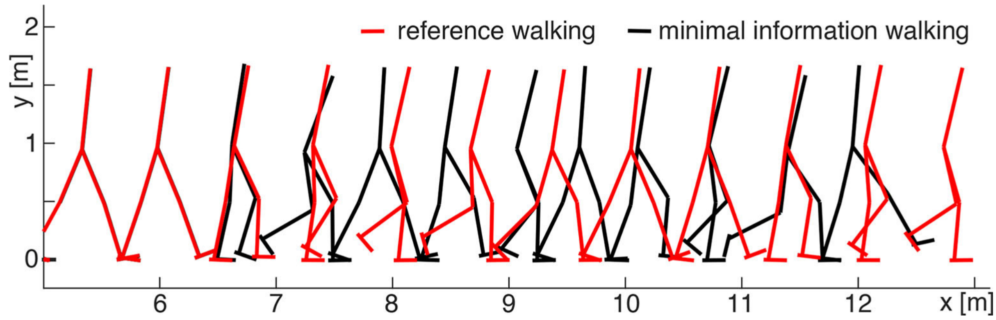

FIGURE 4 | Comparison between walking patterns of the minimal information (SENS model, black) and reference (red) solutions. In the beginning, both solutions overlap until the discretization begins at approximately 6 m walking distance (5 s). Then, the coarse discretization of the minimal information solution affects the walking pattern: the model walks slightly slower than in the reference simulation but still remains within the required performance limit (Equation 11).

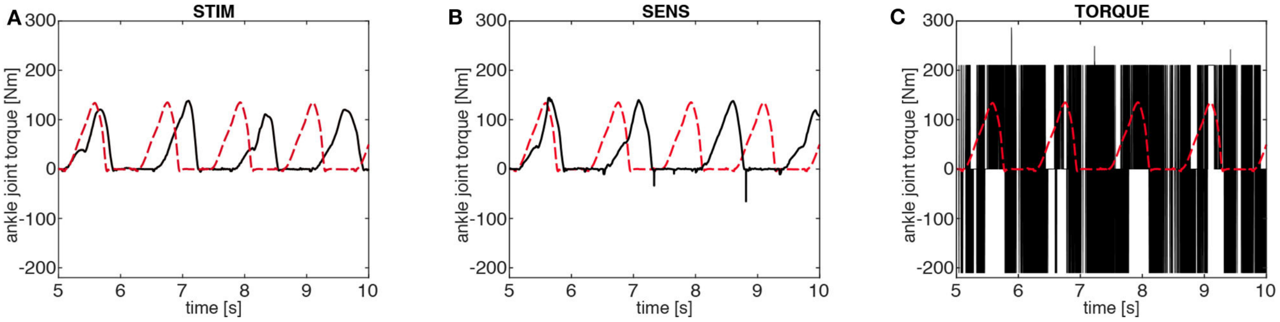

FIGURE 5 | Ankle joint torques of the minimal information solutions. In the STIM **(A)** and SENS **(B)** model, the minimal information solutions (black) involve ankle torques with magnitudes similar to the reference case (red dashed). In the SENS model, the discretization causes over-extensions in the flight phase, which results in short negative torque spikes due to the passive mechanical joint limits of the model. In the TORQUE model **(C)**, the minimal information solution is dominated by a bang-bang pattern between the joint torque limits (±210 Nm). This is a direct result of the coarse discretization of the motor commands u_i^{TORQUE} (see **Figure 1**).

and tested control policies for the neuromuscular POINTING movements without delay (unphysiological) in the muscle-driven and with delay (bad engineering) in the torque-driven model. The resulting optimized control effort is shown in **Figure 6** in relation to the "correct" models. In the muscle-driven models, the control effort increases in the unphysiological zero-delay scenario, while the torque-driven model benefits from zero-delay.

The estimated error of the control effort in walking ΔI_{opt} is small with respect to the difference between the models. The certainty range is an order of magnitude higher than the optimization error. This means that in the last stage of the pattern search, the local neighborhood of the optimal solutions was checked intensively.

Finally, our algorithm is very efficient in finding the control effort. For comparison, we repeated the optimization of the

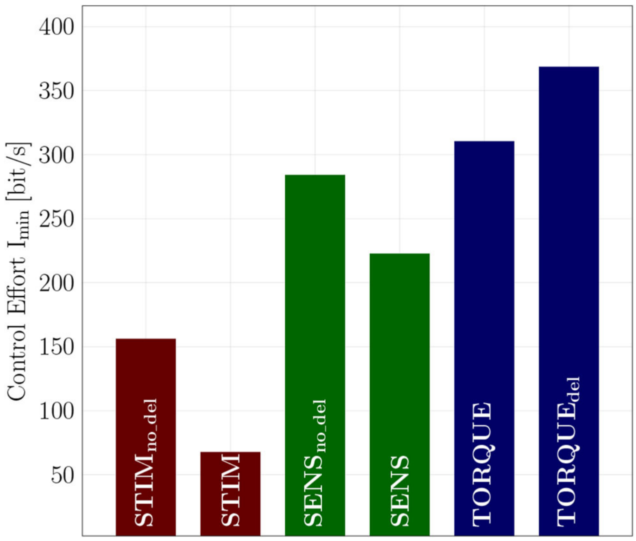

FIGURE 6 | Control effort of the different investigated models, each trained and tested with and without delay for the POINTING movement. The muscle-driven models trained with delay (STIM and SENS) require less information than the corresponding models that were trained and tested without delay ($STIM_{no\_del}$ and $SENS_{no\_del}$). The $TORQUE_{del}$ model, however, requires more information than the TORQUE model without delay.

torque model for the pointing movement with other standard optimization algorithms available in Python and found the following: Our algorithm converged in 42 iterations and found a value of 310 bit. In comparison, *dual annealing* stopped at 385 bit after 1000 iterations (the set limit) with 4,067 total function evaluations. *Differential evolution* stopped at 472 bit after 1,000 iterations (the set limit) with 30,033 total function evaluations. *SHGO* did not converge.

6. DISCUSSION

Control effort is reduced in muscle-driven systems compared to torque-driven systems for pointing and walking movements. This supports the general notion that muscle contraction (van Soest and Bobbert, 1993; Haeufle et al., 2010) and activation dynamics (Kistemaker et al., 2005; Rockenfeller and Günther, 2018, app. A) can serve as a low-level zero-delay feedback system (preflexes; Brown et al., 1995) supporting the generation and control of dynamic movements (Ekeberg et al., 2004; Proctor and Holmes, 2010). Here, we provide quantitative evidence for its contribution and the potential reduction in information load. From our point of view, this is interesting, because the two typical movements chosen differ greatly in their characteristics and by the number of muscles needed for their generation. Thus, control effort seems to be a general measure for the contribution of morphology to perform a specific task in biological and robotic motion.

Minimization of information processing may be a design principle for shaping bodies and structures during biological evolution (Niven and Laughlin, 2008) as it certainly comes along with the minimization in metabolic energy consumption of the information processing structures themselves (Niven et al., 2007). However, it is *competing* with other movement criteria. A prominent example would be the performance, as demonstrated here, but probably other optimization criteria as well, such as maneuverability, jerk, stability, robustness, accuracy, or reproducibility. Pushing this surely incomplete list of potentially relevant movement criteria to extremes, minimization of control effort is definitely competing with the soundness of body tissue: damage and failure are even more costly than corrections and compensations in movement execution. However, we see that the minimization of information processing may be crucial in the evolution of morphology, and our approach allows us to quantify it.

Having this said, we would like to emphasize that we do not expect the actual system to process only this minimal amount of information. Especially in biology, there is an abundance of structures (Latash, 2012)—many muscles, sensors, and neurons—which are not considered here. Also, in robotics, one would never control a robot at this limit, as it is just on the verge of instability. However, by applying this minimal information approach systematically to the same movement but different morphologies, the contribution of the latter can be uncovered and quantified.

6.1. Influence of Delay on Control Effort

Delay in information processing seems per definition unavoidable (Nishikawa et al., 2007; Shadmehr et al., 2010). In robotic systems with their electric cables, the delay can be very small—usually smaller than the typical time resolution Δt. However, it is a universal characteristic of neuronal information processing in biological systems that the delay is, in general, much larger than the time resolution, and scales with the size of the animal (More et al., 2010). Despite these large delays, animals can perform quite well in uncertain environments. In fact, our approach shows that neglecting this delay in the neuromuscular model increases control effort (**Figure 6**). On the other hand, engineers who employ widespread electric motors do good in trying to minimize delay (**Figure 6**).

Neuronal systems have additional possibilities that allow them to compensate drawbacks of delays, which are not considered in our models. They may use open-loop control signals—potentially from an inverse model or a model template (Full and Koditschek, 1999; Holmes et al., 2006)—to drive a movement and only use feedback if a perturbation occurs (Todorov and Jordan, 2003). Furthermore, by predicting sensor states with a forward model (e.g., a template), they may deal with possible instabilities arising from delays (Shadmehr, 2010), at least as long as no external perturbation occurs (Kalveram and Seyfarth, 2009). Despite these neuronal capabilities, the control approach can still rely on the stabilizing response of the visco-elastic muscles to external perturbations (van Soest and Bobbert, 1993; Wagner and Blickhan, 2003; Haeufle et al., 2012; Stollenmaier et al., 2020). Brown et al. (1995) termed these responses “preflexes,” due to their zero time-delay response. There are strong indications that such strain-rate-dependent actuator properties, even more in combination with positive muscle force feedback (Geyer et al., 2003), as well as position-plus-rate characteristics of proprioceptors (McMahon, 1984, p. 154–155) can also provide predictive information that is valuable for movement stabilization. Thus, a delay well-tuned to the controller/control-system interaction may even improve performance (Hedrick and Daniel, 2006; Shadmehr, 2010), and potentially allow to reduce the control effort, as our results indicate.

6.2. Information Processing in Walking Machines

The processed information in a digitally controlled walking machine can be estimated with Appendix A, Equation 17. Although the necessary parameters would be easy to determine for the construction engineer, they are usually not published. As one example, we estimated the parameters for a walking pattern reported for the robot MABEL from information given in Park et al. (2011) and Sreenath et al. (2011). MABEL seems to be interesting for comparison, as it is a 2D walking machine that considers elasticities in the drive. Based on the data provided by the papers, we estimate the total information processed in MABEL per second to be $I = 6.4 \cdot 10^4$ bit/s. The derivation of this is described in more detail in Appendix D.

This value is large in comparison to the minimal information $I_{\min}$ predicted by our models but low in comparison to our initial guess I_0. Obviously, the choice of encoder resolution is not made to generate walking with the least amount of information. This is very well not recommended in a technical system, as low resolutions entail the risk of significant oscillations, as seen in our optimized TORQUE results. However, with this comparison, we speculate that our results are in a reasonable range. To evaluate the contribution of morphology to the control and to verify our model calculations, it would yet be quite interesting to apply our algorithm to MABEL while further modifying the characteristics of this machine's actuators.

6.3. A Hypothetical Scenario Where an Ideal Torque Generator Would Be Advantageous

Above, we exclusively cited papers indicating and demonstrating the benefit of muscles, and our results fit in this picture. Therefore, it is important to point out that control effort cannot be expected to always be lower in muscle-driven systems. For this, we would like to perform a short though experiment. Imagine a hypothetical task: an arm with a single joint has to generate exactly the same tangential endeffector force at any given joint angle (at rest). An ideal torque generator, would require a single constant input signal. Such a signal, per definition of Equation (2), contains the minimally possible control effort as the resolution parameters could be reduced to $m = 1$ and $n = 1$, and, consequently, $I_{\min} = 0$. A muscle-actuated arm, on the other hand, would have to adapt the stimulation to each and every angle as the muscle force depends on its length and therefore also on the joint angle. This is only to highlight that muscles are very well suited for particulary dynamic tasks, but not in general the best actuator for everything.

6.4. Other Optimal Control Approaches for Measuring Simplicity

In the present work, we utilize control effort, which has recently been proposed by us (Haeufle et al., 2014b), to quantify the minimal information required to generate a specific movement. This measure is based on the quantification of the information of the control signals, i.e., sensor signals and actuator command signals, based on SHANNON's information entropy (Shannon and Weaver, 1949, see section 2). By comparing control effort for different morphologies, it quantifies, to some extent, how "simple" it is to generate a specific movement depending on the morphology of the system.

Brockett (1997) argue to consider simplicity as a way to *synthesize* controllers, which they call Minimum Attention Control (MAC). In order to measure simplicity, they introduce the concept of attention, which quantifies the required rate of change of the control to achieve desired changes in the system state. This can be interpreted as the difficulty to implement a respective controller (Brockett, 1997). For example, a control system which can be controlled by just a constant input would require minimal (no) attention. Thus, the basic idea is to find controllers through an optimal control framework where the objective function trades-off system performance with attention, i.e., simplicity of the controller.

In Della Santina et al. (2017), MAC was found as a beneficial solution for controller design in soft robots. Biomechanical systems such as the arm model used in the present work have properties which enable to reach a desired system state with a constant control input. This has been exploited in Driess et al. (2018), Wochner et al. (2020) and Driess et al. (2019) to learn a controller for such systems efficiently. The controllers of Driess et al. (2018) and Driess et al. (2019), Wochner et al. (2020) are, by design, optimal with respect to attention with zero attention, since the controller produces constant controls for each desired system state.

The measure of attention from Brockett (1997) is, in a way, similar to control effort of the present work, as it is also driven by the idea that a specific design of a control system could be beneficial to achieve a certain system behavior without an overly complex controller. Thus, the process of evolving structures and functioning—simultaneous and codependent control system and controller design—can also be supported by MAC.

However, there is also an important difference between MAC and control effort as considered in the present work. MAC is a paradigm to synthesize controllers by integrating it directly into the cost function of an optimal control framework. In contrast, we use control effort here as a measure to analyze the contribution of the systems dynamics to the control of the movement. Therefore, it measures a system property. Indeed, the controllers that are either learned or hand-tuned in this work at no point have the objective to minimize control effort. Solving the optimal control problem with MAC as an objective is non-trivial, especially for nonlinear systems. In the future it could be investigated whether MAC can be extended to nonlinear biomechanical models and to test whether it allows to find controllers that show a difference in attention between musculoskeletal and torque-driven actuators.

6.5. The Optimization Algorithm

Quantifying control effort requires to solve an optimization problem (Equation 3). The algorithm proposed here is novel and specifically designed to efficiently optimize the given problem. The three stages of the algorithm differ in their computational expense, with the first stage being computationally cheap (16 iterations for the walking model), while the other two require more iterations (**Table 1**). For the few control signals discretized in the TORQUE model, the final search in stage 3 is also computationally cheap. For more control signals, the linear combinations tested in the third stage are computationally expensive. It may be considered to exclude the final stage, as we did for the POINTING movements, since the difference in the results between stage two (I_2) and final result ($I_{\min}$) in the walking model are not very large, and the general trend can already be seen. In general, this algorithm can easily be applied to any other simulation of movements, and also to robotic systems (which would, however, require safety measures to avoid damage in the low-resolution trials). By providing it as open source, we hope to foster the quantitative evaluation of control effort and a more systematic study of the contribution of morphology to control in biological systems.

DATA AVAILABILITY STATEMENT

The datasets generated for this study are available on request to the corresponding author.

AUTHOR CONTRIBUTIONS

DFBH, MG, and SS: project idea. DFBH, SS, and MG: control effort algorithm. DFBH, IW, DH, and DD: model. DFBH and IW: data. All authors: paper.

FUNDING

The research was supported by the Ministry of Science, Research and the Arts Baden-Württemberg (Az: 33-7533.-30-20/7/2). This work was funded by Deutsche Forschungsgemeinschaft (DFG, German Research Foundation) under Germanys' Excellence Strategy—EXC 2075-390740016. We further acknowledge support by the International Max-Planck Research School for Intelligent Systems and by the Open Access Publishing Fund of the University of Tübingen.

ACKNOWLEDGMENTS

We would like to thank Daniel Ossig, who spent many hours with a tedious search for specifics of the control frequency and sensor resolution of a humanoid walking robot. We would also like to thank Hartmut Geyer, who provided the walking model, and Dan Suissa, who developed the first version of the arm model. We would like to thank Marc Toussaint for his support in the project. Furthermore, DFBH would like to thank Keyan Ghazi-Zahedi for the fantastic discussions on everything, but also on control effort and morphological computation.

SUPPLEMENTARY MATERIAL

The Supplementary Material for this article can be found online at: https://www.frontiersin.org/articles/10.3389/frobt.2020.00077/full#supplementary-material

REFERENCES

Bayer, A., Schmitt, S., Günther, M., and Haeufle, D. F. B. (2017). The influence of biophysical muscle properties on simulating fast human arm movements. *Comput. Methods Biomech. Biomed. Eng.* 20, 803–821. doi: 10.1080/10255842.2017.1293663

Blickhan, R., Seyfarth, A., Geyer, H., Grimmer, S., Wagner, H., and Günther, M. (2007). Intelligence by mechanics. *Philos. Trans. R. Soc. A* 365, 199–220. doi: 10.1098/rsta.2006.1911

Brockett, W. (1997). "Minimum attention control," in *Proceedings of the 36th IEEE Conference on Decision and Control, Vol. 3* (San Francisco, CA), 2628–2632. doi: 10.1109/CDC.1997.657776

Brown, I. E., Scott, S. H., and Loeb, G. E. (1995). Preflexes–programmable high-gain zero-delay intrinsic responses of perturbed musculoskeletal systems. *Soc. Neurosci.* 21:562.

De Vlugt, E., Schouten, A. C., and Van Der Helm, F. C. (2006). Quantification of intrinsic and reflexive properties during multijoint arm posture. *J. Neurosci. Methods* 155, 328–349. doi: 10.1016/j.jneumeth.2006.01.022

Della Santina, C., Bianchi, M., Grioli, G., Angelini, F., Catalano, M., Garabini, M., et al. (2017). Controlling soft robots: balancing feedback and feedforward elements. *IEEE Robot. Autom. Mag.* 24, 75–83. doi: 10.1109/MRA.2016.2636360

Driess, D., Schmitt, S., and Toussaint, M. (2019). "Active inverse model learning with error and reachable set estimates," in *Proc. of the Int. Conf. on Intelligent Robots and Systems (IROS)* (Macau). doi: 10.1109/IROS40897.2019.8967858

Driess, D., Zimmermann, H., Wolfen, S., Suissa, D., Haeufle, D., Hennes, D., et al. (2018). "Learning to control redundant musculoskeletal systems with neural networks and SQP: exploiting muscle properties," in *Proc. of the Int. Conf. on Robotics and Automation (ICRA)* (Brisbane, QLD). doi: 10.1109/ICRA.2018.8463160

Ekeberg, Ö., Blümel, M., and Büschges, A. (2004). Dynamic simulation of insect walking. *Arthrop. Struct. Dev.* 33, 287–300. doi: 10.1016/j.asd.2004.05.002

Eriten, M., and Dankowicz, H. (2009). A rigorous dynamical-systems-based analysis of the self-stabilizing influence of muscle. *J. Biomech. Eng.* 131, 011011-1-9. doi: 10.1115/1.3002758

Faisal, A. A., Selen, L. P., and Wolpert, D. M. (2008). Noise in the nervous system. *Nat. Rev. Neurosci.* 9, 292–303. doi: 10.1038/nrn2258

Full, R., and Koditschek, D. (1999). Templates and anchors: neuromechanical hypotheses of legged locomotion on land. *J. Exp. Biol.* 202(Pt 23), 3325–3332.

Gerritsen, K. G., van den Bogert, A. J., Hulliger, M., and Zernicke, R. F. (1998). Intrinsic muscle properties facilitate locomotor control–a computer simulation study. *Motor Control* 2, 206–220. doi: 10.1123/mcj.2.3.206

Geyer, H., and Herr, H. (2010). A muscle-reflex model that encodes principles of legged mechanics produces human walking dynamics and muscle activities. *IEEE Trans. Neural Syst. Rehabil. Eng.* 18, 263–73. doi: 10.1109/TNSRE.2010.2047592

Geyer, H., Seyfarth, A., and Blickhan, R. (2003). Positive force feedback in bouncing gaits? *Proc. R. Soc. Lond. B* 270, 2173–2183. doi: 10.1098/rspb.2003.2454

Ghazi-Zahedi, K., Haeufle, D. F. B., Montúfar, G., Schmitt, S., and Ay, N. (2016). Evaluating morphological computation in muscle and dc-motor driven models of human hopping. *Front. Robot. AI* 3:42. doi: 10.3389/frobt.2016.00042

Giszter, S., Mussa-Ivaldi, F., and Bizzi, E. (1993). Convergent force fields organized in the frog's spinal cord. *J. Neurosci.* 13, 467–491. doi: 10.1523/JNEUROSCI.13-02-00467.1993

Gribble, P. L., and Ostry, D. J. (2000). Compensation for loads during arm movements using equilibrium-point control. *Exp. Brain Res.* 135, 474–482. doi: 10.1007/s002210000547

Haeufle, D. F., Grimmer, S., and Seyfarth, A. (2010). The role of intrinsic muscle properties for stable hopping - stability is achieved by the force-velocity relation. *Bioinspir. Biomimet.* 5:016004. doi: 10.1088/1748-3182/5/1/016004

Haeufle, D. F. B., Grimmer, S., Kalveram, K.-T., and Seyfarth, A. (2012). Integration of intrinsic muscle properties, feed-forward and feedback signals for generating and stabilizing hopping. *J. R. Soc. Interface* 9, 1458–1469. doi: 10.1098/rsif.2011.0694

Haeufle, D. F. B., Günther, M., Bayer, A., and Schmitt, S. (2014a). Hill-type muscle model with serial damping and eccentric force-velocity relation. *J. Biomech.* 47, 1531–1536. doi: 10.1016/j.jbiomech.2014.02.009

Haeufle, D. F. B., Günther, M., Wunner, G., and Schmitt, S. (2014b). Quantifying control effort of biological and technical movements: an information-entropy-based approach. *Phys. Rev. E* 89:012716. doi: 10.1103/PhysRevE.89.012716

Hatze, H. (1977). A myocybernetic control model of skeletal muscle. *Biol. Cybern.* 25, 103–119. doi: 10.1007/BF00337268

Hedrick, T. L., and Daniel, T. (2006). Flight control in the hawkmoth manduca sexta: the inverse problem of hovering. *J. Exp. Biol.* 209, 3114–3130. doi: 10.1242/jeb.02363

Holmes, P., Full, R., Koditschek, D., and Guckenheimer, J. (2006). The dynamics of legged locomotion: models, analyses, and challenges. *SIAM Rev.* 48, 207–304. doi: 10.1137/S0036144504445133

John, C. T., Anderson, F. C., Higginson, J. S., and Delp, S. L. (2013). Stabilisation of walking by intrinsic muscle properties revealed in a three-dimensional muscle-driven simulation. *Comput. Methods Biomech. Biomed. Eng.* 16, 451–462. doi: 10.1080/10255842.2011.627560

Kalveram, K. T., and Seyfarth, A. (2009). Inverse biomimetics: how robots can help to verify concepts concerning sensorimotor control of human arm and leg movements. *J. Physiol.* 103, 232–243. doi: 10.1016/j.jphysparis.2009.08.006

Kambara, H., Shin, D., and Koike, Y. (2013). A computational model for optimal muscle activity considering muscle viscoelasticity in wrist movements. *J. Neurophysiol.* 109, 2145–2160. doi: 10.1152/jn.00542.2011

Kistemaker, D., van Soest, A., and Bobbert, M. (2005). Length-dependent [Ca2+] sensitivity adds stiffness to muscle. *J. Biomech.* 38, 1816–1821. doi: 10.1016/j.jbiomech.2004.08.025

Kistemaker, D. a., Van Soest, A. J., and Bobbert, M. F. (2006). Is equilibrium point control feasible for fast goal-directed single-joint movements? *J. Neurophysiol.* 95, 2898–2912. doi: 10.1152/jn.00983.2005

Latash, M. L. (2012). The bliss (not the problem) of motor abundance (not redundancy). *Exp. Brain Res.* 217, 1–5. doi: 10.1007/s00221-012-3000-4

Lewis, R. M., Torczon, V., and Trosset, M. W. (2000). Direct search methods: then and now. *J. Comput. Appl.* Mathematics 124, 191–207. doi: 10.1016/S0377-0427(00)00423-4

McMahon, T. (1984). *Muscles, Reflexes, and Locomotion*. Princeton, NJ: Princeton University Press.

More, H. L., Hutchinson, J. R., Collins, D. F., Weber, D. J., Aung, S. K., and Donelan, J. M. (2010). Scaling of sensorimotor control in terrestrial mammals. *Proc. R. Soc. B* 277, 3563–3568. doi: 10.1098/rspb.2010.0898

Mörl, F., Siebert, T., Schmitt, S., Blickhan, R., and Guenther, M. (2012). Electro-mechanical delay in hill-type muscle models. *J. Mech. Med. Biol.* 12:1250085. doi: 10.1142/S0219519412500856

Neftci, E. O., and Averbeck, B. B. (2019). Reinforcement learning in artificial and biological systems. *Nat. Mach. Intell.* 1, 133–143. doi: 10.1038/s42256-019-0025-4

Nishikawa, K., Biewener, A. A., Aerts, P., Ahn, A. N., Chiel, H. J., Daley, M. A., et al. (2007). Neuromechanics: an integrative approach for understanding motor control. *Integr. Compar. Biol.* 47, 16–54. doi: 10.1093/icb/icm024

Niven, J., Anderson, J., and Laughlin, S. (2007). Fly photoreceptors demonstrate energy-information trade-offs in neural coding. *PLoS Biol.* 5:e116. doi: 10.1371/journal.pbio.0050116

Niven, J., and Laughlin, S. (2008). Energy limitation as a selective pressure on the evolution of sensory systems. *J. Exp. Biol.* 211(Pt 11), 1792–1804. doi: 10.1242/jeb.017574

Park, H. W., Sreenath, K., Hurst, J. W., and Grizzle, J. W. (2011). Identification of a bipedal robot with a compliant drivetrain: parameter estimation for control design. *IEEE Control Syst. Mag.* 31, 63–88. doi: 10.1109/MCS.2010.939963

Paul, C. (2006). Morphological computation: a basis for the analysis of morphology and control requirements. *Robot. Auton. Syst.* 54, 619–630. doi: 10.1016/j.robot.2006.03.003

Pinter, I. J., Van Soest, A. J., Bobbert, M. F., and Smeets, J. B. J. (2012). Conclusions on motor control depend on the type of model used to represent the periphery. *Biol. Cybern.* 106, 441–451. doi: 10.1007/s00422-012-0505-7

Proctor, J., and Holmes, P. (2010). Reflexes and preflexes: on the role of sensory feedback on rhythmic patterns in insect locomotion. *Biol. Cybern.* 102, 513–531. doi: 10.1007/s00422-010-0383-9

Rios, L. M., and Sahinidis, N. V. (2013). Derivative-free optimization: a review of algorithms and comparison of software implementations. *J. Global Optim.* 56, 1247–1293. doi: 10.1007/s10898-012-9951-y

Rockenfeller, R., and Günther, M. (2016). Extracting low-velocity concentric and eccentric dynamic muscle properties from isometric contraction experiments. *Math. Biosci.* 278, 77–93. doi: 10.1016/j.mbs.2016.06.005

Rockenfeller, R., and Günther, M. (2018). Inter-filament spacing mediates calcium binding to troponin: a simple geometric-mechanistic model explains the shift of force-length maxima with muscle activation. *J. Theor. Biol.* 454, 240–252.

Shadmehr, R. (2010). Control of movements and temporal discounting of reward. *Curr. Opin. Neurobiol.* 20, 726–730. doi: 10.1016/j.conb.2010.08.017

Shadmehr, R., Smith, M. A., and Krakauer, J. W. (2010). Error correction, sensory prediction, and adaptation in motor control. *Annu. Rev. Neurosci.* 33, 89–108. doi: 10.1146/annurev-neuro-060909-153135

Shannon, C, and Weaver, W. (1949). *The Mathematical Theory of Communication*. Urbana: University of Illinois Press.

Sreenath, K., Park, H.-W., Poulakakis, I., and Grizzle, J. W. (2011). A compliant hybrid zero dynamics controller for stable, efficient and fast bipedal walking on MABEL. *Int. J. Robot. Res.* 30, 1170–1193. doi: 10.1177/0278364910379882

Stollenmaier, K., Ilg, W., and Haeufle, D. (2020). Predicting Perturbed human arm movements in a neuro-musculoskeletal model to investigate the muscular force response. *Front. Bioeng. Biotechnol.* 8:308. doi: 10.3389/fbioe.2020.00308

Todorov, E., and Jordan, M. I. (2003). "A minimal intervention principle for coordinated movement," in *Advances in Neural Information Processing Systems*, 27–34.

Torczon, V. (1997). On the convergence of pattern search algorithms. *SIAM J. Optim.* 7, 1–25. doi: 10.1137/S1052623493250780

van der Krogt, M. M., de Graaf, W. W., Farley, C. T., Moritz, C. T., Richard Casius, L. J., and Bobbert, M. F. (2009). Robust passive dynamics of the musculoskeletal system compensate for unexpected surface changes during human hopping. *J. Appl. Physiol.* 107, 801–808. doi: 10.1152/japplphysiol.91189.2008

van Soest, A., and Bobbert, M. (1993). The contribution of muscle properties in the control of explosive movements. *Biol. Cybern.* 69, 195–204. doi: 10.1007/BF00198959

Wagner, H., and Blickhan, R. (1999). Stabilizing function of skeletal muscles: an analytical investigation. *J. Theor. Biol*. 199, 163–179. doi: 10.1006/jtbi.1999.0949

Wagner, H., and Blickhan, R. (2003). Stabilizing function of antagonistic neuromusculoskeletal systems: an analytical investigation. *Biol. Cybern*. 89, 71–79. doi: 10.1007/s00422-003-0403-0

Wochner, I., Driess, D., Zimmermann, H., Haeufle, D. F. B., Toussaint, M., Schmitt, S., (2020). Optimality principles in human point-to-manifold reaching accounting for muscle dynamics. *Front. Comput. Neurosci*. 14. doi: 10.3389/fncom.2020.00038

Zahedi, K., and Ay, N. (2013). Quantifying morphological computation. *Entropy* 15, 1887–1915. doi: 10.3390/e15051887

Conflict of Interest: The authors declare that the research was conducted in the absence of any commercial or financial relationships that could be construed as a potential conflict of interest.

V. Contribution 5: Learning with Muscles: Benefits for Data-Efficiency and Robustness in Anthropomorphic Tasks

Learning with Muscles: Benefits for Data-Efficiency and Robustness in Anthropomorphic Tasks

Isabell Wochner[*1] **Pierre Schumacher**[*2,3] **Georg Martius**[2]

Dieter Büchler[2] **Syn Schmitt**[†1] **Daniel F.B. Haeufle**[†1,3]

[1]Institute for Modelling and Simulation of Biomechanical Systems, University of Stuttgart, Germany
[2]Max Planck Institute for Intelligent Systems, Tübingen, Germany
[3]Hertie-Institute for Clinical Brain Research, University of Tübingen, Germany

Abstract: Humans are able to outperform robots in terms of robustness, versatility, and learning of new tasks in a wide variety of movements. We hypothesize that highly nonlinear muscle dynamics play a large role in providing inherent stability, which is favorable to learning. While recent advances have been made in applying modern learning techniques to muscle-actuated systems both in simulation as well as in robotics, so far, no detailed analysis has been performed to show the benefits of muscles when learning from scratch. Our study closes this gap and showcases the potential of muscle actuators for core robotics challenges in terms of data-efficiency, hyperparameter sensitivity, and robustness [2].

Keywords: reinforcement learning, model predictive control, actuator morphology

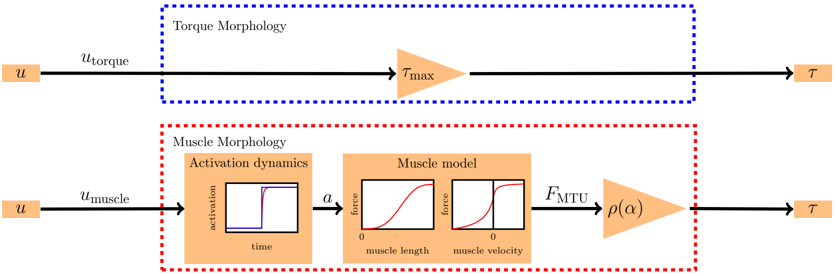

Figure 1: Key differences between torque actuator morphology and muscle actuator morphology.

1 Introduction

Recent developments in new learning methods allow the generation of complex anthropomorphic motions such as grasping, jumping or hopping in robotics. However, current systems still struggle with real-world scenarios beyond the narrow conditions of laboratory experiments. Humans, on the other hand, are capable of quickly adapting to uncertain, complex, and changing environments in a sheer endless variety of tasks. One key difference between biological and robotic systems lies in their actuator morphology: robotic drives are mostly designed to yield a linear relation between control signal and output torque. In contrast, muscles have complex nonlinear characteristics.

It has already been demonstrated, that muscular nonlinearities may provide a benefit for stability and robustness, especially under environmental uncertainties or perturbations [1, 2, 3]. A benefit over linear torque actuator morphology has been observed in computer simulations by exchanging the actuator morphology (similar to Fig. 1) in otherwise identical anthropomorphic tasks like reaching [4]

---

[*] Equal contribution. † Equal contribution.

[2] See `https://sites.google.com/view/learning-with-muscles` for code and videos.

6th Conference on Robot Learning (CoRL 2022), Auckland, New Zealand.

or locomotion [5, 6, 7, 8]. Similarly, reduced demand on the information processing capacity has been shown for muscles when compared to torque actuator morphology [9, 10, 11, 12, 13]. This opens the question whether muscular morphology could also be beneficial for robustness and data-efficiency in the process of *learning* movement control.

Recent advances in deep learning facilitated the generation of complex movements like point-reaching [14, 15, 16, 17] and locomotion [18, 19, 20, 21, 17] in simulations with muscular actuator morphology. In the real world, optimization and learning approaches can also find controllers for robotic systems with pneumatic muscles exhibiting somewhat muscle-like actuator morphology [22, 23]. These examples demonstrate that learning and optimization methods *can* control muscle-driven systems and may enable benefits such as safe learning and robustness [23]. However, investigating advantages of nonlinear muscular actuator morphology over linear torque actuator morphology requires a direct comparison of both, which is—to our knowledge—missing in the literature.

While Peng et al. [24] performed a comparative analysis of different actuator morphologies, their work was focused on replicating reference trajectories. In contrast, we learn behaviors without demonstrations, provide extensive hyperparameter ablations and not only employ RL, but also other optimization methods applied to complex 3D models.

The purpose of this study is to test if learning with muscular actuator morphology is more data-efficient and results in more robust performance as compared to torque actuator morphology when learning from scratch. We investigate this in a very broad approach: we employ different learning strategies on multiple anthropomorphic models for multiple variants of reaching and locomotion tasks solved in physics simulators of differing levels of detail. This provides new and comprehensive evidence of the beneficial contribution of muscular morphology to the learning of diverse movements.

2 Morphological difference between torque and muscle actuators

In contrast to idealized torque actuators, where torque is simply proportional to the control signal $u_{\text{torque}} \in [-1, 1]$,

$$\tau = \tau_{\max} \, u_{\text{torque}} \tag{1}$$

muscular force output nonlinearly depends on the muscle control signal u_{muscle}, the muscle length l_{MTU} and contraction velocity $\dot{l}_{\text{MTU}}$. These biologically observed dependencies can be predicted by so-called *Hill-type* muscle models [25]. In a nutshell, the model captures biochemical processes transforming muscle stimulation $u_{\text{muscle}} \in [0, 1]$ to the force-generating calcium ion activity a. This can be modeled by a first-order differential equation of the form [26]

$$\dot{a} = f_a(u_{\text{muscle}} - a) \tag{2}$$

which induces low-pass filter characteristics (Fig. 1). The model further captures the nonlinear *force-length* and *force-velocity relations* [25]. The *force-length relation* is characterized by a positive slope (increasing force with increasing muscle fiber length) in the typical operating range of biological muscle fibres (Fig. 1). The *force-velocity* relation is characterized by decreasing force for faster shortening velocities and increasing force if the muscle is externally stretched against its contraction direction (Fig. 1). A lever arm $\rho(\alpha)$ translates joint angle α into muscle-tendon-unit length l_{MTU} and muscle force into joint torque

$$\tau = \sum_{i=1}^{N} \rho_i(\alpha) f_\tau \left(l_{\text{MTU},i}(\alpha), \dot{l}_{\text{MTU},i}(\dot{\alpha}), a_i \right) . \tag{3}$$

for N muscles which span a joint—typically at least two in an antagonistic arrangement.

In practice, we employ two different muscle models: A detailed one with more physiological details, contained in demoa [27], and a simpler model that efficiently adds muscular properties to existing MuJoCo [28] simulations without sacrificing computational speed. See Suppl. 6 for details.

3 Methods

3.1 Learning approaches for movement control

We test if muscle actuator morphology facilitates learning by applying state-of-the-art learning algorithms covering an extensive range of approaches currently used in robotics. The common thread of the selected algorithms lies in their independence of the actuator morphology: this allows us to easily exchange idealized torque actuator morphology with muscle actuator morphology. We choose optimal control, model-predictive control and reinforcement learning as learning approaches.

Table 1: **Overview of all models and tasks**

Model	Task	Control	Environment
ArmMuJoCo	precise reaching	RL	MuJoCo
ArmMuJoCo	fast reaching	RL	MuJoCo
ArmDemoa	smooth point-reaching	opt. control, MPC	demoa
ArmDemoa	hitting ball with high-velocity	opt. control, MPC	demoa
Biped	hopping	RL	MuJoCo
FullBody	squatting	opt. control, MPC	demoa
FullBody	high-jumping	opt. control, MPC	demoa


(a) ArmMuJoCo (b) ArmDemoa (c) Biped (d) FullBody

Figure 2: Models used for the experiments.

Optimal control (OC) The control problem with horizon N can be defined as:

$$\min_{\pi_k} J = \min_{\pi_k} \sum_{k=0}^{N} l(x(k), u(k), k), \qquad \text{subject to } x(k+1) = f(x(k), u(k), k),$$
$$u(k) = \pi_k(x(0), ..., x(k)). \tag{4}$$

where $x(k) \in \mathbb{R}^{n_x}$ denotes the current state at time k, and $u(k) \in \mathbb{R}^{n_u}$ is the applied input at time k. Furthermore, l specifies the cost function, and f denotes the system dynamics. To optimize for the best control policy, we use the covariance matrix adaptation evolution strategy (CMA-ES) [29] in the optimal control case (open-loop strategy). CMA-ES is a derivative-free algorithm and widely used in machine learning. It combines different learning mechanisms for adapting the parameters of a multivariate normal distribution. Note, that we choose the same optimization parameters for both actuator morphologies to allow for a fair comparison even though the number of decision variables n_u is always larger in the muscle-actuated case due to the antagonistic setup.

Model predictive control (MPC) In MPC, we solve the control problem in a receding-horizon fashion with varying prediction horizons and recursively apply only the first element of the predicted optimal control sequence $u(0)$ (closed-loop strategy). We employ a warm start procedure using the CMA-ES optimizer and afterwards start the MPC routine with the local optimizer BOBYQA [30]. The parameters of the optimizers are either varied (see Sec. 4) or given in Suppl. 7.

Reinforcement learning (RL) RL allows learning of reusable feedback controllers. Instead of *minimizing* a cost function (see Eq. 4), conventionally the discounted expected reward is *maximized*:

$$\max_{\pi} J = \max_{\pi} \mathbb{E}\left[\sum_{k=0}^{N-1} \gamma^{k-1} r(k)\right] \tag{5}$$

where $r(k)$ is the reward at time k, π is a control policy and $\gamma \in [0, 1]$ is a discount factor such that long-term rewards are weighted less strongly. RL consequently solves a similar problem to MPC, but the resulting controllers are able to act in closed-loop fashion without being given an explicit prediction model. For the point-reaching tasks, we additionally employ goals g characterizing the desired hand position, which then constitutes an additional dependence of the reward function. The aim of the learning process is to learn a controller policy $\pi(u(k)|x(k))$ that takes as input the current sensor values, or state x(k), and outputs a control signal, or action, $u(k)$ such that a task is solved. In practice, we use the RL algorithm MPO [31], implemented in TonicRL [32].

3.2 Models

Arm The Arm model (Fig. 2 a, b) consists of two segments connected with hinge joints (2 joints total) moving against gravity. The ArmMuJoCo [28, 17] model contains four muscles, two for each joint. In the muscle-actuated case in ArmDemoa [33, 34], six Hill-Type muscles generate forces: two muscles for the shoulder and two for the elbow joint, plus two biarticular muscles acting on both joints. All joints are individually controllable.

Biped We converted the geometrical model of an OpenSim bipedal human without arms [19] for use in MuJoCo. The model, consisting of 7 controllable joints (lower back, hips, knees, ankles) moves in a 2D plane. Each joint is actuated by two antagonistic muscles or one torque actuator.

FullBody The FullBody model [35, 36] consists of two legs and an upper body including arms based on a human skeletal geometry. It consists of 8 controllable joints (ankles, knees, hips, lumbar and cervical spine) in 3D, and 14 movable joints in total including the arms. Each controllable joint was either actuated by two antagonistic muscles (muscle-actuated case) or by one idealized torque actuator (torque-actuated case). For more details, we refer to Suppl. 8.

All models and their respective physics differential equations were solved with variable time step (max. time step 0.001s) in demoa and fixed time step (0.005s) in MuJoCo.

3.3 Objectives and rewards

We choose anthropomorphic movement objectives which are highly relevant for robotic applications. We expect that muscular actuator morphology provides benefits for such tasks. All task formulations allow application in muscle and torque actuator morphologies with an identical reward or objective function. For a precise formulation of the used functions and conditions, see Suppl. 9.

Smooth point-reaching This task encourages *smooth* point-reaching. Therefore, the objective minimizes the L2-error between the desired and current joint angle while penalizing the angle velocity and jerk to ensure a smooth motion. The desired angle is 90° for both the shoulder and the elbow joint, as this requires a large motion.

Precise point-reaching Similar to [13], we incentivize reaching a random hand position in a predetermined rectangle, while minimizing the distance of the end effector to the goal. We specifically add a reward term that gives a much larger reward for precise motions that reach the center of the target area. The episode does not terminate until a time limit of 1000 steps elapses.

Fast point-reaching The same objective as for precise point-reaching is used, but the episode terminates if the target is reached, incentivizing reaching speed over precision.

High-velocity ball serve A ball is dropped in front of the Arm model and the controller learns to hit the ball to achieve maximum ball velocity.

Squatting This squatting objective is taken from [35] and encourages desired hip, knee, and ankle angles for a squatting position.

Maximum height jump The objective for the high-jumping task is taken from [37] and maximizes the position and velocity of the centre of mass of the human body model at the time of lift-off. The model is initialized to start from a squatting position.

Hopping We developed an objective based on the z-axis velocity of the center of mass (COM) of the system that encourages periodic hopping with maximum height. The episode terminates if extreme joint angles are exceeded.

4 Results

In the following, we present three major results for the investigated approaches and environments: (**1**) Muscle-like actuators in general improve data-efficiency compared to torque-actuators. (**2**) The investigated learning and optimization algorithms exhibit greater robustness to hyperparameter variations when applied to muscle-driven systems. (**3**) The motions and controllers obtained from the muscular morphology are more robust against force perturbations that were not present during learning. We average results over 5 and 8 random seeds for OC/MPC and RL respectively.

4.1 Data efficiency: Learning with limited resources

Robotics applications in real-world scenarios often suffer from limited resources, which holds true for training and inference time. Therefore, we investigate the advantages of muscle-like actuator morphology in terms of overall learning efficiency and temporal control resolution.

Advantages of muscular morphology Smooth and precise point-reaching generally require more data with torque-driven systems, as seen in Fig. 3. The performance of the muscle actuator, in contrast to torque morphology, varies very little for different settings of the temporal control resolution c. Precise reaching with RL also results in stable performance with fewer training iterations, and a very

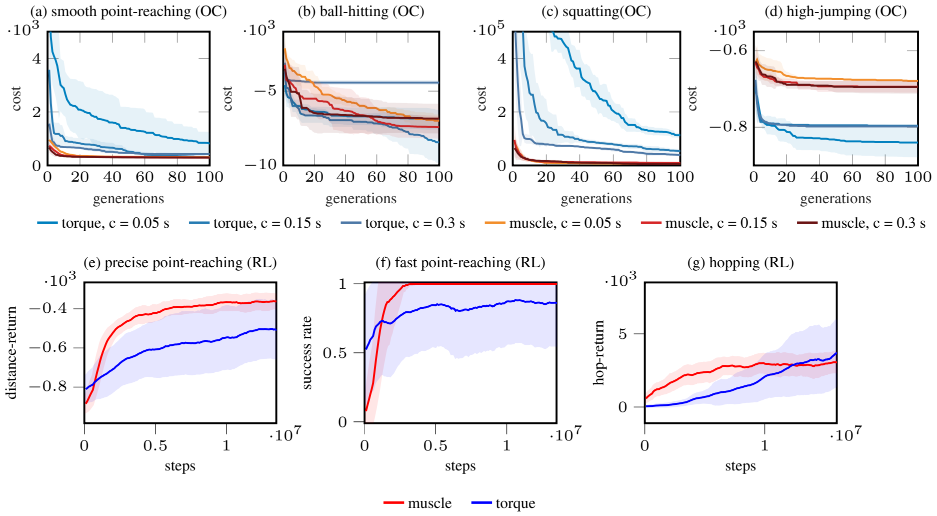

Figure 3: **Cost value or returns for different tasks.** Plotting the mean and standard deviation (shaded area) for 5 (OC/MPC) or 8 (RL) repeated runs for the two actuator morphologies (muscle in red, torque in blue). Additionally, the temporal control resolution c was varied in the OC cases.

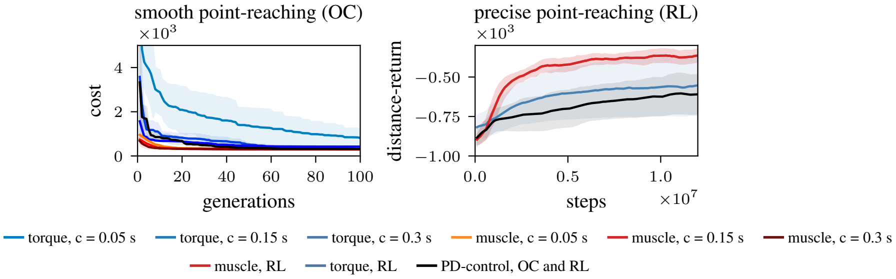

Figure 4: **Cost value or return in comparison with PD-control for torque.** Left: Muscles outperform all other considered morphologies with OC, while PD-control achieves lower cost than torque actuation with large control resolution $c = 0.3$. Right: PD-control does not yield an advantage over torque actuators with RL when applied to the precise point-reaching task.

small standard deviation across runs. Similar findings are seen for the squatting and hopping task, where muscle-actuators achieve better data-efficiency and smaller variation across runs and are able to find a good-enough optimum with fewer iterations.

Advantages of torque morphology In tasks requiring fast and strong motions, without emphasis on stabilization, we find torque actuators to hold certain advantages. In ball hitting and fast reaching, the torque cases show similar or smaller variance, even though both actuators perform well for singular runs. The high-jumping task, where only a strong, swift motion is required to launch the system upwards, is solved much faster in the torque case. We can also observe in the hopping task that, although only after a considerable number of training iterations and exhibiting a large variance, some torque-actuated runs achieve a larger overall return than the best muscle-actuated runs.

We additionally investigated a PD controller for the torque actuator morphology, see Fig. 4. While the PD controller slightly improves the data-efficiency for some cases, for both OC as well as for RL, the muscle actuator outperforms all baselines. See Sec. 11.2 for more experiments.

4.2 Robustness to hyperparameter variations

Tuning a growing number of hyperparameters for learning models typically requires considerable time and computational resources. By analysing hyperparameter sensitivity, we test if tuning with torque or muscle actuator morphologies requires less resources.

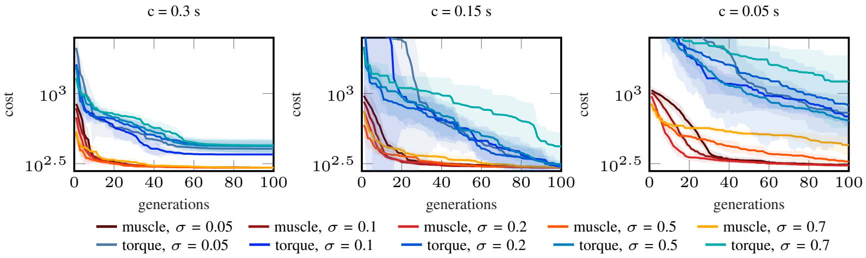

Figure 5: **Muscle morphology is more robust towards hyperparameter variation (σ) in point reaching.** The cost value of the best observation is shown. The mean and standard deviation (shaded area) are plotted for five repeated runs for the two actuator morphologies (muscle in red, torque in blue) with different control resolutions c.

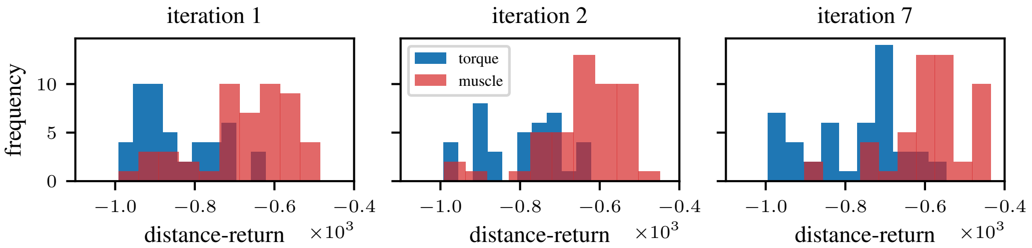

Figure 6: **Muscle actuators need less parameter tuning for good performance.** Hyperparameters are optimized for precise point-reaching following an iterative sampling scheme, each run trains for 2×10^6 iterations. Fifty sets of parameters are sampled randomly from pre-determined distributions, the final performance is evaluated and used to adapt the sampling distributions for the next iteration. We plot the return distributions over the sampled parameters at different iterations.

Figure 5 shows the cost curves for smooth point-reaching for the evolutionary optimization algorithm CMA-ES for different values of σ, which is the principal tuneable parameter for this algorithm. The performance curves vary much more for torque actuators for all considered cases. Furthermore, all muscle-actuated cases find a good-enough optimum with fewer iterations and a smaller variance, independent of the hyperparameter σ and the control resolution c.

The same task was repeated using MPC while varying the main hyperparameter t_{pred}, which represents the prediction horizon in moving horizon strategies. The performance curves and the final cost vary much more for torque actuators (Fig. 7a, note, the cost is plotted logarithmically).

Finally, we performed an extensive hyperparameter optimization for precise point-reaching. For each iteration, 50 sets of parameters are randomly chosen and the final task performance is evaluated after 2×10^6 learning iterations. The sampling distributions for the parameters are then fit to the best performing runs and 50 additional sets are evaluated for the next iteration. We optimize the learning rates of MPO, as well as gradient-clipping thresholds, as these have a strong influence on learning speed and stability. Muscle actuators already outperform torque-actuators in the first iteration, with a greater number of well performing parameter sets (Fig. 6). Almost no low-performing runs remain for iteration 7, while a large torque-performance is only achieved by a small subset of parameter settings. See Suppl. 10 for more hyperparameter variations.

4.3 Robustness to perturbations

In this section, we probe the robustness of the obtained policies against unknown perturbations. In precise point-reaching, we evaluated the RL reaching policies for two modifications that were not present during training: First, the hand-weight of the model is increased by 1.5 kg (dynamic load), and secondly a free spherical weight is attached to the end effector with a cable (chaotic load). We can see in Fig. 8 that the muscle-based policy does not suffer significant changes in performance, except for a small circular motion (3 cm) around the goal position in the chaotic load case. In contrast, the torque actuator morphology leads to unstable reaching and strong oscillations. Both morphologies seem to handle the dynamic load well. See Suppl. 10 for more goals.

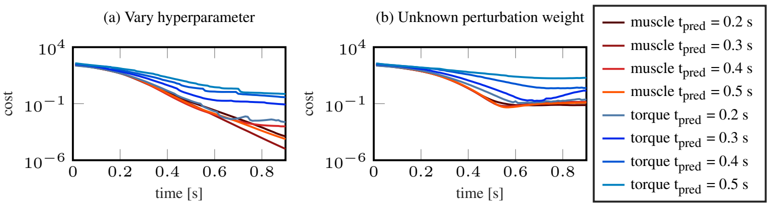

Figure 7: **Muscle morphology is more robust towards variation of hyperparameter t_{pred} and unknown perturbations.** Plotting the development of cost over time for the two actuator morphologies (muscle in red, torque in blue) while varying the hyperparameter t_{pred} denoting the length of the prediction horizon. Left: The unperturbed case. Right: The prediction model is not aware of the added weight to the lower arm.

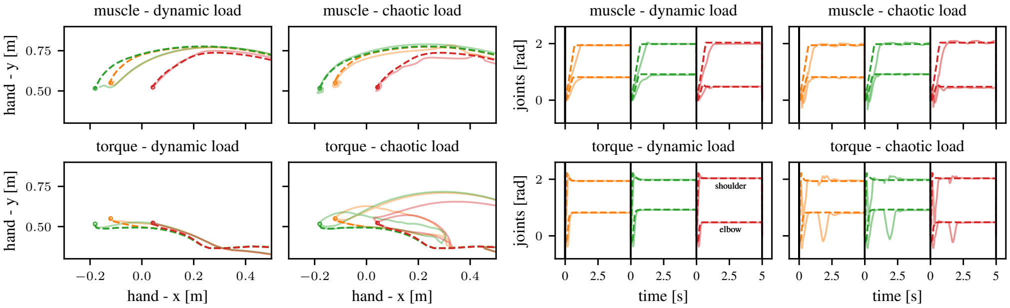

Figure 8: **Trajectories for dynamic (1.5 kg weight) and chaotic (attached ball) load.** Left: Three random goals are exemplarily shown, the respective goal position is marked as a circle. The unperturbed baseline for each goal is shown with a dashed line. Right: Joint trajectories for the same experiment, the unperturbed baselines are shown with dashed lines. Vertical bars mark episode resets.

For the MPC controller, we evaluated robustness by introducing environment changes that are unknown to the prediction model. One example is the lifting of an object with unknown weight, a typical robotics task. When adding 1 kg to the lower arm of the ArmDemoa model (Fig. 7), the performance in both actuator cases is worse than in the unperturbed case (left); the movement is also slower. However, the variance and absolute value of the final cost in the muscle-actuated case are still much lower compared to the torque-actuated case (plotted logarithmically). See Suppl. 11.3 for more weight variations.

For periodic hopping with the Biped model, we evaluated trained RL policies with random forces that were drawn from a Gaussian distribution $F \sim \mathcal{N}(\cdot|0, \sigma_F)$ and applied to the hip, knee, and ankle joints with a probability of 0.05 at each time step. We see in Fig. 10 that the torque actuator morphology is stronger affected in relative performance than the muscle morphology. In the robustness investigation with MPC in the FullBody squatting task, a force is applied to the hip joint after the system has reached its desired position. Figure 9 (left) shows that the desired joint angles are much less affected by the perturbation when muscle actuators are controlled. Furthermore, the cost value associated with the movement recovers much slower for torque actuators (Fig. 9 right).

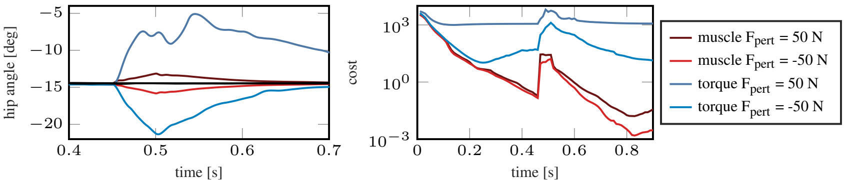

Figure 9: **Hip and cost trajectory for squatting with unknown perturbation forces.** The muscle morphology is shown in red, the torque morphology in blue while varying the perturbation force F_{pert} [N] (applied between $t >= 0.45$ s and $t <= 0.5$ s).

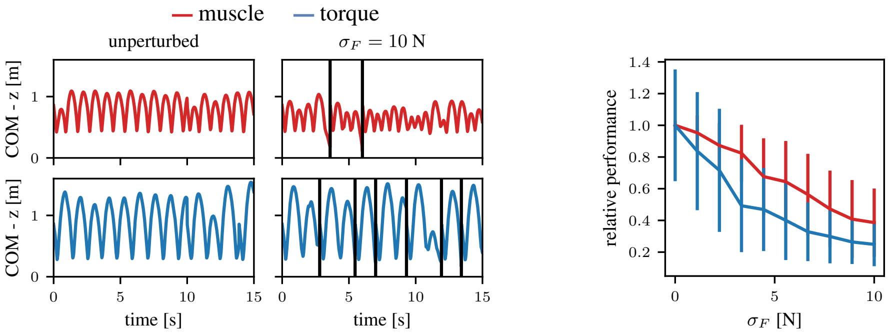

Figure 10: **Muscle actuators lead to more robust hopping.** At each time step, there is a 5 % chance of a random force being applied to the hip, knee, and ankle joints. Left: COM motion over time. Vertical bars mark episode resets due to falls of the Biped. Right: Relative performance for different standard deviations of the random force σ_F. Performance is scaled by the unperturbed mean return.

5 Discussion

We investigated if muscle-like actuators have beneficial effects for modern learning methods in terms of data-efficiency, hyperparameter sensitivity and robustness to perturbations. A multitude of variations across physics simulators, learning algorithms and task domains was considered in order to showcase the potential of the considered morphologies independently of the underlying implementation. We showed that muscles yield benefits in tasks requiring stable motion, even when compared to idealized torque actuators, which can be considered an upper performance bound. Indeed, the used torque actuators are able to instantaneously output any desired force at any point of the trajectory, while muscles only slowly change their output due to activation dynamics and can only produce kinematics-dependent force output. Despite these limitations, the considered learning algorithms learn more efficiently with muscle actuation in all tasks, except for extreme motions where objectives require a strong force application without stability considerations, such as ball-hitting and high-jumping. In bipedal hopping, it was found that muscles result in more efficient learning, even though some torque-runs achieve higher asymptotic performance. Finally, we observe muscle actuation to result in increased robustness to perturbations and hyperparameter variations, which can facilitate learning on real robotic systems that not only present sensor and motor noise, but also prohibit extensive parameter searches.

Outlook for real-world robotics We see two use-cases of our findings: (1) Muscular force-length-velocity and low-pass filter characteristics can be implemented as low-level actuator control for torque-controlled robotic systems (e.g., [38, 39, 40, 41]). This could allow us to exploit the improved data efficiency and robustness observed in our study for RL on a real robotic system. (2) Novel soft robotic actuators, such as artificial muscles [42, 43, 44, 45], promise to revolutionize specific application scenarios of robotics, e.g., wearable rehabilitation devices [46]. While soft actuated systems are hard to control from a classical control theory point of view, our results and other works [24] suggest that RL may even benefit from their properties. In our study, the simplified MuJoCo muscle model is applicable as a low-level controller in the sense of the first use case, while the results with the complex series-elastic muscle model in Demoa highlights the second use-case, making both cases strong arguments to consider RL and muscle properties a promising combination.

Limitations Although we have reported results for a wide variety of algorithms and tasks, we cannot give theoretical statements about the general applicability of our findings. Additionally, some of the tasks we employed were limited in complexity and might also be solvable with classical control algorithms. The MuJoCo muscle model, while computationally efficient, only captures rudimentary properties of biological systems. The demoa implementation, on the other hand, includes visco-elastic, passive tendon characteristics and muscle routing as joint angle-dependent lever arms to account for many physiological details—at substantial additional computational cost. Finally, learning with intermediate control signals given to impedance or position controllers, instead of direct torque commands, might also improve learning performance, while muscle-like properties could have been introduced by learning priors or additional cost terms.

Acknowledgments

We thank Daniel Höglinger for help during the development of the hopping reward function. Furthermore, we like to thank Marc Toussaint, Danny Driess and David Holzmüller for initial discussions regarding the topic of learning with muscles. This work was supported by the Deutsche Forschungsgemeinschaft (DFG, German Research Foundation) under Germanys Excellence Strategy - EXC 2075 - 390740016 (SimTech). We thank the International Max Planck Research School for Intelligent Systems (IMPRS-IS) for supporting all authors. Georg Martius is a member of the Machine Learning Cluster of Excellence, EXC number 2064/1 Project number 390727645. This work was supported by the Cyber Valley Research Fund (CyVy-RF-2020-11 to DH and GM). We acknowledge the support from the German Federal Ministry of Education and Research (BMBF) through the Tübingen AI Center (FKZ: 01IS18039B).

References

[1] H. Wagner and R. Blickhan. Stabilizing function of skeletal muscles: an analytical investigation. *Journal of Theoretical Biology*, 199(2):163–179, 1999.

[2] M. Eriten and H. Dankowicz. A rigorous dynamical-systems-based analysis of the self-stabilizing influence of muscles. *Journal of Biomechanical Engineering*, 131(1):011011, 2009.

[3] S. Brändle, S. Schmitt, and M. A. Müller. Mathematical Biology A systems-theoretic analysis of low-level human motor control : application to a single-joint arm model. *Journal of Mathematical Biology*, 11 2019. doi:10.1007/s00285-019-01455-z.

[4] K. Stollenmaier, W. Ilg, and D. F. B. Haeufle. Predicting Perturbed Human Arm Movements in a Neuro-Musculoskeletal Model to Investigate the Muscular Force Response. *Frontiers in Bioengineering and Biotechnology*, 8(308), 4 2020. doi:10.3389/fbioe.2020.00308.

[5] A. J. van Soest and M. F. Bobbert. The contribution of muscle properties in the control of explosive movements. *Biological Cybernetics*, 69(3):195–204, 1993.

[6] D. Haeufle, S. Grimmer, and A. Seyfarth. The role of intrinsic muscle properties for stable hopping - stability is achieved by the force-velocity relation. *Bioinspiration & Biomimetics*, 5 (1):016004, 2010. doi:10.1088/1748-3182/5/1/016004.

[7] K. G. Gerritsen, A. J. van den Bogert, M. Hulliger, and R. F. Zernicke. Intrinsic muscle properties facilitate locomotor controla computer simulation study. *Motor control*, 2(3):206–220, 1998.

[8] C. T. John, F. C. Anderson, J. S. Higginson, and S. L. Delp. Stabilisation of walking by intrinsic muscle properties revealed in a three-dimensional muscle-driven simulation. *Computer methods in biomechanics and biomedical engineering*, 16(4):451–462, 2013.

[9] R. J. Full and D. E. Koditschek. Templates and anchors: neuromechanical hypotheses of legged locomotion on land. *Journal of Experimental Biology*, 202(23):3325–3332, 1999.

[10] P. Holmes, R. J. Full, D. Koditschek, and J. Guckenheimer. The dynamics of legged locomotion: Models, analyses, and challenges. *SIAM review*, 48(2):207–304, 2006.

[11] R. Blickhan, A. Seyfarth, H. Geyer, S. Grimmer, H. Wagner, and M. Günther. Intelligence by mechanics. *Philosophical Transactions of the Royal Society A: Mathematical, Physical and Engineering Sciences*, 365(1850):199–220, 2007.

[12] D. Haeufle, M. Günther, G. Wunner, and S. Schmitt. Quantifying control effort of biological and technical movements: an information-entropy-based approach. *Physical Review E*, 89(1): 012716, 2014.

[13] D. F. Haeufle, I. Wochner, D. Holzmüller, D. Driess, M. Günther, and S. Schmitt. Muscles reduce neuronal information load: quantification of control effort in biological vs. robotic pointing and walking. *Frontiers in Robotics and AI*, 7:77, 2020.

[14] F. Fischer, M. Bachinski, M. Klar, A. Fleig, and J. Müller. Reinforcement learning control of a biomechanical model of the upper extremity. *Scientific Reports*, 11(1):14445, July 2021. doi:10.1038/s41598-021-93760-1.

[15] E. Joos, F. Péan, and O. Goksel. Reinforcement learning of musculoskeletal control from functional simulations. In *International Conference on Medical Image Computing and Computer-Assisted Intervention*, pages 135–145. Springer, 2020.

[16] V. Caggiano, H. Wang, G. Durandau, M. Sartori, and V. Kumar. Myosuite – a contact-rich simulation suite for musculoskeletal motor control, 2022. URL `https://arxiv.org/abs/2205.13600`.

[17] P. Schumacher, D. Häufle, D. Büchler, S. Schmitt, and G. Martius. Dep-rl: Embodied exploration for reinforcement learning in overactuated and musculoskeletal systems, 2022. URL `https://arxiv.org/abs/2206.00484`.

[18] V. L. Barbera, F. Pardo, Y. Tassa, M. Daley, C. Richards, P. Kormushev, and J. Hutchinson. OstrichRL: A musculoskeletal ostrich simulation to study bio-mechanical locomotion. In *Deep RL Workshop NeurIPS 2021*, 2021. URL `https://arxiv.org/abs/2112.06061`.

[19] Ł. Kidziński, S. P. Mohanty, C. F. Ong, Z. Huang, S. Zhou, A. Pechenko, A. Stelmaszczyk, P. Jarosik, M. Pavlov, S. Kolesnikov, et al. Learning to Run challenge solutions: Adapting reinforcement learning methods for neuromusculoskeletal environments. In *The NIPS'17 Competition: Building Intelligent Systems*, 2018. URL `http://arxiv.org/abs/1804.00361`.

[20] Ł. Kidziński, C. Ong, S. P. Mohanty, J. Hicks, S. Carroll, B. Zhou, H. Zeng, F. Wang, R. Lian, H. Tian, W. Jaśkowski, G. Andersen, O. R. Lykkebø, N. E. Toklu, P. Shyam, R. K. Srivastava, S. Kolesnikov, O. Hrinchuk, A. Pechenko, M. Ljungström, Z. Wang, X. Hu, Z. Hu, M. Qiu, J. Huang, A. Shpilman, I. Sosin, O. Svidchenko, A. Malysheva, D. Kudenko, L. Rane, A. Bhatt, Z. Wang, P. Qi, Z. Yu, P. Peng, Q. Yuan, W. Li, Y. Tian, R. Yang, P. Ma, S. Khadka, S. Majumdar, Z. Dwiel, Y. Liu, E. Tumer, J. Watson, M. Salathé, S. Levine, and S. Delp. Artificial intelligence for prosthetics: Challenge solutions. In S. Escalera and R. Herbrich, editors, *The NeurIPS '18 Competition*, pages 69–128, Cham, 2020. Springer International Publishing. ISBN 978-3-030-29135-8.

[21] S. Song, Ł. Kidziński, X. B. Peng, C. Ong, J. Hicks, S. Levine, C. G. Atkeson, and S. L. Delp. Deep reinforcement learning for modeling human locomotion control in neuromechanical simulation. *Journal of NeuroEngineering and Rehabilitation*, Aug 2021.

[22] D. Driess, H. Zimmermann, S. Wolfen, D. Suissa, D. Haeufle, D. Hennes, M. Toussaint, and S. Schmitt. Learning to control redundant musculoskeletal systems with neural networks and sqp: exploiting muscle properties. In *2018 IEEE International Conference on Robotics and Automation (ICRA)*, pages 6461–6468. IEEE, 2018.

[23] D. Büchler, R. Calandra, and J. Peters. Learning to control highly accelerated ballistic movements on muscular robots. *Robotics and Autonomous Systems*, 2019.

[24] X. B. Peng and M. van de Panne. Learning locomotion skills using deeprl: Does the choice of action space matter? In *Proceedings of the ACM SIGGRAPH/Eurographics Symposium on Computer Animation*, pages 1–13, 2017.

[25] T. Siebert and C. Rode. Computational modeling of muscle biomechanics. In *Computational Modelling of Biomechanics and Biotribology in the Musculoskeletal System*, chapter 6, pages 173–204. Woodhead Publishing, Elsevier, 1 edition, 2014.

[26] R. Rockenfeller, M. Günther, S. Schmitt, and . Götz, Thomas. Comparative sensitivity analysis of muscle activation dynamics. *Computational and Mathematical Methods in Medicine*, 2015: 1–16, 2015. doi:10.1155/2015/585409.

[27] S. Schmitt. demoa-base: A Biophysics Simulator for Muscle-driven Motion, 2022. URL `https://doi.org/10.18419/darus-2550`.

[28] E. Todorov, T. Erez, and Y. Tassa. MuJoCo: A physics engine for model-based control. In *2012 IEEE/RSJ International Conference on Intelligent Robots and Systems*, pages 5026–5033, Oct. 2012. doi:10.1109/IROS.2012.6386109.

[29] N. Hansen, S. D. Müller, and P. Koumoutsakos. Reducing the time complexity of the derandomized evolution strategy with covariance matrix adaptation (cma-es). *Evolutionary computation*, 11(1):1–18, 2003.

[30] M. J. Powell. The bobyqa algorithm for bound constrained optimization without derivatives. *Cambridge NA Report NA2009/06, University of Cambridge, Cambridge*, 26, 2009.

[31] A. Abdolmaleki, J. T. Springenberg, Y. Tassa, R. Munos, N. Heess, and M. Riedmiller. Maximum a posteriori policy optimisation. In *International Conference on Learning Representations*, 2018. URL `https://arxiv.org/abs/1806.06920`.

[32] F. Pardo. Tonic: A deep reinforcement learning library for fast prototyping and benchmarking. *arXiv preprint arXiv:2011.07537*, 2020.

[33] I. Wochner and S. Schmitt. arm26: A Human Arm Model, 2022. URL `https://doi.org/10.18419/darus-2871`.

[34] I. Wochner, D. Driess, H. Zimmermann, D. F. Haeufle, M. Toussaint, and S. Schmitt. Optimality principles in human point-to-manifold reaching accounting for muscle dynamics. *Frontiers in Computational Neuroscience*, 14:38, 2020.

[35] J. R. Walter, M. Günther, D. F. Haeufle, and S. Schmitt. A geometry-and muscle-based control architecture for synthesising biological movement. *Biological Cybernetics*, 115(1):7–37, 2021.

[36] J. R. Walter, I. Wochner, M. Jacob, K. Stollenmaier, P. Lerge, and S. Schmitt. allmin: A Reduced Human All-Body Model, 2022. URL `https://doi.org/10.18419/darus-2982`.

[37] M. G. Pandy, F. E. Zajac, E. Sim, and W. S. Levine. An optimal control model for maximum-height human jumping. *Journal of Biomechanics*, 23(12):1185–1198, 1990.

[38] F. Garcia-Cordova, A. Guerrero-Gonzalez, J. Pedreno-Molina, and J. Moran. Emulation of the animal muscular actuation system in an experimental platform. In *IEEE International Conference on Systems, Man and Cybernetics. e-Systems and e-Man for Cybernetics in Cyberspace*. IEEE, 2001. doi:10.1109/icsmc.2001.969789.

[39] A. Seyfarth, K. T. Kalveram, and H. Geyer. Simulating Muscle-Reflex Dynamics in a Simple Hopping Robot. In *Proceedings of Fachgespräche Autonome Mobile Systeme*, pages 294–300. Springer, 2007. doi:10.1007/978-3-540-74764-2_45. URL `http://link.springer.com/10.1007/978-3-540-74764-2%5F45`.

[40] J. Knüsel, A. Crespi, J.-M. Cabelguen, A. J. Ijspeert, and D. Ryczko. Reproducing five motor behaviors in a salamander robot with virtual muscles and a distributed cpg controller regulated by drive signals and proprioceptive feedback. *Frontiers in Neurorobotics*, 14, 2020. ISSN 1662-5218. doi:10.3389/fnbot.2020.604426. URL `https://www.frontiersin.org/articles/10.3389/fnbot.2020.604426`.

[41] A. Rai, R. Antonova, S. Song, W. Martin, H. Geyer, and C. Atkeson. Bayesian optimization using domain knowledge on the atrias biped. In *2018 IEEE International Conference on Robotics and Automation (ICRA)*, pages 1771–1778. IEEE, 2018.

[42] I. Boblan, R. Bannasch, A. Schulz, and H. Schwenk. A human-like robot torso zar5 with fluidic muscles: Toward a common platform for embodied ai. In *50 Years of Artificial Intelligence*, pages 347–357. Springer, 2007.

[43] G. K. Klute, J. M. Czerniecki, and B. Hannaford. Mckibben artificial muscles: pneumatic actuators with biomechanical intelligence. In *1999 IEEE/ASME International Conference on Advanced Intelligent Mechatronics (Cat. No. 99TH8399)*, pages 221–226. IEEE, 1999.

[44] B. Vanderborght, A. Albu-Schäffer, A. Bicchi, E. Burdet, D. G. Caldwell, R. Carloni, M. Catalano, O. Eiberger, W. Friedl, G. Ganesh, et al. Variable impedance actuators: A review. *Robotics and autonomous systems*, 61(12):1601–1614, 2013.

[45] S. Wolfen, J. Walter, M. Günther, D. F. Haeufle, and S. Schmitt. Bioinspired pneumatic muscle spring units mimicking the human motion apparatus: benefits for passive motion range and joint stiffness variation in antagonistic setups. In *2018 25th International Conference on Mechatronics and Machine Vision in Practice (M2VIP)*, pages 1–6. IEEE, 2018.

[46] M. Zhu, S. Biswas, S. I. Dinulescu, N. Kastor, E. W. Hawkes, and Y. Visell. Soft, wearable robotics and haptics: Technologies, trends, and emerging applications. *Proceedings of the IEEE*, 110(2):246–272, 2022. doi:10.1109/JPROC.2021.3140049.

[47] D. Kistemaker, A. J. Van Soest, and M. F. Bobbert. Is equilibrium point control feasible for fast goal-directed single-joint movements? *Journal of Neurophysiology*, 95(5):2898–912, may 2006. ISSN 0022-3077. doi:10.1152/jn.00983.2005.

[48] H. Geyer and H. Herr. A muscle-reflex model that encodes principles of legged mechanics produces human walking dynamics and muscle activities. *IEEE Transactions on Neural Systems and Rehabilitation Engineering*, 18(3):263–73, jun 2010. ISSN 1558-0210. doi:10.1109/TNSRE.2010.2047592.

[49] A. Bayer, S. Schmitt, M. Günther, and D. F. B. Haeufle. The influence of biophysical muscle properties on simulating fast human arm movements. *Computer Methods in Biomechanics and Biomedical Engineering*, 20(8):803–821, 2017. ISSN 1476-8259. doi:10.1080/10255842.2017.1293663.

[50] S. Behnel, R. Bradshaw, C. Citro, L. Dalcin, D. S. Seljebotn, and K. Smith. Cython: The best of both worlds. *Computing in Science & Engineering*, 13(2):31–39, 2011.

[51] G. Brockman, V. Cheung, L. Pettersson, J. Schneider, J. Schulman, J. Tang, and W. Zaremba. Openai gym, 2016.

[52] H. Hatze. A myocybernetic control model of skeletal muscle. *Biological cybernetics*, 25(2):103–119, 1977.

[53] R. Rockenfeller and M. Günther. Inter-filament spacing mediates calcium binding to troponin: A simple geometric-mechanistic model explains the shift of force-length maxima with muscle activation. *Journal of Theoretical Biology*, 454:240–252, 2018. ISSN 10958541. doi:10.1016/j.jtbi.2018.06.009.

[54] D. F. B. Haeufle, M. Günther, A. Bayer, and S. Schmitt. Hill-type muscle model with serial damping and eccentric force–velocity relation. *Journal of biomechanics*, 47(6):1531–1536, 2014.

[55] M. Hammer, M. Günther, D. F. B. Haeufle, and S. Schmitt. Tailoring anatomical muscle paths: a sheath-like solution for muscle routing in musculoskeletal computer models. *Mathematical Biosciences*, 311:68–81, 2019.

[56] M. M. Wierzbicka, A. W. Wiegner, and B. T. Shahani. Role of agonist and antagonist muscles in fast arm movements in man. *Experimental Brain Research*, 63(2):331–340, 1986.

[57] D. A. Kistemaker, A. K. J. Van Soest, and M. F. Bobbert. Is equilibrium point control feasible for fast goal-directed single-joint movements? *Journal of Neurophysiology*, 95(5):2898–2912, 2006.

[58] D. M. Jessop and M. T. Pain. Maximum velocities in flexion and extension actions for sport. *Journal of human kinetics*, 50(1):37–44, 2016.

[59] G. F. Franklin, J. D. Powell, and A. Emami-Naeini. *Feedback Control of Dynamic Systems (8th Edition) (What's New in Engineering)*. Pearson, 2018. ISBN 0134685717. URL `https://www.amazon.com/Feedback-Control-Dynamic-Systems-Engineering/dp/0134685717?SubscriptionId=AKIAIOBINVZYXZQZ2U3A&tag=chimbori05-20&linkCode=xm2&camp=2025&creative=165953&creativeASIN=0134685717`.

[60] D. Reda, T. Tao, and M. van de Panne. Learning to locomote: Understanding how environment design matters for deep reinforcement learning. In *Motion, Interaction and Games*, MIG '20, New York, NY, USA, 2020. Association for Computing Machinery. ISBN 9781450381710. doi:10.1145/3424636.3426907. URL `https://doi.org/10.1145/3424636.3426907`.

Supplementary Material for Learning with Muscles: Benefits for Data-Efficiency and Robustness in Anthropomorphic Tasks

6 Muscle model

In this section, the implementations of the muscle models for demoa and MuJoCo are described. The demoa model approximates biological muscles with more physiological detail and accuracy, whereas the simpler MuJoCo model allows the simulation of rudimentary muscular properties at minimal computational cost, rendering it usable for machine learning.

6.1 Muscle model in Mujoco

Even though the MuJoCo simulator includes the capability of simulating muscles, it requires the explicit definition of tendon insertion points and wrapping surfaces for each model. We, therefore, use our own muscle implementation for the MuJoCo experiments, that does not contain tendons. As a direct consequence, the muscle-fiber length is *uniquely* determined by the joint angle.

In the following, we describe activation dynamics, definitions of muscle-fiber length and velocity, the computation of the resulting torque and the parametrization.

Muscle-tendon-unit Each controllable joint of the MuJoCo model is actuated by two monoarticular muscles and we do **not** compute tendon length. We assume that:

$$l_{\mathrm{MTU}} = l_{\mathrm{CE}}, \tag{6}$$

where l_{MTU} is the length of the entire muscle-tendon-unit and l_{CE} is the length of the muscle fiber, or contractile element. We define muscle-fiber length and velocity by a linear equation [47, 48, 49]:

$$l_{\mathrm{CE},i} = m_i\,\phi_j + l_{\mathrm{ref},i} \tag{7}$$

$$\dot{l}_{\mathrm{CE},i} = m_i\,\dot{\phi}_j, \tag{8}$$

where ϕ_j is the joint angle, m_i and $l_{\mathrm{ref},i}$ are computed from user-defined parameters, and $i \in \{1, 2\}$, as we assume two antagonistic muscles per joint. The parameter m_i acts as a constant moment arm in our model, see Eq. 11.

Activation dynamics The evolution of muscle activity obeys the following first-order ordinary differential equation:

$$\dot{a}(t) = \frac{1}{\Delta t_a}(u(t) - a(t)), \tag{9}$$

where $u(t)$ is a control signal.

Muscle force Given the previous quantities, the muscle force is computed by:

$$F_i = \Big[\mathrm{FL}(l_{\mathrm{CE},i})\,\mathrm{FV}(v_{\mathrm{scale}}\,\dot{l}_{\mathrm{CE},i})a_i + \mathrm{FP}(l_{\mathrm{CE},i})\Big]\,F_{\mathrm{max}}, \tag{10}$$

where v_{scale} is a scaling parameter to adjust in which region of the force-velocity (FV)-curve typical fiber velocities operate. We can then compute the resulting joint torque:

$$\tau = -(m_1\,F_1 + m_2\,F_2). \tag{11}$$

The functions FL, FV and FP are given by MuJoCo internal functions that phenomenologically model experimental data and are applied to normalized muscle lengths and velocities, see MuJoCo documentation [28] and Fig. 11.

Parametrization As the there is a one-to-one mapping of joint angle to muscle lengths in our model, we can determine the required parameters m_i and $l_{\mathrm{ref},i}$, if a mapping of l_{min} to ϕ_{min} and l_{max} to ϕ_{max} is specified (assuming l_{max} to be the maximal muscle-fiber length l_{CE}). Inserting them into

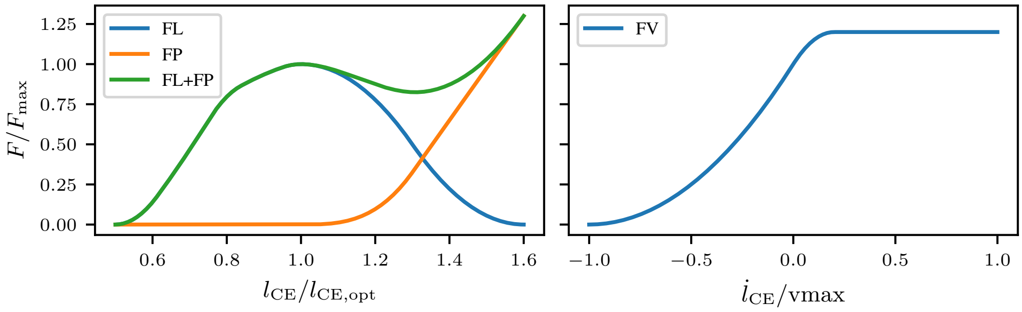

Figure 11: Force-length (FL) and force-velocity (FV) relationships and passive force (FP) used in MuJoCo [28]. We use the same phenomenological functions in our own MuJoCo muscle model. While FL and FV get scaled by the current muscle activity a, FP does not (see Eq. 10).

Table 2: Parameters for the MuJoCo muscle morphology.

(a) Muscle parameters

Parameter	**Value**
$l_{\max}$	1.05
$l_{\min}$	0.95
$\phi_{\max}$	$\pi/2$ [rad]
$\phi_{\max}$	-$\pi/2$ [rad]
Δt_a	0.01 [s]
v_{scale}	0.5

(b) Maximum isometric force

Task	**Value**
ArmMuJoCo	295 [N]
Biped	5000 [N]

Eq. 6 and solving the resulting system of equations gives:

$$m_1 = \frac{l^{\max} - l^{\min}}{\phi^{\max} - \phi^{\min} + \epsilon} \tag{12}$$

$$l_1^{\mathrm{ref}} = l_{\min} - m_1\,\phi_{\min} \tag{13}$$

$$m_2 = \frac{l^{\max} - l^{\min}}{\phi^{\min} - \phi^{\max} + \epsilon} \tag{14}$$

$$l_2^{\mathrm{ref}} = l_{\min} - m_2\,\phi_{\max} \tag{15}$$

$$\tag{16}$$

All in all, $\phi^{\min}$, $\phi^{\max}$, $l^{\min}$, $l^{\max}$ and $F_{\max}$ are required to be specified. The constant $\epsilon = 0.01$ ensures numerical stability. We use the same parametrization for each MuJoCo task, see Table 2.

The maximum and minimum joint angles were chosen to allow for a large range of motion. They do not constitute hard limits, but the passive elastic force FP will increase strongly when reaching them. The maximum and minimum fiber lengths are identical to the MuJoCo default values. As we want to study the benefits of muscular properties in learning, we chose the time and velocity scales $\Delta t_a = 0.01$ and $v_{\mathrm{scale}} = 0.5$ to be large enough to produce noticeable effects, such as low-pass filtering and self-stabilization properties, across all performed tasks. To determine maximum muscle forces, we trained muscle-actuator policies for a chosen maximum force value, after which we adjusted maximum torque-actuator forces to be identical or slightly larger to the maximally observed muscle forces in the final task policies. We repeated this procedure with different force values until good performance could be observed for both morphologies, see Suppl. 10.1 for an evaluation across different force values. All other MuJoCo internal parameters related to muscle modeling are kept to their default values.

In practice, we implement the muscle model in Cython [50], interfacing with OpenAI gym [51], which achieves similar execution speed to native MuJoCo.

6.2 Muscle model in demoa

The muscle model implemented in demoa [27] includes additionally visco-elastic, passive tendon characteristics and muscle routing as joint angle-dependent lever arms to account for many physiological details. In the following, we describe the activation and contraction dynamics of the muscle model, as well as the tendon characteristics and the nonlinear lever arms.

Activation dynamics The muscles are activated with the learned and optimized control signal u, which is nonlinearly transformed into an activation signal. The activity a is following a first-order differential equation of normalized calcium ion concentration γ as introduced by Hatze [52] and simplified by Rockenfeller et al. [26, 53]:

$$\dot{\gamma}(t) = M_{\mathrm{H}}(u(t) - \gamma(t)) \tag{17}$$

and a nonlinear mapping onto the muscles activity

$$a(t) = \frac{a_0 + \varpi}{1 + \varpi}, \tag{18}$$

with $\varpi(\gamma(t), l_{\mathrm{CE}}(t)) = (\gamma(t) \cdot \rho(l_{\mathrm{CE}}))^{\nu}$ and $\rho(l_{\mathrm{CE}}) = \varpi_{\mathrm{opt}} \cdot \frac{l_{\mathrm{CE}}}{l_{\mathrm{opt}}} = \gamma_{\mathrm{c}} \cdot \rho_0 \cdot \frac{l_{\mathrm{CE}}}{l_{\mathrm{opt}}}$. The parameter values are chosen muscle non-specifically and are given in the description of the models (see [33, 36]).

Muscle-tendon-unit The predicted forces are modeled using Hill-type muscle models [54] including four spring-damper components (see Fig. 12): The contractile element (CE) models the active force production of biological muscle fibers, including the nonlinear *force-length* and nonlinear *force-velocity* relation. The parallel elastic element (PEE) models the passive connective tissue in the muscle belly and is arranged in parallel to the CE. The visco-elastic properties of the tendons are modeled using a serial elastic element (SEE) and a serial damping element (SDE). All in all, the governing model dependencies for all muscles $i = 1, ..., n$ are:

$$\begin{aligned} \dot{l}_{\mathrm{CE},i} &= f_{\mathrm{CE}}(l_{\mathrm{CE},i}, l_{\mathrm{MTU},i}, \dot{l}_{\mathrm{MTU},i}, a_i) && (19) \\ \dot{a}_i &= f_a(a_i, u_i, l_{\mathrm{CE},i}) && (20) \\ f_{\mathrm{MTU},i} &= f_{\mathrm{MTU},i}(l_{\mathrm{MTU},i}, \dot{l}_{\mathrm{MTU},i}, l_{\mathrm{CE},i}, a_i)\,, && (21) \end{aligned}$$

where the first differential equation (Eq. 19) denotes the contraction dynamics which models the velocity $\dot{l}_{\mathrm{CE}}$ of the contractile element. This contraction velocity is dependent on the current CE length l_{CE}, the length and contraction velocity of the muscle-tendon unit l_{MTU} and $\dot{l}_{\mathrm{MTU}}$ respectively, and the activity a. The latter is modeled by the activation dynamics (see Eq. 17,18,20). Finally, a force $f_{\mathrm{MTU},i}$ for each muscle is produced which is translated into joint torques.

Nonlinear lever arms To translate the force into joint torques, the muscle path around the joints is routed via deflection ellipses in demoa [55]. If the length of the half-axises of all ellipses are set to zero, this approach can be simplified to the more commonly used fixed via-point approach for muscle routing. Based on the resulting moment arms of the muscles, the force f_{MTU} is translated to generalized torques acting on the degrees of freedom of the system.

State of the system Using a musculoskeletal model with a Hill-type muscle model, as described in this section, increases the number of state variables because two additional differential equations need to be solved for each included muscle. The entire state vector x can therefore be formulated as:

$$x \in \mathbb{R}^{2n_{\mathrm{musc}} + 2n_{\theta}} = \{\gamma_i, l_{\mathrm{CE},i}, \theta_j, \dot{\theta}_j\} \tag{22}$$

where θ and $\dot{\theta}$ represent the generalized joint angle coordinates and their respective velocities, and n_{musc} and n_{θ} denote the number of muscles and the number of joints, respectively.

7 Experimental details and hyperparameters

In this section, we describe algorithm implementation details while also reporting additional settings that were used to obtain previously shown results, as well as used hyperparameters. The section is divided such that experiment details are shown with the control algorithm that was used to generate the results.

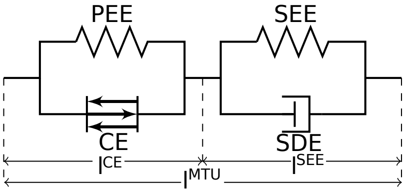

Figure 12: The muscle model in demoa is modeled as lumped Hill-type muscle model (figure adapted from Haeufle et al. [54]).

7.1 Optimal Control (OC)

In the optimal control case, we used the covariance matrix adaptation evolution strategy (CMA-ES) [29] to find the control policy $u(k)$. As mentioned in the main paper, we chose the same population size and number of generations for both actuator morphologies to allow for a fair comparison, even though the number of decision variables n_u is always larger in the muscle-actuated case. In all cases, if not otherwise mentioned, we use a fixed population size of 36 and a fixed number of generations of 100 while varying the control resolution c. If the control resolution is refined, this correlates to an increase in the number of decision variables n_u, however, we specifically did not change the population size or generation number because we wanted to compare the data-efficiency and learning with limited resources for the chosen actuators. The temporal control resolution c was typically varied for $c = \{0.05, 0.15, 0.3\}$ s. The upper bound of these control resolutions ($c = 0.3$ s) corresponds to a triphasic control pattern for a typical movement duration of 0.9 s as it was selected in the smooth point-reaching and squatting task. This selection of c was inspired by biological experiments, where it was shown that triphasic patterns occur in muscle surface electromyograms in typical point-reaching movements (e.g. see [56, 57]). The main hyperparameter of the CMA-ES algorithm σ was set to the default value of 0.2 if not otherwise stated.

7.2 Model Predictive Control MPC

We employed a warm start procedure using the CMA-ES optimizer and afterwards started the MPC routine with a local optimizer BOBYQA [30] (part of the standard python optimization package NLOPT). As temporal control resolution in this closed-loop setting, we chose a very fine resolution of $c = 0.01$ s, similar to the RL setup. This allows counteracting perturbations. The prediction horizon was varied between $t_{\text{pred}} = \{0.2, 0.3, 0.4, 0.5\}$ s as shown in the result section of the main paper.

7.3 Reinforcement Learning (RL)

We use the RL algorithm MPO [31], implemented in TonicRL [32]. Hyperparameters were optimized with a simplified in-house CEM optimizer. All RL experiments are averaged over 8 random seeds except for the hyperparameter optimization, which would have been computationally intractable. Each experimental run was computed with 1 NVIDIA V100 GPU and 20 CPUs of varying speed and type. We use a fixed control resolution of $c = 0.01$ s for all RL experiments.

7.3.1 Experimental details

We give further experimental details in this section.

Data-efficiency For the point-reaching experiments, we used the hyperparameters that were found in the meta-optimization (see Fig. 6) for both morphologies. For the hopping task, we used default MPO parameters. The updated learning curves with optimized parameters, as well as additional results on hyperparameters and maximum force settings can be found in Suppl. 10.

Hyperparameter optimization We optimized the performance of both actuator morphologies in the precise point-reaching task in MuJoCo (see Fig. 15). For each iteration, N_{sets} sets of random parameters are drawn from fixed normal and log-normal distributions. For each of these sets, the task performance is evaluated after T_{train} environment interactions, where T_{train} is chosen such that a noticeable increase in performance can be observed with both actuator morphologies. After each iteration, M_{elite} elite parameter sets are chosen and the mean and standard deviation of each parameter-generating distribution is updated by fitting a (log-)normal distribution to the M_{elite} elite sets with maximum-likelihood estimation. See Table 3 for exact specifications. The meta-optimization for hopping can be found in Fig. 16.

Table 3: Settings for the hyperparameter search.

(a) Precise point-reaching

Parameter	Value
N_{sets}	50
T_{train}	2×10^6
M_{elite}	10

(b) Hopping

Parameter	Value
N_{sets}	20
T_{train}	5×10^6
M_{elite}	10

(c) Initial distributions

Parameter	Distribution	Bounds
lr_{a}	truncated log-normal	$[2.5 \times 10^{-4}, 3 \times 10^{-2}]$
lr_{c}	truncated log-normal	$[0.5 \times 10^{-2}, 10^{-1}]$
lr_{d}	truncated log-normal	$[0.5 \times 10^{-2}, 1]$
clip_{a}	truncated log-normal	$[10^{-7}, 10^{-4}]$
clip_{c}	truncated log-normal	$[10^{-7}, 10^{-4}]$

In the experiments, we only used truncated log-normal distributions to generate parameters. The samples were clipped to the bounds given in Table 3 and initial mean and standard deviation were chosen to lie inside the bounded interval. More precisely, we defined $\log(\mu) = (a + b)/2$ and $\log(\sigma) = (b - a)/4$, where a and b are the chosen bounds. The chosen parameters were the actor learning rate lr_{a}, the critic learning rate lr_{c}, the learning rate of the dual optimizer lr_{d}, the gradient clipping threshold for the actor clip_{a} and the critic clip_{a}.

Robustness point-reaching We trained policies with both morphologies in precise point-reaching for 1.5×10^7 iterations. The best performing policies were then evaluated for the perturbation experiments. For dynamic load, the mass of the hand is increased by 1.5 kg to simulate an object. For chaotic load, a ball with radius 0.12 m and a density of 1000 kg/m^3 is attached to a cable of length 0.6 m, that is connected to the hand. We sample 10 random goals from the training distribution and visualize three trajectories such that there are no overlapping paths. All 10 goals are shown in Fig. 14.

Robustness hopping We trained policies for both morphologies for hopping with the hyperparameters obtained in Fig. 16 and for 1.5×10^7 iterations. We then record 100 evaluation episodes where random forces drawn from $F_i \sim \mathcal{N}(\cdot|0, \sigma_F)$ are applied with a probability of $p = 0.05$ to the hip, knee and ankle joints and to the pelvis position and rotation. Center of mass trajectories are shown for an interval of 15 s in the main manuscript, black vertical bars mark episode resets due to extreme angles of the biped, which would cause it to fall to the ground. The performance for each perturbation level is divided by the unperturbed performance for each morphology to yield a relative performance comparison.

7.3.2 Hyperparameters

The hyperparameters for all RL tasks were set to the best performing runs in the shown hyperparameter optimization. They best trained policies were then used for the perturbation experiments.

8 Models

We give detailed descriptions of the used models in this section. See Table 5 for more information about the MuJoCo models.

8.1 Arm

The Arm model consists of two segments connected with hinge joints moving against gravity. The ArmDemoa [33] is freely available using the multi-body software demoa [27]. In the muscle-actuated case, six muscles were included, modeled as Hill-Type muscles (6.2). Here, two monoarticular muscles, each for the shoulder and elbow joint, and two biarticular muscles acting on both joints are included. The segments are modeled as rigid bodies, and the dynamics are solved using the Euler-Lagrange equation. In the torque-actuated case, each joint is driven by one torque actuator. For more details on the demoa model, we refer to the Technical Report [33]. The variant ArmMuJoCo was derived from an implementation of Arm26 included in MuJoCo [28], it was modified to yield a

Table 4: RL parameters for MPO in TonicRL for the different tasks. Non-reported values are left to their default setting in TonicRL [32]. Common MPO settings are equal for all experiments.

(a) Point-reaching MPO (muscle)

Parameter	**Value**
$\mathrm{lr_a}$	3×10^{-4}
$\mathrm{lr_c}$	10^{-3}
$\mathrm{lr_d}$	2×10^{-2}
$\mathrm{clip_a}$	4×10^{-5}
$\mathrm{clip_c}$	3×10^{-5}
batch size	100
return-normalizer	No

(b) Point-reaching MPO (torque)

Parameter	**Value**
$\mathrm{lr_a}$	10^{-3}
$\mathrm{lr_c}$	5×10^{-3}
$\mathrm{lr_d}$	8.2×10^{-3}
$\mathrm{clip_a}$	7×10^{-6}
$\mathrm{clip_c}$	10^{-6}
batch size	100
return-normalizer	No

(c) Hopping MPO (muscle and torque)

Parameter	**Value**
$\mathrm{lr_a}$	3×10^{-4}
$\mathrm{lr_c}$	3×10^{-4}
$\mathrm{lr_d}$	10^{-2}
$\mathrm{clip_a}$	None
$\mathrm{clip_c}$	None
batch size	256
return-normalizer	Yes

(d) Hopping perturbation (muscle)

Parameter	**Value**
$\mathrm{lr_a}$	9×10^{-4}
$\mathrm{lr_c}$	3×10^{-3}
$\mathrm{lr_d}$	10^{-2}
$\mathrm{clip_a}$	10^{-5}
$\mathrm{clip_c}$	3×10^{-7}
batch size	256
return-normalizer	Yes

(e) Hopping perturbation (torque)

Parameter	**Value**
$\mathrm{lr_a}$	10^{-3}
$\mathrm{lr_c}$	7×10^{-4}
$\mathrm{lr_d}$	2×10^{-2}
$\mathrm{clip_a}$	2×10^{-5}
$\mathrm{clip_c}$	10^{-6}
batch size	256
return-normalizer	Yes

(f) Common MPO settings

Parameter	**Value**
buffer size	10^6
steps before batches	5×10^4
steps between batches	50
number of batches	50
n-step return	3
n parallel	20
n sequential	10

Table 5: State information for all MuJoCo environments. The elements actuator lengths and velocities are directly derived from MuJoCo internal attributes `actuator_length` and `actuator_velocity` and keep the two morphologies as consistent as possible.

model	**observations**
ArmMuJoCo (muscle)	joint positions, joint velocities, muscle positions, muscle velocities, muscle forces, muscle activities, goal position, hand position
ArmMuJoCo (torque)	joint positions, joint velocities, actuator positions, actuator velocities, actuator forces, goal position, hand position
Biped (muscle)	joint positions, joint velocities, muscle lengths, muscle velocities, muscle forces, muscle activities, head position, pelvis position, torso angle, scaled COM-velocity
Biped (torque)	joint positions, joint velocities, actuator lengths, actuator velocities, actuator forces, head position, pelvis position, torso angle, scaled COM-velocity

torque-variant similar to [17]. We additionally created a muscle-variant consisting of 2 muscles per joint. The maximum torques for the torque actuators were matched to the highest achieved torques by the trained muscle policies for both versions independently.

8.2 Biped

We converted the geometrical model of an OpenSim bipedal human without arms [19] for use in MuJoCo. The model, consisting of 7 controllable joints (lower back, hip, knee, ankle) moves in a 2D-plane. Each joint is actuated by two antagonistic muscles or one idealized torque actuator. During execution, we only allow control signals for one leg, the actions for the other leg are kept identical to the first one. This incentivizes symmetric hopping motions, even though both legs can still move differently due to differing initial configurations or external forces. The maximum torques for the torque actuators were matched to the highest achieved torques by the trained muscle policies.

8.3 FullBody

For the squatting and high-jumping task, we used the FullBody (allmin) model [36] which is freely available using the multi-body software demoa [27]. It consists of two legs and an upper body with a skeletal geometry similar to humans and moves in 3D. The ankle, knee and hip joints, as well as a lumbar and a cervical spine joint are controllable (8 controllable joints). The model also consists of two arms with their respective joints, however, these joints were not controlled in this study. In total, 14 joints are modeled with 20 degrees of freedom. Each controllable joint was either actuated by two muscles (6.2) set up in an agonistic-antagonistic setup (muscle-actuated case) or by one idealized torque actuator (torque-actuated case). The maximum allowed torques were matched to the highest torques that occurred in the optimization in the muscle-actuated case to allow for a fair comparison. Only monoarticular muscles (spanning one joint) were used. Furthermore, we reduced the number of control inputs n_u for this study by using symmetrical control signals for the left and right legs. Additional to the torques generated by the actuators, also joint limitations are modeled as linear one-sided spring-damper elements. We refer to the Technical Report [36] for more details.

9 Tasks

We chose movement objectives which represent both, robotic challenges and naturally observed movements of humans.

Smooth point-reaching (OC/MPC) This task encourages smooth point-reaching. Therefore, the objective minimizes the L2-error between the desired angle endpoint and the desired joint angle velocity, as well as penalizing the angle jerk to ensure a smooth motion. The objective for smooth point-reaching is given by:

$$\varepsilon = \frac{\omega_i}{S_\mathrm{i}}(\theta_\mathrm{i} - \theta_\mathrm{i}^\mathrm{des})^2 + \frac{\omega_i}{S_\mathrm{i}}(\dot{\theta}_\mathrm{i} - \dot{\theta}_\mathrm{i}^\mathrm{des})^2 + \dddot{\theta}^2, \tag{23}$$

where θ_i denotes the joint angle, $\dot{\theta}_\mathrm{i}$ the joint angle velocity and the last term $\dddot{\theta}$ penalizes the angle jerk to ensure a smooth motion. ω_i and S_i are weighting and scaling parameters, respectively. Their values (shoulder and elbow) are given in Table 6. The scaling parameters were chosen based on

Table 6: Parameters for cost functions of OC/MPC tasks.

(a) Scaling parameters

parameter	value
$S_{\theta,\text{sh}}$	2.45 [rad]
$S_{\theta,\text{elb}}$	2.45 [rad]
$S_{\theta,\text{hip}}$	1.92 [rad]
$S_{\theta,\text{knee}}$	2.11 [rad]
$S_{\theta,\text{ank}}$	1.05 [rad]
$S_{\theta,\text{ls}}$	0.52 [rad]
$S_{\theta,\text{cs}}$	1.05 [rad]
$S_{\dot{\theta},\text{sh}}$	18.7 [rad/s]
$S_{\dot{\theta},\text{elb}}$	27.9 [rad/s]
$S_{\dot{\theta},\text{hip}}$	14.1 [rad/s]
$S_{\dot{\theta},\text{knee}}$	28.4 [rad/s]
$S_{\dot{\theta},\text{ank}}$	12.6 [rad/s]
$S_{\dot{\theta},\text{ls}}$	5.2 [rad/s]
$S_{\dot{\theta},\text{cs}}$	10.4 [rad/s]

(b) Weighting parameters

parameter	value
$\omega_{\theta,\text{sh}}$	2
$\omega_{\theta,\text{elb}}$	2
$\omega_{\theta,\text{hip}}$	2
$\omega_{\theta,\text{knee}}$	2
$\omega_{\theta,\text{ank}}$	2
$\omega_{\theta,\text{ls}}$	2
$\omega_{\theta,\text{cs}}$	2
$\omega_{\dot{\theta},\text{sh}}$	1
$\omega_{\dot{\theta},\text{elb}}$	1
$\omega_{\dot{\theta},\text{hip}}$	1
$\omega_{\dot{\theta},\text{knee}}$	1
$\omega_{\dot{\theta},\text{ank}}$	1
$\omega_{\dot{\theta},\text{ls}}$	1
$\omega_{\dot{\theta},\text{cs}}$	1

measured upper limits for human joint angular velocity [58] and human joint angle limits (Table 2 in [36]). The desired angle $\theta_\text{i}^\text{des}$ is set to $90°$ for both the shoulder (sh) and the elbow (elb) joint, as this requires a large motion. The movement duration in this task was set to 0.9 s.

Precise point-reaching (RL) We employ a similar reward function to [13]:

$$r = -\lambda_1(d - \log(d + \epsilon^2)) - \frac{\lambda_2}{N} \sum a_i^2 - 2, \tag{24}$$

where d is the Euclidean distance between end effector and target position, $\epsilon = 10^{-4}$ prevents numerical instabilities, $\lambda_1 = 0.1$ and $\lambda_2 = 10^{-4}$. A smaller distance d increases the overall reward, but in contrast to the usual Euclidean distance, the log-term increases rewards for very small distances even further, incentivizing precision. The episode does not terminate until a time limit of 1000 steps elapses.

Fast point-reaching (RL) This task is identical to the previous one, but, in addition to the time limit, the episode also terminates if the distance between end effector and target position is below 5 cm, which incentivizes reaching speed over precision.

Hitting a ball with a high velocity (OC/MPC) A ball with a mass of 250 g is dropped in front of the arm model and the controller learns to hit the ball with a high velocity by optimizing the following objective:

$$\varepsilon = -\max \dot{z}_\text{ball}, \tag{25}$$

where $\dot{z}_\text{ball}$ denotes the ball-velocity in z-direction (direction of gravity).

Squatting (OC/MPC) The objective for squatting is given by:

$$\varepsilon = \frac{\omega_i}{S_\text{i}}(\theta_\text{i} - \theta_\text{i}^\text{des})^2 + \frac{\omega_i}{S_\text{i}}(\dot{\theta}_\text{i} - \dot{\theta}_\text{i}^\text{des})^2, \tag{26}$$

where θ_i denotes the joint angle, $\dot{\theta}_\text{i}$ the joint angle velocity. ω_i and S_i are weighting and scaling parameters, respectively. Their values are given in Table 6. The scaling parameters were chosen based on measured upper limits for human joint angular velocity [58] and human joint angle limits (Table 2 in [36]). The movement duration in this task was set to 0.9 s. This squatting objective is taken from [35], where the desired hip $\theta_\text{hp}^\text{des}$, knee $\theta_\text{kn}^\text{des}$ and ankle $\theta_\text{an}^\text{des}$ joint angle are defined to be:

$$\begin{aligned}
\theta_\text{an}^\text{des} &= -20°, \\
\theta_\text{kn}^\text{des} &= \sin^{-1}(-\frac{L_s}{L_t} \cdot \sin(\theta_\text{an}^\text{des})) - \theta_\text{an}^\text{des} - \theta_\text{an,0}, \\
\theta_\text{hp}^\text{des} &= -\theta_\text{kn}^\text{des} - \theta_\text{an}^\text{des}.
\end{aligned}$$

High-Jumping (OC/MPC) The objective for the high-jumping is taken from [37] and maximizes the position and velocity of the centre of mass of the human body model at the time of lift-off t_l. Additionally, we slightly expanded this objective to account for the three-dimensionality of our jumping model by penalizing deviations of the centre of mass in the x and y-direction:

$$\varepsilon = z_{\text{com}}(t_l) + \frac{\dot{z}^2_{\text{com}}(t_l)}{2g} - |(x_{\text{com}}(t_l) - 0)| - |(y_{\text{com}}(t_l) - 0)|. \tag{27}$$

Note, that z_{com} denotes the centre of mass position (CoM) in z-direction (direction of gravity). The model is initialized to start from a squatting position in this task.

Hopping (RL) We developed a reward function that is able to induce hopping in different leg-driven systems and can be applied independently of the actuator morphology. We did not obtain good results with height-based rewards or the gym hopper [51] reward function. The reward for hopping is given by:

$$r = \exp(\max\{0, \hat{v}_z^{\text{COM}}\}) - 1, \tag{28}$$

where v_z^{COM} is the z-velocity of the center of mass. The transformation $\hat{v} = \min\{10, 100\, v\}$ adjusts the sensitivity of the reward function while also preventing numerical overflows of the exponential function. Crucially, large positive velocities are weighted much more strongly than small or negative velocities, driving the system to maximum height periodic hopping. The second term prevents positive rewards for velocities close to zero, as $\exp(0) = 1$. We additionally use regularizing cost terms:

$$r_{\text{reg}} = r_{\text{alive}} - \lambda_1\, r_{\text{action}} - \lambda_2\, r_{\text{joint}}, \tag{29}$$

where $\lambda_1 = 10^{-4}$, $\lambda_2 = 10^{-3}$, r_{alive} is 1 if the episode does not terminate and 0 otherwise, $r_{\text{action}} = \sum a_i^2/N$ punishes large actions and r_{joint} punishes joint angles close to the limits of the system. Specifically:

$$r_{\text{joint}} = \begin{cases} -1, & \text{if } |q_{\max,i} - q_i| < 0.1 \\ -1, & \text{if } |q_{\min,i} - q_i| < 0.1 \\ 0, & \text{otherwise.} \end{cases} \tag{30}$$

Finally, we terminate the episode after the lapse of a time limit of 1000 iterations, or if different parts of the model are very close to the ground, as this indicates a fall. The termination conditions are:

$$\begin{aligned} h_{\text{skull}} &< 0.3 \text{ [m]} \\ h_{\text{pelvis}} &< 0.2 \text{ [m]} \\ h_{\text{tibia}_\text{l}} &< 0.3 \text{ [m]} \\ h_{\text{tibia}_\text{r}} &< 0.3 \text{ [m]} \\ \theta_{\text{torso}} &> 1.22 \text{ [rad]} \\ \theta_{\text{torso}} &< -0.88 \text{ [rad]}, \end{aligned}$$

where h is the height of the respective body part and θ_{torso} marks the torso angle deviation from the upright position.

10 Additional experiments (RL)

10.1 Maximum force variation

Although the maximum force of the actuators is not freely adjustable in real systems, it is trivial to do so in simulation and has a strong influence on performance. We, therefore, used the biped parameters resulting from our hyperparameter optimization and recorded learning curves for the hopping task for both actuator morphologies for different maximum actuator forces. For each setting, we set the maximum isometric force for all muscle actuators to a certain value, trained the systems to convergence, and then recorded the torque values occurring at each controllable joint during execution of the hopping behavior. We then trained torque-actuator policies while setting $\tau_{\max}$ to the previously observed maximum values for *each* individual joint. The results are shown in Fig. 13. Even though singular torque-driven runs are able to outperform all muscle-driven runs at the end of training, this not only takes a considerable number of learning iterations, but also comes at the cost of strong learning instabilities. Looking at the learned behaviors, the torque-driven policies tend to jump very high, but violate the allowed torso-angles at the peak due to their unstable explorative policies. No periodic hopping could be observed. The muscle-driven policies, on the other hand, achieve periodic hopping, even though the apex hopping height is smaller.

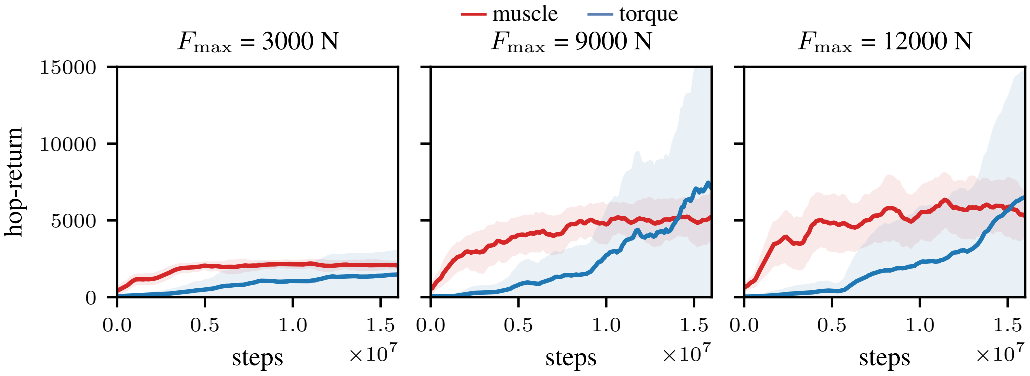

Figure 13: **Hopping performance for different actuator strengths.** Hyperparameters are optimized for hopping with a maximum muscle strengh of $F_{\max} = 5000$ N as used in the previous hopping experiment. The maximum isometric muscle force is set to different values and the policies are trained for the task. Afterwards, the maximum used torques for the learned behaviors are recorded for each joint and set to identical values for the torque actuator. Muscle-actuators lead to more consistent performance and yield periodic hopping. Torque-actuators yield unstable policies that manage to jump very high once, but terminate the episode due to falls.

10.2 Additional goals for point-reaching with perturbations

We show ten random arm goals for precise point-reaching with perturbations that were not present during training in Fig. 14.

10.3 Additional hyperparameter variations

We show the relative performance of all runs of the hyperparameter searches in polar coordinates for precise point-reaching and hopping for both actuator morphologies (Fig. 15 and Fig. 16). The angles mark the specified hyperparameter (see Suppl. 7.3.1 for definitions), while the radius marks the chosen value in $\log_{10}$-coordinates. The top row marks performance with muscle-actuators, the middle row with torque-actuators and the bottom row shows histograms of returns for both morphologies at different iterations. For point-reaching, muscle morphology leads to a return distribution that is centered around the top-performing parameter sets, with almost no badly performing sets left at iteration 7. In contrast, for torque-morphology a large number of runs is still distributed at low return values. For hopping, a much harder task, muscle-morphology quickly leads to a large number of runs at the top-performance level, while some badly performing parameter sets remain even at iteration 5. For torque-morphology, a large peak can be observed for returns close to 0, as most sampled parameter sets do not achieve any kind of hopping. Only at iteration 7, a few singular well-performing runs appear, that strongly outperform even the best muscle-driven run. This was to be expected, as any muscle-actuator behavior can in principle be replicated by torque actuators, given that the policy is able to learn it. Muscle actuators, on the other hand, are restricted to trajectory-dependent output.

10.4 Additional actuator models

Similar to Peng et al. [24], we present more actuator models that are widely used in robotics. We consider the ideal torque actuator to be neutral in its properties—only executing exactly what it was told. In contrast, a PD-controller [59] embeds additional knowledge about position control elements and error propagation dynamics. For the RL experiments, we use an identical PD formulation to Peng et al. [24]:

$$u(t) = k_p\left(\hat{q}(t) - q(t)\right) + k_d\left(\hat{\dot{q}} - \dot{q}\right), \tag{31}$$

with the joint angles q, the joint velocities $\dot{q}$, the desired position $\hat{q}$ and the desired velocity $\hat{\dot{q}}$. We also set $\hat{\dot{q}} = 0$, similar to [24]. We tuned the PD-controller by hand to achieve good step-wise trajectory tracking, see Fig. 17. We also ensured that it remains stable for faster position changes.

As a second additional actuator, we implemented a low-pass filtered torque actuator. The control signal is filtered according to the simplified muscle activation dynamics in the MuJoCo muscle model

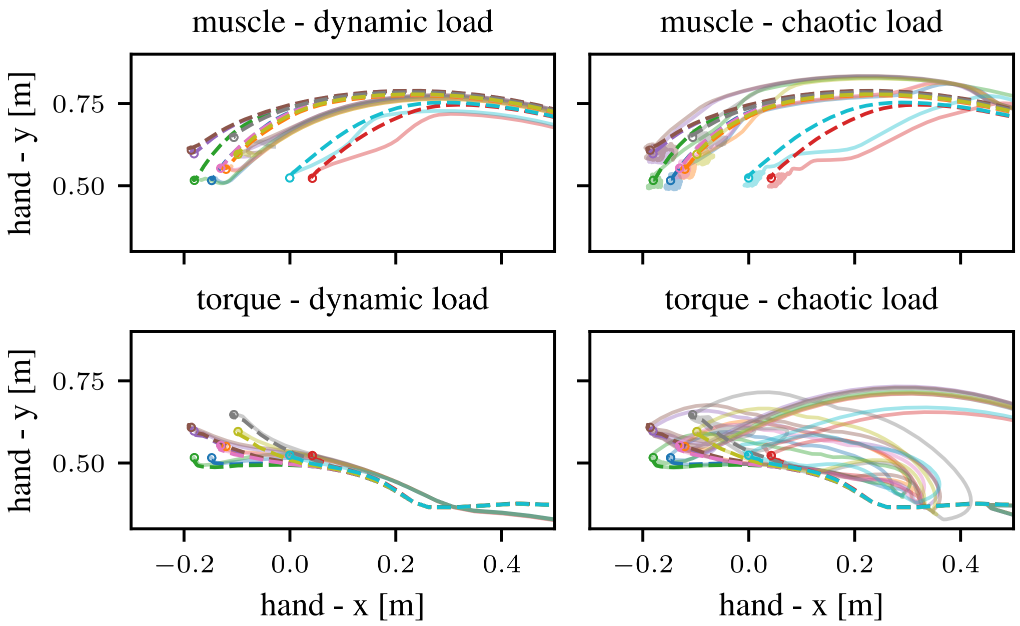

Figure 14: **Trajectories for dynamic (1.5 kg weight) and chaotic (attached ball) load.** Left: The torque actuator handles the dynamic load case slightly better than the muscle actuator for all goals, especially compared to the goals in grey, brown and purple. Right: The muscle-actuator performs very well for all chaotic load goals, except for a small deviation from the end-point. The torque actuator exhibits strong instabilities. The respective goal positions are marked as circles, the unperturbed baseline for each goal is shown with a dashed line, the perturbed trajectories with slightly transparent solid lines.

Eq. 9, which effectively act as a low-pass filter:

$$\dot{a}(t) = \frac{1}{\Delta t}(u(t) - a(t)), \tag{32}$$

which gets approximated in practice as:

$$a_{t+1} = a_t + \frac{\Delta t_{\text{sim}}}{\Delta t}(u(t) - a(t)). \tag{33}$$

The variable $a(t)$ denotes the effective action that is applied to the underlying torque actuator, $u(t)$ is the control signal, Δt is the time scale of the low-pass filter and Δt_{sim} is the time step of the *physics simulation*, which is not to be confused with the *control time step*: $\Delta t_{\text{control}} = 2\,\Delta t_{\text{sim}}$ for the MuJoCo simulations. All actuator properties such as the muscle dynamics, the low-pass filter and the PD controller are updated with the physics simulation time step, while the RL policy computes new actions only with the control frequency.

We repeated the precise point-reaching task with ArmMuJoCo with muscle actuation, torque actuation, PD actuation and two low-pass filter variants. The fast variant uses the time scale $\Delta t = 0.01$, which is the same as used in the muscle model and reacts very fast to new control signals. The slow variant uses $\Delta t = 1$ and produces a much stronger filtering effect. The results in Fig. 18 show that the muscle actuator outperforms all other variants.

Individual runs are shown in the right column in order to obtain an accurate picture of the variance across seeds for all actuators. Even when not considering the badly performing outliers, torque actuation seems to present larger variance than muscle actuation. The PD-controller performs worse than pure torque control for this task, which validates results by [60]: They found PD-controllers to perform worse than torque control when learning behaviors from scratch as opposed to tracking reference motions [24].

We noticed that, while the muscle only uses a maximum of ≈ 30 Nm during normal reaching, its properties allow it to intermittently use larger torques when perturbations are applied. We therefore

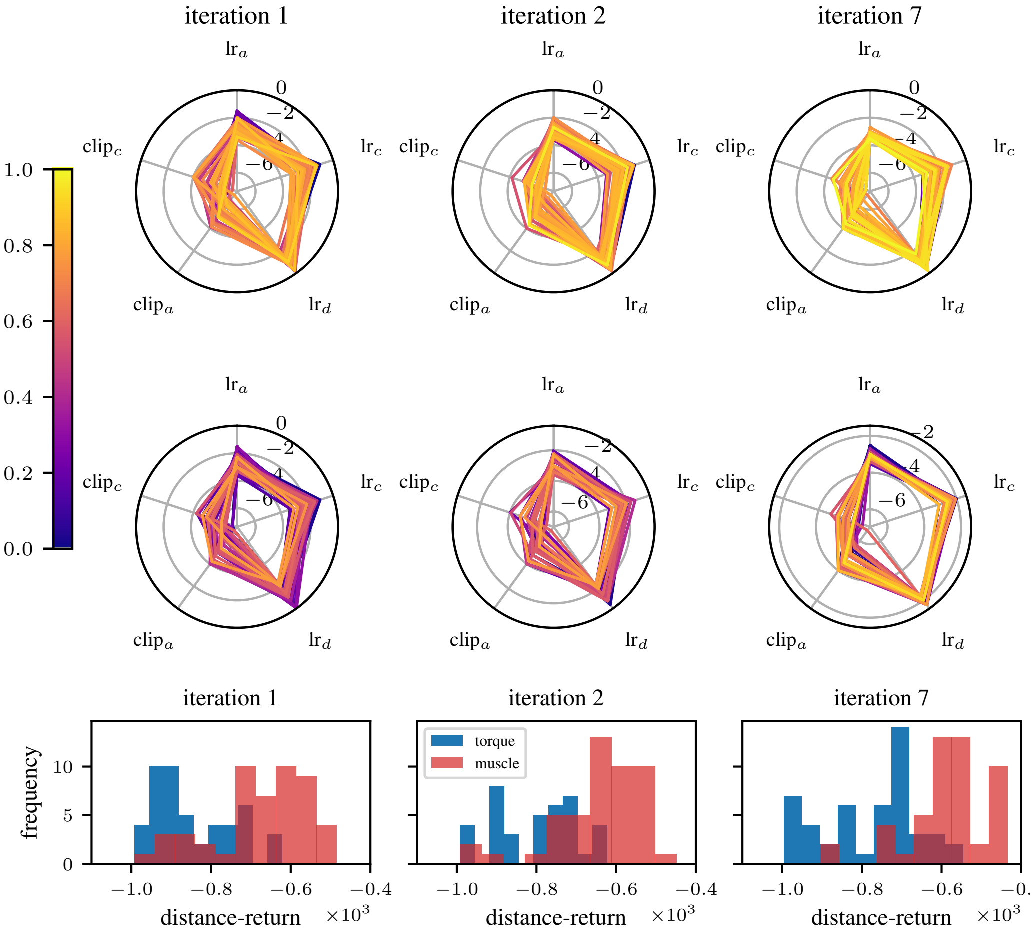

Figure 15: **Hyperparameter variation for precise point-reaching.** Hyperparameters are optimized following an iterative sampling scheme and individual runs train for 2×10^6 iterations. Fifty sets of parameters are sampled randomly from pre-determined distributions, the final performance is evaluated and used to adapt the sampling distributions for the next iteration. We record 7 iterations which equals 350 runs in total. We optimize 5 parameters related to MPO. The angle of the radarplot marks the parameter, the radius marks the value (in $\log_{10}$-coordinates). Top: Radarplot of parameters for the muscle in precise point-reaching at iteration 1, 2 and 7. The color marks the achieved performance of the parameter sample relative to the best achieved performance over **all** sampled parameters. Middle: precise point-reaching torque. Bottom: Histogram of returns for all sets of parameters at iterations 1, 2 and 7.

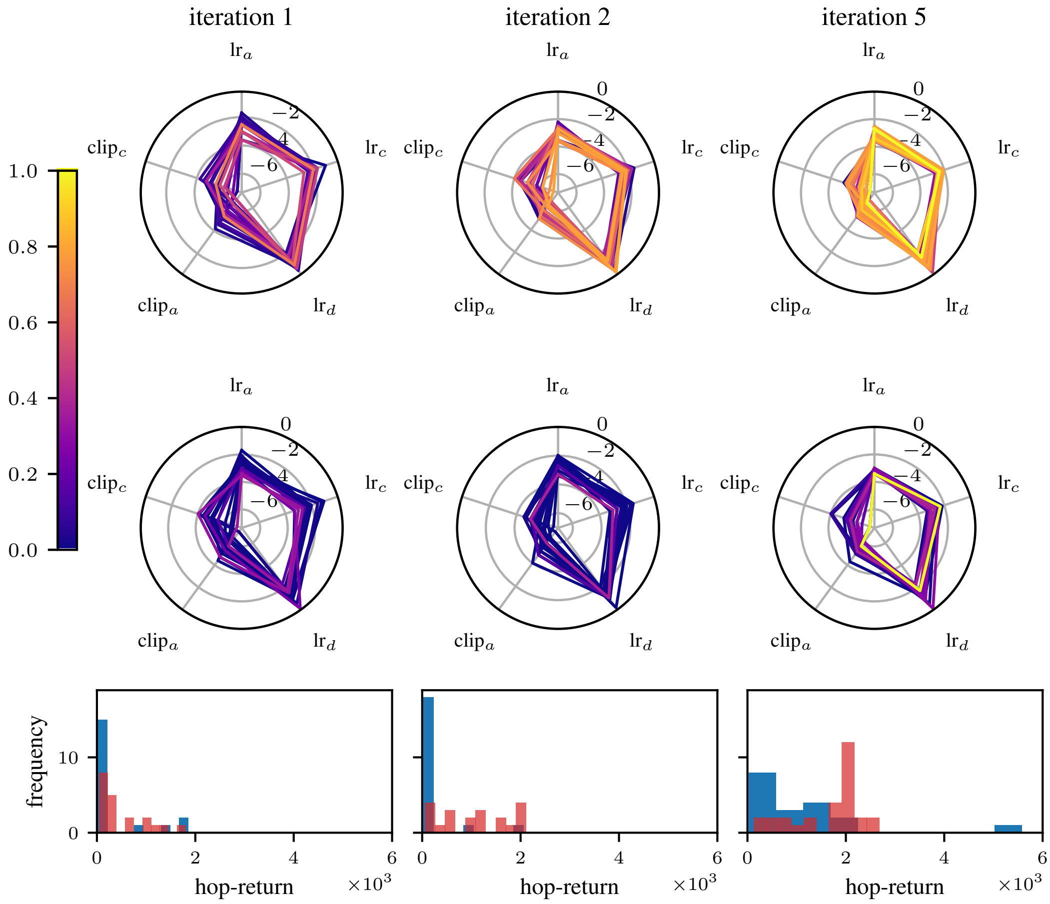

Figure 16: **Hyperparameter variation for hopping.** Hyperparameters are optimized following an iterative sampling scheme and individual runs train for 5×10^6 iterations. Twenty sets of parameters are sampled randomly from pre-determined distributions, the final performance is evaluated and used to adapt the sampling distributions for the next iteration. We record 5 iterations which equals 100 runs in total. We optimize 5 parameters related to MPO. The angle of the radarplot marks the parameter, the radius marks the value (in $\log_{10}$-coordinates). Top: Radarplot of parameters for the muscle in the hopping task at iteration 1, 2 and 5. The color marks the achieved performance of the parameter sample relative to the best achieved performance over **all** sampled parameters. Middle: hopping torque. Bottom: Histogram of returns for all sets of parameters at iterations 1, 2 and 5.

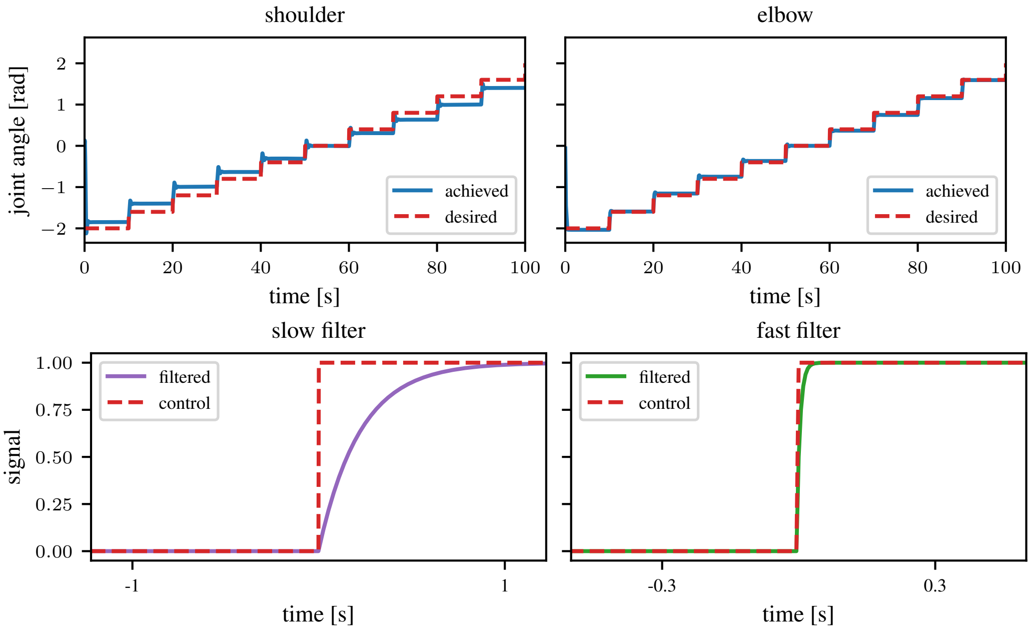

Figure 17: Top row: We tuned a PD-controller for ArmMuJoCo that is then used as an intermediate control layer for an RL agent. We tuned the parameters by hand to achieve good joint angle control over the workspace, shown in the figure for both joint angles. The slight mismatch in the shoulder joint (left) is due to gravitational forces, which are not counteracted in the controller design. An RL agent easily learns to compensate for this shift. Bottom row: We show two low-pass filtered torque actuators for an exemplary step-signal. The fast-filter uses the same parameters as the activation dynamics in the MuJoCo muscle model.

conduct a second series of experiments where we adjust the maximum allowed torque for all torque actuators to the intermittent upper limit of the muscle, which is $\tau_{\max} = 60$ Nm. New learning curves were recorded for ArmMuJoCo point-reaching and are shown in Fig. 19. Generally, the performance for the non-muscular actuators decreases with larger torque limits. Only the PD-controller seems to exhibit smaller variance than in the small torque limit case.

10.5 Additional robustness experiments

In this section, we present evaluation of the robustness of the learned policies with a wide variety of masses and additional actuators. The results are reported for two different maximum torque limits for the non-muscle-based actuators, following the reasoning of Sec. 10.4.

The variations are investigated for policies trained for point-reaching with ArmMuJoCo. All weights are added as a chaotic load that is attached with a rope. The results can be seen in Fig. 20 and Fig. 21 for $\tau_{\max} = 30$ Nm and $\tau_{\max} = 60$ Nm respectively. We use masses varying from 1 to 4 kg in the high force case, while they are halved in the other case. Even though the muscle actuator is the most stable across all variations, the pure torque actuator variant performs quite well when large forces are allowed. However, large torque limits also diminish the learning performance, as seen previously in Fig. 19. The results suggest a trade-off between learning speed and robustness for the torque controller, while the muscle actuator is able to leverage low forces during learning and automatically reacts to perturbations with stronger forces. The PD-controller only outperforms raw torque control for the large torque limit $\tau_{\max} = 60$ Nm and a comparatively small perturbation mass of 1 kg, see Fig. 21 (second row, middle).

10.6 MuJoCo simulation time step ablation

To assess the influence of simulation accuracy on the obtained results, we record additional muscle and torque actuator learning curves with a much smaller simulation time step of $\Delta t_{\text{sim}} = 0.001$ instead of $\Delta t_{\text{sim}} = 0.005$. We additionally increase the frameskip of the simulation to achieve an equal control time step of $\Delta t_{\text{control}} = 0.01$ in both cases. The results are shown in Fig. 22. With

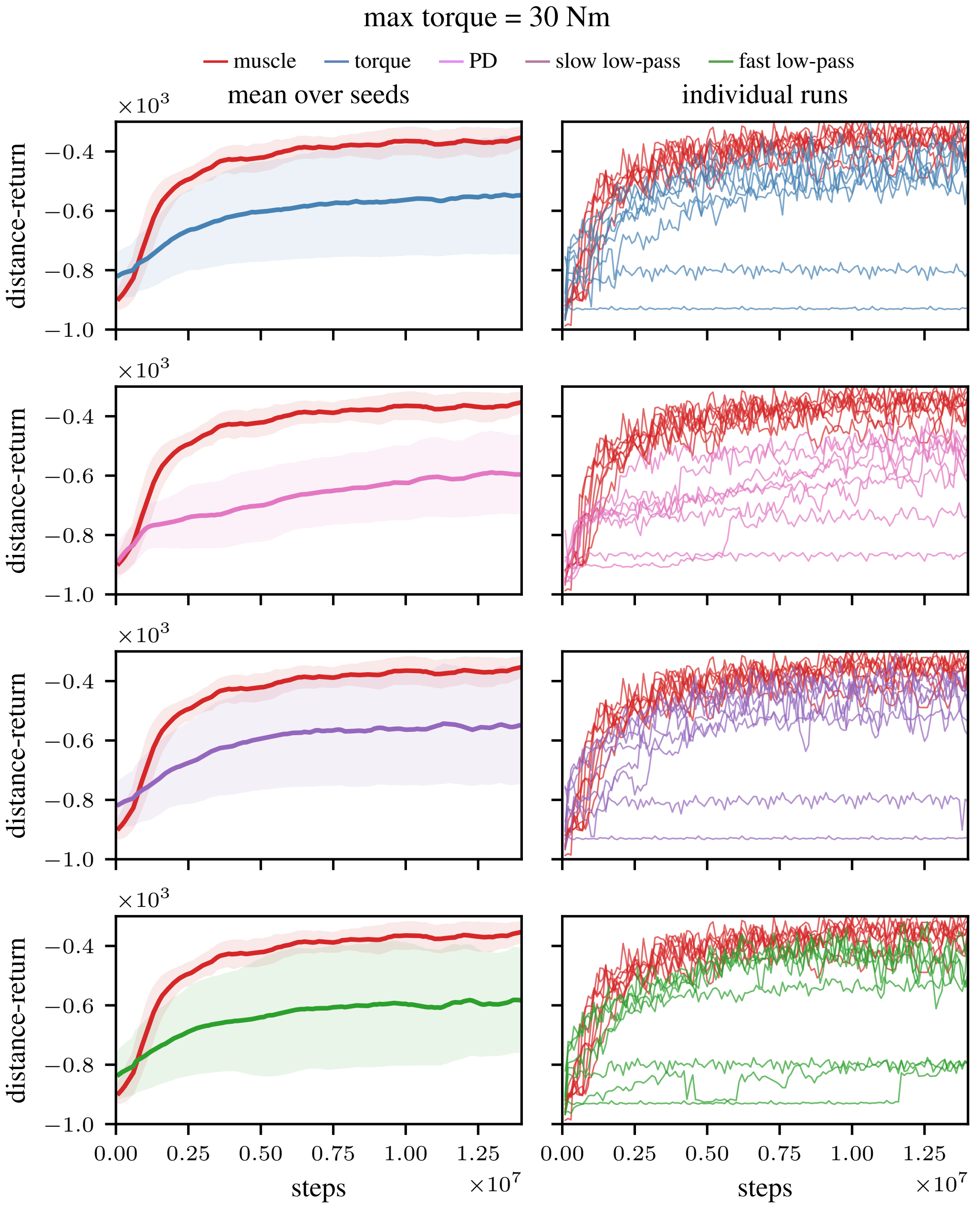

Figure 18: **The muscle actuator outperforms all other considered actuator designs.** We compare the learning curves for muscle, torque, PD and two low-pass filter actuators in the precise point-reaching task for ArmMuJoCo. Averages across random seeds and standard deviation are shown in the left column, individual runs in the right column. The torque actuator and the low-pass filter variants perform quite well, but their variance across seeds is larger than for the muscle, even when outliers are not considered. The PD-controller seems to exhibit less variance than a pure torque-driven approach, but the overall performance is worse. We recorded 8 random seeds for each actuator.

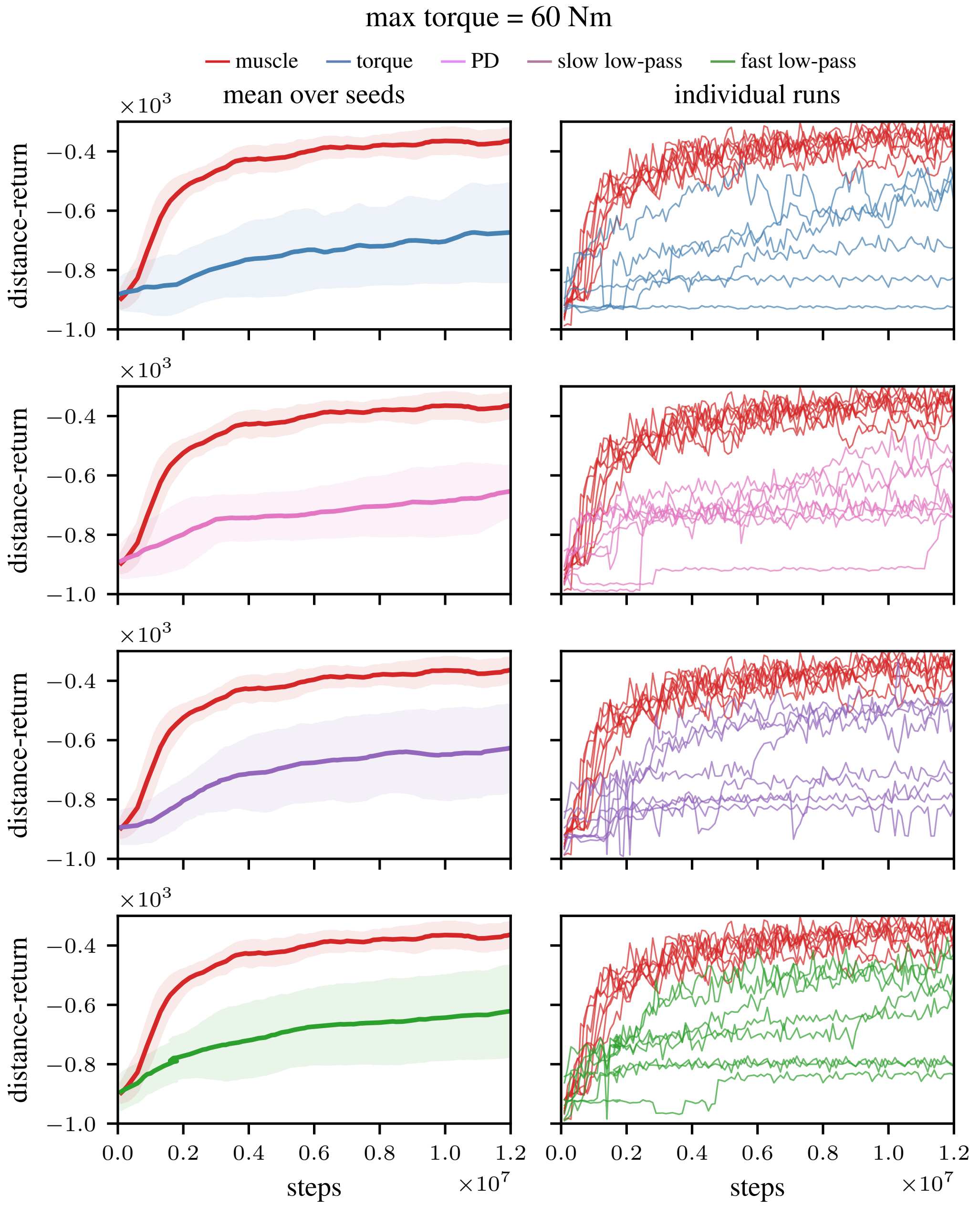

Figure 19: **Torque actuators perform worse when the maximum allowed force is increased.** We repeat the experiment in Fig. 19, but allow the torque actuator to use a maximum torque of $\tau_{\max} = 60$ Nm. This value is the maximum torque that the muscle actuator can output in perturbation experiments, even though it is not reached during point-reaching under normal conditions. While singular runs still perform well for the torque actuator variants and the PD controller achieves even less variance across seeds than before, the overall performance suffers when increasing the maximum force. We recorded 8 random seeds for each actuator.

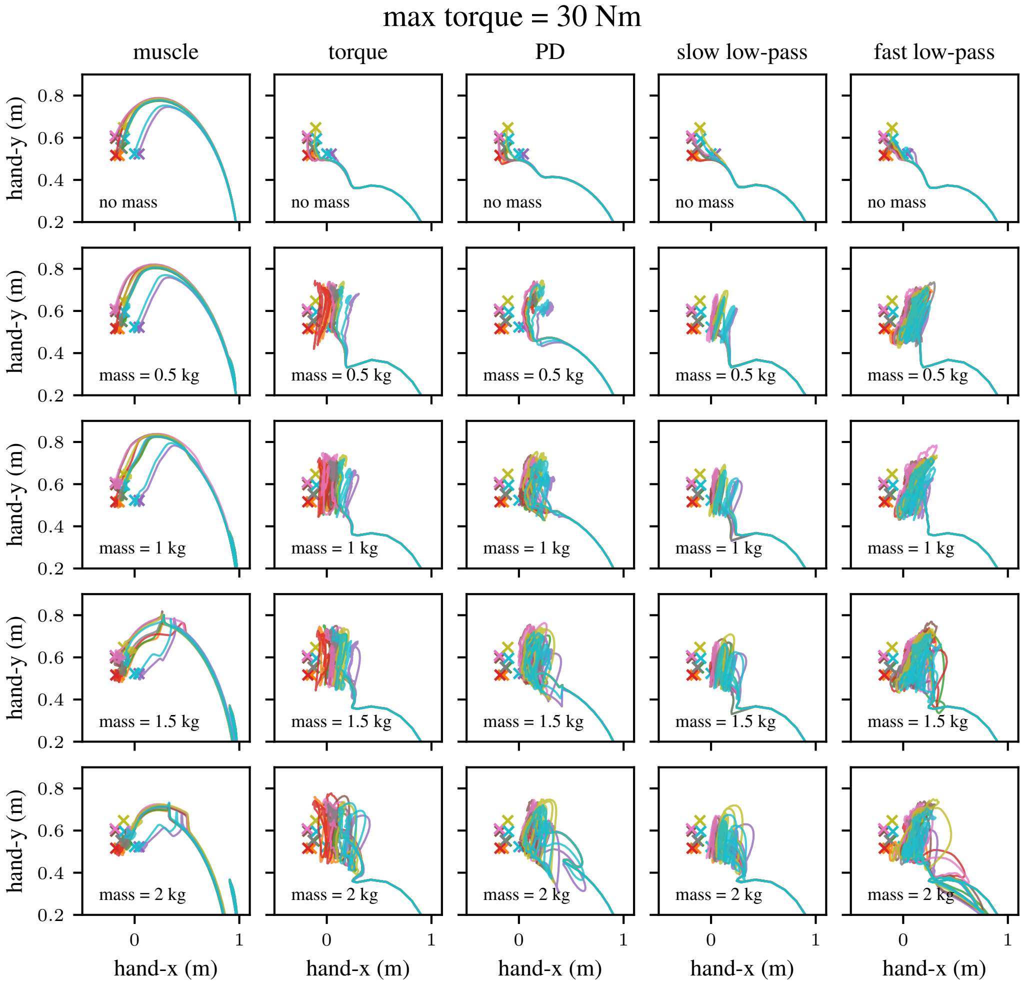

Figure 20: **The muscle actuator is more robust for all considered masses than the alternative.** We conducted perturbation experiments for all actuator models during which chaotic loads of differing masses were attached to the robot which were not present during training. The muscle actuator performs well up to 1.5 kg, when deviations start to get bigger. It does not reliably reach the goal for $m = 2$ kg. The torque actuator exhibits strong lateral oscillations for all masses and slight undershooting of the goal position. The PD-controller oscillates less for small masses, but undershoots the goals by a larger amount, as it was not tuned for this scenario. The low-pass filtered actuators perform similar to the pure torque case. For each experiment we used the best performing policy of each learning curve in Fig. 18 at the end of training. Ten goals were randomly chosen and used for all experiments.

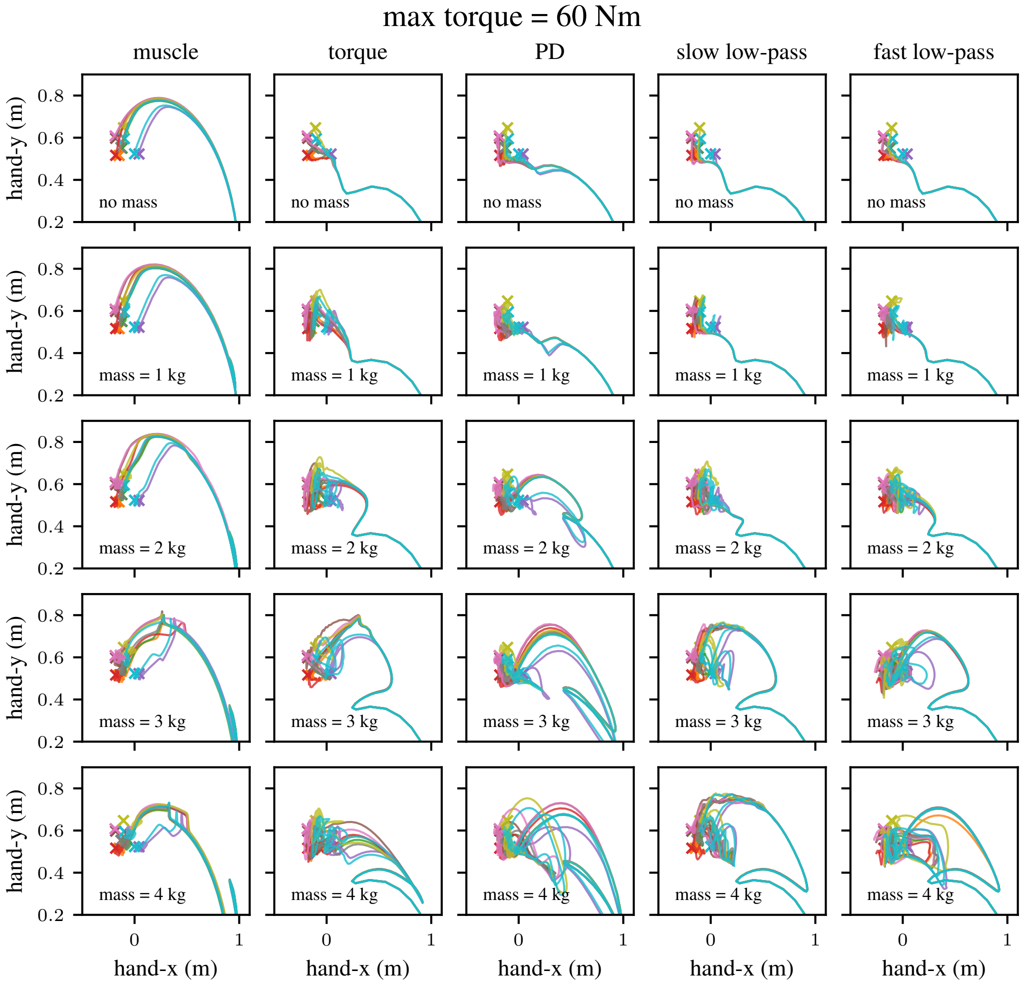

Figure 21: **Torque control is more robust with larger torque limits, but is still outperformed by muscles.** We repeat the experiment in Fig. 20 with a larger maximum torque limit of 60 Nm. All torque-variants seem to perform better than in the low torque limit case. For $m = 1$ kg, the PD-controller and the low-pass filter versions slightly outperform the pure torque actuator. Nevertheless, the muscle reacts more robustly for all considered masses. For each experiment we used the best performing policy of each learning curve in Fig. 19 at the end of training. The same ten goals as in Fig. 20 were used.

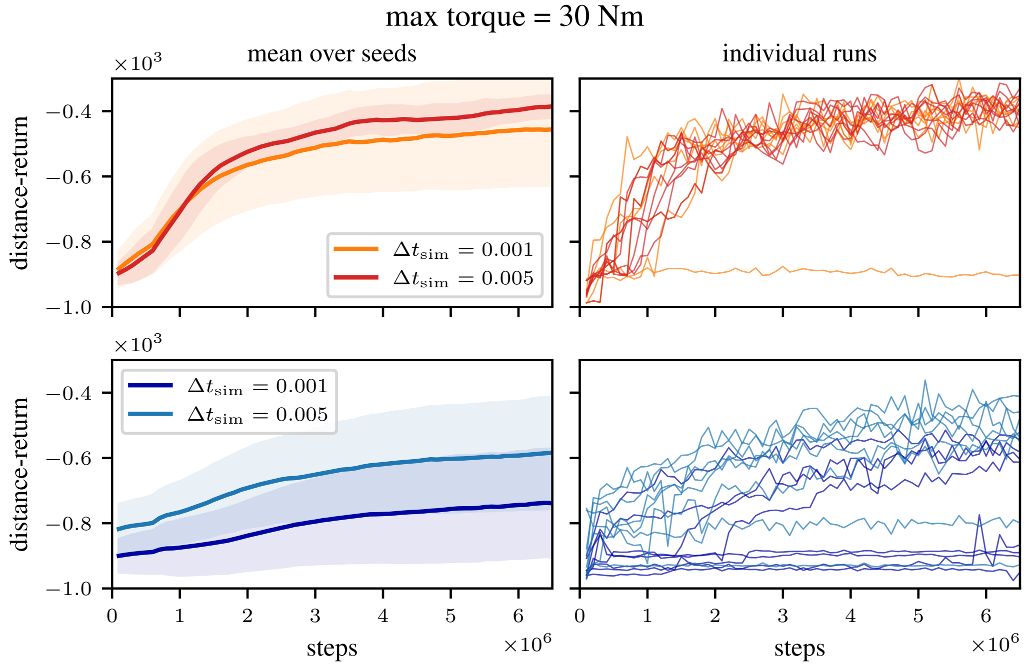

Figure 22: We present physical simulation time step ablations for ArmMuJoCo and precise point-reaching. While the Δt_{sim} was varied, the frameskip parameter was adjusted to achieve the same control time step $\Delta t_{\mathrm{control}} = 0.01$ in all cases. Top: With the exception of a single unlucky run, the simulation time step does not seem to affect the performance of the muscle actuator in this task. Bottom: Surprisingly, the torque actuator performs much worse with a *smaller* simulation time step. As simulation accuracy increases with a smaller time step, we do not suspect this to be the result of numerical instability. A setting of $\Delta t_{\mathrm{sim}} = 0.005$ was used for the all other MuJoCo experiments. We recorded 8 random seeds for each actuator.

the exception of one unlucky run, the muscle actuator performance seems to be unchanged under the more accurate simulation setting. The torque actuator, in contrast, seems to perform worse. As simulation accuracy increases with a smaller time step, we do not suspect this to be the result of numerical instability. As this only reinforces prior results, we conclude that the improved muscle actuator data-efficiency is not a result of numerical instability.

11 Additional experiments (OC/MPC)

11.1 Nonlinearity in muscle model

In our study, we conclude that the nonlinear muscle properties can be beneficial for learning in terms of data-efficiency and robustness. To show-case the influence of individual properties, we performed additional smooth point-reaching and squatting experiments. The four major properties that differ between the torque actuator morphology and the muscle actuator morphology are the nonlinear activation dynamics, the nonlinear force-length, the nonlinear force-velocity relation and the nonlinear lever arms (see also Fig. 1 in the main paper). We switched each of these properties separately off to test which nonlinear muscle property contributes the most to the beneficial behavior. The results can be seen in Fig. 23. As shown in this figure, switching off the nonlinear force-velocity relation (no Fv) has the strongest impact and leads to results that are even worse than the torque actuator optimization. Additionally, the nonlinear activation dynamics (no actdyn) has some influence on the performance of the data-efficiency results. With these results, we would like to give a first indication that indeed the non-linearity of different muscle properties are beneficial for the data-efficiency in learning anthropomorphic tasks.

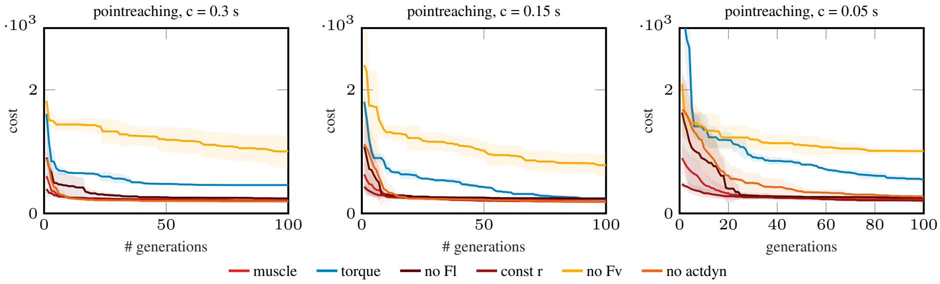

Figure 23: **Cost value for point-reaching while switching off different muscle properties.** Plotting the mean and standard deviation (shaded area) for 5 repeated runs for the two main actuator morphologies (muscle in red, torque in blue). Additionally, different morphologies are tested where muscle properties are switched off separately: We switched off the force-length relation (no Fl), set moment arms to be constant (const r), switched off the force-velocity (no Fv) and excluded the activation dynamics (no actdyn).

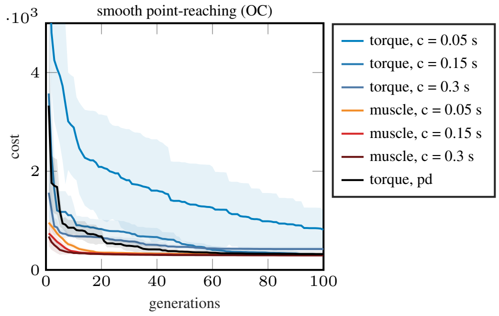

Figure 24: **Cost value for smooth point-reaching with additional baseline using PD control for torque actuator.** Plotting the mean and standard deviation (shaded area) for 5 repeated runs for the three main actuator morphologies (muscle in red, torque in blue, torque with PD controller in black).

11.2 Proportional-derivative torque control for learning

In the results presented in the main paper, we mainly compared the muscle actuator morphology to an idealized torque actuator without embedding any additional knowledge, e.g. position control which is typically used with a PD controller. Nevertheless, we consider the comparison with the PD control action space as a valuable baseline comparison. Therefore, we performed additional experiments for the smooth point-reaching task, where we added this additional baseline using PD control on top of the torque actuator morphology. Similar to the RL experiments (10.4), we use an identical PD formulation to Peng et al. [24]:

$$u(t) = k_p \left(\hat{q}(t) - q(t)\right) + k_d \left(\hat{\dot{q}} - \dot{q}\right), \tag{34}$$

with the joint angles q, the joint velocities $\dot{q}$, the desired position $\hat{q}$ and the desired velocity $\hat{\dot{q}}$. We also set $\hat{\dot{q}} = 0$, similar to [24] and our original cost function for smooth point-reaching (Eq. 23). In contrast to the RL experiments where we directly learn the desired angles for the control signal $u(t)$ for PD controller, here, with OC, we instead learn the k_p and k_d parameters. We allow for changes in these parameters every $c = 0.3$ s, whereas the control signal was updated continuously. Fig. 24 shows that the data-efficiency is slightly improved using a PD controller for the torque-actuated case in the smooth point-reaching task but it does not reach the performance of the muscle actuator.

11.3 Additional robustness experiments

In this section, we present additional robustness experiments for perturbing the arm model in the point-reaching task while adding unknown weights to the lower arm. In contrast to the main paper, we do not only show the perturbation using 1 kg, but varied the unknown weight up until 5 kg in 1 kg steps. The resulting angle trajectories are shown in Fig. 25. We see that both actuators are able to counteract unknown perturbation weights with 1 kg. For larger weights, the perturbations result in

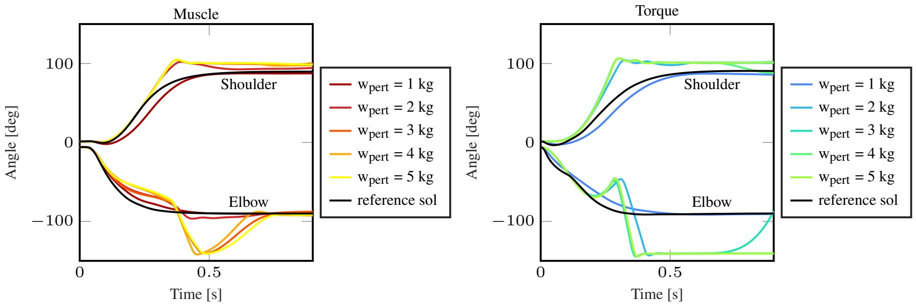

Figure 25: **Muscle morphology is more robust towards unknown weight perturbations.** Plotting the angle trajectories of the shoulder and elbow angle over time for the two actuator morphologies (left: muscle, right: torque) while varying the unknown weight (between 1 and 5 kg in 1 kg steps).

overshoots in the elbow joint angle which can be corrected in the muscle-actuated case, whereas the torque actuator struggles to counteract these perturbations. Summed up, the muscle morphology is more robust towards perturbations for a wide range of different unknown weights.

Appendices

A. Arm26: A Human Arm model

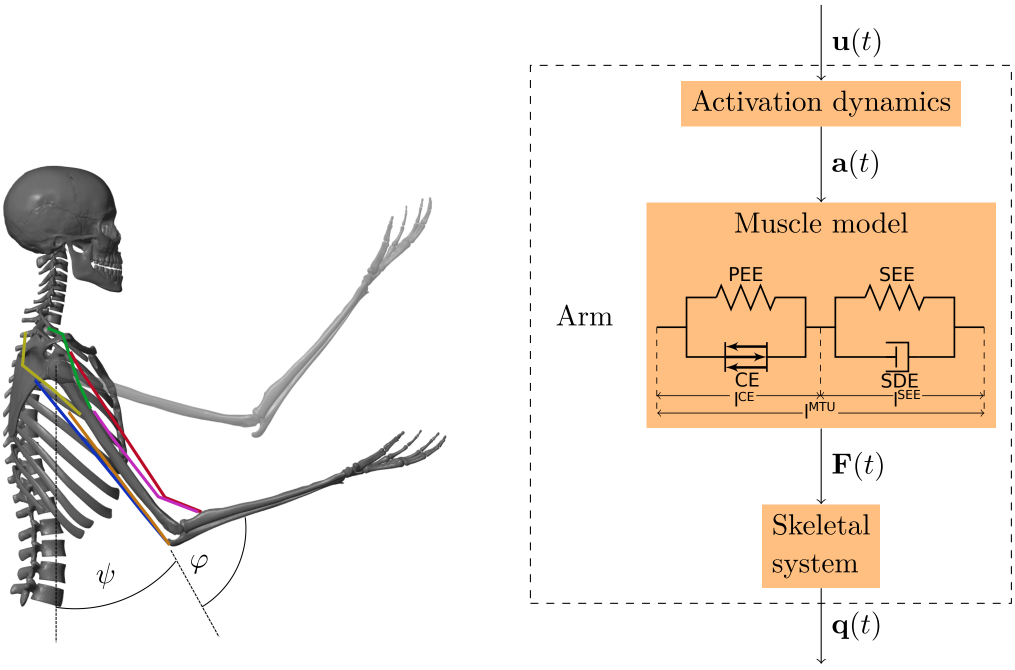

(a) (b)

Figure A.1.: (a) Visualization of the musculoskeletal model of the arm and the definition of the shoulder angle $\psi(t)$ and the elbow angle $\varphi(t)$ and (b) Structure of the arm model: the motor command $\mathbf{u}(t)$ is fed into the model of the activation dynamics of muscles which relates the neuronal stimulation to muscular activity $\mathbf{a}(t)$ that drives the muscle model. The muscles produce forces $\mathbf{F}(t)$ that act on the skeletal system resulting in a simulated movement $\mathbf{q}(t) = [\varphi(t), \psi(t)]$ of the arm.

This supplementary material describes the neuro-musculoskeletal model *Arm26* modeling a reduced human arm model. Large parts of the following model description were published as electronic supplementary material accompanying Stollenmaier et al. (2020); Wochner et al. (2020). The code and an actively maintained version of this description can be found online (Wochner and Schmitt, 2022). The neuro-musculoskeletal model *Arm26* consists of a musculoskeletal model of the arm with two degrees of freedom actuated by six muscles and a controller. The model is implemented in C/C++ code within the freely available multi-body software demoa (Schmitt, 2022). For a better overview, the implementation of the model is divided into three parts: the mechanical part (representing the bone structure and the muscle routing), the actuation of this mechanical part (muscle-tendon structures) and the controller (nervous system) which provides the input to the actuation part.

A.1. Musculoskeletal model of the arm: Mechanics and Actuation

The musculoskeletal model *Arm26* of the human arm uses the same geometry and muscle parameters as the simulation model described in Driess et al. (2018) which is based on Bayer et al. (2017). It consists of two rigid bodies (lower and upper arm) that are connected via two one-degree-of-freedom revolute joints that represent the shoulder and elbow joint. This multibody system is actuated by six muscle-tendon units (MTU), four monoarticular and two biarticular muscles (see Figure A.1a). The muscles are modeled as lumped muscles, i.e. they represent a multitude of anatomical muscles:

1. monarticular elbow flexor (MEF) (short: elbow flexion (EF)):
   m. brachioradialis, m. brachialis, m. pronator teres, m. extensor carpi radialis
2. monarticular elbow extensor (MEE) (short: elbow extension (EE)):
   m. triceps lateralis, m.triceps medialis, m. an-coneus, m. extensor carpi ulnaris
3. biarticular elbow flexor shoulder anteversion (BEFSA) (short: biarticular flexor (BF)):
   m. biceps brachii caput longum and caput breve
4. biarticular elbow extensor shoulder retroversion (BEESR) (short: biarticular extensor (BE)):
   m. triceps brachii caput longum
5. monoarticular shoulder anteversion (MSA) (short: shoulder flexion (SF)):
   m. deltoideus (pars clavicularis, anterior, lateral), m. superior pectoralis major, m. coracobrachialis
6. monoarticular shoulder retroversion (MSR) (short: shoulder extension (SE)):
   m. deltoideus (pars spinalis, posterior), m. latissimus dorsi

The MTU structure is modeled using an extended Hill-type muscle model as described in Haeufle et al. (2014c) with muscle activation dynamics as introduced by Hatze (1977). The muscle model is a macroscopic model consisting of four elements: the contractile element (CE), the parallel elastic element (PEE) and the serial elastic element (SEE) and serial damping element (SDE), as illustrated in Figure A.1b. The inputs to the muscle model are the length of the MTU l^{MTU}, the contraction velocity of the MTU $\dot{l}^{\mathrm{MTU}}$ and the muscular activity a. The output of the muscle model is a one-dimensional muscle force F^{MTU}. This force drives the movement of the skeletal system. For the routing of the muscle path around the joints, deflection ellipses are implemented as described by Hammer et al. (2019) (see Figure A.2). The muscle path can move within these ellipses and is deflected as soon as it touches the boundary.

All in all, the governing model dependencies for all muscles $i = 1, ..., n$ are:

$$\dot{l}_i^{\mathrm{CE}} = f_{\mathrm{CE}}(l_i^{\mathrm{CE}}, l_i^{\mathrm{MTU}}, \dot{l}_i^{\mathrm{MTU}}, a_i) \tag{A.1}$$

$$\dot{a}_i = f_a(a_i, u_i, l_i^{\mathrm{CE}}) \tag{A.2}$$

$$F_i^{\mathrm{MTU}} = f_F(l_i^{\mathrm{MTU}}, \dot{l}_i^{\mathrm{MTU}}, l_i^{\mathrm{CE}}, a_i) \tag{A.3}$$

$$\ddot{\mathbf{q}} = f_q(\dot{\mathbf{q}}, \mathbf{q}, \mathbf{F}^{\mathrm{MTU}}), \tag{A.4}$$

where $\mathbf{q}$ denotes a generalized state vector, in this case it can be defined as $\mathbf{q} = [\varphi, \psi]$ and $\mathbf{F}^{\mathrm{MTU}} = \{F_i^{\mathrm{MTU}}\}_{i=1}^{n}$.

The mechanical parameters of the arm segments are taken from Kistemaker et al. (2006) and can be found in Table A.1. The positions and sizes of the deflection ellipses were chosen in order to match moment arms in literature (see Figure A.3). For more details on this see Suissa (2017). The (non-)muscle-specific parameters can be found in Table A.2 and Table A.3.

	Length [m]	d [m]	Mass [kg]	I [kgm^2]
Upper arm	0.335	0.146	2.10	0.024
Lower arm	0.263	0.179	1.65	0.025

Table A.1.: Mechanical parameters of the skeletal structure (Kistemaker et al. (2006)) with d: distance from proximal joint to center of mass and I: moment of inertia with respect to the center of mass.

	$F^{\max}$ [N]	$l^{\mathrm{CE,opt}}$ [m]	$l^{\mathrm{SEE,0}}$ [m]
monarticular elbow flexor (MEF)	1420	0.092	0.182
monarticular elbow extensor (MEE)	1550	0.093	0.187
monoarticular shoulder anteversion (MSA)	838	0.134	0.039
monoarticular shoulder retroversion (MSR)	1207	0.140	0.066
biarticular elbow flexor shoulder anteversion (BEFSA)	414	0.151	0.245
biarticular elbow extensor shoulder retroversion (BEESR)	603	0.152	0.260

Table A.2.: Muscle-specific actuation parameters (Kistemaker et al. (2006) and Kistemaker et al. (2013)), with $F^{\max}$: maximum isometric force, $l^{\mathrm{CE,opt}}$: optimal length of the contractile element, $l^{\mathrm{SEE,0}}$ rest length of the serial elastic element. The lengths of $l^{\mathrm{CE,opt}}$ and $l^{\mathrm{SEE,0}}$ were adapted to match the muscle path routed through the ellipses in order to allow for a big range of motion. For this parameter adaptation method see Suissa (2017).

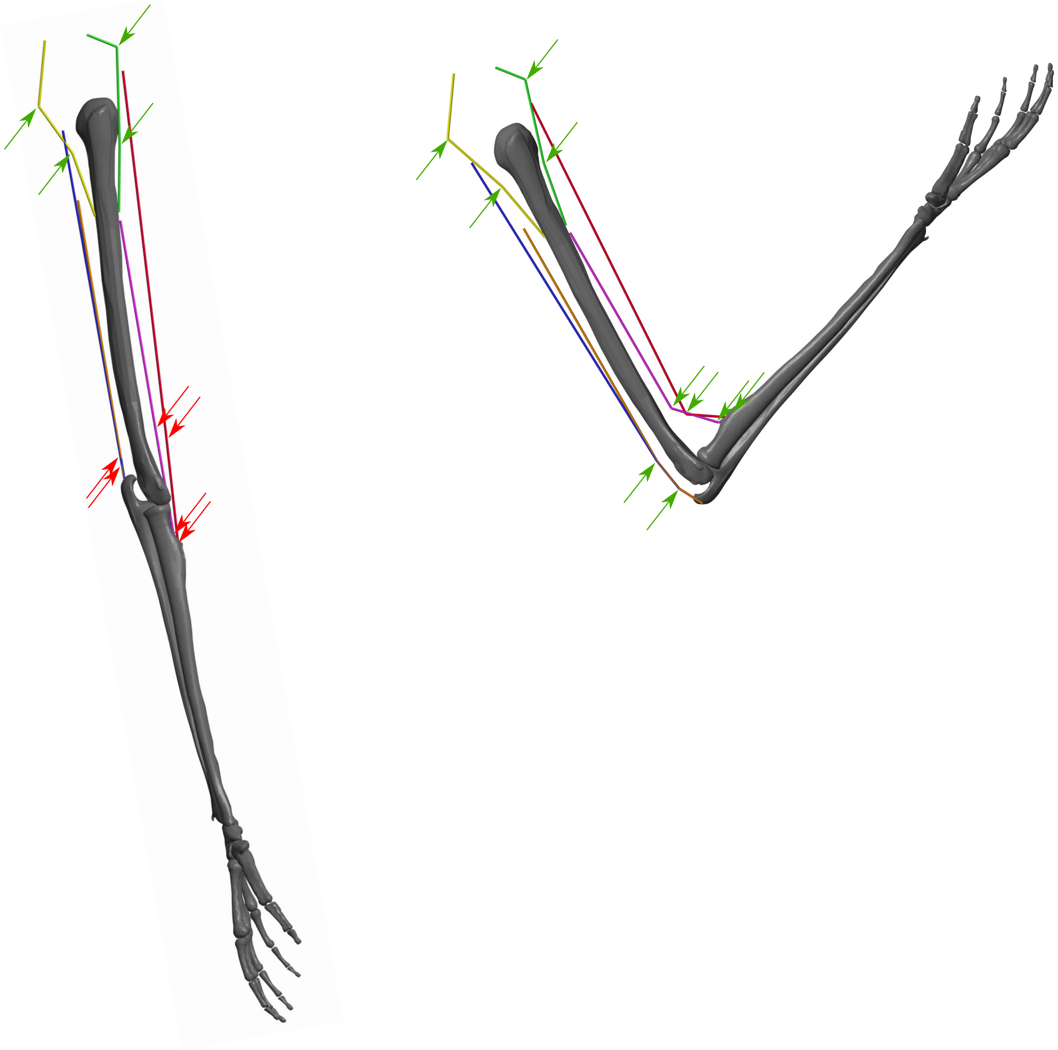

Figure A.2.: Illustration of the positions of the deflection ellipses that are used for the muscle routing in two different arm positions. Green arrows indicate active ellipses that deflect the muscle path, while red arrows indicate inactive ellipses that do not change the muscle path.

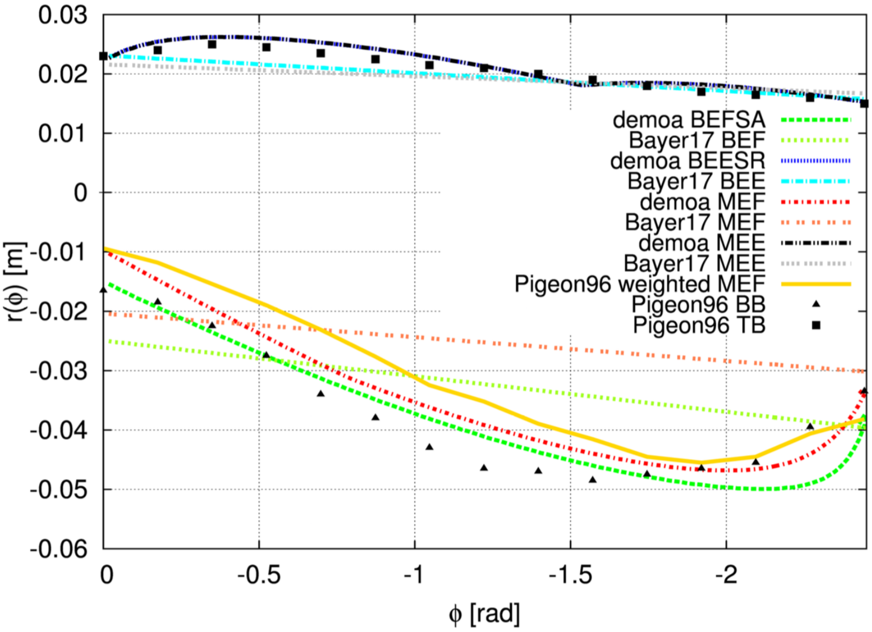

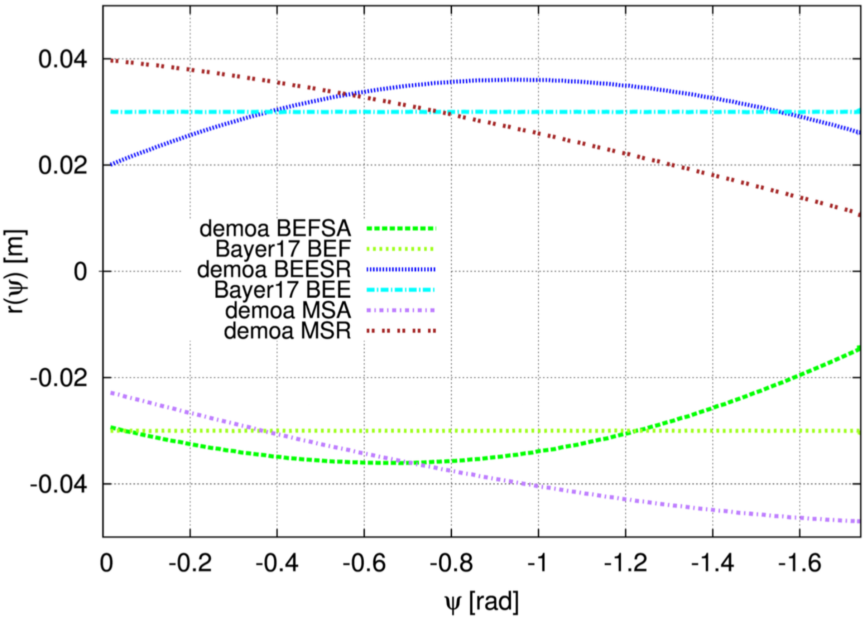

Figure A.3.: Comparison of the moment arms of the muscles in the model with simulation and experimental data from literature for the elbow muscles (upper plot) and the shoulder muscles (lower plot). The lines marked with “demoa” refer to our model (for the naming of the muscles see Table A.2). The moment arms are compared to a calculatory model by Bayer et al. (2017) (here M/B stands for mono- and biarticular, E stands for elbow and F/E stands for flexion and extension, respectively) and to experimental data. The black marks show experimental data of the biceps brachii (BB) and the triceps brachii (TB) taken from Pigeon et al. (1996). The yellow line shoes a weighted combination of the monoarticular flexor muscles that are represented by the MEF in the model. They are weighted according to their proportion of the joint torques, see Sobotta (2010); Aumüller et al. (2017). The figure was taken from Suissa (2017) with kind permission of the author.

	Parameter	Unit	Value	Source	Description
CE	ΔW^{des}	[ ]	0.45	similar to Bayer et al. (2017); Kistemaker et al. (2006)	width of normalized bell curve in descending branch, adapted to match observed force-length curves
	ΔW^{asc}	[ ]	0.45	similar to Bayer et al. (2017); Kistemaker et al. (2006)	width of normalized bell curve in ascending branch, adapted to match observed force-length curve
	$\nu^{\text{CE,des}}$	[ ]	1.5	Mörl et al. (2012)	exponent for descending branch
	$\nu^{\text{CE,asc}}$	[ ]	3.0	Mörl et al. (2012)	exponent for ascending branch
	$A^{\text{rel},0}$	[ ]	0.2	Günther (1997)	parameter for contraction dynamics: maximum value of A^{rel}
	$B^{\text{rel},0}$	[1/s]	2.0	Günther (1997)	parameter for contraction dynamics: maximum value of B^{rel}
	$\mathcal{S}^{\text{ecc}}$	[ ]	2.0	van Soest and Bobbert (1993)	relation between $F(v)$ slopes at $v^{\text{CE}} = 0$
	$\mathcal{F}^{\text{ecc}}$	[ ]	1.5	van Soest and Bobbert (1993)	factor by which the force can exceed F^{isom} for large eccentric velocities
PEE	$\mathcal{L}^{\text{PEE},0}$	[ ]	0.95	Günther (1997)	rest length of PEE normalized to optimal length of CE
	ν^{PEE}	[ ]	2.5	Mörl et al. (2012)	exponent of F^{PEE}
	$\mathcal{F}^{\text{PEE}}$	[ ]	2.0	Mörl et al. (2012)	force of PEE if l^{CE} is stretched to ΔW^{des}
SDE	D^{SDE}	[ ]	0.3	Mörl et al. (2012)	dimensionless factor to scale $d^{\text{SDE,max}}$
	R^{SDE}	[ ]	0.01	Mörl et al. (2012)	minimum value of d^{SDE} (at $F^{MTU} = 0$), normalized to $d^{\text{SDE,max}}$
SEE	$\Delta U^{\text{SEE,nll}}$	[ ]	0.0425	Mörl et al. (2012)	relative stretch at nonlinear linear transition
	$\Delta U^{\text{SEE,l}}$	[ ]	0.017	Mörl et al. (2012)	relative additional stretch in the linear part providing a force increase of $\Delta F^{\text{SEE},0}$
	$\Delta F^{\text{SEE},0}$	[N]	$0.4\,F^{\text{max}}$		both force at the transition and force increase in the linear part
Hatze	m	[1/s]	11.3	Kistemaker et al. (2006)	time constant for the activation dynamics
	c	[mol/l]	1.37e-4	Kistemaker et al. (2006)	constant for the activation dynamics
	η	[l/mol]	5.27e4	Kistemaker et al. (2006)	constant for the activation dynamics
	k	[ ]	2.9	Kistemaker et al. (2006)	constant for the activation dynamics
	q_0	[ ]	0.005	Günther (1997)	resting active state for all activated muscle fibers
	ν	[ ]	3	Kistemaker et al. (2006)	constant for the activation dynamics

Table A.3.: Muscle non-specific actuation parameters for the muscles and the activation dynamics.

Name	Type	Movement	Range of Motion (RoM) [rad]
Shoulder	Revolute	flexion/extension	$[-1.75 \ldots 0.7]$
Elbow	Revolute	flexion/extension	$[-2.45 \ldots 0]$
Wrist	Revolute	flexion/extension	$[0 \ldots 0]$

Table A.4.: List of all joints included in the model.

A.2. The Multibody System

The skeletal system is modeled as a chain of rigid bodies, connected by rotational joints and described by differential equations. The resulting Degrees of Freedom (DoFs) $\mathcal{Q}(t) = [q_1(t), \ldots, q_{n_\text{DoF}}(t)]^T \in \mathbb{R}^{n^\text{DoF}}$ of these rotational joints describe the movement of the rigid bodies over time and are referred to as generalized coordinates. For the equations of motion, a Lagrangian formulation with the generalized coordinates $\mathcal{Q}(t)$ as state variables is realized, which can be set up algorithmically, e.g. as described by Legnani et al. (1996). The evaluation of this algorithm leads to the differential equation of motion of the rigid body system in the form

$$\mathbf{M}(\mathcal{Q})\ddot{\mathcal{Q}} + C(\mathcal{Q}, \dot{\mathcal{Q}}) = \mathcal{F}, \tag{A.5}$$

where $\mathbf{M} \in \mathbb{R}^{n^\text{DoF} \times n^\text{DoF}}$ is the mass matrix, $C \in \mathbb{R}^{n^\text{DoF}}$ is a vector of gravitational, centrifugal and Coriolis forces and $\mathcal{F} \in \mathbb{R}^{n_\text{DoF}}$ is a vector of forces (internal and external) acting on the mechanical part of the system. Hereby $\mathcal{F}$ includes forces, e.g. due to contact of the body to the environment (external), as well as forces of the biological structures, such as muscles, joint limitations (internal).

A.3. Joint limitations

The joint limitations are modeled as linear one-sided spring-damper elements, acting directly on the respective DoF:

$$f_i^\text{lmt} = \begin{cases} k_l(q_i - q_{l,i}) + d_l\dot{q}_i, & q_i < q_{l,i} \\ 0, & q_{l,i} \leq q_i \leq q_{u,i} \\ k_u(q_i - q_{u,i}) + d_u\dot{q}_i, & q_i > q_{u,i} \end{cases} \tag{A.6}$$

with the lower and upper threshold angles $q_{l/u}$, corresponding to the respective RoM (Table A.4), and linear spring and damping parameters $k_{l/u} = 1000\,[\frac{\text{Nm}}{\text{rad}}]$ and $d_{l/u} = 10\,[\frac{\text{Nm}\cdot\text{s}}{\text{rad}}]$.

B. Allmin: A Reduced Human All-Body Model

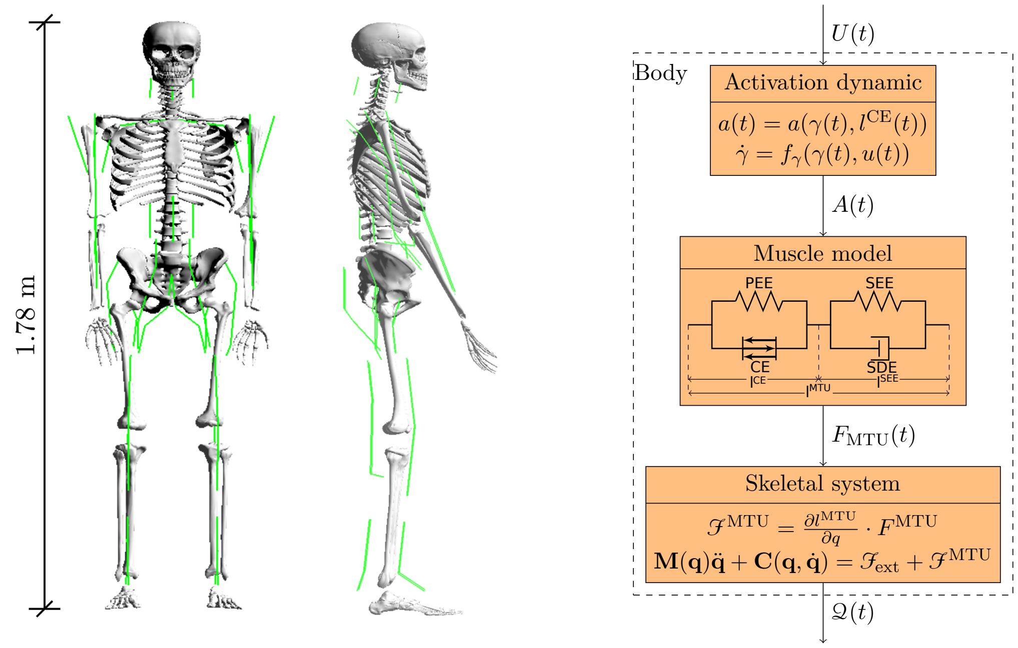

(a) (b)

Figure B.1.: (a) Frontal and side view of the visualization of the musculoskeletal model of the human body. The green lines show the muscle geometry. (c) Structure of the model: the motor command $U(t) \in \mathbb{R}^{n^{\mathrm{MTU}}}$ is fed into the model of activation dynamics (Hatze, 1977; Rockenfeller and Günther, 2018) of muscles which relates the neuronal stimulation to muscular activity $A(t) \in \mathbb{R}^{n^{\mathrm{MTU}}}$ that drives the muscle model (Haeufle et al., 2014c). The muscles produce forces $F^{\mathrm{MTU}}(t) \in \mathbb{R}^{n^{\mathrm{MTU}}}$ that act on the rigid bodies of the skeletal system. The resultant joint torques $\mathcal{T}^{\mathrm{MTU}}$ depend on the respective moment arms $\frac{\partial l^{\mathrm{MTU}}}{\partial q}$. In combination with external forces, this results in a movement of the DoFs $\mathbf{q}(t) \in \mathbb{R}^{n^{\mathrm{DoF}}}$ of the body.

This supplementary material describes the neuromusculoskeletal model *allmin* modeling a reduced whole-body model. Large parts of the following model description were published as electronic supplementary material accompanying Walter et al. (2021); Wochner et al. (2022b). The code and an actively maintained version of this description can be found online (Walter et al., 2022). The musculoskeletal model *allmin* consists of $n^{\mathrm{RGB}} = 15$ rigid bodies (see

Table B.1). The rigid bodies are connected via 14 joints (see Table B.2) including $n^{\mathrm{DoF}} = 20$ degrees of freedom. Each Degree of Freedom (DoF) (except for the wrist) is controlled by an agonistic-antagonistic setup (AAS) beeing congruent with the elementary biological drive (EBD) as described by Schmitt et al. (2019). The musculoskeletal model is actuated by $n^{\mathrm{MTU}} = 36$ MTU (see Table B.4 and Figure B.1a for first impression).

The model is implemented in C/C++ code within the freely available multi-body software demoa (Schmitt, 2022).

B.1. The Multibody System

The skeletal system is modeled as a chain of rigid bodies, connected by rotational joints and described by differential equations. The resulting DoFs $\mathbf{q}(t) = [q_1(t), \ldots, q_{n^{\mathrm{DoF}}}(t)]^T \in \mathbb{R}^{n^{\mathrm{DoF}}}$ of these rotational joints describe the movement of the rigid bodies over time and are referred to as generalized coordinates. For the equations of motion, a Lagrangian formulation with the generalized coordinates $\mathbf{q}(t)$ as state variables is realized, which can be set up algorithmically, e.g. as described by Legnani et al. (1996). The evaluation of this algorithm leads to the differential equation of motion of the rigid body system in the form

$$\mathbf{M}(\mathbf{q})\ddot{\mathbf{q}} + \mathbf{C}(\mathbf{q}, \dot{\mathbf{q}}) = \mathcal{F}, \tag{B.1}$$

where $\mathbf{M} \in \mathbb{R}^{n^{\mathrm{DoF}} \times n^{\mathrm{DoF}}}$ is the mass matrix, $\mathbf{C} \in \mathbb{R}^{n^{\mathrm{DoF}}}$ is a vector of gravitational, centrifugal and Coriolis forces and $\mathcal{F} \in \mathbb{R}^{n_{\mathrm{DoF}}}$ is a vector of forces (internal and external) acting on the mechanical part of the system. Hereby $\mathcal{F}$ includes forces, e.g. due to contact of the body to the environment (external), as well as forces of the biological structures, such as muscles, joint limitations (internal).

B.2. Joint limitations

The joint limitations are modeled as linear one-sided spring-damper elements, acting directly on the respective DoF:

$$f_i^{\mathrm{lmt}} = \begin{cases} k_l(q_i - q_{l,i}) + d_l\dot{q}_i, & q_i < q_{l,i} \\ 0, & q_{l,i} \le q_i \le q_{u,i} \\ k_u(q_i - q_{u,i}) + d_u\dot{q}_i, & q_i > q_{u,i} \end{cases} \tag{B.2}$$

with the lower and upper threshold angles $q_{l/u}$, corresponding to the respective RoM (Table B.2), and linear spring and damping parameters $k_{l/u} = 50\,[\frac{\mathrm{Nm}}{\mathrm{deg}}]$ and $d_{l/u} = 10\,[\frac{\mathrm{Nm{\cdot}s}}{\mathrm{deg}}]$. For the elbow joint q_{el}, the wrist q_{wr}, as well as the knee q_{kn} and ankle joint q_{ank} the same force law is used to model passive properties but with different parameters. The upper and lower threshold angles are set as shown in Table B.2 and the spring and damping parameters are set to $k_{el} = 100\,[\frac{\mathrm{Nm}}{\mathrm{deg}}]$, $d_{el} = 0.001\,[\frac{\mathrm{Nm{\cdot}s}}{\mathrm{deg}}]$, $k_{wr} = 15\,[\frac{\mathrm{Nm}}{\mathrm{deg}}]$, $d_{wr} = 1\,[\frac{\mathrm{Nm{\cdot}s}}{\mathrm{deg}}]$, $k_{kn,ank} = 20\,[\frac{\mathrm{Nm}}{\mathrm{deg}}]$, $d_{kn,ank} = 1\,[\frac{\mathrm{Nm{\cdot}s}}{\mathrm{deg}}]$.

B.3. Muscles

The muscles are modeled as lumped muscles, i.e. they represent a multitude of anatomical muscles and motor units. A list of all included muscle elements can be found in Table B.4. The MTU structure is modeled using an extended Hill-type muscle model as described in Haeufle et al. (2014c) with muscle activation dynamics as introduced by Hatze (1977) and simplified by Rockenfeller and Günther (2018). Herein, the muscles are activated using a 1st order differential equation of normalized calcium ion concentration (Rockenfeller et al., 2014)

$$\dot{\gamma}(t) = M^{\mathrm{H}}(u(t) - \gamma(t)) \tag{B.3}$$

and a nonlinear mapping onto the muscles activation

$$a(t) = \frac{a^{\mathrm{nll}} + \varpi}{1 + \varpi}, \tag{B.4}$$

with $\varpi(\gamma(t), l^{\mathrm{CE}}(t)) = (\gamma(t) \cdot \rho(l^{\mathrm{CE}}))^{\nu}$ and $\rho(l^{\mathrm{CE}}) = \varpi_{\mathrm{opt}} \cdot \frac{l^{\mathrm{CE}}}{l^{\mathrm{CE,opt}}} = \gamma^{\mathrm{c}} \cdot \rho^{\mathrm{nll}} \cdot \frac{l^{\mathrm{CE}}}{l^{\mathrm{CE,opt}}}$. The parameter values are chosen muscle non specifically and are given in Table B.5.

The muscle model is a macroscopic model consisting of four elements: the CE, the PEE, the SEE and SDE, as illustrated in Figure B.1b. Herein, the muscle fibers and their contraction dynamics are described by a contractile element (CE) representing the cross-bridge-cycle of the myosin heads and a parallel elastic element (PEE) representing the passive connective tissue in the muscle belly. The viscoelastic properties of tendons are approximated using a series elastic element (SEE) and a serial damping element (SDE).

The inputs to the muscle model are the length of the MTU l^{MTU}, the contraction velocity of the MTU $\dot{l}^{\mathrm{mtu}}$ and the muscular activity a. The output of the muscle model is a one-dimensional muscle force F^{MTU}. This force drives the movement of the skeletal system.

For the routing of the muscle path around the joints, deflection ellipses are implemented as described by Hammer et al. (2019). The muscle path can move within these ellipses and is deflected as soon as it touches the boundary. For the investigations presented here, we set the length of both half-axes of all ellipses to zero, resulting in fixed via points. The position of these points can be found in Table B.3. The resulting moment arms translate the muscle force F^{MTU} to generalized forces $\mathscr{F}^{\mathrm{MTU}}$ acting on the DoFs of the system

$$\mathscr{F}^{\mathrm{MTU}} = \frac{\partial l^{\mathrm{MTU}}}{\partial q} \cdot F^{\mathrm{MTU}}. \tag{B.5}$$

All in all, the governing model dependencies for all muscles $i = 1, ..., n$ are:

$$
\begin{aligned}
\dot{l}_i^{\mathrm{CE}} &= f^{\mathrm{CE}}(l_i^{\mathrm{CE}}, l_i^{\mathrm{MTU}}, \dot{l}_i^{\mathrm{MTU}}, a_i) && \text{(B.6)}\\
\dot{a}_i &= f^{a}(a_i, u_i, l_i^{\mathrm{CE}}) && \text{(B.7)}\\
F_i^{\mathrm{MTU}} &= f^{\mathrm{MTU}}(l_i^{\mathrm{MTU}}, \dot{l}_i^{\mathrm{MTU}}, l_i^{\mathrm{CE}}, a_i) && \text{(B.8)}\\
\ddot{q} &= f^{q}(\dot{q}, q, F^{\mathrm{MTU}}, \mathscr{F}^{\mathrm{lmt}}, \mathscr{F}^{\mathrm{ext}}), && \text{(B.9)}
\end{aligned}
$$

where $q = \{q_i\}_{i=1}^{n^{\mathrm{DoF}}}$ denotes a generalized state vector that contains all joint angles and $F^{\mathrm{MTU}} = \left\{F_i^{\mathrm{MTU}}\right\}_{i=1}^{n}$, $\mathscr{F}^{\mathrm{lmt,i}} = \left\{f_i^{\mathrm{lmt}}\right\}_{i=1}^{n}$ and $\mathscr{F}^{\mathrm{ext}} = \left\{f_i^{\mathrm{ext}}\right\}_{i=1}^{n}$ contain the muscle forces, the joint limitation forces and the external forces, respectively.

B.4. Model parameters

Body Name	m [kg]	r_x [m]	r_y [m]	h_z [m]	$\mathbf{d}_1$ $[m]$	Child	$\mathbf{d}_2$ $[m]$
Pelvis (world)	10.2516	0.1224	0.1643	0.18783	[0,0,0]	Spine	[0.000557293, 0.0000, 0.12213]
						Thigh (l/r)	$[0.0147, \pm 0.0796, -0.0657]$
Spine	33.2397	0.1224	0.1643	0.4166	[-0.00055, 0.0000, -0.2083]	Head	[0.00055, 0.0000, 0.2083]
						Uparm (l/r)	$[0.00677703, \pm 0.1816, 0.10507988]$
Head	4.8869	0.0993	0.0778	0.278194	[-0.0092, 0.0000, -0.11]	-	-
Uparm (l/r)	2.1631	0.0495	–	0.3065	[0.0000, 0.0000, 0.1456]	Forearm (l/r)	[0.0000, 0.0000, -0.1609]
Forearm (l/r)	1.3389	0.0477	–	0.2725	[0.0000, 0.0000, 0.1117]	Hand (l/r)	[0.0000, 0.0000, -0.1608]
Hand (l/r)	0.5252	0.028	0.089	0.192	[0.0000, 0.0000, 0.0574]	-	-
Thigh (l/r)	8.1719	0.0947	–	0.4347	$[0.0000, \mp 0.0188, 0.1782]$	Shank (l/r)	[0.0000, 0.0000, -0.2565]
Shank (l/r)	3.3541	0.0597	–	0.4239	$[0.0000, \mp 0.0059, 0.1865]$	Foot (l/r)	[0.0000, 0.0000, -0.2374]
Foot (l/r) $*$	1.0172	0.0398	–	0.272	[-0.0656, 0.0000, 0.0402]	-	-

Table B.1.: List of all bodies included in the model with their mechanical properties with m: mass, r_x,r_y: radius in x and y direction, h_z: height in z direction, $\mathbf{d}_1$: distance proximal joint to the body's center of mass and $\mathbf{d}_2$: distance center of mass to distal joint. The spine body has an underlying curvature based on Kitazaki and Griffin (1997). The allover body dimensons are based on data describing a 50th percentile male from NASA (1978).

Name	Type	Movement	RoM [°]
Lumbar spine	Universal	left/right	$[-30 \dots 30]$
Lumbar spine	Universal	flexion/extension	$[0 \dots 30]$
Cervival spine	Universal	left/right	$[-30 \dots 30]$
Cervival spine	Universal	flexion/extension	$[-30 \dots 30]$
Shoulder (Right)	Universal	abduction/adduction	$[-10 \dots 60]$
Shoulder (Right)	Universal	flexion/extension	$[-100 \dots 10]$
Ellbow (Right)	Revolute	flexion/extension	$[-120 \dots 10]$
Wrist (Right)	Revolute	flexion/extension	$[0 \dots 0]$
Shoulder (Left)	Universal	abduction/adduction	$[-10 \dots 60]$
Shoulder (Left)	Universal	flexion/extension	$[-100 \dots 10]$
Ellbow (Left)	Revolute	flexion/extension	$[-120 \dots 10]$
Wrist (Left)	Revolute	flexion/extension	$[0 \dots 0]$
Hip (Right)	Universal	flexion/extension	$[-120 \cdots - 10]$
Hip (Right)	Universal	abduction/adduction	$[-10 \dots 70]$
Knee (Right)	Revolute	flexion/extension	$[-1 \dots 120]$
Ankle (Right)	Revolute	flexion/extension	$[-20 \dots 40]$
Hip (Left)	Universal	flexion/extension	$[-120 \dots 10]$
Hip (Left)	Universal	abduction/adduction	$[-10 \dots 70]$
Knee (Left)	Revolute	flexion/extension	$[-1 \dots 120]$
Ankle (Left)	Revolute	flexion/extension	$[-20 \dots 40]$

Table B.2.: List of all joints included in the model.

Name	R_O [m]			Parent	R_{DF1} [m]			Parent	R_{DF2} [m]			Parent	R_I [m]			Parent
LSE	−0.028	0.000	0.108	Pelvis	−0.040	0.000	0.110	Pelvis	−0.042	0.000	−0.131	Spine	−0.032	0.000	−0.129	Spine
LSF	0.018	0.000	0.101	Pelvis	0.088	0.000	0.089	Pelvis	0.069	0.000	−0.106	Spine	0.009	0.000	−0.120	Spine
LSSBL	−0.005	0.050	0.104	Pelvis	−0.005	0.050	0.104	Pelvis	−0.011	0.050	−0.124	Spine	−0.011	0.050	−0.124	Spine
LSSBR	−0.005	−0.050	0.104	Pelvis	−0.005	−0.050	0.104	Pelvis	−0.011	−0.050	−0.124	Spine	−0.011	−0.050	−0.124	Spine
CSE	−0.054	0.000	0.199	Spine	−0.054	0.000	0.199	Spine	−0.056	0.000	−0.070	Head	−0.056	0.000	−0.070	Head
CSF	0.043	0.000	0.175	Spine	0.043	0.000	0.175	Spine	0.044	0.000	−0.080	Head	0.044	0.000	−0.080	Head
CSSBL	−0.006	0.050	0.187	Spine	−0.006	0.050	0.187	Spine	−0.006	0.050	−0.075	Head	−0.006	0.050	−0.075	Head
CSSBR	−0.006	−0.050	0.187	Spine	−0.006	−0.050	0.187	Spine	−0.006	−0.050	−0.075	Head	−0.006	−0.050	−0.075	Head
HE (l/r)	−0.075	±0.080	0.025	Pelvis	−0.075	±0.090	−0.095	Pelvis	−0.075	∓0.019	0.121	Thigh	−0.020	∓0.009	0.031	Thigh
HF (l/r)	0.065	±0.040	0.101	Pelvis	0.075	±0.040	0.021	Pelvis	0.015	∓0.019	0.101	Thigh	0.015	∓0.019	0.020	Thigh
HAbd (l/r)	−0.025	±0.120	0.050	Pelvis	0.000	±0.152	−0.030	Pelvis	−0.030	±0.040	0.035	Thigh	−0.020	±0.030	0.005	Thigh
HAdd (l/r)	0.000	0.000	0.000	Pelvis	−0.010	±0.010	−0.100	Pelvis	−0.005	∓0.035	0.090	Thigh	0.000	∓0.020	0.010	Thigh
KF (l/r)	−0.050	0.000	0.000	Thigh	−0.050	0.000	−0.108	Thigh	−0.059	0.000	0.106	Shank	−0.030	0.000	0.100	Shank
KE (l/r)	0.040	0.000	0.000	Thigh	0.030	0.000	0.253	Thigh	0.030	0.000	0.050	Shank	0.030	0.000	0.050	Shank
FE (l/r)	−0.050	0.000	−0.025	Shank	−0.050	0.000	−0.175	Shank	−0.125	0.000	0.050	Foot	−0.125	0.000	0.050	Foot
FF (l/r)	0.030	0.000	−0.025	Shank	0.030	0.000	−0.175	Shank	0.030	0.000	0.050	Foot	0.030	0.000	0.050	Foot
SE (l/r)	−0.069	±0.182	0.113	Spine	−0.050	0.000	0.125	Uparm	−0.017	0.000	0.000	Uparm	−0.017	0.000	0.000	Uparm
SF (l/r)	0.022	±0.182	0.139	Spine	0.022	±0.182	0.139	Spine	0.017	0.000	0.000	Uparm	0.017	0.000	0.000	Uparm
SAbd (l/r)	−0.026	±0.242	0.135	Spine	−0.026	±0.242	0.135	Spine	0.000	±0.017	0.000	Uparm	0.000	±0.017	0.000	Uparm
SAdd (l/r)	−0.024	0.000	0.126	Spine	0.007	±0.125	0.103	Spine	0.000	∓0.040	0.125	Uparm	0.000	∓0.017	0.000	Uparm
EF (l/r)	0.025	0.000	0.000	Uparm	0.030	0.000	−0.050	Uparm	0.030	0.000	0.014	Forearm	0.024	0.000	−0.100	Forearm
EE (l/r)	−0.025	0.000	0.000	Uparm	−0.049	0.000	−0.160	Uparm	−0.048	0.000	0.100	Forearm	−0.024	0.000	0.000	Forearm

Table B.3.: Muscle routing parameters: Origin R_O, Deflection Point 1 R_{DF1} and 2 R_{DF2} and Insertion R_I relative to their parent body. All numbers in this table are rounded to four decimal digits. Muscle names: EF, EE, foot flexion (FF), foot extension (FE), hip abduction (HAbd), hip adduction (HAdd), hip flexion (HF), hip extension (HE), cervical spine flexion (CSF), cervical spine side bend left (CSSBL), cervical spine side bend right (CSSBR), cervical spine extension (CSE), knee flexion (KF), knee extension (KE), lumbar spine flexion (LSF), lumbar spine side bend left (LSSBL), lumbar spine side bend right (LSSBR), lumbar spine extension (LSE), shoulder abduction (SAbd), shoulder adduction (SAdd), SF, SE.

	F^{max} [N]	$l^{\text{CE,opt}}$ [m]	ΔW^{asc}	$l^{\text{SEE,0}}$ [m]
EF	1420.0	0.1885	1.0	0.1845
EE	1550.0	0.171	0.525	0.18
FF	3000.0	0.15	1.0	0.133
FE	3000.0	0.13	1.0	0.115
HAbd	2000.0	0.18	1.0	0.121
HAdd	2000.0	0.204	0.75	0.136
HF	5000.0	0.195	1.0	0.135
HE	5000.0	0.192	1.0	0.191
CSF	5000.0	0.07	1.5	0.01
CSSBL	5000.0	0.05	1.5	0.01
CSSBR	5000.0	0.046	1.5	0.01
CSE	5000.0	0.062	1.5	0.01
KF	6000.0	0.258	0.525	0.112
KE	6000.0	0.264	1.0	0.28
LSF	15000.0	0.2	1.5	0.11
LSSBL	15000.0	0.09	1.5	0.02
LSSBR	15000.0	0.09	1.5	0.02
LSE	15000.0	0.075	1.5	0.04
SAbd	6000.0	0.12	1.0	0.08
SAdd	6000.0	0.225	1.0	0.12
SF	10000.0	0.1	1.0	0.073
SE	6000.0	0.165	1.0	0.105

Table B.4.: Muscle-specific actuation parameters, with F^{max}: maximum isometric force, $l^{\text{CE,opt}}$: optimal length of the CE, ΔW^{asc}: width of normalized bell curve in ascending branch of the force-length relationship, $l^{\text{SEE,0}}$ rest length of the SEE, $l^{\text{CE,init}}$: initial length of the CE. Muscle names: elbow flexion (EF), elbow extension (EE), foot flexion (FF), foot extension (FE), hip abduction (HAbd), hip adduction (HAdd), hip flexion (HF), hip extension (HE), cervical spine flexion (CSF), cervical spine side bend left (CSSBL), cervical spine side bend right (CSSBR), cervical spine extension (CSE), knee flexion (KF), knee extension (KE), lumbar spine flexion (LSF), lumbar spine side bend left (LSSBL), lumbar spine side bend right (LSSBR), lumbar spine extension (LSE), shoulder abduction (SAbd), shoulder adduction (SAdd), shoulder flexion (SF), shoulder extension (SE).

	Parameter	Unit	Value	Source	Description
CE	ΔW^{des}	[ ]	0.45	similar to Bayer et al. (2017); Kistemaker et al. (2006)	width of normalized bell curve in descending branch, adapted to match observed force-length curves
	$\nu^{\mathrm{CE,des}}$	[ ]	1.5	Mörl et al. (2012)	exponent for descending branch
	$\nu^{\mathrm{CE,asc}}$	[ ]	3.0	Mörl et al. (2012)	exponent for ascending branch
	$A^{\mathrm{rel},0}$	[ ]	0.2	Günther (1997)	parameter for contraction dynamics: maximum value of A^{rel}
	$B^{\mathrm{rel},0}$	[1/s]	2.0	Günther (1997)	parameter for contraction dynamics: maximum value of B^{rel}
	$\mathcal{S}^{\mathrm{ecc}}$	[ ]	2.0	van Soest and Bobbert (1993)	relation between $F(v)$ slopes at $v^{\mathrm{CE}} = 0$
	$\mathcal{F}^{\mathrm{ecc}}$	[ ]	1.5	van Soest and Bobbert (1993)	factor by which the force can exceed F^{isom} for large eccentric velocities
PEE	$\mathcal{L}^{\mathrm{PEE},0}$	[ ]	0.95	Günther (1997)	rest length of PEE normalized to optimal length of CE
	ν^{PEE}	[ ]	2.5	Mörl et al. (2012)	exponent of F^{PEE}
	$\mathcal{F}^{\mathrm{PEE}}$	[ ]	2.0	Mörl et al. (2012)	force of PEE if l^{CE} is stretched to ΔW^{des}
SDE	D^{SDE}	[ ]	0.3	Mörl et al. (2012)	dimensionless factor to scale $d^{\mathrm{SDE,max}}$
	R^{SDE}	[ ]	0.01	Mörl et al. (2012)	minimum value of d^{SDE} (at $F^{MTU} = 0$), normalized to $d^{\mathrm{SDE,max}}$
SEE	$\Delta U^{\mathrm{SEE,nll}}$	[ ]	0.0425	Mörl et al. (2012)	relative stretch at nonlinear linear transition
	$\Delta U^{\mathrm{SEE,l}}$	[ ]	0.017	Mörl et al. (2012)	relative additional stretch in the linear part providing a force increase of $\Delta F^{\mathrm{SEE},0}$
	$\Delta F^{\mathrm{SEE},0}$	[N]	$0.4\,F^{\mathrm{max}}$		both force at the transition and force increase in the linear part
activation dynamics	M^{H}	[1/s]	11.3	Kistemaker et al. (2006)	time constant for the activation dynamics
	γ^{c}	[mol/l]	1.37e-4	Kistemaker et al. (2006)	constant for the activation dynamics
	ρ^{nll}	[l/mol]	5.27e4	Kistemaker et al. (2006)	constant for the activation dynamics
	a^{nll}	[ ]	0.005	Günther (1997)	resting active state for all activated muscle fibers
	ν	[ ]	3	Kistemaker et al. (2006)	constant for the activation dynamics

Table B.5.: Muscle non-specific actuation parameters for the muscles and the activation dynamics.